TECHNISCHE UNIVERSITÄT WIEN



DISSERTATION

Control Strategies for On-Orbit Servicing Manipulators

Ausgeführt zum Zwecke der Erlangung des akademischen Grades eines
Doktors der technischen Wissenschaften (Dr. techn.)

unter der Leitung von
Univ.Prof. Dipl.-Ing. Dr.-Ing. Christian Ott (Betreuung)
E376
Institut für Automatisierungs- und Regelungstechnik

eingereicht an der
Technischen Universität Wien
Fakultät für Elektrotechnik und Informationstechnik

von
Ria Vijayan
Matrikelnummer: 12347553

Wien, August 2026

Studiendekan:	Univ.Prof. Dr.sc. Silvan Schmid
Betreuer:	Univ.Prof. Dipl.-Ing. Dr.-Ing. Christian Ott
Tag des Rigorosums:	30 Oktober, 2026
Prüfungsvorsitzender:	Univ.Prof. Dipl.-Ing. Dr.-Ing Christoph Mecklenbräuker
Erster Gutachter:	Prof. Dr. Miguel Angel Olivares-Mendez
Zweiter Gutachter:	Univ.Prof. Dipl.-Ing. Dr.-Ing. Wolfgang Kemmetmüller

ABSTRACT

The field of on-orbit servicing (OOS) is approaching commercial maturity as the demand for satellite repair, maintenance, and life extension increases. Robotics-based solutions typically involve a spacecraft equipped with a suite of tools, and some means to achieve automated docking and subsequent servicing of a malfunctioning satellite. The great benefit of having a robotic arm is that it expands the range of dexterous manipulation tasks, such as inspection, capture, and upgrade of components. The autonomous solutions demonstrated thus far have focused either on docking technologies or the capture of non-spinning, fully cooperative satellites. However, malfunctioning satellites may exhibit residual spin, thereby invalidating the assumption of zero spin, which adds significant complexities in guidance, navigation, and coordinated robot-spacecraft control.

This thesis specifically examines the case of spinning satellites. Current methods often fall short in these dynamic environments, where uncontrolled rotation imposes strict constraints on approach and capture. Additionally, the field lacks robust solutions for on-ground validation of space robots, as most testing platforms that compensate gravitational loads are limited to a few degrees of freedom (DoF). This thesis proposes a solution that can overcome these limitations and especially cope with the configuration-dependent loads of a seven-DoF robot. Therefore, the thesis addresses these gaps by investigating coordinated control and validation strategies tailored to servicing spinning satellites and more accurate hardware-in-the-loop ground testing.

The primary contributions of this thesis are: (1) a control framework unified across the pre- and post-capture phases, while handling multiple mission objectives in on-orbit servicing using a novel hierarchical decomposition adapted for spinning and uncooperative targets; (2) a new hybrid scheme unifying discrete and continuous task hierarchies, enabling robust and stable control of servicing platforms and robotic manipulators at differing control frequencies; (3) a generalized ground validation approach for space robot systems that allows external gravity compensation to be independent of both the offloading carrier design and coupling mechanisms. Analyses of the nullspace hierarchy across the different schemes and applications shed light on the structure, dimensions, existence, and stability of the proposed controllers. The validation of the proposed methods is supported by several simulation studies and experiments conducted at state-of-the-art facilities for on-ground testing of robotic missions. The methods were applied in ongoing OOS mission developments under ESA, EU, and CNES space programs. Thus, the thesis contributes novel approaches to improve the reliability and effectiveness of future OOS missions.

KURZFASSUNG

Der Bereich der Wartung im Orbit nähert sich der kommerziellen Reife, da die Nachfrage nach Reparatur, Wartung und Lebensdauerverlängerung von Satelliten steigt. Robotergestützte Lösungen umfassen in der Regel ein Raumfahrzeug, das mit einer Reihe von Werkzeugen sowie Möglichkeiten zum automatisierten Andocken und zur anschließenden Wartung eines defekten Satelliten ausgestattet ist. Der große Vorteil eines Roboterarms besteht darin, dass er das Spektrum an präzisen Manipulationsaufgaben erweitert, wie beispielsweise die Inspektion, das Einfangen und die Aufrüstung von Komponenten. Die bisher vorgestellten autonomen Lösungen konzentrierten sich entweder auf Andocktechnologien oder auf das Einfangen von nicht rotierenden, vollständig kooperativen Satelliten. Satelliten mit Fehlfunktionen können jedoch eine Restdrall aufweisen, wodurch die Annahme einer Nullrotation hinfällig wird, was die Führung, Navigation und koordinierte Steuerung von Roboter und Raumfahrzeug erheblich verkompliziert.

Diese These befasst sich speziell mit dem Fall rotierender Satelliten. Aktuelle Methoden stoßen in diesen dynamischen Umgebungen häufig an ihre Grenzen, da eine unkontrollierte Rotation das Anfliegen und Einfangen erheblich erschwert. Zudem mangelt es in diesem Bereich an robusten Lösungen für die Validierung von Weltraumrobotern am Boden, da die meisten Testplattformen, die Gravitationsbelastungen kompensieren, auf wenige Freiheitsgrade (DoF) beschränkt sind. Diese Arbeit schlägt eine Lösung vor, die diese Einschränkungen überwinden und insbesondere die konfigurationsabhängigen Belastungen eines Roboters mit sieben Freiheitsgraden bewältigen kann. Daher befasst sich die Arbeit mit diesen Lücken, indem sie koordinierte Steuerungs- und Validierungsstrategien untersucht, die speziell auf die Wartung rotierender Satelliten zugeschnitten sind, sowie genauere Hardware-in-the-Loop-Bodentests.

Die wichtigsten Beiträge dieser Arbeit sind: (1) ein Steuerungskonzept, das die Phasen vor und nach der Erfassung vereint und gleichzeitig mehrere Missionsziele bei Wartungsarbeiten im Orbit unter Verwendung einer neuartigen hierarchischen Zerlegung berücksichtigt, die für rotierende und unkooperative Ziele angepasst ist; (2) ein neues hybrides Schema, das diskrete und kontinuierliche Aufgabenhierarchien vereint und eine robuste und stabile Steuerung von Wartungsplattformen und Robotermanipulatoren bei unterschiedlichen Steuerfrequenzen ermöglicht; (3) ein verallgemeinerter Ansatz zur Bodenvalidierung für Weltraumrobotersysteme, der es ermöglicht, den Ausgleich der externen Schwerkraft unabhängig sowohl von der Konstruktion des Lastenträgers als auch von den Kopplungsmechanismen zu gestalten. Analysen der Nullraumhierarchie über die verschiedenen Schemata und Anwendungen hinweg geben Aufschluss über die Struktur, die Dimensionen, die

Existenz und die Stabilität der vorgeschlagenen Regler. Die Validierung der vorgeschlagenen Methoden wird durch mehrere Simulationsstudien und Experimente gestützt, die in hochmodernen Einrichtungen für Bodentests von Robotermissionen durchgeführt wurden. Die Methoden wurden im Rahmen laufender Entwicklungen für OOS-Missionen unter den Raumfahrtprogrammen von der ESA, EU und CNES angewandt. Somit liefert die Dissertation neuartige Ansätze zur Verbesserung der Zuverlässigkeit und Effektivität zukünftiger Wartungsmissionen im Orbit.

PREFACE

This research was conducted between 2021 and 2026 at the Institute of Robotics and Mechatronics (RM) of the German Aerospace Center (DLR) in Oberpfaffenhofen. The five years of research led to a learning experience far richer than I anticipated when I began. The credit for this journey is owed to the guidance of incredible advisors, collaboration with talented colleagues, and the support of family and friends.

It began when I realized I wanted to pursue my doctoral studies after reading and rereading a paper on advanced robust control, having reproduced its results on perhaps the eleventh read. The personal sense of triumph was a little intoxicating, and I knew then that I wanted to do my research in control theory. Given my background in space technologies, I wanted to combine the two domains. This pursuit brought me into the fortuitous guidance of the then department head at RM and now professor of robotics at TUW, Dr. Christian Ott. Robotics was never a conscious choice, but it seemed to have a way of following me around. That being said, I came to find robotics a very amicable field with well-behaved systems (at least the rigid-body manipulators) and the perfect playground for algebra and control theory.

I am deeply indebted to Professor Ott for his diligent and insightful guidance, without which this thesis would have been impossible, and this journey would have been a voyage without a compass. I have admired his ingenuity, rigor, and patience for detail over the five years of dedicated supervision. His humility and encouragement were my source of inspiration and motivation during this research.

I want to express my deepest gratitude to Dr. Marco De Stefano, who has been my closest collaborator, guide, and critic. I am grateful for his crucial support over long days of experiments at the OOS-Sim. I also learned a great deal about cogent exposition from him. Thanks to his unique ability to put himself in the shoes of a wider audience, the manuscripts we co-authored were much improved compared to my drafts.

Special thanks to Dr. Alexander Dietrich for many fruitful discussions on hierarchical control. It was a pleasure to find someone on a similar wavelength regarding pedagogy, and I'm very grateful to him for giving me the opportunity to deliver my first guest lecture.

I want to thank Prof. Dr. Alin Albu-Schäffer, under whose leadership the Institute of Robotics and Mechatronics is a cradle for research and collaboration. It is a pleasure to work at the lab with highly motivated colleagues dedicated to advancing the state of the art. It has been particularly rewarding to work in a collective atmosphere where peers encourage and celebrate each other's successes.

Several colleagues have played important roles in different capacities throughout this thesis. I

want to thank Bernhard Brunner, with whom the camaraderie established made work joyful and fun. I'm very grateful for his support and impressed by his balance of life. I want to thank Ribin, who has been a close friend and confidant, for reflecting on the frustrations and aspirations of life and research over multiple coffee breaks. Thanks to Seth for the honest conversations.

Thanks to numerous other colleagues who provided support that facilitated the research work. Thanks to M. Mühlbauer, M. Stelzer, A. Raffin, F. Beck, H. Singh, F. Elhardt, A. Shu, F. Sena, T. Vicariotto, M. Hansjorg, S. Engelhardt, A. Vögele, A. Kotow, M. Schmidt, L. Suchenwirth and J. Laskey. Thanks to M. Roa and M. Schedl, who have made me feel valued in the DIANE project. Thanks to Marco for entrusting me with coordinating the control team for the RISE project. This role unwittingly helped provide a mental balance between the uncertainty of research and the certainty of application. More often than not, I have benefited from my advisors and colleagues having more faith in my abilities than I did myself. For this, I am immensely grateful.

My hours of research would not have been balanced without the after-hours with my friends. I'm especially grateful to Manish, who has been my pillar of support and anchor of wisdom through the years. Munich would not have felt like home if it weren't for Olivia (and Mira). Thanks to Olivia for the warmth, laughter, and bright spark of energy. Thanks to dearest Pavi, who's been by my side since childhood and whom I could always count on. Thanks to Shravan for his joviality and vivacity. Thanks to Elli for our wonderful music sessions and concerts, which were a refreshing break from research. Thanks to Nitya, Ritu, Eva, Gabriel, Xuming, Annika and Miguel.

Last but not least, I want to thank my parents, Preeja and Anand, for the values they instilled in me, which helped me persevere through the different stages of research. Thanks to Naija, Prasanna, Sanjeev, Sylvie, Philippe, Annie, and my grandparents. Thanks to my extended family, who have encouraged and supported me. Finally, thanks to my husband, Antonin, whose humor, love, and kindness brought peace and harmony to life, including the thesis journey.

Merci. Danke. Grazie. Nandi.

Munich, August 2026 Ria Vijayan

TABLE OF CONTENTS

Page

Abstract **i**

List of Tables **xi**

List of Figures **xiii**

Abbreviations and Symbols **xvii**

1 Introduction **1**

1.1 Motivation . . . 6

1.2 Related work . . . 9

1.3 Research gap . . . 12

1.4 Contributions . . . 14

2 Test facilities and fundamentals **21**

2.1 On-ground test facilities . . . 22

2.1.1 OOS-Sim - A robotic HIL platform . . . 22

2.1.2 MSS - A cable-suspended platform . . . 23

2.2 Orbital manipulator dynamics . . . 24

2.2.1 Newton-Euler formulation . . . 24

2.2.2 Reduced Euler-Lagrange formulation . . . 30

2.3 Stability . . . 32

2.3.1 Asymptotic stability and invariance theorems . . . 33

2.3.2 Cascade stability theorems . . . 34

3 Post-grasp stabilization and reconfiguration **37**

3.1 Related work and contributions . . . 37

3.2 Control strategy . . . 40

3.3 Controller for post-grasp phase . . . 41

3.3.1 Hierarchical control law . . . 42

3.3.2 Stability of the controller . . . 44

3.4 Optimal QP-based control . . . 47
3.5 Controller for post-stabilization phase . . . 50
3.5.1 Reduced dynamic model . . . 50
3.5.2 Reduced Jacobian . . . 51
3.5.3 Hierarchical control law . . . 52
3.5.4 Stability of the controller . . . 53
3.6 Weighted-damping control . . . 55
3.7 Validation results . . . 56
3.7.1 Post-grasp phase — Stabilization and reconfiguration . . . 57
3.7.2 Post-stabilization phase — Preparation for berthing . . . 59
3.8 Discussion and summary . . . 63

4 Unified control framework for pre- and post-grasp phases 65
4.1 Relevant work and contributions . . . 66
4.2 Unified control strategy . . . 68
4.3 Unified control framework . . . 70
4.3.1 Definition of coordinates . . . 71
4.3.2 Dynamic decoupling and nominal control design . . . 73
4.3.3 Stability of the controller . . . 76
4.3.4 Optimizing nominal controller for constraints . . . 78
4.4 Validation results . . . 80
4.4.1 Simulation (SIM) results . . . 83
4.4.2 Experimental (HIL) results . . . 86
4.4.3 Momentum and interaction constraint . . . 88
4.4.4 Robustness and sensitivity analysis . . . 89
4.4.5 Joint reconfiguration in whole-body nullspace . . . 90
4.4.6 Stabilizing external disturbances . . . 92
4.5 Discussion and summary . . . 95

5 Sampling-aware multi-rate control 97
5.1 Related work and contributions . . . 98
5.2 Control strategy . . . 100
5.3 Controller design . . . 102
5.3.1 High-rate manipulator control . . . 102
5.3.2 Stability of the high-rate control . . . 103
5.3.3 Low-rate base control . . . 103
5.3.4 Stability of the low-rate control . . . 105
5.3.5 Interpretation of the sample-aware control . . . 106
5.3.6 Interpretation as a hierarchical controller . . . 108

5.4 Low-dimensional benchmark of sampled-data controller . . . 109
5.5 Validation results . . . 110
5.5.1 Simulation (SIM) results . . . 111
5.5.2 Experimental (HIL) results . . . 112
5.5.3 Robustness and sensitivity analysis . . . 114
5.5.4 Evaluation of the first-order approximation . . . 116
5.5.5 Significance of manipulator compensation torques . . . 116
5.5.6 Comparison to a passivity-based controller . . . 117
5.6 Discussion and summary . . . 119

6 Gravity compensation strategy for on-ground validation 121
6.1 Related work and contributions . . . 122
6.2 Compensation strategy . . . 124
6.3 Compensation design . . . 125
6.3.1 Dynamics and constraint . . . 125
6.3.2 Influence of coupling point . . . 127
6.3.3 Optimal distribution of gravity load . . . 128
6.3.4 Existence of solution . . . 129
6.4 Validation results . . . 131
6.4.1 Simulation (SIM) results . . . 132
6.4.2 Hardware (HW) results . . . 134
6.5 Discussion and summary . . . 137

7 Applications 139
7.1 EROSS — EU mission . . . 139
7.1.1 On-ground testing with gravity-compensation . . . 140
7.1.2 Robot motion disturbance on spacecraft . . . 140
7.1.3 Spacecraft actuation disturbance on robot . . . 142
7.1.4 Evaluation of achievable end-effector forces . . . 144
7.2 DIANE — CNES mission . . . 145
7.2.1 Control strategies for spin-synchronized capture . . . 145
7.2.2 On-ground validation with impedance-matched robots . . . 148
7.3 RISE — ESA mission . . . 150
7.3.1 Client manipulation loads at spacecraft-robot interface . . . 150
7.3.2 End-effector axis alignment control . . . 152
7.3.3 End-effector docking with tool . . . 153
7.4 Summary . . . 155

8 Conclusion and outlook 157

Appendix

A Operators, identities and expressions for REL formulation **161**
A.1 Useful operators and identities 161
A.2 Complete expressions for Reduced Euler-Lagrange formulation 162

B Definitions for conditional stability **163**

C Computing nullspace bases using eigen decomposition **165**

D Linear analysis for pre- and post-grasp control gain selection **167**
D.1 Linearized hierarchical dynamics 167
D.2 Transfer functions 168
D.3 Step and impulse responses 168

E Deriving the discrete Lyapunov difference equation **171**
E.1 Power associated with potential energy 172
E.2 Power associated with kinetic energy 172
E.3 Total power 174

F One-DoF sampled-data system **175**

G Multimedia and credits **177**
G.1 Multimedia 177
G.2 Credits and disclosure 178

Bibliography **179**

LIST OF TABLES

TABLE		Page
1.1	Publications and patents	19
1.2	Media articles	20
3.1	Proposed control strategy: post-grasp and stabilization phases	40
3.2	SIM parameters	57
4.1	Proposed control strategy: unified hierarchy for pre- and post-grasp phases	70
4.2	SIM and HIL parameters	81
4.3	Performance metrics	85
5.1	Proposed control strategy: for multi-rate combined control	102
5.2	SIM and HIL parameters	111
5.3	Performance metrics	114
6.1	Proposed control strategy: gravity compensation	125
6.2	Existence of solutions: weight, dimension and singularity cases	130
6.3	SIM and HW parameters	132
8.1	Summary of applications, hierarchies, and methodologies	158
D.1	Step response for gain tuning	169
G.1	Multimedia	177

List of Figures

Figure **Page**

1.1 Skylab missions . . . 2
1.2 STS-41-C and STS-51-A missions . . . 3
1.3 Hubble repair missions . . . 3
1.4 Canadarm2 on the ISS . . . 4
1.5 ROTEX mission 1993 . . . 5
1.6 ETS-VII mission 1999 . . . 6
1.7 Modern OOS missions . . . 8
1.8 Approach to grasp phases . . . 9
1.9 On-ground OOS test facilities . . . 12
1.10 Thesis overview . . . 18

2.1 Control-design workflow . . . 21
2.2 OOS-Sim facility . . . 22
2.3 Motion Suspended System . . . 23
2.4 Orbital manipulator schematic . . . 25
2.5 Servicer with reaction wheels . . . 28
2.6 Post-grasp servicer-client . . . 29

3.1 Servicer with grasped client satellite . . . 38
3.2 Controller for post-grasp phase . . . 44
3.3 EE-client grasp interface . . . 48
3.4 QP-augmented controller . . . 49
3.5 Controller for post-stabilization phase with RWs . . . 54
3.6 Hyperbolic cosine weighting function . . . 56
3.7 Reaction wheel speed limitation . . . 56
3.8 Post-grasp client detumbling . . . 58
3.9 Post-grasp arm reconfiguration . . . 59
3.10 Post-grasp QP-based client detumbling . . . 60
3.11 Post-grasp energy rates with QP-control . . . 60
3.12 Servicer-client reconfiguration animation . . . 61

3.13 Maximum interaction wrench deviation with uncertainties 61
3.14 Post-stabilization arm reconfiguration 62
3.15 Post-stabilization attitude maintenance 62
3.16 Post-stabilization arm reconfiguration with RW limit 63

4.1 SIM and HIL setup with relevant frames 66
4.2 Problem statement: low manipulability and unsafe configuration 69
4.3 Block diagram for nominal controller 75
4.4 Controller overview in closed loop with dynamics 76
4.5 QP-adapted controller including constraints 80
4.6 SIM/HIL scenarios 82
4.7 SIM results: task T1 84
4.8 SIM results: tasks T2 and T3 85
4.9 HIL results: task T1 87
4.10 HIL results: tasks T2 and T3 88
4.11 SIM results: momentum 89
4.12 SIM results: with and without QP-adaptation 89
4.13 Robustness analysis 90
4.14 Experimental view: whole-body nullspace 91
4.15 Experimental data: whole-body nullspace 92
4.16 Experimental view: stabilizing disturbances 93
4.17 Experimental data: stabilizing disturbances 94

5.1 Multi-rate control problem 98
5.2 Problem statement: stable vs unstable multi-rate control 101
5.3 Zero-order multi-rate control block diagram 105
5.4 First-order multi-rate control block diagram 105
5.5 0th-order versus 1st-order control 107
5.6 Zoomed inset of 1st-order control 108
5.7 Stability region for 1-DoF plant control 110
5.8 Exemplary maneuvers in SIM and HIL 112
5.9 SIM results: stabilized actuation profiles 113
5.10 HIL results: actuation profiles and trajectories 113
5.11 Efficiency: difference in linear and angular impulse 115
5.12 Grid search simulation snapshots 115
5.13 First-order approximation of Lyapunov difference 116
5.14 Significance of compensation torques 117
5.15 Passivity Observer monitoring system activity 117
5.16 Passivity Controller and Observer comparison 118

5.17 Comparison with passivity-based control 118

6.1 On-ground validation with external carrier for gravity compensation 122
6.2 7-DoF space manipulator with coupling point 124
6.3 Distributed gravity compensation 129
6.4 SIM results: end-effector motion 132
6.5 SIM results: gravity torques with and without strategy 133
6.6 SIM results: optimal wrench for carrier and joints 133
6.7 Hardware setup: manipulator with cable-suspended carrier 134
6.8 Experimental setup: CAESAR motion with MSS 135
6.9 HW results: desired vs measured joint positions 135
6.10 HW results: optimal joint torques 136
6.11 HW results: optimal carrier force and error 136
6.12 HW results: gravity torque comparison 137
6.13 CAESAR on-ground testing 138

7.1 EROSS SC 140
7.2 Dominant pole distribution across workspace 141
7.3 Robot to spacecraft disturbance: step response 142
7.4 Spacecraft to robot disturbance: 100 samples 143
7.5 Spacecraft to robot disturbance: samples above 1Nm 143
7.6 Achievable EE forces 144
7.7 DIANE 145
7.8 Approach phase: free-floating versus decoupled control 147
7.9 Post-grasp phase: decoupled control 148
7.10 Scaling mission scenario to OOS-Sim 149
7.11 Impedance matching experiment: interaction with robot 149
7.12 Impedance matching experiment: measurements 150
7.13 RISE 151
7.14 Client manipulation maneuver 151
7.15 Client maneuvering loads 152
7.16 Axis alignment 152
7.17 End-effector alignment with client 153
7.18 Tool docking maneuver 153
7.19 Tool docking forces 154

8.1 Other applicable manipulator systems 159
8.2 Future of OOS 160

C.1 Generalized nullspace 165

D.1 Step and impulse response 169

F.1 One-DoF sampled-data system 175

Abbreviations

Abbreviation	Description
OOS	On-Orbit Servicing
DLR	Deutsches Zentrum für Luft- und Raumfahrt (German Aerospace Center)
RM	Institute of Robotics and Mechatronics at DLR
ESA	European Space Agency
EU	European Union
NASA	National Aeronautics and Space Administration, USA
CNES	Centre national d'études spatiales, the French space agency
CSA	Canadian Space Agency
JAXA	Japan Aerospace Exploration Agency
EROSS	European Robotic Orbital Support Services
DIANE	Démonstration d'Inspection et Amarrage Novatrice Embarquée
RISE	Resilient In-orbit Servicing for Europe
STS	Space Transportation System (Space Shuttle)
SMM	Solar Maximum Mission
HST	Hubble Space Telescope
ETS-VII	Engineering Test Satellite No. 7, a JAXA (formerly NASDA) mission
ROTEX	Robot Technology Experiment, DLR's space robotics mission
EVA	Extra-Vehicular Activity
ISS	International Space Station
ORU	Orbital Replacement Unit
RMS	Remote Manipulator System (Candarm and Canadarm 2)
HIL	Hardware-in-the-Loop
CAESAR	Compliant Assistance and Exploration SpAce Robot, a space robot by DLR
OOS-Sim	On-Orbit Servicing Simulator, a robotic HIL facility at DLR
MSS	Motion Suspension System, a cable-suspended platform at DLR
CC	Coriolis/Centrifugal
DoF	Degree of Freedom
PD	Proportional-Derivative
QP	Quadratic Programming
EE	End-Effector
RW	Reaction Wheels

Mathematical Symbols

*Note: Boldface (**x**, **X**) denotes vectors and matrices. Common subscripts used throughout the thesis are: b = base, m = manipulator joints, e = EE, r = reaction wheel, s = servicer, c = client.*

Symbol	Description
States and Coordinates	
$\boldsymbol{v}_k$	k-th link Cartesian velocity (linear + angular), $\in \mathbb{R}^6$
$\boldsymbol{v}_L$	Locked velocity associated with generalized momentum, $\in \mathbb{R}^6$
$\boldsymbol{v}_b$	Servicer base Cartesian velocity (linear + angular), $\in \mathbb{R}^6$
$\boldsymbol{\omega}_b$	Servicer base angular velocity, $\in \mathbb{R}^3$
$\boldsymbol{V}_s$	Servicer states (base + joints + optionally RW), $\in \mathbb{R}^{6+n(+r)}$
$\boldsymbol{v}_c$	Client Cartesian velocity (linear + angular), $\in \mathbb{R}^6$
$\boldsymbol{v}_e$	End-effector Cartesian velocity, $\in \mathbb{R}^6$
$\boldsymbol{q}$	Manipulator joint positions, $\in \mathbb{R}^n$
$\dot{\boldsymbol{q}}$	Manipulator joint velocities, $\in \mathbb{R}^n$
$\boldsymbol{r}$	RW angular positions, $\in \mathbb{R}^r$
$\dot{\boldsymbol{r}}$	RW angular velocities, $\in \mathbb{R}^r$
$\dot{\tilde{\boldsymbol{q}}}$	Stacked manipulator joint & reaction wheel velocities, $\in \mathbb{R}^{n+r}$
$\Delta\boldsymbol{q}$	Joint pose error, $\in \mathbb{R}^n$
$\Delta\boldsymbol{x}_b$	Base pose error (position and quaternion error vector), $\in \mathbb{R}^6$
$\Delta\boldsymbol{x}_e$	End-effector pose error (position and quaternion error vector), $\in \mathbb{R}^6$
$\Delta\boldsymbol{\epsilon}$	Quaternion error vector, $\in \mathbb{R}^3$
$\Delta\eta$	Quaternion error scalar, $\in \mathbb{R}$
$\boldsymbol{v}_n$	Nullspace velocity of whole-body EE, $\in \mathbb{R}^n$
$\boldsymbol{v}_{\bar{n}}$	Nullspace velocity of reduced base attitude, $\in \mathbb{R}^n$
$\boldsymbol{v}_m$	Partitioned nullspace of whole-body EE for manipulator task, $\in \mathbb{R}^n$
$\boldsymbol{v}_r$	Partitioned nullspace of whole-body EE + manipulator for RW task, $\in \mathbb{R}^r$
$\boldsymbol{V}_T$	Augmented task velocities
$\boldsymbol{V}_N$	Nullspace-projected augmented task velocities
Inertia Matrices	
$\boldsymbol{M}_k$	k-th link inertia matrix, $\in \mathbb{R}^{6\times6}$
$\boldsymbol{M}_s$	Servicer inertia matrix (base + joints + optionally RW), $\in \mathbb{R}^{(6+n+(+r))\times(6+n+(+r))}$
$\boldsymbol{M}_c$	Client inertia matrix, $\in \mathbb{R}^{6\times6}$
$\boldsymbol{M}_{sc}$	Combined servicer-client inertia matrix
$\boldsymbol{M}_{bb}$	Base sub-block of $\boldsymbol{M}_s$ or $\boldsymbol{M}_{sc}$, for approach or post-grasp phase, $\in \mathbb{R}^{6\times6}$
$\boldsymbol{M}_{mm}$	Manipulator sub-block of $\boldsymbol{M}_s$ or $\boldsymbol{M}_{sc}$, for approach or post-grasp phase, $\in \mathbb{R}^{n\times n}$

Symbol	Description
$\boldsymbol{M}_{rr}$	RW sub-block of $\boldsymbol{M}_s$ or $\boldsymbol{M}_{sc}$, for approach or post-grasp phase, $\in \mathbb{R}^{r\times r}$
$\boldsymbol{M}_{bm}$	Base-manipulator sub-block of $\boldsymbol{M}_s$ or $\boldsymbol{M}_{sc}$, for approach or post-grasp phase, $\in \mathbb{R}^{6\times n}$
$\boldsymbol{M}_{br}$	Base-RW sub-block of $\boldsymbol{M}_s$ or $\boldsymbol{M}_{sc}$, for approach or post-grasp phase, $\in \mathbb{R}^{6\times r}$
$\boldsymbol{M}_{vv}$	Base linear sub-block of $\boldsymbol{M}_{bb}$, $\in \mathbb{R}^{3\times 3}$
$\boldsymbol{M}_{\omega\omega}$	Base angular sub-block of $\boldsymbol{M}_{bb}$, $\in \mathbb{R}^{3\times 3}$
$\boldsymbol{M}_{v\omega}$	Base linear to angular coupling of $\boldsymbol{M}_{bb}$, $\in \mathbb{R}^{3\times 3}$
$\boldsymbol{M}_{vm}$	Base-manipulator linear sub-block of $\boldsymbol{M}_{bm}$, $\in \mathbb{R}^{3\times n}$
$\boldsymbol{M}_{\omega m}$	Base-manipulator angular sub-block of $\boldsymbol{M}_{bm}$, $\in \mathbb{R}^{3\times n}$
$\boldsymbol{M}_{\omega r}$	Base-RW angular sub-block of $\boldsymbol{M}_{br}$,$\in \mathbb{R}^{3\times r}$
$\bar{\boldsymbol{M}}$	Reduced inertia matrix (joints + RW), $\in \mathbb{R}^{(n+r)\times(n+r)}$
$\boldsymbol{\Lambda}_{qq}$	Generalized joint-space inertia of the orbital manipulator, $\in \mathbb{R}^{n\times n}$
$\boldsymbol{\Lambda}_{ee}$	Cartesian whole-body EE inertia of the orbital manipulator, $\in \mathbb{R}^{6\times 6}$
$\boldsymbol{\Lambda}_{bb}$	Angular inertia of orbital manipulator base, $\in \mathbb{R}^{3\times 3}$
$\boldsymbol{\Lambda}_{nn}$	Nullspace inertia of whole-body EE (for servicer without RW) $\in \mathbb{R}^{n\times n}$
$\boldsymbol{\Lambda}_{\bar{n}\bar{n}}$	Reduced nullspace inertia of base angular velocity (for servicer with RW) $\in \mathbb{R}^{n\times n}$
$\boldsymbol{\Lambda}_{mm}$	Partitioned nullspace inertia of whole-body EE for manipulator task, $\in \mathbb{R}^{n\times n}$
$\boldsymbol{\Lambda}_{rr}$	Partitioned nullspace inertia whole-body EE + manipulator for RW task, $\in \mathbb{R}^{r\times r}$
$\boldsymbol{\Lambda}$	Inertially-decoupled task-space inertia (block diagonal)
$\boldsymbol{\Lambda}'$	Nullspace-projected task-space inertia (lower-triangular)
Coriolis-Centrifugal (CC) Matrices	
$\boldsymbol{\psi}_k$	CC matrix of the k-th link, $\in \mathbb{R}^{6\times 6}$
$\boldsymbol{C}_s$	Servicer CC matrix (base + joints + optionally RW)
$\boldsymbol{C}_c$	Client CC matrix, $\in \mathbb{R}^{6\times 6}$
$\boldsymbol{C}_{sc}$	Combined servicer-client Coriolis matrix
$\boldsymbol{\mu}$	Task-coupled CC matrix in nullspace coordinates
$\boldsymbol{\mu}'$	Nullspace-projected task-space CC matrix (lower-triangular)
Wrenches and Torques	
$\boldsymbol{\Gamma}$	Servicer control input (base + joints + optionally RW)
$\boldsymbol{F}_b$	Base actuation wrench, $\in \mathbb{R}^6$
$\boldsymbol{\tau}_b$	Base actuation torque, $\in \mathbb{R}^3$
$\boldsymbol{\tau}_m$	Manipulator joint actuation torque, $\in \mathbb{R}^n$
$\boldsymbol{\tau}_r$	RW actuation torque, $\in \mathbb{R}^r$
$\bar{\boldsymbol{\tau}}$	Stacked manipulator joint & RW actuation torques, $\in \mathbb{R}^3$
$\boldsymbol{F}_e$	End-effector control wrench, $\in \mathbb{R}^6$

Symbol	Description
$\boldsymbol{F}_c$	Interaction wrench at the EE and client grasp-interface, $\in \mathbb{R}^6$
$\boldsymbol{F}_e^*$	Optimized EE control wrench (QP result), $\in \mathbb{R}^6$
$\boldsymbol{\Gamma}_{\mathrm{T}\bullet}$	Control input at task levels T$\bullet$
$\boldsymbol{\tau}_{\mathrm{T}\bullet}$	Control torques at task levels T$\bullet$
$\boldsymbol{g}$	Gravity torques on manipulator joints, $\in \mathbb{R}^m$
$\boldsymbol{g}_A$	Gravity torques in the set A (joints coupled by carrier), $\in \mathbb{R}^m$
$\boldsymbol{g}_B$	Gravity torques in the set B (joints decoupled from carrier), $\in \mathbb{R}^{n-m}$
$\boldsymbol{F}_{\mathrm{cp}}$	Carrier wrench acting on manipulator at coupling point, $\in \mathbb{R}^6$
$\boldsymbol{\gamma}_c$	Carrier wrench components, $\in \mathbb{R}^i$
Jacobians	
$\boldsymbol{J}_k$	k-th link Jacobian, $\in \mathbb{R}^{6\times n}$
$\boldsymbol{J}_m$	Manipulator EE Jacobian, $\in \mathbb{R}^{6\times n}$
$\boldsymbol{J}_b$	Base to EE Adjoint matrix, $\in \mathbb{R}^{6\times 6}$
$\boldsymbol{J}_c$	Client frame to grasp frame Adjoint matrix, $\in \mathbb{R}^{6\times 6}$
$\boldsymbol{J}_e$	Whole-body EE Jacobian (servicer optionally with RW), $\in \mathbb{R}^{6\times(6+n(+r))}$
$\bar{\boldsymbol{J}}_\omega$	Reduced base angular velocity Jacobian (servicer with RW), $\in \mathbb{R}^{3\times(n+r)}$
$\boldsymbol{J}_q$	Manipulator joints selector (servicer optionally with RW), $\in \mathbb{R}^{6\times(6+n(+r))}$
$\boldsymbol{J}_r$	RW joints selector, $\in \mathbb{R}^{r\times 6+n+r}$
$\bar{\boldsymbol{J}}_q$	Nullspace-projected $\boldsymbol{J}_q$
$\bar{\boldsymbol{J}}_r$	Nullspace-projected $\boldsymbol{J}_r$
$\boldsymbol{J}_T$	Augmented task Jacobian
$\boldsymbol{J}_N$	Nullspace augmented task Jacobian
$\boldsymbol{J}_{\mathrm{cp}}$	Manipulator Jacobian to coupling point of carrier, $\in \mathbb{R}^{6\times n}$
$\boldsymbol{J}_A$	Subset of $\boldsymbol{J}_{\mathrm{cp}}$ for i joints coupled with carrier, $\in \mathbb{R}^{6\times i}$
$\boldsymbol{J}_{cA}^T$	Jacobian $\boldsymbol{J}_A$ mapping carrier wrench components to joints, $\in \mathbb{R}^{m\times i}$
$\boldsymbol{J}_e^{M+}$	Generalized-inverse of $\boldsymbol{J}_e$ weighted with $\boldsymbol{M}_\bullet^{-1}$
Nullspace Bases	
$\boldsymbol{N}_e$	Nullspace basis for whole-body EE (servicer without RW)
$\boldsymbol{N}_\omega$	Nullspace basis for reduced base attitude
$\boldsymbol{N}_1$	Nullspace basis for whole-body EE (servicer with RW)
$\boldsymbol{N}_2$	Nullspace basis for whole-body EE + manipulator (servicer with RW)
$\boldsymbol{N}_q$	Nullspace basis for manipulator joints
$\boldsymbol{N}_e^{M\dagger}$	Generalized-inverse of $\boldsymbol{N}_e$ weighted with $\boldsymbol{M}_\bullet$

Symbol	Description
Control Gains	
$\boldsymbol{K}_{Pe}$	Proportional gain, EE, $\in \mathbb{R}^{6\times 6}$
$\boldsymbol{K}_{De}$	Derivative gain, EE, $\in \mathbb{R}^{6\times 6}$
$\boldsymbol{K}_{Pb}$	Proportional gain, base, $\in \mathbb{R}^{6\times 6}$
$\boldsymbol{K}_{Db}$	Derivative gain, base, $\in \mathbb{R}^{6\times 6}$
$\boldsymbol{K}_{Dr}$	Derivative gain, RW , $\in \mathbb{R}^{r\times r}$
$\boldsymbol{K}_{P\omega}$	Proportional gain, attitude, $\in \mathbb{R}^{3\times 3}$
$\boldsymbol{K}_{D\omega}$	Derivative gain, attitude, $\in \mathbb{R}^{3\times 3}$
$\boldsymbol{K}_{Pm}$	Proportional gain, manipulator joints, $\in \mathbb{R}^{n\times n}$
$\boldsymbol{K}_{Dm}$	Derivative gain, manipulator joints, $\in \mathbb{R}^{n\times n}$
Lie Group Operators	
$\mathrm{Ad}_{\bullet}$	Adjoint action using homogeneous transformation
Ad_{bk}^{-1}	Inverse adjoint from base to the k-th link frame
$\mathrm{ad}_{\bullet}$	Lie bracket using a Cartesian velocity
Miscellaneous	
h	Sampling interval
$\mathbf{0}$	Zero vector or matrix
$\boldsymbol{I}$	Identity matrix
$\bullet^{\times}$	Skew-symmetric matrix from a 3D vector

CHAPTER 1

INTRODUCTION

It was a race against time when, in 1973, engineers at NASA had to devise a contraption to save their first space station, Skylab, from becoming a furnace in which to grill astronauts. The station had lost its heat shield during launch on May 14, 1973, leaving the interior uninhabitable for the astronauts scheduled to launch a day later. The launch of the crew was pushed back by 10 days to allow time to conceive, plan, and build a parasol for the spacecraft that could be launched with the crew for repair. A space umbrella for the space station. A first-of-its-kind, on-orbit servicing mission.

Eventually, up in space, more adventurous than the parasol deployment was the spacewalk during which the astronauts were flung while freeing a solar array jammed by debris from the damaged heat shield. Fortunately, the safety tethers did their job, and the station was restored to safe temperatures and full power supply (see Figure 1.1 and [Bel77] for more details on the mission).

The Skylab station was lucky to be repaired by human intervention, given that crewed flights were part of the mission plan. However, the first time a satellite, not intended for visitors, was repaired in orbit was when a dedicated crew aboard the STS-41-C captured and serviced the ailing Solar Maximum Mission (SMM) spacecraft in April 1984. In an almost sci-fi-like manner, flying on untethered jetpacks, or Manned Maneuvering Units (MMUs), astronauts propelled themselves in an attempt to grapple with the SMM. Unfortunately, the first three attempts to grapple with the SMM via a specialized interface failed. As a last resort, the astronaut tried instead to grapple with the satellite with their hands and de-spin it using propulsion on the MMU. This only exacerbated the problem and put the SMM into an unstable spin, making it unfit to return to the Space Shuttle's payload bay for repair. Eventually, SMM was stabilized by ground control, the MMUs abandoned, and the Shuttle's robotic arm, Canadarm, summoned for rescue. Thus, the first servicing activity on an uncrewed orbiting satellite was enabled by the robotic arm, Remote Manipulator System (RMS)

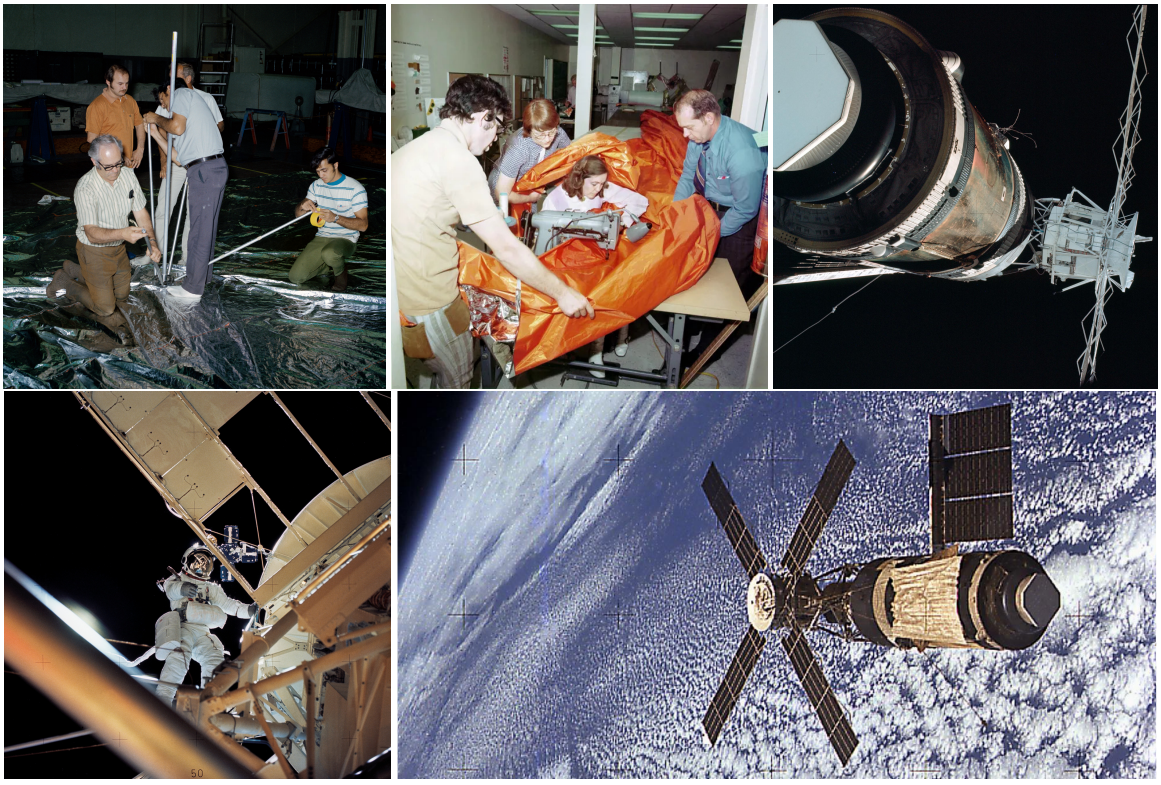

Figure 1.1: Image credits: NASA. Skylab missions, 1973-1974. Top left: technicians at NASA working on the parasol mechanism. Top middle: parasol fabricated using a sewing machine. Top right: fly-around inspection by Skylab 2 showing missing micrometeoroid shield and partially deployed solar array. Bottom left: Skylab 3 EVA during which Astronaut Owen K. Garriott deployed a second solar shield. Bottom right: as seen by Skylab 4 crew during departure, gold parasol covers the space station and the solar array at the top is freed.

or Canadarm. The robotic arm was operated manually by the astronauts to grapple and dock the SMM to the Shuttle's payload bay for subsequent repair (see Figure 1.2 and [Nat01] for more details on the mission). Later that year in November 1984, MMUs were successfully used by the crew of the STS-51-A mission to retrieve communication satellites Westar VI and Palapa B2, that were in improper orbits due to malfunctioning kick motors, back to Earth (see Figure 1.2 right).

The most renowned servicing history is perhaps that of the Hubble Space Telescope (HST), which was designed to accommodate upgrades by crewed missions (see Figure 1.3 and [Nat23] for more details on the mission). The upgrade became a pressing need when, soon after launch in April 1990, astronomers were irked by the telescope's rather impressionistic rendering of galaxies. These blurry images, caused by an optical aberration in the design, meant the telescope needed corrective optics, like spectacles, to restore it to the resolution required for wider scientific observations. Consequently, HST's first servicing mission, STS-61, launched in December 1993, witnessed some of the most challenging extravehicular activities (EVAs) performed by astronauts to install crucial upgrades, including the Corrective Optics Space Telescope Axial Replacement (COSTAR) unit, solar

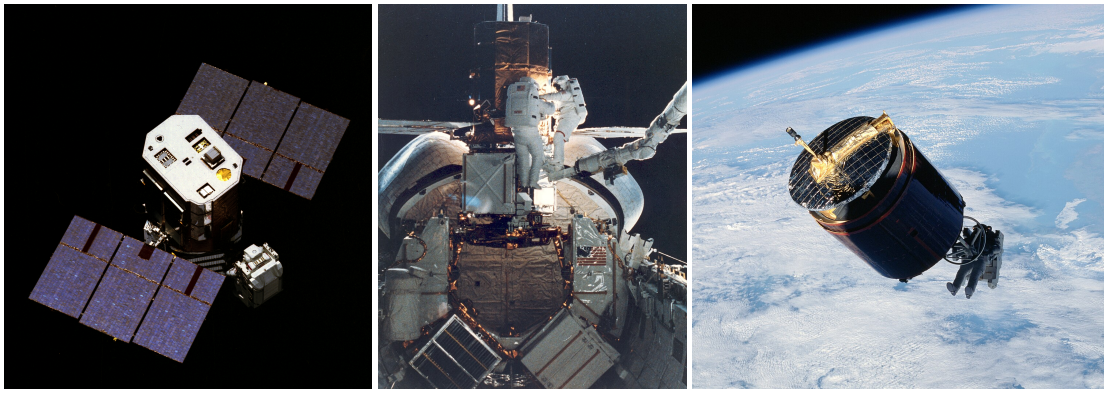

Figure 1.2: Image credits: NASA. Left: STS-41-C, Solar Maximum Mission (SMM) repair, 1984. Astronaut George D. Nelson approaches the damaged satellite with an MMU in a capture attempt. Middle: Astronauts George D. Nelson, right, and James D. Van Hoften, left, repair SMM while anchored to the foot restraint on the Canadarm. Right: STS-51-A, 1984. Astronaut Dale A. Gardner, wearing an MMU, retrieves the Westar VI satellite.

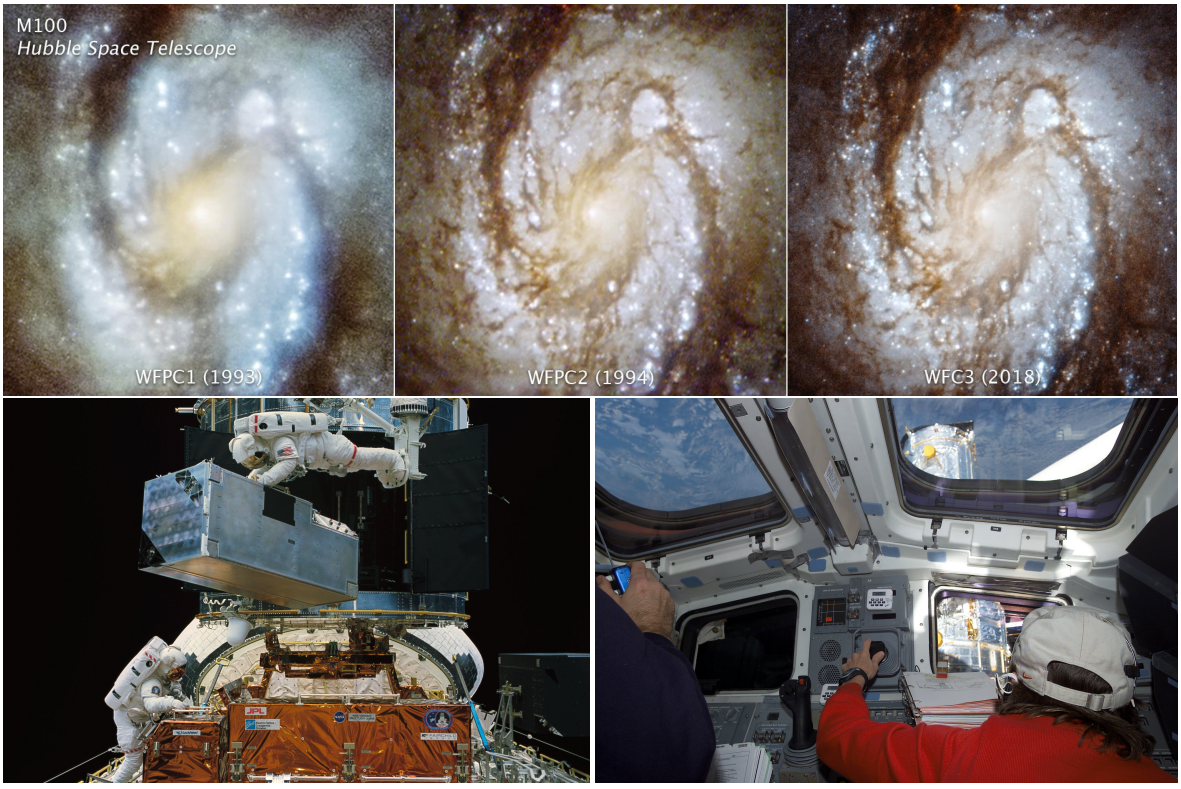

Figure 1.3: Image credits: NASA. Hubble Space Telescope (HST) repair missions, 1983-2009. Top: successively improved images of the galaxy M100 taken with three generations of cameras upgraded over servicing missions. Bottom left: 1993, Astronaut Kathryn C. Thornton (above), anchored to the Canadarm (RMS), lifts the Corrective Optics Space Telescope Axial Replacement for installation into HST. Bottom right: 2002, Astronaut Nancy J. Currie, controls the RMS as two astronauts work on HST.

arrays, and magnetometers. Over the course of five servicing missions from 1993 to 2009, several repairs and upgrades were made, and one of the last installments made by the fifth and final repair mission, STS-125, in May 2009, was in fact a soft capture mechanism for future docking by robotic servicing missions to dispose HST at its end-of-life.

These early examples of repair missions in space are a trademark of the human endeavor in expanding the boundaries of space exploration and a testament to technological ingenuity and foresight. Human commitment to space exploration could not be better attested to than by the recent ARTEMIS II mission that literally pushed the boundaries of space, setting the record distance for human spaceflight during its lunar flyby in April 2026.

It is evident that, to extend the realm of on-orbit servicing, the challenge lies in developing reliable autonomous technologies that can standardize repair, maintenance, and assembly of space infrastructure. As the number of satellites in orbit rapidly increases, robotic servicing offers a way to extend satellite lifetimes, reduce debris, lower mission costs, and relieve humans from potentially risky, infeasible, and impractical servicing missions.

Historical Foundations of Robotic Proximity Operations

The domain of on-orbit servicing today envisions a large scope of in-orbit activities like inspection, repair, maintenance, de-orbiting, re-fueling, upgrade and assembly. In order to provide these servicing activities, a servicer first needs to perform rendezvous and proximity operations to maneuver and approach the client satellite or space structure safely. Following the approach, the servicer needs to engage with the client, which typically involves some type of docking technology. In particular, developments are being made to dock or grasp a satellite using a robotic arm with a gripper mechanism.

The foundations for today's zealous push for robotic servicing have been set by impressive precursors to automation in space. While the first crewed space docking was made by the Gemini VIII

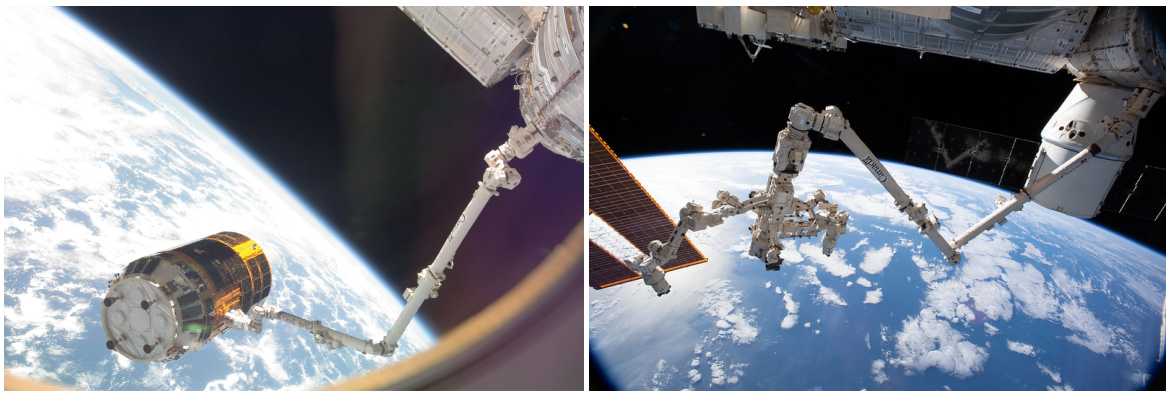

Figure 1.4: Image credits: NASA. Left: 2009. Astronauts on the ISS control Canadarm2 to unberth JAXA's cargo resupply ship H-II Transfer Vehicle (HTV). Right: 2019. View of Canadarm2 and Dextre robot on the ISS.

mission in 1966, the first automated uncrewed docking in space occurred in 1967 between the Soviet spacecrafts Kosmos 186 and Kosmos 188 [Por95]. This was followed by the Progress cargo ship, which, since its maiden flight in 1978, became the standard workhorse for uncrewed resupply to the Salyut, Mir, and International Space Station (ISS) [Por95].

Other examples include ESA's Automated Transfer Vehicle's (ATV) automated docking with the International Space Station in 2008 [DP12] and China's Shenzhou 8 docking with the Tiangong space laboratory in 2011 [XHW+13]. Since 2019, SpaceX's Crew Dragon Demo-1 and its successors have provided automated docking for resupply missions to the ISS [MDF+20].

The Advent of Robotic Arms for Servicing

The word *robotic* has been used to describe technologies not only in the sense of manipulators (robotic arms) and rovers but also in the sense of any mechanism capable of autonomous operation i.e. without human teleoperation. Even a satellite can technically be considered a robot in the sense of its ability to operate autonomously in orbit. Nevertheless, robots in the sense of robotic arms, which are of interest in this thesis, have some notable history in space.

A famous example of robotics in space is the Canadarm designed by the Canadian Space Agency (CSA), which debuted on NASA's Space Shuttle Columbia (STS-2) in November 1981. The 15 m arm, designed to be operated by astronauts, has been used on the Space Shuttle and ISS missions to deploy, manipulate, and capture payloads [AZ24]. Its successors Canadarm2 and Dextre continue to provide servicing capabilities to the ISS (see Figure 1.4).

The ROTEX mission, by the German Aerospace Center (DLR), was the first to demonstrate teleoperation of a robotic arm to catch a free-floating object in space, aboard the Spacelab-Mission D2 in 1993 (see Figure 1.5 and [HBDH94] for more details on the mission). It could also perform semi-autonomous tasks like assembling a truss structure [GBB+25]. Further developments led to DLR's ROKVISS robotic arm, which was used to test telepresence control concepts as well as the reliability

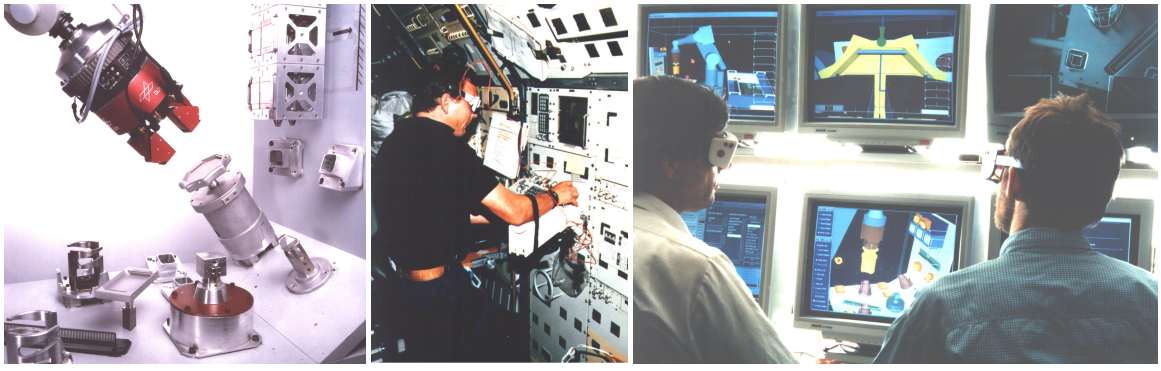

Figure 1.5: Image credits: DLR. ROTEX mission 1993. Left: gripper designed to capture free-floating object. Middle: experiment on the Space Shuttle controlled by astronaut Hans Schlegel. Right: telepresence experiment monitored on ground by Klaus Landzettel (left) and Bernhard Brunner (right).

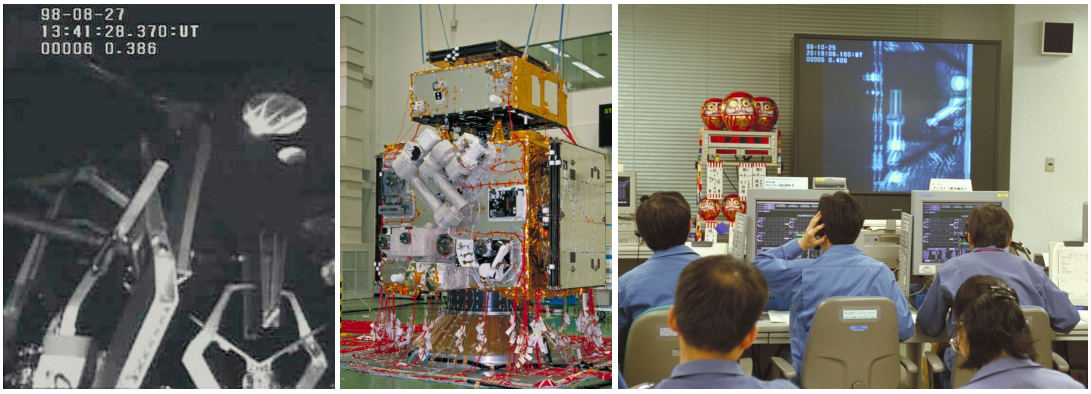

Figure 1.6: Image credits: ©JAXA. ETS-VII mission 1999. Left: claws of Hikoboshi (servicer) grasping the latching handle of Orihime (client) during a rendezvous and docking experiment. Middle: ETS-VII Proto-flight model. Right: ETS-VII ground operations.

of its highly developed joint electronics on the ISS in 2005.

JAXA's ETS-VII mission in 1999 also pioneered robotic servicing experiments [FAMPU14] (see Figure 1.6). It included a robotic arm mounted on a spacecraft i.e. a *servicer*, that demonstrated capture of a cooperative satellite, meaning, one equipped with well-defined fixtures, visual markers, signal reflectors, GPS and well maintained attitude [Yos00]. It further performed liquid transfer, peg-insertion and exchange of an Orbital Replacement Unit (ORU). Unlike the operation of the 15 m long, 1500 kg heavy Canadarm2 atop the approximately 420,000 kg space station, the ETS-VII mission operated a 2 m long, 140 kg heavy arm atop a 2000 kg satellite [Yos00]. Thus, the mass ratios differ by almost a factor of 20 and this makes the modeling of the spacecraft coupling to the robotic motions more relevant due to the floating dynamics. Another difference is that in the case of the Shuttle Remote Manipulator System (Canadarm), its long and flexible structure implies that it has a tendency to oscillate when its configuration is changed [Ryb24].

DARPA's demonstration mission of 2007, Orbital Express, also had a robotic arm, which was used for autonomous docking, fuel transfer, and ORU exchange [CHD22, Fri08].

1.1 Motivation

The increasing demand for maintenance, repair, refueling, and debris mitigation has made on-orbit servicing (OOS) a critical focus in space robotics. As a result, OOS has moved beyond technology demonstrations to commercial efforts aimed at cost-effective solutions. Over the past decade, commercial enterprises, supported by space agencies, have made attempts to advance the industry toward large-scale orbital servicing. While challenges remain, ongoing research and technology transfer are driving progress, as shown by recent and planned missions.

Modern Missions in On-Orbit Servicing

As a commercial successor to Orbital Express, the Mission Extension Vehicle (MEV)—developed by Northrop Grumman's SpaceLogistics—docked with Intelsat 901 (2020) and Intelsat 1002 (2021), marking the first commercial on-orbit servicing [CHD22]. The MEV mission did not include a robotic arm, as their main objectives were docking, refueling, and repositioning of client satellites in space. A follow-up mission to the MEV is planned: the Mission Robotic Vehicle (MRV), which is expected to incorporate a robotic arm. Similarly, the ELSA-d (2021) and ASTRA-J (2024) missions by Astroscale demonstrated end-of-life services [Ale22] for de-orbiting client satellites using advanced docking technologies. The follow-up mission, ASTRA-J2, includes a robotic arm and has been selected by JAXA for commercialization. Another recent mission, the Space Docking Experiment (SpaDex) by ISRO, focused on autonomous docking and power transfer between satellites in 2025.

Challenges for Next-Generation of Robotic Servicing

Unlike the docking technologies surveyed above, the primary advantage of equipping the servicing spacecraft with robotic manipulators is that it significantly expands the range of possible operations, enabling dexterous manipulation such as ORU exchanges, and offers greater versatility for tool changes during complex inspection and repair tasks. In addition, exploiting the robotic arm for docking (grasping) further expands the utility of the servicing spacecraft across a wider range of client satellites that may not have a dedicated docking interface [BCH$^+$11].

Furthermore, the distinction between upcoming robotic on-orbit servicing missions versus space robots on the ISS like the Canadarm2, Japanese Experiment Module Remote Manipulator System (JEMRMS), and European Robotic Arm (ERA), is the autonomy versus human operation. Another distinction is the autonomy in rendezvous, docking and capture of *non-cooperative* satellites, which typically can be tumbling, uncontrolled and missing tracking aids [PAML21a]. In the case of the ETS-VII and Orbital Express missions, the client was a prototype satellite that did not have any spin or tumbling motion, which is often not representative of most commercial servicing applications. Further, robotic on-orbit servicing missions seek to provide life-extension and de-orbiting services to more than one satellite in different orbits.

At the core of upcoming robotic OOS missions are *servicers* i.e. orbital manipulators—robotic arms mounted on servicer spacecraft capable of servicing malfunctioning client satellites in space. Robotic servicing missions in the pipeline (see Figure 1.7) include RISE (Resilient In-orbit Servicing for Europe), by ESA/D-Orbit, and EROSS (European Robotic Orbital Support Services), by Thales Alenia Space, where DLR's Institute of Robotics and Mechatronics is making contributions to the robotic subsystem. ESA's ClearSpace mission aims to remove the non-cooperative satellites from orbit using robotic technology. Thus, the strong demand for orbital servicing missions using robotic arms supports research focused on overcoming the diverse challenges these missions present.

Robotic servicing missions present many challenges for RPO. These challenges arise in guidance, navigation, and control [PAML21a]. For example, non-cooperative clients lack retro-reflectors or



Figure 1.7: Illustrations of (top left) EROSS mission (image credit: ©Thales Alenia Space), (top right) ClearSpace mission (image credit: ESA), and (bottom) RISE mission (image credit: ESA).

other rendezvous sensor tracking features which complicates guidance and navigation [BCH+11]. Control algorithms designed for a space robot must account for the dynamic coupling effect of the manipulator's motion [SSN21], ensuring the manipulator operates as intended for critical tasks such as grasping and stabilization. The control of orbital manipulators presents unique challenges due to the lack of a fixed base, uncertainties in client motion, and the need for autonomous operation.

In particular, the close-proximity operation of a robotic arm for capturing and servicing a spinning, non-cooperative satellite poses significant challenges for guidance, navigation, and control. Such scenarios necessitate the investigation of combined control of the robot and spacecraft for approaching and capturing a dynamically spinning satellite. When spacecraft control is inactive during motion control of the robotic arm, this is called *free-floating* control. If spacecraft control is active during robotic operation, it is called *free-flying* or *combined control*.

Close-proximity operations are typically divided into three phases. The first is the approach, or pre-grasp phase, during which motion toward capture is initiated as the client satellite enters the servicing manipulator's workspace. The grasp phase follows, marking the conclusion of the approach. After capture, the post-grasp stabilization phase begins. These phases are illustrated using the EROSS mission scenario in Figure 1.8.



Figure 1.8: Image credits: ©Thales Alenia Space, EROSS mission. Left: Approach phase. Middle: Grasp phase. Right: Post-grasp phase.

This thesis investigates control strategies for a servicing spacecraft equipped with a robotic manipulator. It addresses the close-proximity operations—approach, grasp, and stabilization—of a non-cooperative client satellite. Control strategies are developed and tested using state-of-the-art robotic facilities used for OOS robotic mission validation. The research also examines a combined control scheme for an orbital manipulator to support both spacecraft and arm operation at different control frequencies. Additionally, a strategy to compensate for gravity during on-ground testing of space robots is studied.

1.2 Related work

OOS entails repair, maintenance, and life-extension operations performed on satellites or other space structures. The state-of-the-art in this context for control design and on-ground testing of space robotic manipulators are reviewed ahead. The review is organized into three parts. The first part reviews works from the perspective of control *methodologies* like nonlinear, optimal, robust, predictive and intelligent methods proposed for orbital manipulators. The second part reviews works from the perspective of control *strategies* that specifically take into account dynamic aspects unique to orbital manipulators like the floating-base dynamics or momentum-conservation. The third part reviews works related particularly to on-ground testing technologies for gravity compensation of space robots. A more *focused* literature review of the related works is also given in the respective chapters contrasting the specific details with the proposed methods.

Control Methodologies for Orbital Manipulators

Nonlinear control methods like backstepping have been presented for orbital manipulators in [TWF10] for underactuated systems, in [ZD25] with neural networks for uncertainty estimation, and in [WRS24]

to tackle nonholonomy. An adaptive postcapture backstepping control for tethered space robot is reported in [HWM+16].

Optimal control methods addressing objectives like time-optimal manipulator control with reaction torque constraints have been studied in [ONY08] and in particular for detumbling in [Agh08]. Further studies on optimal pose and time of capture of the target are reported in [FAWMP13] and the corresponding optimal control to achieve this in [FAWMP14]. An optimal rendezvous trajectory for minimizing the energy has also been studied in [ZE20].

Robust control methods like H-infinity control have been applied to a linearized model of the free-floating space robot in [RPA+24]. A robust adaptive controller for a free-flying space robot subject to uncertainties is studied in [JSKK16]. An LQR (Linear Quadratic Regulator) and H-infinity controller are compared in their application to a free-floating space manipulator with two arms in [BSBG16] using the Dynamically Equivalent Manipulator model [LXB97]. An H-infinity controller for spacecraft with attitude control is developed in [SS19] using dynamics modeled relative to the target.

Robust control methods like sliding mode control (SMC) of a space robot are investigated in [KT11] for capturing a target and controlling its motion under unknown parameters, like mass and inertia tensor. An SMC has been studied in [ABB+11] for a one degree-of-freedom (DoF) flexible link space robotic arm with payload. In [HYL07] an adaptive SMC algorithm for handling unknown payload and impact force is proposed. A chattering avoidance SMC is developed for free-flying space robot with Kalman filter estimates of parameters in [KRH10]. A method that combines optimization, trajectory planning and SMC is used in [ARB25] to minimize contact forces during space robot captures.

Predictive control methods like MPC are shown in [RSS17] for a free-floating space robot using simulations performed for a simplified planar case. A non-linear model predictive controller (NMPC) with obstacle avoidance for a space robot has been proposed in [WLW16] for a free-floating spacecraft. An NMPC algorithm to minimize joint torques, spacecraft actuator moments and contact forces for a dual arm chaser capturing a target is presented in [KdR23a]. A passivity-based NMPC of space robots is presented in [KDR23b] to incorporate closed-loop stability benefits of Lyapunov-based control into NMPC. An NMPC's performance is compared with that of SMC to control the attitude of the spacecraft and the end-effector motion in [KSKP17] for a 3-link planar space manipulator.

Intelligent control methods like reinforcement learning (RL) and fuzzy-logic are also explored in some recent works. Adaptive small chattering SMC scheme that uses RL for the motion control of free-floating space robotic manipulators is studied in [XSK+20] subject to model uncertainties. A fuzzy sliding mode controller is developed in [ST22] for a free-flying space robot to examine tracking performance and robustness. A machine learning strategy is proposed in [SRdF22] for path planning of the end-effector considering collision avoidance and torque minimization, subject to uncertainty inside a berthing box.

Control Strategies for Floating-Base Dynamics and Capture

Aside from the control methodologies reviewed above, it is worth reviewing the different control strategies for operating orbital manipulators. The choice of strategy is often dictated by the objectives, uncertainties and constraints. Control strategies particularly for the floating-base manipulator must account for the dynamic coupling between the manipulator and spacecraft base. The Virtual Manipulator approach was developed in [VD87] suggesting cyclic joint motions to self-correct for disturbance in attitude caused by the end-effector tracking a desired trajectory. Another concept called the Enhanced Disturbance Maps by [TD92] was proposed to minimize spacecraft fuel usage to compensate for attitude disturbances caused due to manipulator motion. Based on the Virtual Manipulator concept, the dynamics of a space robot were mapped to a fixed-base manipulator, called Dynamically Equivalent Manipulator in [LXB97].

Control strategies with a focus on capture and post-capture operations have also been investigated in some works. The concept of Virtual-mass for Impedance Matching was introduced in [YNU+04] to determine that the contact between the robot hand and target can be maintained on collision, if the impedance controller achieves an impedance of the robot hand to be equal to or smaller than the target's mass. In [PP13a] the analysis uses percussion points of bodies to predict the best configuration of the space manipulator for impact minimization while capturing a target. The work in [FAZWM17] presents a method to determine the optimal time and configuration for capturing a target, such that the contact forces pass through the system's center of mass (CoM) at the moment of impact. The concept of Reaction Null Space [NYVU02], initially called Fixed-Attitude-Restricted Jacobian Control, has been studied in the case of detumbling a rotating target under the constraint of having a fixed base attitude.

Gravity-Compensation Strategies for On-Ground Testing

Following the design of controllers for orbital manipulators, on-ground validation methods for these controllers rely on different hardware setups for 0-g emulation. Several gravity compensation mechanisms specific to robotics have been studied and a summary of the broad categories of mechanisms is reported in [Ara16]. These include gravity compensation methods using counterweights, springs and auxiliary actuators. Existing strategies for 0-g simulation (e.g., air bearings, parabolic flights, neutral buoyancy systems) each have limitations — they may only simulate planar motion, are time-limited, or generate other artifacts due to limitations of the compensation mechanism.

An air bearing system was used to test the control algorithms of the Japanese free-floating robot [Yos03], the Canadarm and the European Robotic Arm (ERA). The conservation of momentum principle of a similar setup, was verified in [ULA+10]. In [SUM+04], experiments were performed in a 0-g parabolic flight for a four degree-of-freedom robot. A planar robotic platform mounted with a planar space robot is used in [MIG16] to simulate a 0-g environment. Full six-dimensional motion can also be simulated with robots equipped with force-torque sensors in closed loop with a desired dynamic model [DSMG+21], like the OOS-Sim at DLR (see Figure 1.9, left). This robotic Hardware-in-the-

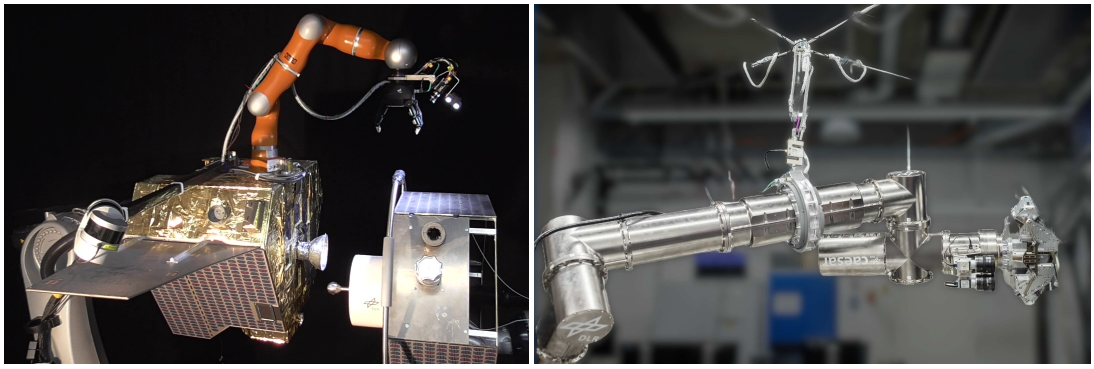

Figure 1.9: Left: The OOS-Sim facility [DSRB+24], a platform for 6-DoF zero-gravity dynamics validation. Right: Space robot, CAESAR [BGH+18] supported by the Motion Suspension System (MSS) [EDSS+24] to compensate for gravity on ground. More details on the facilities are given in Section 2.1.

loop (HIL) facility is used for experimental validation of control strategies developed in Chapter 4 and Chapter 5. More details on the facility are given in Section 2.1.1.

In [BD94] a mechanical structure using a beam and carriage with pulleys attached to a floor-mounted counterweight passively compensate the vertical motion of the robot, while actively adjusting the carriage over the moving robot. Undesirable inertial effects introduced due to the counterbalance, have been mitigated using a controller for actively modulating the tension in the support cable from the robot to the counterweight [WX94]. A cable-driven method that requires constant-tension cables which have to be kept vertical is proposed in [DLGD10]. A method based on singular perturbation theory is used to tackle flexibility of a cable-driven robot in [AATA24]. A cable-suspended platform at DLR (see Figure 1.9, right) is considered in this thesis for testing the gravity-compensation strategy proposed for space robots whose motors are too weak to support gravitational loads. More details on the facility are given in Section 2.1.2.

1.3 Research gap

Autonomous solutions for OOS demonstrated until now have primarily focused on docking with or capturing non-spinning, fully cooperative satellites. However, malfunctioning satellites usually retain residual spin, which renders the zero-spin assumption invalid and introduces significant challenges for guidance, navigation, and robot-spacecraft coordination.

In such dynamic environments, existing methods often fail because uncontrolled rotation presents substantial obstacles to safe approach and capture. Therefore, this thesis addresses the specific challenges associated with servicing spinning satellites. Unlike data-driven methods, which are gaining traction in terrestrial applications, the stringent verification and validation requirements of space qualification necessitate stability guarantees of the control algorithms. The methods presented herein are designed to establish the stability of the combined control approaches required

to address spinning clients.

In particular, in existing approaches, the combined control of a floating-base manipulator has not been thoroughly examined with respect to the kinematic and dynamic redundancy inherent in whole-body manipulator control. Examining the system from this perspective enables the straightforward assignment of priorities to multiple mission objectives within the control law.

Since the mission objectives related to approach, grasp, and stabilization have primarily a task-priority rather than time-priority, nullspace-based hierarchical control is an appropriate candidate for further investigation. Specifically, the nullspace concept is employed in this work to leverage the fully-actuated dynamics of the orbital manipulator, thereby enabling effective prioritization of control tasks. This thesis also harmonizes the benefits of optimization-based control with those of nullspace-based hierarchical control within a unified framework. Physics-based concepts such as energy and passivity are employed to develop Lyapunov-based controllers that ensure stable, robust, and convergent performance.

For post-grasp stabilization, previous methods typically focused on identifying optimal detumbling trajectories and considered force limitations during the planning phase. Few approaches explicitly limit interaction forces at the grasp interface through the controller to maintain safety thresholds; most rely on indirect methods or utilize force and torque measurements. Many existing approaches address detumbling and joint reconfiguration as separate processes rather than simultaneously. Consequently, existing controllers do not guarantee that the manipulator can be reconfigured into a desired state for subsequent servicing operations while stabilizing the client's tumbling motion. Furthermore, the validity of controllers in singular configurations has not been systematically addressed. Certain earlier methods may fail when the manipulator encounters kinematic singularities, which are configurations where nullspace control becomes ill-conditioned.

In addition to grasping strategies, previous studies on coordinated control using thrusters or reaction wheels for close-proximity operations, even when prioritizing spacecraft attitude preservation (as in [NYVU02]), do not adequately address constraints arising from reaction wheel saturation. Therefore, there is a need for a controller that can first address practical issues such as reaction wheel speed limits and saturation by adapting damping torques as needed. Second, maintain the servicer spacecraft's attitude while reconfiguring a manipulator arm that has already grasped a client satellite, particularly following momentum exchange during capture. Third, leverage reaction wheel redundancy to decouple manipulator motion from base attitude, thereby enhancing flexibility and reducing reliance on thrusters.

Previous studies typically focus on a single mission phase, either the approach-to-grasp or the post-grasp stabilization phase, rather than addressing both within a unified framework. These approaches do not offer a unified control framework capable of smoothly managing the transition from approaching a target satellite to controlling forces after grasping. They also often overlook the efficient utilization of onboard actuators, such as reaction wheels, which can result in suboptimal thruster consumption and momentum management during these phases.

Standard combined control approaches often assume similar update rates for both the spacecraft and the manipulator, or they overlook the stability and performance degradation resulting from the servicer's low sampling rates in the combined control loop. The effects of sampling disparity or multi-rate operation, particularly the interaction between discrete low-rate spacecraft actuation and continuous high-frequency manipulator dynamics, are typically not explicitly addressed in controller design.

Furthermore, most ground-based testing platforms for space robots are limited to a few degrees of freedom, resulting in insufficient validation under realistic conditions. For multi-body space manipulators, configuration-dependent gravitational torques present significant challenges for gravity off-loading approaches. No general gravity-compensation method in the literature accommodates a generic carrier system, such as a carrier robot or cable-driven pulleys, with arbitrary degrees of freedom to facilitate realistic testing of control algorithms intended for 0-g conditions. Therefore, a method is needed that minimizes the manipulator's joint torques in 1-g gravity, ensures comprehensive gravity compensation throughout the workspace, and optimizes the balance between joint actuation limits and external support forces.

1.4 Contributions

An overview of the chapters and the key contributions is summarized ahead.

Chapter 2 summarizes the most relevant preliminaries required for the main contents of the thesis. First, the on-ground test facilities used in the validation of the proposed control strategies are described. Second, a derivation of the dynamics of a floating-base orbital manipulator is given, that is useful for practical implementation. Finally, the most pertinent theorems used to argue cascade stability for the majority of the hierarchical control schemes are stated.

Chapter 3 develops the hierarchical control laws by modeling the floating-base orbital manipulator from the perspective of the whole-body kinematic and dynamic redundancy. In addition, a novel adaptation of the nominal control law is shown to optimize for constraints (e.g., interaction forces or thruster limits) within the hierarchical control law. Therefore, using the same philosophy, different DoF, constraints and objectives of the post-grasp stabilization and post-stabilization reconfiguration phases are addressed. This showcases the versatility of the controller design as per the requirements of the phases of an OOS mission. Chapter 3 covers the work published in [VDSO22] and [VDO22].

Chapter 4 builds upon the strategies of Chapter 3 to present a unified control framework for an orbital manipulator applicable from approach to grasp and the post-grasp phase. The controller hierarchically fulfills various requirements of each phase while considering optimal control distribution between depletable (e.g. thrusters) and saturating (e.g. reaction wheels) actuators. The results are verified in simulation for robustness and validated using the hardware-in-the-loop facility OOS-Sim. In summary, the research gap addressed in Chapter 4 is the absence of a unified, constraint-

aware control strategy that manages both mission phases concurrently while ensuring efficiency and safety. Chapter 4 covers the work published in [VDSDO25].

Chapter 5 presents a control strategy motivated by practical considerations for low-sampling-rate spacecraft control when implementing combined controllers like those presented in Chapters 3 and 4. A novel discrete controller accounting for the first-order effects of the servicer's low sampling rate is designed, and its performance is benchmarked. The low-rate spacecraft control is carefully decoupled by actuating it in the nullspace of the high-rate arm control. The results are verified in simulation for robustness and validated using the hardware-in-the-loop facility, OOS-Sim. Accordingly, the research gap addressed in Chapter 5 is the lack of control laws specifically designed to manage multi-rate operation in orbital manipulators, with consideration for both stability and efficiency (such as energy use and impulse). Chapter 5 covers the work published in [VDSO26b].

Chapter 6 presents a strategy for gravity compensation of an orbital manipulator using external forces. An optimal problem balances the motor torques acting on the manipulator arm and the external force to be tracked by an external carrier. The method aims at generality, such that it can be applied to any robot while using a generic admittance-controlled carrier. Consequently, the research gap addressed in Chapter 6 is the absence of an effective strategy for achieving gravity compensation for orbital manipulators during on-ground testing, specifically one that overcomes joint torque limitations and enables full workspace validation. The effectiveness and generality of the proposed method is also evidenced by its recent application on a different platform in [CKK+26]. Chapter 6 covers the work published in [DSVS+23]. The author's specific contribution to this work is the *generalization* of the optimal method to a carrier with any number of degrees-of-freedom and any coupling point.

Chapter 7 illustrates several methods presented in the previous chapters that found application in ongoing OOS mission developments. In particular, challenges addressed during the mission analysis and development of three ongoing OOS missions - EROSS, and EU initiative, DIANE, a CNES mission study, and RISE, an ESA mission development, are presented.

Chapter 8 concludes the work with a summary of the different hierarchies dealt with for space robots, and how they address the outlined research gap. An outlook on how these concepts could transfer to other vehicle manipulator systems is also presented.

To summarize, the **key contributions** of this thesis are:

I. **Approach, grasp and stabilization strategy**

- A novel control strategy for the post-grasp stabilization using whole-body nullspace of the servicer's end-effector. The validity of the proposed control is also shown for kinematically singular configurations of the manipulator.

- A control framework, which allows the inclusion of constraints through quadratic-programming (QP) based adaptations within the nullspace projection-based control paradigm.

- A unified framework for the approach (pre-grasp) phase and post-grasp phase, that respects multiple space mission constraints. In addition to limiting the interaction forces at the manipulator's end-effector, thruster limits are tackled through redistribution of reaction wheel torques within the nullspace.

- Experimental validation of the unified control strategy on the hardware-in-the-loop robotic facility, OOS-Sim.

II. **Multi-rate combined control strategy**

- A novel combined control strategy applied to an orbital manipulator operated under a multi-rate control scheme. This considers low-rate (e.g., 10 Hz) control of spacecraft and high-rate (e.g., 1 kHz) control of manipulator.

- A novel sampling-aware discrete control that accounts for first-order energy leaks due to low-rate spacecraft control.

- Experimental validation of the proposed multi-rate combined controller on the hardware-in-the-loop robotic facility, OOS-Sim.

III. **Gravity-compensation strategy**

- A generalization of a gravity-compensation strategy for an external carrier with any DoFs and coupling point for on-ground testing of space manipulators.

- Experimental validation of the gravity compensation strategy with the CAESAR space manipulator using a cable-suspended system, MSS.

Publications

Over the course of the research conducted for this thesis, several publications resulted from the work. The contents of this thesis are based on the primary publications listed in Table 1.4. Contributions to other closely related works resulting from collaborations during this research are listed as secondary contributions in Table 1.4.

Patents

The outcomes of this research also led to the registration of 4 patent applications, of which one is granted and currently in force in Germany and USA. The patent applications with primary and secondary contributions are listed in Table 1.4.

Awards

- *2026 Best Paper Award Finalist* - The journal article [VDSDO25] underlying Chapter 4 was selected as one of the top five finalists for the *Best Paper Award* among articles published in the year 2025 in the IEEE/ASME Transactions on Mechatronics journal.
- *2024 Amelia Earhart Fellow* - In 2024, the author received the *Amelia Earhart Fellowship*, an international recognition for women pursuing doctoral degrees with distinctive merit in aerospace engineering and space sciences.

Guest lectures

The author gave guest lectures based on the contents of the journal article [VDSO26b] underlying Chapter 5 in the following graduate degree courses.

- *Regelung moderner Leichtbauroboter* at Technische Universität München (TUM) (27 January, 2026)
- *Manipulation and Locomotion* at Technische Universität Wien (TUW) (08 June, 2026)

Space missions

The author contributed to several mission development phases of ongoing space programs during their research at DLR. Examples of these contributions are covered in more detail in Chapter 7.

- *EROSS mission*, EU project, Phases B and C: Conducted mission analysis of robotic operations, evaluating spacecraft-robot disturbances with different control strategies, and implemented gravity compensation (detailed in Chapter 6) for on-ground testing of a space robot.
- *DIANE mission*, CNES project, Phase 1: Performed mission analysis while comparing control strategies for robotic approach and stabilization of a client, and implemented impedance matching between a space robot and laboratory robot for on-ground testing.
- *RISE mission*, ESA project, Phases A and B: Served as technical lead for the control team, analyzing the Concept of Operations (CONOPS) for robotic activities. Performed mission analysis of robotic CONOPS for different operations including tool docking, and client manipulation.

Media articles

A collection of videos and news articles related to the awards and lectures resulting from this research work is summarized in Table 1.2, and are available online.

The main contributions of the thesis are summarized in relation to the chapters in Figure 1.10.

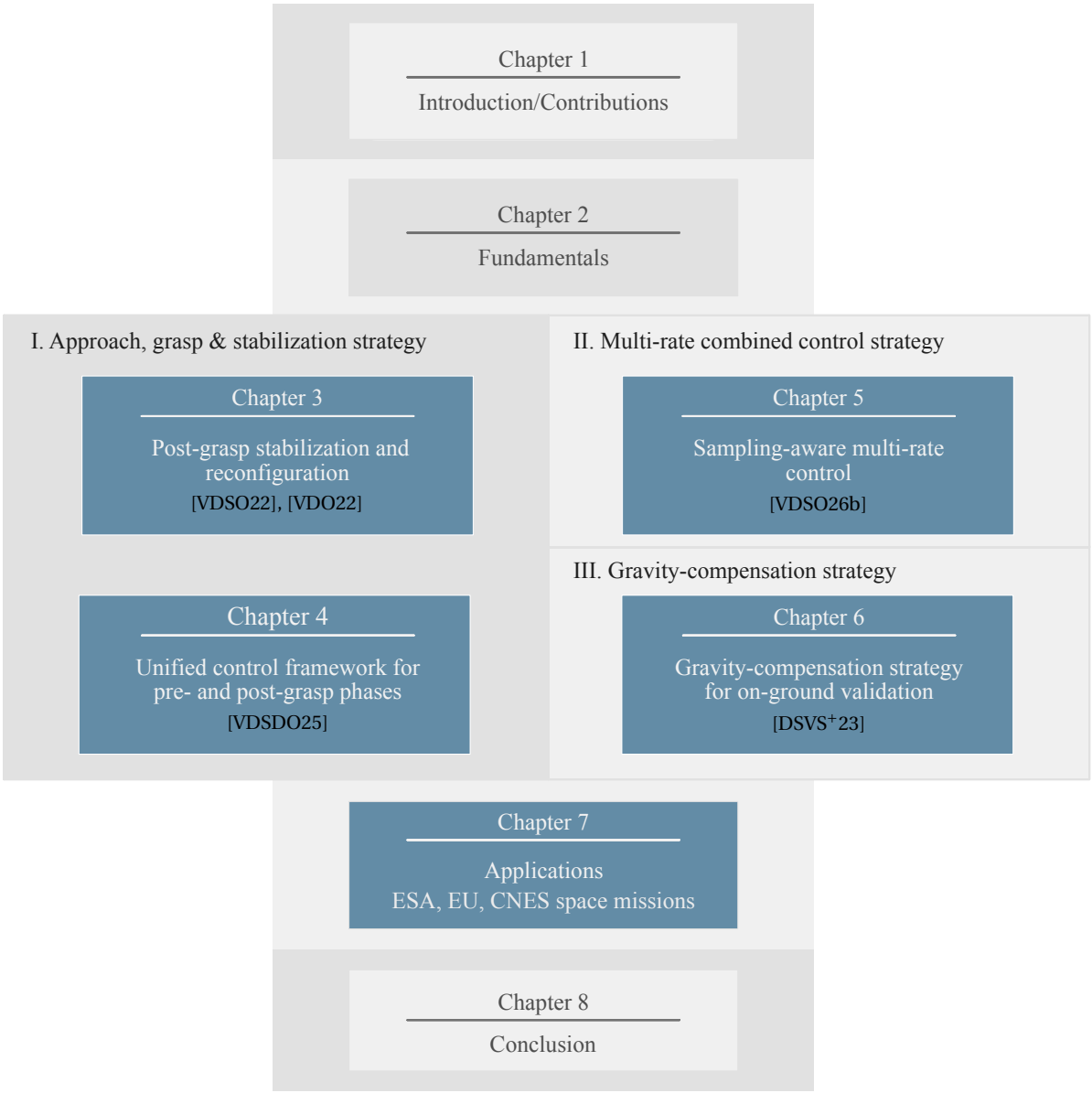

Figure 1.10: Overview of the thesis chapters and their association to contributions/publications.

Table 1.1: Publications and patents resulting from the research conducted during this thesis.

Primary contributions	
Reference	**Details**
Journal: [VDSO26b]	**R. Vijayan**, M. De Stefano and C. Ott, "Sampling-Aware Multi-Rate Combined Control for an Orbital Manipulator," in IEEE Robotics and Automation Letters, vol. 11, no. 3, pp. 3294-3301, 2026, doi: 10.1109/LRA.2026.3656723.
Journal: [VDSDO25]	**R. Vijayan**, M. De Stefano, A. Dietrich and C. Ott, "Unified Control of an Orbital Manipulator for the Approach and Grasping of a Free-Floating Satellite," in IEEE/ASME Transactions on Mechatronics, vol. 30, no. 6, pp. 5710-5721, 2025, doi: 10.1109/TMECH.2025.3545201. (**Award Finalist**)*
Conference: [DSVS+23]	M. De Stefano, **R. Vijayan**, A. Stemmer, F. Elhardt and C. Ott, "A Gravity Compensation Strategy for On-ground Validation of Orbital Manipulators," IEEE International Conference on Robotics and Automation (ICRA), London, United Kingdom, 2023, pp. 11859-11865, doi: 10.1109/ICRA48891.2023.10161480.
Conference: [VDO22]	**R. Vijayan**, M. De Stefano, C. Ott, "Control of an Orbital Manipulator with Reaction Wheels for On-orbit Servicing", IFAC Symposium on Robot Control (SYROCO), IFAC-PapersOnLine, vol. 55, no. 38, pp. 26-32, 2022, doi: 10.1016/j.ifacol.2023.01.129
Conference: [VDSO22]	**R. Vijayan**, M. De Stefano and C. Ott, "A Detumbling Strategy for an Orbital Manipulator in the Post-Grasp Phase," International Conference on Robotics and Automation (ICRA), Philadelphia, PA, USA, 2022, pp. 4080-4086, doi: 10.1109/ICRA46639.2022.9812067.
Patent: [DSOV+23]	M. De Stefano, C. Ott, **R. Vijayan**, H. Mishra, F. Elhardt, "Method for controlling a robot device", granted, 2023, DE102023113815.4A, US20240391102A1.
Patent: [VDSO25]	**R. Vijayan**, M. De Stefano, C. Ott, "Method for Controlling a Space Manipulator", pending, registered on 24 March 2025 under DE102025111079.4.
Patent: [VDSO26a]	**R. Vijayan**, C. Ott, M. De Stefano, "Method and System for operating an Orbital Manipulator arranged on a Spacecraft", pending, registered on 16 March 2026 under DE102026101406.2.
Secondary contributions	
Reference	**Details**
Journal: [SVMDS26]	F. Sena, **R. Vijayan**, H. Mishra and M. De Stefano, "Center-of-Mass and Attitude Control of an Orbital Manipulator: A Novel Control Strategy," in IEEE Robotics and Automation Letters, vol. 11, no. 6, pp. 6871-6878, 2026, doi: 10.1109/LRA.2026.3682621.
Conference: [SMVDS25]	F. Sena, H. Mishra, **R. Vijayan** and M. De Stefano, "A Control Strategy for an Orbital Manipulator Equipped with an External Actuator at the End-Effector," IEEE International Conference on Robotics and Automation (ICRA), Atlanta, GA, USA, 2025, pp. 14617-14623, doi: 10.1109/ICRA55743.2025.11128098.
Conference: [EDSS+24]	F. Elhardt, M. De Stefano, M. Schedl, M. Stelzer, A. Stemmer, I. Rodriguez, **R. Vijayan**, M.A. Roa, and T. Bruckmann, "The Motion Suspension System for On-Ground Tests of Space Robots: Demonstration and Results," IEEE Aerospace Conference, Big Sky, MT, USA, 2024, pp. 1-9, doi: 10.1109/AERO58975.2024.10521208.
Patent: [SDSMV26]	F. Sena, M. De Stefano, H. Mishra and **R. Vijayan** "Raumfahrtsystem", pending, registered on 15 May 2025 under DE102025118932.3.

* Finalist of the TMECH *Best Paper Award* among papers published in 2025 in the IEEE/ASME Transactions on Mechatronics (TMECH).

Table 1.2: Media articles

Awards Coverage and Lecture Recording
2026 Best Paper Award Results IEEE/ASME Transactions on Mechatronics News (Accessed: 5 July 2026) http://www.ieee-asme-mechatronics.info/2024-results/
RM Research Scientist Ria Vijayan Wins Amelia Earhart Fellowship DLR Robotics and Mechatronics News (Accessed: 5 July 2026) https://www.dlr.de/en/rm/latest/news/2024/rm-research-scientist-ria-vijayan-wins-amelia-earhardt-fellowship
DLR Robotic Orbital Servicing - Amelia Earhart Fellow 2024 (Ria Vijayan) DLR Robotics and Mechatronics YouTube (Accessed: 5 July 2026) https://www.youtube.com/watch?v=jcAWKQtHZKU
Introducing the 2024 Amelia Earhart Fellows Zonta International News (Accessed: 5 July 2026) https://www.zonta.org/Web/Web/News_Events/Articles/Introducing_the_2024_Amelia_Earhart_Fellows.aspx
Amelia Earhart Fellows Zonta International District 14 News (Accessed: 5 July 2026) https://www.zonta-district14.org/awards-projects/amelia-earhart/
Guest Lecture – Multi-Rate Control for an Orbital Manipulator TUM Live Lecture Recording (Accessed: 5 July 2026) https://live.rbg.tum.de/w/WiSe25_26_CE_RmL/63680?t=1620

CHAPTER 2

TEST FACILITIES AND FUNDAMENTALS

This chapter traces a broad outline of the key elements involved in developing and validating control strategies in the chapters ahead. Figure 2.1 shows the abstraction of a dynamic model that governs the dynamics of the simulated and/or hardware setup (right). The dynamic model is also used to design a stable control law (left) for closed-loop validation of different control strategies.

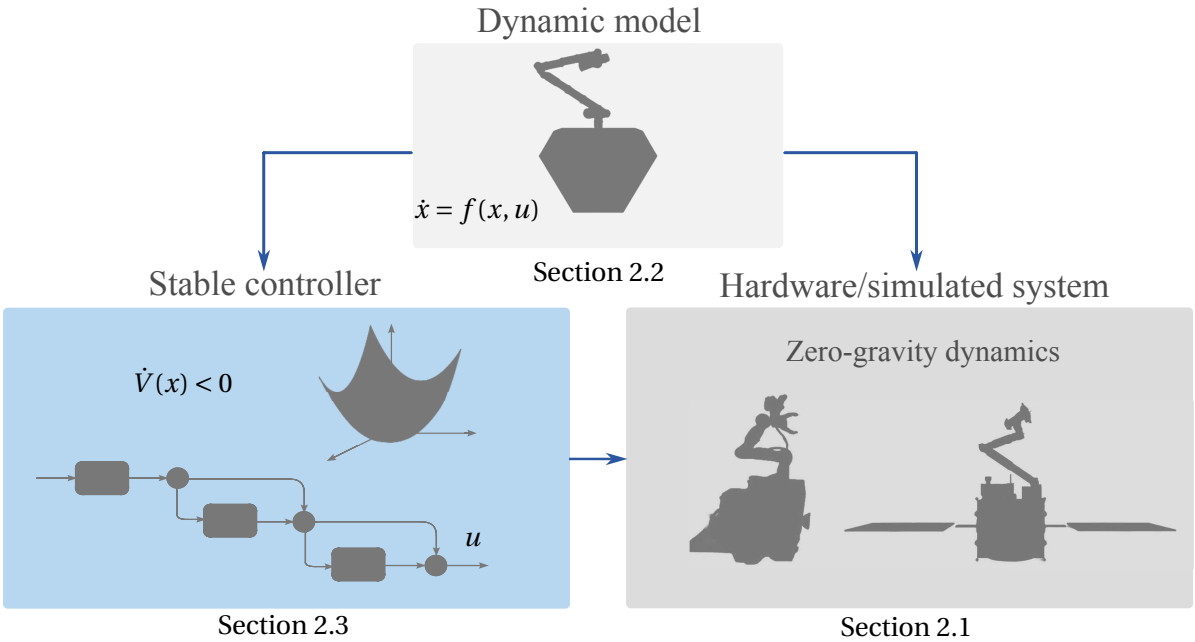

Figure 2.1: Controllers are designed to validate the control objectives on hardware and simulated systems which are modeled using a dynamic model. The sections in this chapter give some background on the hardware setup, dynamic modeling and controller stability.

Accordingly, this chapter describes the hardware setups and theoretical concepts necessary for a reader to acquire preliminaries on the contents of the following chapters. Section 2.1 presents an overview of the on-ground test facilities used to validate the proposed methods. Section 2.2 provides a detailed derivation of the orbital manipulator dynamics, which serves as the basis for control development and hardware validation of floating dynamics. Finally, an overview of stability and the relevant theorems for cascade stability analysis are stated in Section 2.3.

2.1 On-ground test facilities

The OOS-Sim facility, described in Section 2.1.1, is the main experimental facility used for validating the control strategies developed for orbital manipulators in this thesis in Chapter 4 and Chapter 5. A second experimental facility used to validate the gravity compensation strategy for orbital manipulators developed in Chapter 6 is the MSS facility described in Section 2.1.2.

2.1.1 OOS-Sim - A robotic HIL platform

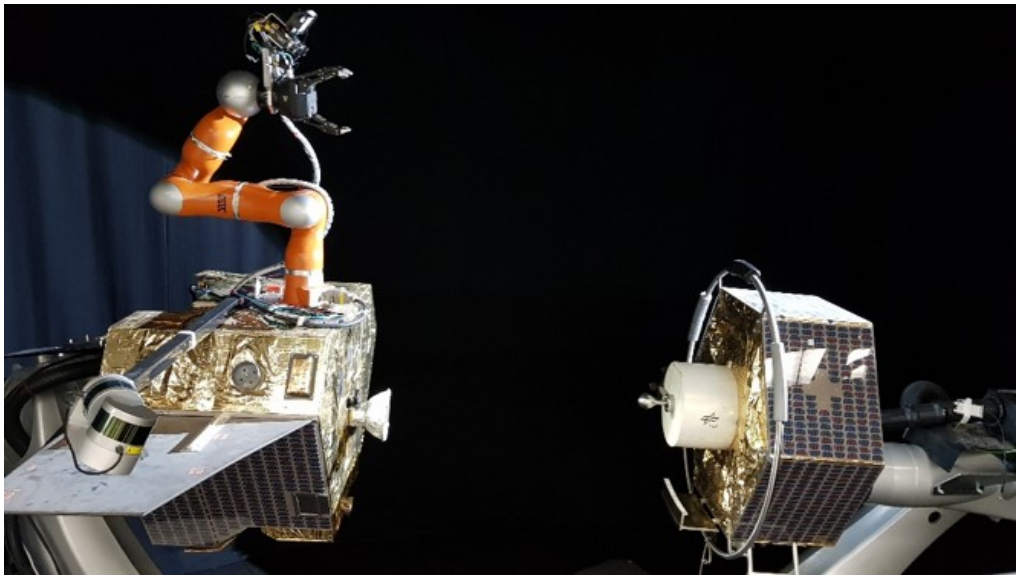

Figure 2.2: The DLR, OOS-SIM (on-orbit servicing simulator) - a state-of-the-art hardware-in-the-loop platform for on-ground validation of close-proximity operations under zero-gravity conditions [A$^+$15]. Left: servicer equipped with Light-Weight-Robot and right: client satellite mockup.

OOS-Sim (On-Orbit Servicing Simulator) is a robotic experimental facility [A$^+$15] developed by DLR's Institute of Robotics and Mechatronics that emulates the floating dynamics of spacecraft and robots in space. The platform uses industrial and lightweight robotic arms to represent both a servicer ("chaser") and a client satellite, enabling zero-gravity behavior and multibody interactions to be replicated on ground.

The OOS-Sim integrates real physical hardware (robots, sensors, actuators) with real-time dynamic simulation software to create a feedback loop. Force/torque measurements and motion from the robots are fed into simulation models of floating dynamics, and vice versa, so that control algorithms for the orbital manipulators are tested with 6-DoF zero-gravity motion. The testbed is therefore capable of validating close-proximity operations like the approach, capture, and stabilization of non-cooperative client satellites.

In particular, the floating dynamics of the servicer and client are emulated using the reduced Euler-Lagrange equations of motion from [M$^+$23] presented in Section 2.2.2. The servicer robot of the OOS-Sim, controlled in admittance mode at 250Hz, is equipped with a 7-DoF Light-Weight-Robot (LWR) arm that is torque-controlled at 1kHz. A 6-DoF force-torque sensor on the client is used to measure the real contact forces that occur during grasp and stabilization, which are then transmitted to a model-based dynamics emulator.

The experimental results presented in Chapter 4 and Chapter 5 for validation of control strategies are performed using the OOS-Sim platform.

2.1.2 MSS - A cable-suspended platform

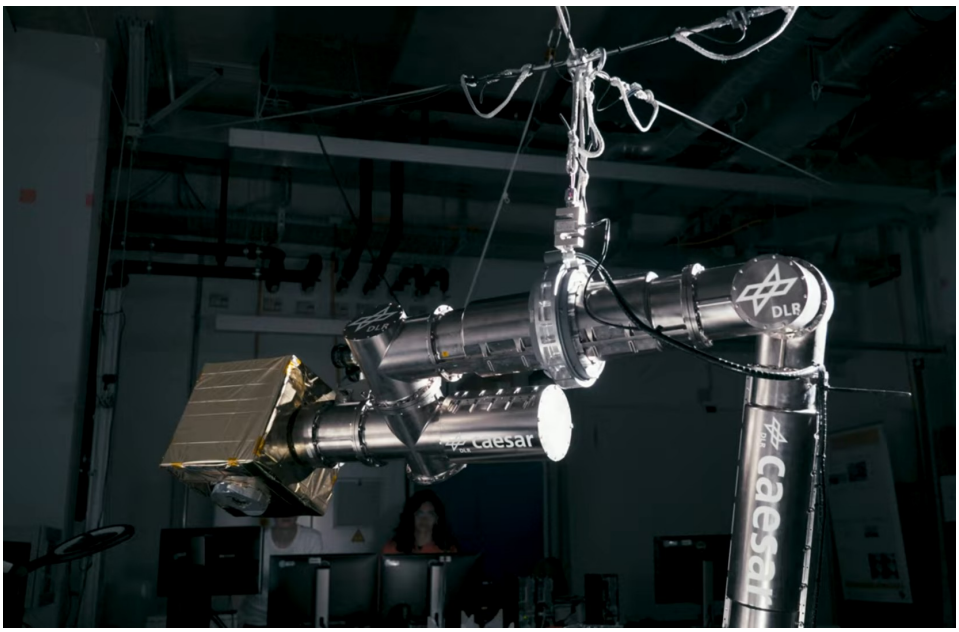

Figure 2.3: Image credit: DLR [RM25]. The Motion Suspended System (MSS) - a cable-suspended platform for gravity compensation used to perform on-ground validation of a space robot, CAESAR.

Space robots are typically designed such that the joint motor sizing is optimized for mass and torques expected for operating under zero-gravity conditions in space. This implies that they are not designed to lift their own weight on Earth. Due to the limited joint torques of the optimized motor, the operational workspace is severely restricted on-ground [DSVS$^+$23, EDSS$^+$24]. To address

this, the Institute of Robotics and Mechatronics (RM) at DLR and the University of Duisburg-Essen developed the Motion Suspension System (MSS), a cable-driven parallel robot that allows space robots to move freely in a full three-dimensional workspace on ground.

The MSS is a type of external carrier system that uses multiple cables controlled by motors to support the space robot's arm and actively counteract the effects of gravity. Thus, the MSS enhances the scope of on-ground testing compared to gravity compensation methods like air bearings (e.g., [MAB01]) that only allow motion in a two-dimensional plane which is insufficient for many space tasks such as complex trajectories, contact-oriented manipulation, or vision-based approaches.

In particular, on-ground validation of the CAESAR arm, a space-qualified robotic arm developed at DLR RM, is performed using the MSS. CAESAR is a 7-degree-of-freedom robotic manipulator (see [BGH$^+$18] for details on the arm) with joint torque limits rated at approximately 80 Nm for each of the seven joints. During on-ground testing gravitational loads on the CAESAR arm frequently produce joint torques that exceed operational limits, which is compensated by the MSS.

The MSS platform is used for experimental results presented in Chapter 6 for validating the proposed gravity-compensation strategy.

2.2 Orbital manipulator dynamics

This section presents preliminaries on the dynamic modeling of an orbital manipulator, which are used for the control design and for hardware-in-the-loop implementation. The orbital manipulator is henceforth used interchangeably with the servicer. The *servicer* is composed of a floating-base spacecraft equipped with an n-DoF manipulator arm (see Figure 2.4). It may be fully-actuated or partially, depending on the mission scenario, using a combination of thrusters, reaction wheels and joint torques. The *client* is a non-cooperative (not actively controlled) satellite modeled as a floating-base rigid body.

In Section 2.2.1, the Newton-Euler formulation of orbital manipulator dynamics is presented. As outlined in Figure 2.1, these dynamics form the basis for the control design and closed-loop stability. In Section 2.2.2, an alternate dynamic formulation based on the Lagrangian method is presented. In contrast with the Newton-Euler formulation which balances forces, the Lagrangian formulation balances energies. As seen in Figure 2.1 the HIL implementation relies on a floating-base dynamic model. The particular form of Lagrangian-based dynamics in [M$^+$23] has been shown to be robust to simple numerical integration (forward-Euler) for preserving momentum. This is useful for real-time hardware-in-the-loop simulation of floating-dynamics and is the implementation used on the HIL platform, OOS-Sim.

2.2.1 Newton-Euler formulation

The floating-base dynamics of an orbital manipulator can be modeled as a kinematic chain of constrained rigid bodies using the Newton-Euler formulation. This approach starts with the force bal-

ance in Cartesian space for each link in the manipulator's kinematic chain and applies constraint conditions by eliminating reaction forces that act in equal and opposite directions at the link attachments. The resulting formulation enables the derivation of the dynamics in generalized coordinates, or joint space, for the floating-base manipulator, analogous to the process used for a fixed-base manipulator. Here, we shall follow the approach similar to [GOAS13] with the difference that the floating base's dynamics shall be written separately from the manipulator's kinematic chain. This is done in order to arrive at the explicit block matrix form commonly used to represent the orbital manipulator dynamics.

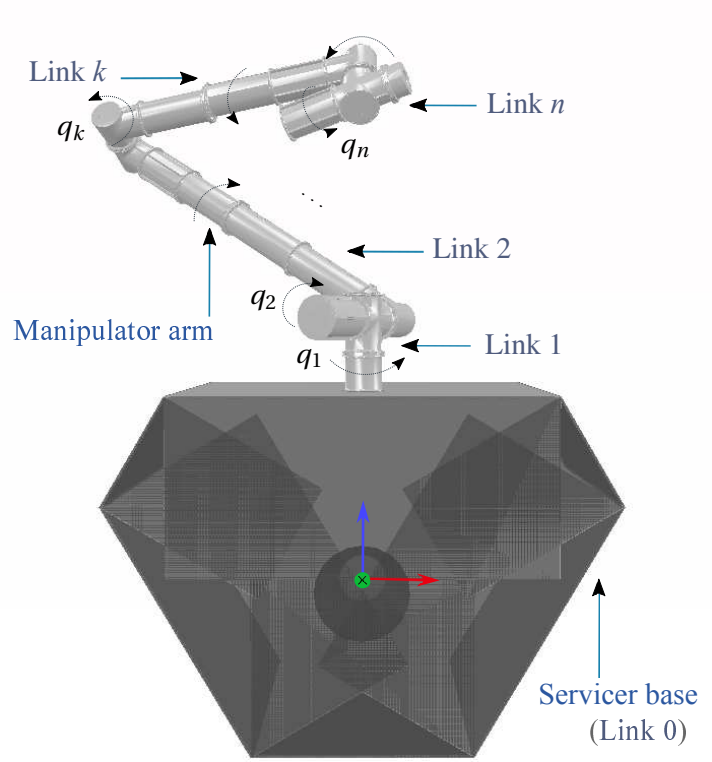

Figure 2.4: Schematic of an orbital manipulator (servicer) composed of a satellite base and an n-DoF manipulator.

First, we can write the dynamics of the base and each manipulator link ($k = 1...n$) in the kinematic chain using a body twist as follows (see Figure 2.4).

$$\begin{aligned} &\text{Spacecraft base :} && \boldsymbol{M}_0\dot{\boldsymbol{v}}_b + \boldsymbol{\psi}_0\boldsymbol{v}_b = \boldsymbol{f}_0 \\ &k\text{-th Manipulator link :} && \boldsymbol{M}_k\dot{\boldsymbol{v}}_k + \boldsymbol{\psi}_k\boldsymbol{v}_k = \boldsymbol{f}_k \end{aligned} \tag{2.1}$$

The inertia, body twist (Cartesian velocity) and forces, of the spacecraft base and k-th link of an n-DoF manipulator, are denoted by $\boldsymbol{M}_0, \boldsymbol{M}_k \in \mathbb{R}^{6\times6}$, $\boldsymbol{v}_b, \boldsymbol{v}_k \in \mathbb{R}^6$, and $\boldsymbol{f}_0, \boldsymbol{f}_k \in \mathbb{R}^6$, respectively. The

forces on the base and links are a sum of constraint forces and control forces. The Coriolis/centrifugal (CC) matrix, $\boldsymbol{\psi}_k$ can be written in a skew-symmetric form as

$$\begin{aligned} &\text{Spacecraft CC}: && \boldsymbol{\psi}_0 = \boldsymbol{M}_0 \mathrm{ad}_{\boldsymbol{v}_b} - \mathrm{ad}_{\boldsymbol{v}_b}^T \boldsymbol{M}_0 \\ &k\text{-th link CC}: && \boldsymbol{\psi}_k = \boldsymbol{M}_k \mathrm{ad}_{\boldsymbol{v}_k} - \mathrm{ad}_{\boldsymbol{v}_k}^T \boldsymbol{M}_k \end{aligned} \tag{2.2}$$

As $\boldsymbol{M}_k, \boldsymbol{M}_0$ are constant, they satisfy the passivity property $\dot{\boldsymbol{M}}_0 = \boldsymbol{\psi}_0 + \boldsymbol{\psi}_0^T$ and $\dot{\boldsymbol{M}}_k = \boldsymbol{\psi}_k + \boldsymbol{\psi}_k^T$. The Lie bracket matrix $\mathrm{ad}_\bullet$ (defined in Appendix A.1) maps the Lie algebra of body twists onto itself. Its transpose maps wrenches.

The link velocities $\boldsymbol{v}_k$ in (2.1) can be substituted with base velocity $\boldsymbol{v}_b$, link Jacobian $\boldsymbol{J}_k \in \mathbb{R}^{6\times n}$ and minimal coordinates $\dot{\boldsymbol{q}} \in \mathbb{R}^n$ (joint velocities) as

$$\text{Link velocity}: \qquad \boldsymbol{v}_k = \mathrm{Ad}_{bk}^{-1} \boldsymbol{v}_b + \boldsymbol{J}_k \dot{\boldsymbol{q}} \tag{2.3}$$

The adjoint matrix Ad_{bk}^{-1} (defined in Appendix A.1) maps the base velocity to the k-th link frame. Its transpose maps wrenches. Then, the dynamics of the manipulator links and base are stacked using the operator col( ) that vertically stacks the k link dynamics in a column vector. Further, substituting with (2.3), and left-multiplying with the stacked Jacobian-transpose, we have

$$\text{Stacked dynamics}: \qquad \boldsymbol{J}^T \left(\boldsymbol{\Omega} \boldsymbol{J} \dot{\boldsymbol{V}}_s + (\boldsymbol{\psi} \boldsymbol{J} + \boldsymbol{\Omega} \dot{\boldsymbol{J}}) \boldsymbol{V}_s \right) = \boldsymbol{\Gamma} \tag{2.4}$$

$$\boldsymbol{V}_s = \begin{bmatrix} \boldsymbol{v}_b \\ \dot{\boldsymbol{q}} \end{bmatrix}, \ \boldsymbol{\Gamma} = \begin{bmatrix} \boldsymbol{F}_b \\ \boldsymbol{\tau}_m \end{bmatrix}, \ \boldsymbol{J} = \begin{bmatrix} \boldsymbol{I} & \boldsymbol{0} \\ \mathrm{col}(\mathrm{Ad}_{bk}^{-1}) & \mathrm{col}(\boldsymbol{J}_k) \end{bmatrix}, \ \boldsymbol{\Omega} = \begin{bmatrix} \boldsymbol{M}_0 & \boldsymbol{0} \\ \boldsymbol{0} & \mathrm{blkdiag}(\boldsymbol{M}_k) \end{bmatrix}, \ \boldsymbol{\psi} = \begin{bmatrix} \boldsymbol{\psi}_0 & \boldsymbol{0} \\ \boldsymbol{0} & \mathrm{blkdiag}(\boldsymbol{\psi}_k) \end{bmatrix}$$

The right-hand-side of (2.4) is a consequence of the vanishing constraint reaction forces [GOAS13], leaving the control forces, $\boldsymbol{\Gamma} \in \mathbb{R}^{6+n}$. Here, $\boldsymbol{F}_b \in \mathbb{R}^6$ is the full actuation wrench (force and torque) applied on the base and $\boldsymbol{\tau}_m \in \mathbb{R}^n$ are the manipulator control torques. The resulting dynamics can be written in the explicit block matrix form as,

$$\text{Orbital manipulator dynamics}: \quad \underbrace{\begin{bmatrix} \boldsymbol{M}_{bb} & \boldsymbol{M}_{bm} \\ \boldsymbol{M}_{bm}^T & \boldsymbol{M}_{mm} \end{bmatrix}}_{\boldsymbol{M}_s(\boldsymbol{q})} \begin{bmatrix} \dot{\boldsymbol{v}}_b \\ \ddot{\boldsymbol{q}} \end{bmatrix} + \underbrace{\begin{bmatrix} \boldsymbol{C}_{bb} & \boldsymbol{C}_{bm} \\ \boldsymbol{C}_{mb} & \boldsymbol{C}_{mm} \end{bmatrix}}_{\boldsymbol{C}_s(\boldsymbol{q},\boldsymbol{V}_s)} \underbrace{\begin{bmatrix} \boldsymbol{v}_b \\ \dot{\boldsymbol{q}} \end{bmatrix}}_{\boldsymbol{V}_s} = \underbrace{\begin{bmatrix} \boldsymbol{F}_b \\ \boldsymbol{\tau}_m \end{bmatrix}}_{\boldsymbol{\Gamma}} \tag{2.5}$$

Here, $\boldsymbol{M}_{bb} \in \mathbb{R}^{6\times 6}, \boldsymbol{M}_{mm} \in \mathbb{R}^{n\times n}, \boldsymbol{M}_{bm} \in \mathbb{R}^{6\times n}$ are the inertia matrices of the servicer, manipulator and their coupling, respectively. They are a function of the joint positions $\boldsymbol{q} \in \mathbb{R}^n$. Similarly, $\boldsymbol{C}_{bb} \in \mathbb{R}^{6\times 6}, \boldsymbol{C}_{mm} \in \mathbb{R}^{n\times n}, \boldsymbol{C}_{bm} \in \mathbb{R}^{6\times n}, \boldsymbol{C}_{mb} \in \mathbb{R}^{n\times 6}$ are sub-elements of the Coriolis/Centrifugal (CC) matrix. They depend on joint positions and velocities $\boldsymbol{q}, \dot{\boldsymbol{q}} \in \mathbb{R}^n$, and the Cartesian base velocity (linear and angular), $\boldsymbol{v}_b \in \mathbb{R}^6$.

In particular, the submatrices of the inertia and CC matrix in (2.5) can be computed iteratively for $k = 1...n$, while making use of the property $\dot{\mathrm{Ad}}_{bk}^{-1} = -\mathrm{ad}_{\boldsymbol{v}_k}\mathrm{Ad}_{bk}^{-1}$

- $\boldsymbol{M}_{bb} = \boldsymbol{M}_0 + \sum_k \mathrm{Ad}_{bk}^{-T}\boldsymbol{M}_k\mathrm{Ad}_{bk}^{-1}$
- $\boldsymbol{M}_{mm} = \sum_k \boldsymbol{J}_k^T\boldsymbol{M}_k\boldsymbol{J}_k$
- $\boldsymbol{M}_{bm} = \sum_k \mathrm{Ad}_{bk}^{-T}\boldsymbol{M}_k\boldsymbol{J}_k$
- $\boldsymbol{C}_{bb} = \boldsymbol{\psi}_0 + \sum_k \mathrm{Ad}_{bk}^{-T}\boldsymbol{\psi}_k\mathrm{Ad}_{bk}^{-1} - \mathrm{Ad}_{bk}^{-T}\boldsymbol{M}_k\mathrm{ad}_{\boldsymbol{v}_k}\mathrm{Ad}_{bk}^{-1}$
- $\boldsymbol{C}_{mm} = \sum_k \boldsymbol{J}_k^T\boldsymbol{\psi}_k\boldsymbol{J}_k + \boldsymbol{J}_k^T\boldsymbol{M}_k\dot{\boldsymbol{J}}_k$
- $\boldsymbol{C}_{bm} = \sum_k \mathrm{Ad}_{bk}^{-T}\boldsymbol{\psi}_k\boldsymbol{J}_k + \mathrm{Ad}_{bk}^{-T}\boldsymbol{M}_k\dot{\boldsymbol{J}}_k$
- $\boldsymbol{C}_{mb} = \sum_k \boldsymbol{J}_k^T\boldsymbol{\psi}_k\mathrm{Ad}_{bk}^{-1} - \boldsymbol{J}_k^T\boldsymbol{M}_k\mathrm{ad}_{\boldsymbol{v}_k}\mathrm{Ad}_{bk}^{-1}$

With the above expressions, one can verify that the passivity property $\dot{\boldsymbol{M}}_s = \boldsymbol{C}_s + \boldsymbol{C}_s^T$ is satisfied. The *servicer* (orbital manipulator) dynamics used to develop the controllers in this thesis shall be represented by (2.5), with adaptations when reaction wheels are included or when the client satellite is attached like in the post-grasp phase. These cases are also detailed ahead.

Servicer dynamics including reaction wheels

The servicer is typically equipped with actuation systems designed to control the base. These systems may utilize external actuation, such as thrusters, or internal mechanisms, such as reaction wheels. Reaction wheels are devices that control only the attitude, enabling stabilization of the spacecraft base during rotation by applying internal torques.

When the servicer base is equipped additionally with reaction wheels (see Figure 2.5) the dynamics in (2.5) can be augmented to include reaction wheels as,

$$\underbrace{\begin{bmatrix} \boldsymbol{M}_{bb} & \boldsymbol{M}_{bm} & \boldsymbol{M}_{br} \\ \boldsymbol{M}_{bm}^T & \boldsymbol{M}_{mm} & \boldsymbol{0} \\ \boldsymbol{M}_{br}^T & \boldsymbol{0} & \boldsymbol{M}_{rr} \end{bmatrix}}_{\boldsymbol{M}_s(\boldsymbol{q})} \begin{bmatrix} \dot{\boldsymbol{v}}_b \\ \ddot{\boldsymbol{q}} \\ \ddot{\boldsymbol{r}} \end{bmatrix} + \underbrace{\begin{bmatrix} \boldsymbol{C}_{bb} & \boldsymbol{C}_{bm} & \boldsymbol{C}_{br} \\ \boldsymbol{C}_{mb} & \boldsymbol{C}_{mm} & \boldsymbol{C}_{mr} \\ \boldsymbol{C}_{rb} & \boldsymbol{C}_{rm} & \boldsymbol{C}_{rr} \end{bmatrix}}_{\boldsymbol{C}_s(\boldsymbol{q},\boldsymbol{V}_s)} \underbrace{\begin{bmatrix} \boldsymbol{v}_b \\ \dot{\boldsymbol{q}} \\ \dot{\boldsymbol{r}} \end{bmatrix}}_{\boldsymbol{V}_s} = \underbrace{\begin{bmatrix} \boldsymbol{F}_b \\ \boldsymbol{\tau}_m \\ \boldsymbol{\tau}_r \end{bmatrix}}_{\boldsymbol{\Gamma}} \tag{2.6}$$

The servicer's states, $\boldsymbol{V}_s$ are extended here with $\dot{\boldsymbol{r}} \in \mathbb{R}^r$ for velocities of r reaction wheels. Similarly, the actuation on the servicer, $\boldsymbol{\Gamma}$ is also extended by $\boldsymbol{\tau}_r \in \mathbb{R}^r$, to include the torques applied to the reaction wheels. Observe the inertia coupling between the reaction wheels and base via $\boldsymbol{M}_{br} \in \mathbb{R}^{6\times r}$, while the reaction wheels are inertially decoupled from the manipulator, which is in a separate kinematic chain originating from the base. As seen in (2.6), the couplings between the reaction wheels and manipulator manifest via the cross-coupling terms of the CC matrix.

The servicer's states, actuation, inertia and Coriolis matrices in general are $\boldsymbol{V}_s, \boldsymbol{\Gamma} \in \mathbb{R}^{6+n+r}$, $\boldsymbol{M}_s, \boldsymbol{C}_s \in \mathbb{R}^{6+n+r}$ (with $r = 0$ if reaction wheels are excluded).

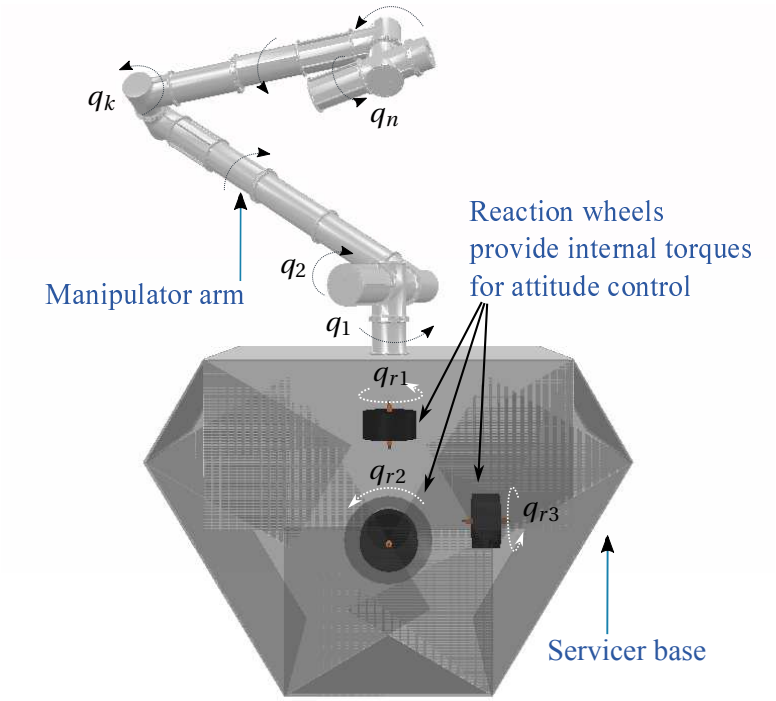

Figure 2.5: Schematic of a servicer composed of a satellite base equipped with a set of three orthogonal reaction wheels and an n-DoF manipulator.

Servicer dynamics in post-grasp phase

The post-grasp phase refers to the phase starting from the moment where the client satellite has been captured (see Figure 2.6) by a gripper mechanism mounted at the end-effector of the manipulator on the servicer satellite. This mechanism is usually designed to create a rigid connection between the client and servicer. The post-grasp dynamics is modeled using the velocity constraint imposed by the condition of having a rigid grasp between the servicer end-effector and client. Following the standard approach in robotic grasp dynamics [MLS94], the servicer and client dynamics subject to equal and opposite client interaction forces is given by,

(2.7) Servicer dynamics : $\boldsymbol{M}_s\dot{\boldsymbol{V}}_s + \boldsymbol{C}_s\boldsymbol{V}_s = \boldsymbol{\Gamma} + \boldsymbol{J}_e^T\boldsymbol{F}_c,$

(2.8) Client dynamics : $\boldsymbol{M}_c\dot{\boldsymbol{v}}_c + \boldsymbol{C}_c\boldsymbol{v}_c = -\boldsymbol{J}_c^T\boldsymbol{F}_c,$

where $\boldsymbol{M}_c, \boldsymbol{C}_c \in \mathbb{R}^{6\times6}$, are the inertia and CC matrices of the client dynamics. The servicer's states, actuation, inertia and Coriolis matrices $\boldsymbol{V}_s, \boldsymbol{\Gamma}, \boldsymbol{M}_s, \boldsymbol{C}_s$ are substituted from (2.6) or (2.5) depending on the inclusion of reaction wheels or not. The servicer's end-effector Jacobian, $\boldsymbol{J}_e$ maps $\boldsymbol{V}_s$ to $\boldsymbol{v}_e \in \mathbb{R}^6$, the end-effector Cartesian velocity. The client's Jacobian matrix $\boldsymbol{J}_c \in \mathbb{R}^{6\times6}$ maps the client velocity $\boldsymbol{v}_c \in \mathbb{R}^6$ to the Cartesian velocity at the grasping point. The client Jacobian $\boldsymbol{J}_c$ is an invertible adjoint transformation, considering the grasping point to be a fixed point on the client. Lastly, $\boldsymbol{F}_c \in \mathbb{R}^6$ is the interaction wrench acting between the manipulator's end-effector and the client's grasping point

expressed in the end-effector frame.

Given a rigid grasp, the velocity constraint can be used to obtain the combined dynamics of the servicer-client system ([Agh09]). This implies that the velocity at the servicer's end-effector and client's grasping point are equal.

(2.9) Grasp velocity constraint : $\boldsymbol{v}_e = \boldsymbol{J}_e \boldsymbol{V}_s = \boldsymbol{J}_c \boldsymbol{v}_c$

Using the constraint in (2.9), $\boldsymbol{v}_c$ and its time-derivative can be substituted in (2.8). Combining (2.7) and (2.8) the post-grasp dynamics are obtained in terms of purely the servicer's states as follows [Agh09],

(2.10) Post-grasp dynamics : $\boldsymbol{M}_{sc}\dot{\boldsymbol{V}}_s + \boldsymbol{C}_{sc}\boldsymbol{V}_s = \boldsymbol{\Gamma}$

where,
- $\boldsymbol{M}_{sc} = \boldsymbol{M}_s + \boldsymbol{J}_e^T \boldsymbol{J}_c^{-T} \boldsymbol{M}_c \boldsymbol{J}_c^{-1} \boldsymbol{J}_e$: Inertia with grasped client
- $\boldsymbol{C}_{sc} = \boldsymbol{C}_s + \boldsymbol{J}_e^T \boldsymbol{J}_c^{-T} \boldsymbol{C}_s \boldsymbol{J}_c^{-1} \boldsymbol{J}_e + \boldsymbol{J}_e^T \boldsymbol{J}_c^{-T} \boldsymbol{M}_c \frac{d}{dt}(\boldsymbol{J}_c^{-1} \boldsymbol{J}_e)$: CC with grasped client

In the post-grasp phase, the interaction forces, $\boldsymbol{F}_c$, being internal constraint forces at the grasping point, vanish from the combined dynamics. The post-grasp model in (2.10) can accommodate the servicer's dynamics both when it excludes or includes reaction wheels, in which cases, the inertia, CC matrices, states and control inputs are taken from (2.5) or (2.6), respectively.

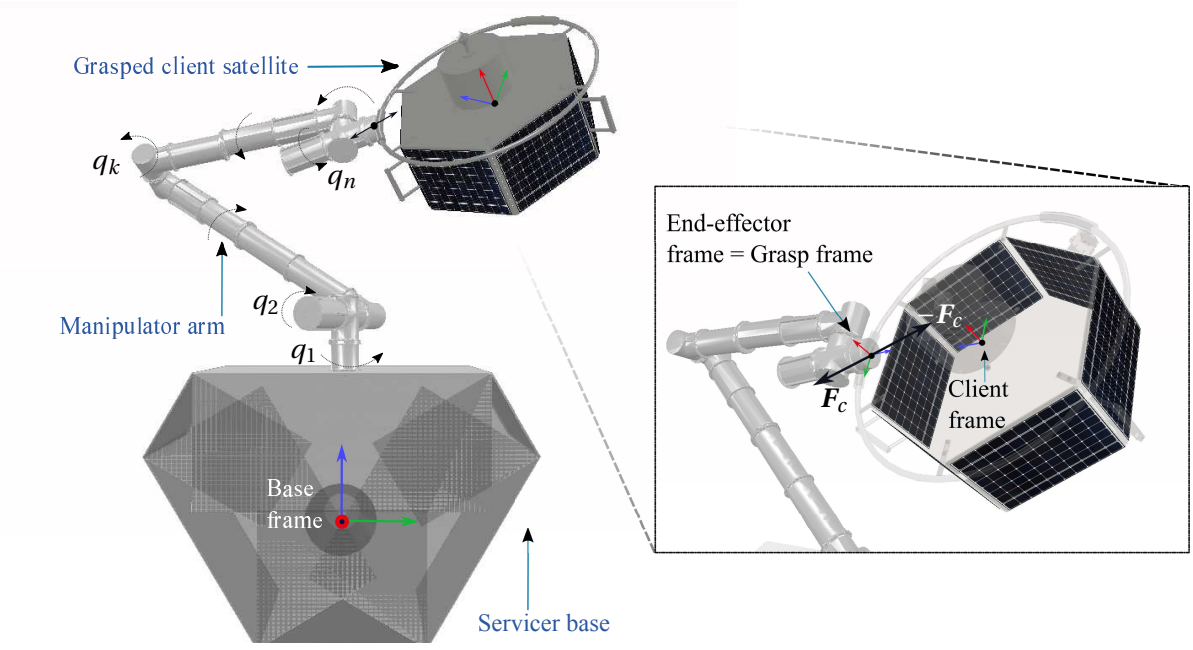

Figure 2.6: Schematic of a servicer in the post-grasp phase with a client satellite grasped by an n-DoF manipulator. The zoomed inset shows the equal and opposite interaction forces, $\boldsymbol{F}_c$, acting at the interface between the grasping point of the servicer and client.

2.2.2 Reduced Euler-Lagrange formulation

The floating-base manipulator dynamics in (2.5) can alternatively be expressed with a block-diagonal inertia matrix using the generalized momentum instead of the body twist. This was done in [GHEO15] starting from the Newton-Euler formulation to show the decoupled structure of the inertia matrix between the generalized momentum and manipulator joint coordinates.

Similarly, the dynamics in [M$^+$23] were also formulated with a diagonal inertia matrix, however using the so-called *locked* velocity, instead of the generalized momentum, which is the instantaneous velocity of the locked shape of the orbital manipulator. Further, the Newton-Euler formulation of the floating-base dynamics were correlated with the Reduced Euler-Lagrange (REL) equations and the structure of the CC matrix and interpretation therein highlighted. Previous works [Hol07], [Sil82] have also shown algorithms for computing the dynamics matrices of inertia and Coriolis forces to be equivalent between the Newton-Euler and Euler-Lagrangian formulations. The dynamic representation in [M$^+$23], used on the OOS-Sim, is derived ahead.

In contrast with the Newton-Euler formulations which begin with force equations (as in (2.1)), the Lagrangian formulations begin with energy equations. Here, we shall explicitly derive the locked velocity and manipulator dynamics using the Principle of Least Action to arrive at the REL equations. The Lagrangian of the floating base robot, in terms of the manipulator velocities $\dot{\boldsymbol{q}}$ and locked velocity $\boldsymbol{v}_L$ can be defined as,

$$\text{Lagrangian}: \qquad l = \frac{1}{2}\dot{\boldsymbol{q}}^T \boldsymbol{\Lambda}_{qq}\dot{\boldsymbol{q}} + \frac{1}{2}\boldsymbol{v}_L^T \boldsymbol{M}_{bb}\boldsymbol{v}_L \tag{2.11}$$

where,
- $\boldsymbol{\Lambda}_{qq} = \boldsymbol{M}_{mm} - \boldsymbol{M}_{bm}^T \boldsymbol{M}_{bb}^{-1}\boldsymbol{M}_{bm}$: generalized manipulator inertia
- $\boldsymbol{v}_L = \boldsymbol{v}_b + \boldsymbol{A}_I\dot{\boldsymbol{q}}$: locked velocity associated with generalized momentum
- $\boldsymbol{A}_I = \boldsymbol{M}_{bb}^{-1}\boldsymbol{M}_{bm}$: mechanical connection

The action S is then given by the integral of the Lagrangian and its variation δS can be written as,

$$\text{Action}: \qquad S = \int_{t_1}^{t_2} l(\boldsymbol{q}, \dot{\boldsymbol{q}}, \boldsymbol{v}_L)\,dt$$

$$\delta S = \underbrace{\int_{t_1}^{t_2} \partial_{\boldsymbol{q}}^T l\,\delta\boldsymbol{q}\,dt}_{\text{i}} + \underbrace{\int_{t_1}^{t_2} \partial_{\dot{\boldsymbol{q}}}^T l\,\delta\dot{\boldsymbol{q}}\,dt}_{\text{ii}} + \underbrace{\int_{t_1}^{t_2} \partial_{\boldsymbol{v}}^T l\,\delta\boldsymbol{v}_L\,dt}_{\text{iii}} \tag{2.12}$$

The operators $\partial_{\boldsymbol{q}}, \partial_{\dot{\boldsymbol{q}}}$ and $\partial_{\boldsymbol{v}}$ denote the partial derivatives with respect to the joint position, joint velocity and locked velocity, respectively. The terms ii and iii will be expanded ahead. In the following text, partial derivatives are taken on vectors instead of matrices, thus avoiding tensors. Relevant Lie operators and associated identities used in the derivation ahead are summarized in Appendix A.1.

For a variation in the pose of the floating-base $\delta\boldsymbol{g}_b \in \mathrm{SE}(3)$, the corresponding variation of the base velocity $\delta\boldsymbol{v}_b$ and thus locked velocity $\delta\boldsymbol{v}_L$ is given by,

$$\text{Base variation}: \qquad \delta\boldsymbol{v}_b = \mathrm{ad}_{\boldsymbol{v}_b}\boldsymbol{\eta}_b + \dot{\boldsymbol{\eta}}_b, \qquad \boldsymbol{\eta}_b^\wedge = \boldsymbol{g}_b^{-1}\delta\boldsymbol{g}_b$$

$$\delta\boldsymbol{v}_L = \delta\boldsymbol{v}_b + \delta\boldsymbol{A}_I\dot{\boldsymbol{q}} + \boldsymbol{A}_I\delta\dot{\boldsymbol{q}} \tag{2.13}$$

where the wedge operator $\wedge$ (defined in Appendix A.1) maps the variation $\boldsymbol{\eta}_b \in \mathbb{R}^6$ to an element in $se(3)$.

By the Principle of Least Action, the equations of motion satisfy the condition $\delta S = 0$ for variations that vanish at the end-points in time [Hol11] i.e. the trajectories along which the action integral is said to be stationary. The boundary conditions impose the variations at the start and end of the trajectory to be zero. Using (2.13) and expanding the terms ii and iii of δS in (2.12) by applying the rule of integration by parts,

$$\text{ii}: \quad \int_{t_1}^{t_2} \partial_{\dot{\boldsymbol{q}}}^T l \, \delta \dot{\boldsymbol{q}} \, dt = \left[\partial_{\dot{\boldsymbol{q}}}^T l \, \delta \boldsymbol{q}\right]_{t_1}^{t_2} - \int_{t_1}^{t_2} \frac{d}{dt}\left(\partial_{\dot{\boldsymbol{q}}}^T l\right) \delta \boldsymbol{q} \, dt \tag{2.14}$$

$$\begin{aligned}\text{iii}: \quad \int_{t_1}^{t_2} \partial_{\boldsymbol{v}}^T l \, \delta \boldsymbol{v}_L \, dt &= \int_{t_1}^{t_2} \partial_{\boldsymbol{v}}^T l \, \mathrm{ad}_{\boldsymbol{v}_b}^T \boldsymbol{\eta}_b \, dt + \int_{t_1}^{t_2} \partial_{\boldsymbol{v}}^T l \, \partial_{\boldsymbol{q}}^T (\boldsymbol{A}_l \dot{\boldsymbol{q}}) \delta \boldsymbol{q} \, dt \\ &\quad + \left[\partial_{\boldsymbol{v}}^T l \, \boldsymbol{\eta}_b\right]_{t_1}^{t_2} - \int_{t_1}^{t_2} \frac{d}{dt}\left(\partial_{\boldsymbol{v}}^T l\right) \boldsymbol{\eta}_b \, dt \\ &\quad + \left[\partial_{\boldsymbol{v}}^T l \, \boldsymbol{A}_l \delta \boldsymbol{q}\right]_{t_1}^{t_2} - \int_{t_1}^{t_2} \frac{d}{dt}\left(\partial_{\boldsymbol{v}}^T l \, \boldsymbol{A}_l\right) \delta \boldsymbol{q} \, dt\end{aligned}$$

Applying boundary conditions, $\boldsymbol{\eta}_b(t_1) = \boldsymbol{\eta}_b(t_2) = \mathbf{0}$ and $\delta \boldsymbol{q}(t_1) = \delta \boldsymbol{q}(t_2) = \mathbf{0}$ due to vanishing variations at start and end points of the trajectory. Finally, all the terms of (2.12) with the expansions in (2.14) can be combined and the variation of the action integral set to zero.

(2.15)

$$\begin{aligned}&\delta S = \text{i} + \text{ii} + \text{iii} = 0 \\ &= \int_{t_1}^{t_2} \left(\mathrm{ad}_{\boldsymbol{v}_L - \boldsymbol{A}_l \dot{\boldsymbol{q}}}^T \partial_{\boldsymbol{v}} l - \frac{d}{dt}\left(\partial_{\boldsymbol{v}} l\right)\right)^T \boldsymbol{\eta}_b \, dt + \left(\partial_{\boldsymbol{q}} l - \frac{d}{dt}\left(\partial_{\dot{\boldsymbol{q}}} l\right) + \partial_{\boldsymbol{q}} (\boldsymbol{A}_l \dot{\boldsymbol{q}})^T \partial_{\boldsymbol{v}} l - \frac{d}{dt}\left(\boldsymbol{A}_l^T \partial_{\boldsymbol{v}} l\right)\right)^T \delta \boldsymbol{q} \, dt\end{aligned}$$

Since $\delta S = 0$ must hold for any arbitrary variations $\boldsymbol{\eta}_b$ and $\delta \boldsymbol{q}$ in (2.15), the resulting equations for the momentum (expressed by locked velocity) and the equations for the shape (expressed by joint velocities) are,

$$\begin{aligned}&\text{Locked velocity dynamics}: && \mathrm{ad}_{\boldsymbol{v}_L - \boldsymbol{A}_l \dot{\boldsymbol{q}}}^T \partial_{\boldsymbol{v}} l - \frac{d}{dt}\left(\partial_{\boldsymbol{v}} l\right) = \mathbf{0} \\ &\text{Manipulator joint dynamics}: && \partial_{\boldsymbol{q}} l - \frac{d}{dt}\left(\partial_{\dot{\boldsymbol{q}}} l\right) + \partial_{\boldsymbol{q}} (\boldsymbol{A}_l \dot{\boldsymbol{q}})^T \partial_{\boldsymbol{v}} l - \frac{d}{dt}\left(\boldsymbol{A}_l^T \partial_{\boldsymbol{v}} l\right) = \mathbf{0}\end{aligned} \tag{2.16}$$

where,

- $\partial_{\boldsymbol{v}} l = \boldsymbol{M}_{bb} \boldsymbol{v}_L$
- $\partial_{\dot{\boldsymbol{q}}} l = \boldsymbol{\Lambda}_{qq} \dot{\boldsymbol{q}}$
- $\partial_{\boldsymbol{q}} l = \frac{1}{2} \partial_{\boldsymbol{q}} \left(\boldsymbol{\Lambda}_{qq} \dot{\boldsymbol{q}}\right)^T \dot{\boldsymbol{q}} + \frac{1}{2} \partial_{\boldsymbol{q}} \left(\boldsymbol{M}_{bb} \boldsymbol{v}_L\right)^T \boldsymbol{v}_L$
- $\frac{d}{dt}\left(\boldsymbol{A}_l^T \partial_{\boldsymbol{v}} l\right) = \dot{\boldsymbol{A}}_l{}^T \boldsymbol{M}_{bb} \boldsymbol{v}_L + \boldsymbol{A}_l^T \left(\boldsymbol{M}_{bb} \dot{\boldsymbol{v}}_L + \dot{\boldsymbol{M}}_{bb} \boldsymbol{v}_L\right)$

Using coordinate transformations, we can project the control forces acting on the base and manipulator using the corresponding Jacobian-transpose [1]. This is obtained by defining the Jacobian between the base twist and locked velocity coordinates as, $\boldsymbol{v}_b = \boldsymbol{J}_{\boldsymbol{v}_L}\begin{bmatrix}\boldsymbol{v}_L^T & \dot{\boldsymbol{q}}^T\end{bmatrix}^T$ where $\boldsymbol{J}_{\boldsymbol{v}_L} = \begin{bmatrix}\boldsymbol{I} & \boldsymbol{A}_l\end{bmatrix}$ Finally, when a wrench $\boldsymbol{F}_b$ is applied on the base and torques $\boldsymbol{\tau}_m$ are applied to the manipulator joints in (6.12), the base wrench gets projected as $\boldsymbol{J}_{\boldsymbol{v}_L}^T\boldsymbol{F}_b$, resulting in the Reduced Euler-Lagrange (REL) dynamics written explicitly as,

(2.17) REL equations :

$$\begin{bmatrix}\boldsymbol{M}_{bb} & \boldsymbol{0}\\ \boldsymbol{0} & \boldsymbol{\Lambda}_{qq}\end{bmatrix}\begin{bmatrix}\dot{\boldsymbol{v}}_L\\ \ddot{\boldsymbol{q}}\end{bmatrix} = \begin{bmatrix}\boldsymbol{F}_b\\ \boldsymbol{A}_l^T\boldsymbol{F}_b + \boldsymbol{\tau}_m\end{bmatrix} - \underbrace{\begin{bmatrix}\frac{1}{2}\dot{\boldsymbol{M}}_{bb} & \boldsymbol{0}\\ \boldsymbol{0} & \frac{1}{2}\dot{\boldsymbol{\Lambda}}_{qq}\end{bmatrix}}_{\text{symmetric}}\begin{bmatrix}\boldsymbol{v}_L\\ \dot{\boldsymbol{q}}\end{bmatrix} + \ldots$$

$$+ \underbrace{\begin{bmatrix}\mathrm{ad}^{\sim}_{\boldsymbol{M}_{bb}\boldsymbol{v}_L} & \frac{1}{2}S(\boldsymbol{v}_L) - \mathrm{ad}^{\sim}_{\boldsymbol{M}_{bb}\boldsymbol{v}_L}\boldsymbol{A}_l\\ -\frac{1}{2}S^T(\boldsymbol{v}_L) - \boldsymbol{A}_l^T\mathrm{ad}^{\sim}_{\boldsymbol{M}_{bb}\boldsymbol{v}_L} & S_1(\boldsymbol{v}_L) + \frac{1}{2}S_2(\dot{\boldsymbol{q}}) - \boldsymbol{A}_l^T\mathrm{ad}^{\sim}_{\boldsymbol{M}_{bb}\boldsymbol{v}_L}\boldsymbol{A}_l\end{bmatrix}}_{\text{skew-symmetric}}\begin{bmatrix}\boldsymbol{v}_L\\ \dot{\boldsymbol{q}}\end{bmatrix}$$

(2.18) where,

- $S(\boldsymbol{v}_L) = \partial_{\boldsymbol{q}}^T(\boldsymbol{M}_{bb}\boldsymbol{v}_L)$
- $S_1(\boldsymbol{v}_L) = \left(\boldsymbol{A}_l^T\partial_{\boldsymbol{q}}^T(\boldsymbol{M}_{bb}\boldsymbol{v}_L) - \partial_{\boldsymbol{q}}(\boldsymbol{M}_{bb}\boldsymbol{v}_L)^T\boldsymbol{A}_l\right) + \left(\partial_{\boldsymbol{q}}^T(\boldsymbol{M}_{bm}^T\boldsymbol{v}_L) - \partial_{\boldsymbol{q}}(\boldsymbol{M}_{bm}^T\boldsymbol{v}_L)^T\right)$
- $S_2(\dot{\boldsymbol{q}}) = \partial_{\boldsymbol{q}}^T(\boldsymbol{\Lambda}_{qq}\dot{\boldsymbol{q}}) - \partial_{\boldsymbol{q}}(\boldsymbol{\Lambda}_{qq}\dot{\boldsymbol{q}})^T$

The $\mathrm{ad}^{\sim}_{\bullet}$ (defined in Appendix A.1) is the matrix such that $\mathrm{ad}^{\sim}_{\boldsymbol{x}}\boldsymbol{y} = \mathrm{ad}_{\boldsymbol{y}}^T\boldsymbol{x}$. Besides the diagonal structure of the inertia matrix in (2.17), of significance is the detailed structure of the CC matrix. Several other forms of the Coriolis matrix factorization for the Newton-Euler formulation exist, e.g., in [FDP+10] presented for vehicle-manipulator systems. However, the separation of quadratic and cross-coupling terms of $\boldsymbol{v}_L$ and $\dot{\boldsymbol{q}}$ in (2.17), lends itself to effective use in physics-based controller and observer designs [M+23]. For complete expressions of the partials in (2.18), see the Appendix A.2.

The REL formulation has been shown to be robust to real-time implementation of momentum-conserving dynamics [M+23] and is therefore the implementation used on the HIL platform, OOS-Sim. The HIL facility, OOS-Sim is used extensively for validating the control strategies of this thesis.

2.3 Stability

The stability analyses that will be encountered in this thesis are concerned with stability of equilibrium points, specifically in the sense of Lyapunov stability. Lyapunov stability theorems establish sufficiency conditions for the type of stability being evaluated (e.g., asymptotic, exponential etc.) [Kha08]. In particular, asymptotic stability shall be discussed in a cascaded sense, given that the control strategies developed across this thesis use a hierarchical approach for task prioritization.

[1] Alternatively, control forces acting on the momentum and shape can also be modeled as gradients of a potential by including these potentials in the lagrangian (2.11).

When analyzing cascaded stability, the notion of conditional stability in a partial subset of equilibrium points comes into play. For conditional stability, all requirements for the definition of stability must hold only for those initial conditions which lie in a particular set [Ott08]. For definitions related to conditional stability, see Appendix B and for a more rigorous discourse on the fundamental stability theorems, the reader is referred to sources such as [Kha08], [SL$^+$91].

The sections ahead summarize the most relevant stability theorems sufficient to follow the scope of stability analysis in this thesis. First, theorems for asymptotic stability and LaSalle's invariance theorems are stated. Subsequently, conditional stability theorems using semi-definite Lyapunov functions are covered.

2.3.1 Asymptotic stability and invariance theorems

Consider an autonomous system of the form

$$\dot{x} = f(x), \tag{2.19}$$

where $f : D \to \mathbb{R}^n$ is a locally Lipschitz map from a domain $D \subset \mathbb{R}^n$ into $\mathbb{R}^n$.

Theorem 1. ***(Lyapunov's stability theorem)*** *[Kha08] Let $\bar{x} \in D$ be an equilibrium point of (2.19) that is, $f(\bar{x}) = 0$ and $D \subset \mathbb{R}^n$ be a domain containing $\bar{x}$. Let $V : \mathbb{R}^n \to \mathbb{R}$ be a continuously differentiable function such that*

- $V(0) = 0 \quad and \quad V(x) > 0$ *in* $D - \{0\}$,
- $\dot{V}(x) \leq 0$ *in* D.

Then $x = 0$ is stable. Moreover, if

- $\dot{V}(x) < 0$ *in* $D - \{0\}$,

then $x = 0$ is asymptotically stable.

Theorem 2. ***(Barbashin-Krasovskii theorem)*** *[Kha08] Let $\bar{x}$ be an equilibrium point of (2.19). Let $V : \mathbb{R}^n \to \mathbb{R}$ be a continuously differentiable function such that*

- $V(0) = 0 \quad and \quad V(x) > 0, \ \forall x \neq 0$,
- $\|x\| \to \infty \ \Rightarrow \ V(x) \to \infty$,
- $\dot{V}(x) < 0, \ \forall x \neq 0$.

Then $\bar{x}$ is globally asymptotically stable.

Theorem 3. ***(Local Invariant Set Theorem)*** *[SL$^+$91] Consider an autonomous system of the form (2.19), with f continuous, and let $V(x)$ be a scalar function with continuous first partial derivatives. Assume that*

- *for some $l > 0$, the region Ω_l defined by $V(x) < l$ is bounded*
- $\dot{V}(x) \leq 0$ *for all* $x \in \Omega_l$

Let R be the set of all points within Ω_l where $\dot{V}(x) = 0$, and M be the largest invariant set in R. Then, every solution $x(t)$ originating in Ω_l tends to M as $t \to \infty$.

Theorem 4. ***(Global Invariant Set Theorem)*** *[SL+91] Consider the autonomous system (2.19), with f continuous, and let $V(x)$ be a scalar function with continuous first partial derivatives. Assume that*

- $V(x) \to \infty$ *as* $\|x\| \to \infty$
- $\dot{V}(x) \leq 0$ *over the whole state space*

Let R be the set of all points where $\dot{V}(x) = 0$, and M be the largest invariant set in R. Then all solutions globally asymptotically converge to M as $t \to \infty$.

2.3.2 Cascade stability theorems

Theorem 5. *[IKO96] Consider a system of the form (2.19) with equilibrium point $\bar{x}$. Let $V(x)$ be a C^1 positive semi-definite function which has a negative semi-definite time derivative along the solutions of the system, i.e.*

- $\dot{V}(x) = \dfrac{\partial V(x)}{\partial x} f(x) \leq 0.$

Let $\mathscr{A}$ be the largest positively invariant set contained in

- $\{x \in \mathbb{R}^n \mid V(x) = 0\}$.

If $\bar{x}$ is asymptotically stable conditionally to $\mathscr{A}$, then it is a stable equilibrium of $\dot{x} = f(x)$.

The discrete equivalent of this theorem is further detailed in [GK01].

Theorem 6. *[VdS00] Consider the system*

$$\dot{x} = g_1(x) + g_2(x)u,$$
$$y = h(x)$$

with state $x \in \mathbb{R}^n$, input $u \in \mathbb{R}^m$, and output $y \in \mathbb{R}^m$ be strictly output passive for the output $y = h(x)$. Let $\mathscr{A}$ further be the largest positively invariant set contained in

- $\{x \in \mathbb{R}^n \mid h(x) = 0\}$

If the equilibrium $\bar{x}$ is asymptotically stable conditionally to $\mathscr{A}$, then it is asymptotically stable for $u = 0$.

Theorem 7. *[W+ 08] Consider a non-autonomous system of the form*

$$\dot{x} = f(t,x), \qquad x(t_0) = x_0, \tag{2.20}$$

where $f : \mathbb{R}_{\geq 0} \times D \to \mathbb{R}^n$, is continuous and locally Lipschitz in x uniformly in t, $D \subset \mathbb{R}^n$ is a domain with $x = 0 \in D$ and $f(t,0) = 0$ for all $t \geq t_0$. Assume that there exists a function $V(t,x) \in C^1\big(\mathbb{R}_{\geq t_0} \times D, \mathbb{R}_{\geq 0}\big)$ such that

- $W_1(x) \leq V(t,x) \leq W_2(x)$,
- $\dfrac{\partial V}{\partial t} + \left(\dfrac{\partial V}{\partial x}\right)^T f(t,x) \leq 0$,

for all $t \geq 0$ and $x \in D$, where $W_j(x) \geq 0$ is a positive semi-definite function for any $j = 1,2$. Then the equilibrium $\bar{x}$ of (2.20) is uniformly stable if it is uniformly asymptotically stable in Ω, where $\Omega = \{x \in D \mid W_1(x) = 0\}$.

Theorem 8. *[W+ 08] Consider a system of the form (2.20). Assume that there exists a function $V(t,x) \in C^1(\mathbb{R}_{\geq t_0} \times D, \mathbb{R}_{\geq 0})$ with positive semi-definite functions $W_j(x)$, $j = 1,2$, such that*

- $W_1(x) \leq V(t,x) \leq W_2(x)$,
- $\dfrac{\partial V}{\partial t} + \left(\dfrac{\partial V}{\partial x}\right)^T f(t,x) \leq -\alpha(W_1(x))$,

are satisfied for all $t \geq 0$ and $x \in D$, and $\alpha \in \mathcal{K}$[2]. Then the equilibrium $\bar{x}$ of (2.20) is uniformly asymptotically stable if it is uniformly asymptotically stable in Ω, where $\Omega = \{x \in D \mid W_1(x) = 0\}$.

[2] This means α is a continuous, strictly increasing function and $\alpha(0) = 0$.

CHAPTER 3

POST-GRASP STABILIZATION AND RECONFIGURATION

During an on-orbit servicing operation, a servicer spacecraft, mounted with a robotic arm, approaches and captures a target satellite, referred to as the client (Figure 3.1). Once the satellite is captured, the mission enters the post-grasp phase. This chapter addresses how the combined servicer–client assembly is stabilized and reconfigured immediately after capture. In this context, stabilization refers to the damping of the client's momentum post-capture and reconfiguration refers to achieving a desired manipulator joint pose suitable for further operations.

The structure of the chapter is as follows. Section 3.1 reviews related works and highlights the contributions. Section 3.2 describes the scenario and proposes the control strategies for the objectives of the mission phase. Section 3.3 introduces the controller design for the proposed strategies. Section 3.4 presents a quadratic-programming (QP) based approach to limit the interaction forces. Section 3.5 introduces the controller design for the proposed post-stabilization reconfiguration. Section 3.6 presents a velocity-dependent damping of the reaction wheels to limit them from saturating. Section 3.7 illustrates the results from a dynamic simulation, and Section 3.8 summarizes and concludes the work.

3.1 Related work and contributions

Various strategies have been developed for the capture phase from different perspectives like optimal detumbling time, minimizing transfer of angular momentum and contact forces. An analysis of a space robot's center of percussion was performed in [PP13b] to establish impact-minimization principles during client capture. The concept of virtual-mass for impedance matching control was introduced in [YN03] to determine that, the contact between the end-effector and client is maintained, if the impedance at the end-effector equals at most that of the client's mass. A disturbance observer is implemented in [FANGT18] to estimate the contact forces during impact, which is then

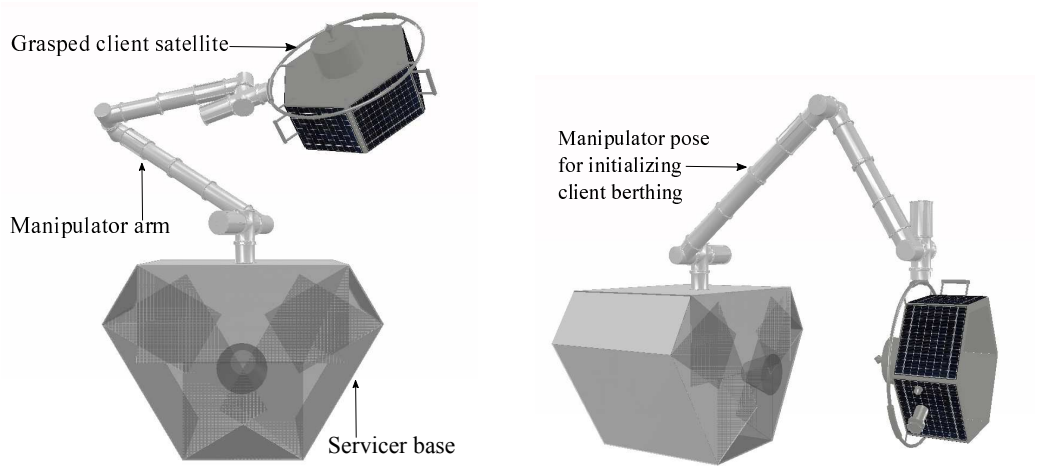

Figure 3.1: Servicer with a grasped client satellite (left) in the post-grasp phase, and (right) initialized for berthing in the post-stabilization phase.

compensated in an impedance controller to achieve compliant capture. A momentum dumping strategy is presented in [GGAS17] using external actuation to remove the accumulated momentum from contacts occurring during the capture phase.

To stabilize spinning satellites, a typical strategy involves designing specialized detumbling trajectories. The work of [Agh09] implemented feedback-linearized control to track time-optimal detumbling paths that restrict interaction torque during grasping, with the servicer's attitude control system offsetting transferred angular momentum. Their method was later enhanced for energy-optimal trajectories in [Agh20]. Parallel work by [OANY11] developed time-optimal maneuvers permitting arbitrary manipulator motion while bounding measurable contact forces. For post-grasp arm rigidization, [L$^+$18] introduced energy-optimal joint tracking control using uniform B-splines for trajectory parameterization. Alternative strategies include the methods of [GLdR19] for direct force controller enforcing contact force constraints during detumbling, of [SXSW22] for hybrid motion/force control along polynomial trajectories, and of [ALH06] using an impedance controller that dampens target motion by modeling grasp contact forces as end-effector external forces.

Post-grasp momentum stabilization approaches that lead to minimum disturbance in the attitude of the base, have been proposed in the past. These were motivated by saving fuel or power needed by momentum compensating actuators on the base. In [NY99], a strategy to transfer the impact momentum from the base to the manipulator is proposed, while simultaneously damping the joint velocities through the reaction null space [YN95]. In [DY04], two approaches for post-grasp momentum stabilization were proposed - first using the distributed momentum control concept at a velocity level, to design the joint rates such that the base rotation is kept zero, second using the reaction nullspace concept at a dynamic level to decouple the base attitude and manipulator dynamics while minimizing joint velocities.

Controlling orbital manipulators without thrusters on the servicer spacecraft offers less flexi-

bility than coordinated control approaches. Consequently, control strategies for these free-floating systems must account for momentum conservation principles. [MM89] designed a resolved rate controller using the generalized Jacobian resulting from the reduced dynamics of the floating-base system. In [WW93], trajectory planning in joint space using redundancy of manipulator is used to minimize impulse force at contact, while trajectory planning Cartesian space is done with the generalized Jacobian using the manipulator and reaction wheels. [ONY08] incorporated reaction wheels into the generalized Jacobian framework, devising a kinematic-level controller. Subsequently, a time-optimal manipulator trajectory was designed that limited reaction wheel torques and yielded zero base reaction torques through momentum conservation. [OANY11] extended this work to dynamic-level control, implementing feedback-linearized impedance control to track detumbling trajectories constrained by grasping forces. [GLdR19] adopted the same dynamics model as in [OANY11] but replaced planned detumbling paths with a proportional-integral force controller that constrained force/torque within client parameter uncertainty bounds.

Contributions

This chapter focuses on post-grasp motion stabilization (detumbling), while ensuring constraints on grasping interaction forces and specific manipulator configurations. The stabilization damps the momentum of the combined servicer and client system. Unlike [NY99, YN95, DY04], the autonomous operation of the stabilization phase relaxes restrictions on base attitude. Instead of the base attitude, the priority for autonomous operation is to ensure a safe configuration via a desired manipulator reconfiguration (which may be required for a detumbling strategy, see e.g. [L$^+$18]). This is achieved by exploiting the motion of the base while considering its full 6-DoF actuation. Additionally, in contrast to [OANY11, Agh20, L$^+$18], optimal detumbling trajectories are not required, and unlike [OANY11, YN03, GLdR19], force or torque measurements are not required. The proposed controller rather prioritizes safe detumbling while respecting interaction force limits imposed by mission requirements without direct force/torque measurements.

This chapter also proposes a post-stabilization control strategy to initialize berthing. This phase is initiated after the momentum of the system has been fully damped in the previous phase of stabilization. Therefore, the proposed method considers a zero-momentum system in this phase, and the control stabilizes the base attitude, a requirement for the berthing phase of an OOS mission, while reconfiguring the manipulator arm in the nullspace of the base's attitude. In contrast to [NY99, YN95, DY04], the proposed method uses a passivity-based control instead of feedback-linearized controllers to achieve dynamic consistency ([Kha95]) while employing a similar nullspace approach.

The contributions of this chapter can be summarized as follows:

- A novel control strategy for post-grasp motion stabilization of a free-tumbling client is developed, enabling both detumbling of the client satellite and manipulator arm reconfiguration

to a desired joint pose. This exploits the nullspace of the servicer's end-effector with full actuation and is valid for kinematically singular manipulator configurations.

- The controller is extended using a quadratic programming (QP) approach to optimally constrain interaction forces in the post-grasp phase, without requiring force feedback.
- The control design philosophy is adapted to maintain the servicer base attitude with a grasped client. The controller guarantees desired joint reconfiguration in the nullspace of the base attitude and operates under kinematic singularities, using reaction wheels and joint torques in the nullspace.
- The controller prevents reaction wheel saturation by limiting the torque applied for arm reconfiguration.

This chapter is based on the works published in [VDSO22] and [VDO22].

3.2 Control strategy

The challenging scenario considered is that of stabilizing a non-cooperative client, which means that the support of its attitude and orbit control system is not available. From the moment of capture to stabilization, the mission is typically in a fully autonomous mode, without ground intervention. Therefore, the post-grasp phase prioritizes safe and rapid stabilization while strictly limiting

Table 3.1: *Proposed strategy* – for post-grasp and post-stabilization phases in decreasing order of priority.

Task		**Post-grasp phase**	**Post-stabilization phase**
		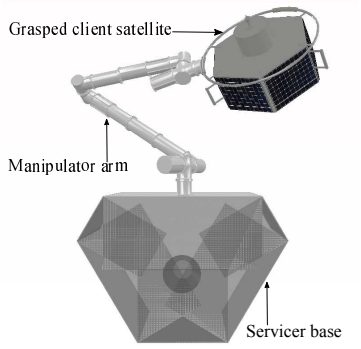	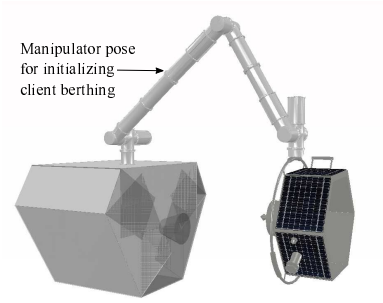
T1:	*Subsystem*	*End-effector*	*Spacecraft base*
	Objective	Stabilize client while limiting interaction forces at the end-effector	Stabilize base attitude to avoid depointing of spacecraft
T2:	*Subsystem*	*Manipulator joints*	*Manipulator joints*
	Objective	Damp out joint velocities and reach a safe configuration	Reconfigure arm for berthing while limiting reaction wheel speed

interaction forces at the grasp interface. After stabilization, the berthing and servicing phase follows, during which tasks are less time-critical and may be performed under greater ground observation. To allow for operations under ground observation, the spacecraft's pointing requirements need to be respected for the challenging case with directional antennas. Therefore, the post-stabilization phase prioritizes spacecraft attitude control during berthing initialization and subsequent tasks. The objectives of these consecutive phases, i.e. post-grasp stabilization (Figure 3.1, left) and initialization of berthing (Figure 3.1, right), are addressed using a similar control design, highlighting its adaptability to different mission requirements.

A critical aspect of the post-grasp phase is keeping interaction forces at the grasp interface within safe limits. Mission requirements may also specify a manipulator configuration for further servicing. The proposed strategy damps the velocities at the end-effector attached to the client in order to achieve detumbling. The strategy further reconfigures the manipulator arm using the servicer's full actuation. The proposed controller guarantees joint task convergence in the nullspace of the manipulator's end-effector and remains valid for kinematically singular configurations. It is also augmented with a quadratic programming (QP) approach to optimally constrain interaction forces.

After stabilization, that is momentum damping, the desired manipulator configuration and base attitude are set to start phases like berthing. This phase may have strict attitude requirements for antenna pointing to maintain ground contact during servicing. The approach prioritizes maintaining the servicer's attitude with the grasped client and reconfigures the manipulator in the nullspace of the servicer's attitude. It uses redundancy in rotational degrees of freedom via reaction wheels to decouple manipulator motion from base attitude. The proposed controller ensures convergence of both attitude and joint-level tasks, even in kinematic singularities, and handles reaction wheel saturation by reducing torque input with weighted damping. The proposed strategies are summarized in the form of control task hierarchies for the two phases in Table 3.1.

3.3 Controller for post-grasp phase

In the post-grasp phase, the goal of the servicer is to detumble the system, i.e. to stabilize the combined motion (see Table 3.1). Later, servicing tasks such as refuelling and maintenance can be executed using the manipulator arm [FAMPU14]. The stabilization of a non-cooperative satellite, which means that the support from the attitude and orbit control of the client satellite is not available, poses a challenge for the control design, which further needs to respect the force limits of the grasping interface to avoid damage, and consequently, loss of the client [OANY11].

The dynamic model that shall be used for the control design considers the post-grasp phase dynamics (2.10) with the servicer dynamics in (2.7) substituted with the orbital manipulator dynamics in (2.5). For the controller design, the dynamic parameters of the client are assumed to be known (as considered in e.g. [Agh09]). The system is composed of a fully-actuated (6-DoF) orbital manipulator called the *servicer*, i.e. a base spacecraft equipped with an n-DoF manipulator arm, and the *client*,

i.e. the non-cooperative satellite that has been captured.

3.3.1 Hierarchical control law

The controller aims to stabilize the servicer-client assembly while reconfiguring the manipulator arm. In line with the control task objectives summarized in Table 3.1, the strategy adopted considers a Cartesian damping control acting on the end-effector, while nullspace control is used to reconfigure the joints and damp the motion of the base.

To achieve these control objectives, the control task coordinates can be defined by the end-effector velocity, $\boldsymbol{v}_e \in \mathbb{R}^6$, and augmented nullspace velocity, $\boldsymbol{v}_n \in \mathbb{R}^n$ as follows.

$$\text{(3.1)} \qquad \text{Augmented task coordinates}: \qquad \begin{matrix}\text{T1:}\\ \text{T2:}\end{matrix} \begin{bmatrix}\boldsymbol{v}_e\\ \boldsymbol{v}_n\end{bmatrix} = \boldsymbol{J}_N \boldsymbol{V}_s, \quad \boldsymbol{J}_N = \begin{bmatrix}\boldsymbol{J}_e\\ \boldsymbol{N}_e^{M\dagger}\end{bmatrix}$$

The floating-base end-effector Jacobian has the form, $\boldsymbol{J}_e = \begin{bmatrix}\boldsymbol{J}_b & \boldsymbol{J}_m\end{bmatrix} \in \mathbb{R}^{6\times 6+n}$, which maps $\boldsymbol{V}_s$ to $\boldsymbol{v}_e \in \mathbb{R}^6$, the end-effector Cartesian velocity. The base Jacobian is $\boldsymbol{J}_b \in \mathbb{R}^{6\times 6}$ and manipulator's end-effector Jacobian is $\boldsymbol{J}_m \in \mathbb{R}^{6\times n}$. The extended Jacobian, $\boldsymbol{J}_N$ (see [Ott08] for details), is invertible as long as $\boldsymbol{J}_e$ is non-singular, which is guaranteed due to the following. Observe that the base Jacobian $\boldsymbol{J}_b$ is an invertible adjoint transformation between the end-effector and base. As can be seen from the previously defined adjoint transformations for the k-th manipulator link in (2.3), here, the k-th link is the last link, which is of the end-effector. Therefore, $\boldsymbol{J}_e$ always has full row rank independent of the kinematic singularities of the manipulator.

Therefore, $\boldsymbol{N}_e \in \mathbb{R}^{n\times 6+n}$, a basis matrix for the nullspace of $\boldsymbol{J}_e$, and $\boldsymbol{N}_e^{M\dagger}$, the generalized-inverse of $\boldsymbol{N}_e$, can be given by,

$$\text{(3.2)} \qquad \begin{matrix}\text{Actuated servicer's}\\ \text{end-effector nullspace}:\end{matrix} \qquad \begin{matrix}\boldsymbol{N}_e^T = \begin{bmatrix}-\boldsymbol{J}_m^T \boldsymbol{J}_b^{-T} & \boldsymbol{I}\end{bmatrix}\\ \boldsymbol{N}_e^{M\dagger} = (\boldsymbol{N}_e^T \boldsymbol{M}_{sc} \boldsymbol{N}_e)^{-1} \boldsymbol{N}_e^T \boldsymbol{M}_{sc}\end{matrix}$$

such that the property $\boldsymbol{J}_e \boldsymbol{N}_e = \boldsymbol{0}$ is satisfied [CW93]. $\boldsymbol{I} \in \mathbb{R}^{n\times n}$ is an identity matrix. Hence, the nullspace is n-dimensional since $\boldsymbol{J}_b$ is an invertible adjoint transformation. Notice that substituting $\boldsymbol{M}_{sc}$ from (2.10) into $\boldsymbol{N}_e^{M\dagger}$ in (3.2) leads to the cancellation of client parameters.

$$\text{(3.3)} \qquad \text{Client independence}: \qquad \begin{matrix}\boldsymbol{N}_e^T \boldsymbol{M}_{sc} = \boldsymbol{N}_e^T (\boldsymbol{M}_s + \boldsymbol{J}_e^T \boldsymbol{J}_c^{-T} \boldsymbol{M}_c \boldsymbol{J}_c^{-1} \boldsymbol{J}_e),\\ \Rightarrow \boldsymbol{N}_e^{M\dagger} = (\boldsymbol{N}_e^T \boldsymbol{M}_s \boldsymbol{N}_e)^{-1} \boldsymbol{N}_e^T \boldsymbol{M}_s\end{matrix}$$

Here, the relation between the servicer's Jacobian and its nullspace, $\boldsymbol{N}_e^T \boldsymbol{J}_e^T = \boldsymbol{0}$ is used. Therefore, the inertia parameters of the client do not affect the nullspace velocities. This observation aligns with the load-independence property of nullspaces [FK97].

To facilitate the design of the controller at a task level as proposed in Table 3.1, the dynamics in (2.10) is transformed to the augmented task velocity coordinates in (3.1) to obtain inertially-

decoupled dynamics,

$$\text{(3.4)}\qquad \begin{array}{ll} \text{Inertially-decoupled} & \text{T1:} \\ \text{nullspace dynamics :} & \text{T2:} \end{array} \underbrace{\begin{bmatrix} \boldsymbol{\Lambda}_{ee} & \mathbf{0} \\ \mathbf{0} & \boldsymbol{\Lambda}_{nn} \end{bmatrix}}_{\boldsymbol{\Lambda}} \begin{bmatrix} \dot{\boldsymbol{v}}_e \\ \dot{\boldsymbol{v}}_n \end{bmatrix} + \underbrace{\begin{bmatrix} \boldsymbol{\mu}_{ee} & \boldsymbol{\mu}_{en} \\ \boldsymbol{\mu}_{ne} & \boldsymbol{\mu}_{nn} \end{bmatrix}}_{\boldsymbol{\mu}} \begin{bmatrix} \boldsymbol{v}_e \\ \boldsymbol{v}_n \end{bmatrix} = \underbrace{\begin{bmatrix} \boldsymbol{F}_e \\ \boldsymbol{F}_n \end{bmatrix}}_{\boldsymbol{F}}$$

where,

$$\text{(3.5)}\qquad \begin{aligned} \boldsymbol{\Lambda} &= \boldsymbol{J}_N^{-T} \boldsymbol{M}_{sc} \boldsymbol{J}_N^{-1}, & \boldsymbol{\mu} &= \boldsymbol{J}_N^{-T} \boldsymbol{M}_{sc} \frac{d}{dt}(\boldsymbol{J}_N^{-1}) + \boldsymbol{J}_N^{-T} \boldsymbol{C}_{sc} \boldsymbol{J}_N^{-1}, \\ \boldsymbol{J}_N^{-1} &= \begin{bmatrix} \boldsymbol{J}_e^{M+} & \boldsymbol{N}_e \end{bmatrix}, & \boldsymbol{F} &= \boldsymbol{J}_N^{-T} \boldsymbol{\Gamma}, \end{aligned}$$

and $\boldsymbol{J}_e^{M+} = \boldsymbol{M}_{sc}^{-1} \boldsymbol{J}_e (\boldsymbol{J}_e \boldsymbol{M}_{sc}^{-1} \boldsymbol{J}_e^T)^{-1}$ is the dynamically consistent generalized inverse of $\boldsymbol{J}_e$ [Kha95]. Since $\boldsymbol{N}_e^{M\dagger}$ in (3.3) was shown to be independent of the client's inertia parameters, consequently $\boldsymbol{J}_N^{-1}$ will also be independent of $\boldsymbol{M}_c$.

The controller is designed such that the Cartesian space control, $\boldsymbol{F}_e$, damps the end-effector velocity, thus stabilizing the client. Whereas, the null space control, $\boldsymbol{F}_n$, reconfigures the arm while stabilizing the base. Therefore, the control inputs in augmented task coordinates are chosen as,

$$\text{(3.6)}\qquad \text{Augmented task control :} \qquad \text{T1:} \quad \boldsymbol{F}_e = -\boldsymbol{K}_{De} \boldsymbol{v}_e + \boldsymbol{\mu}_{en} \boldsymbol{v}_n,$$

$$\text{(3.7)}\qquad \text{T2:} \quad \boldsymbol{F}_n = \boldsymbol{N}_e^T \begin{bmatrix} \mathbf{0} \\ \boldsymbol{K}_{Pm} \Delta \boldsymbol{q} \end{bmatrix} - \boldsymbol{N}_e^T \begin{bmatrix} \boldsymbol{K}_{Db} \boldsymbol{v}_b \\ \boldsymbol{K}_{Dm} \dot{\boldsymbol{q}} \end{bmatrix},$$

where $\boldsymbol{K}_{De}, \boldsymbol{K}_{Db} \in \mathbb{R}^{6\times 6}$ and $\boldsymbol{K}_{Dm} \in \mathbb{R}^{n\times n}$ are positive-definite damping gain matrices of the end-effector, servicer base and manipulator joints, respectively. $\boldsymbol{K}_{Pm} \in \mathbb{R}^{n\times n}$ is the positive-definite joint stiffness matrix. $\Delta \boldsymbol{q} = \boldsymbol{q}^d - \boldsymbol{q}$ is the error between the desired joint angles $\boldsymbol{q}^d$ and measured angles $\boldsymbol{q}$. The last term in (3.6) compensates the Coriolis coupling in order to decouple the end-effector task from the nullspace dynamics.

Finally, the control input to the servicer dynamics $\boldsymbol{\Gamma}$ in (2.10) is obtained by mapping the task-level control (3.6)-(3.7) using the extended Jacobian-transpose $\boldsymbol{J}_N^T$ as per (3.5).

$$\text{(3.8)}\qquad \text{Control in actuator coordinates :} \qquad \boldsymbol{\Gamma} = \underbrace{\boldsymbol{J}_e^T \boldsymbol{F}_{De}}_{\boldsymbol{\Gamma}_{\text{T1}}} + \underbrace{\boldsymbol{N}_e^{T_{M\dagger}} \boldsymbol{N}_e^T \boldsymbol{\Gamma}_0}_{\boldsymbol{\Gamma}_{\text{T2}}} + \underbrace{\boldsymbol{J}_e^T \boldsymbol{\mu}_{en} \boldsymbol{v}_n}_{\boldsymbol{\Gamma}_{\mu}}$$

where,

$$\begin{aligned} \boldsymbol{F}_{De} &= -\boldsymbol{K}_{De} \boldsymbol{v}_e & \boldsymbol{\Gamma}_0 &= \begin{bmatrix} \boldsymbol{F}_{Db}^T & \boldsymbol{\tau}_{PD}^T \end{bmatrix}^T \\ \boldsymbol{F}_{Db} &= -\boldsymbol{K}_{Db} \boldsymbol{v}_b & \boldsymbol{\tau}_{PD} &= \boldsymbol{K}_{Pm} \Delta \boldsymbol{q} - \boldsymbol{K}_{Dm} \dot{\boldsymbol{q}}. \end{aligned}$$

Note that $\boldsymbol{\Gamma}_0$ is projected onto the nullspace of $\boldsymbol{J}_e^T$ through $\boldsymbol{N}_e^{T_{M\dagger}} \boldsymbol{N}_e^T$. It is worth mentioning that $\boldsymbol{N}_e^{T_{M\dagger}} \boldsymbol{N}_e^T = \boldsymbol{I} - \boldsymbol{J}_e^T \boldsymbol{J}_e^{T_{M+}}$, which is a common form of the nullspace projection matrix [Kha95].

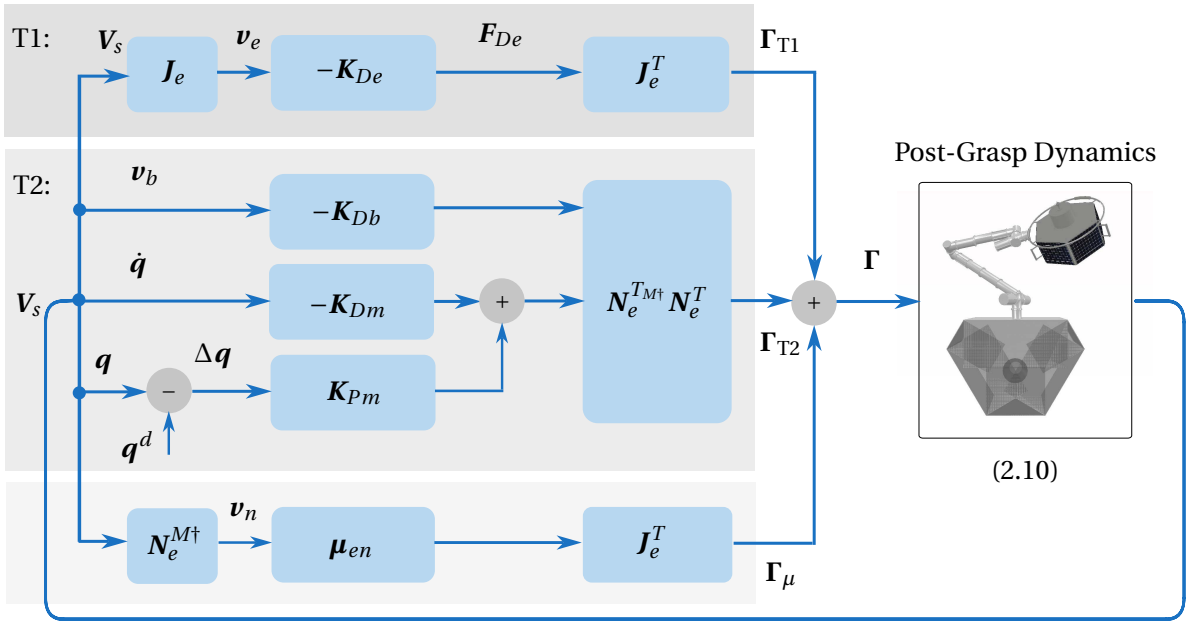

(2.10)

Figure 3.2: *Controller for post-grasp phase* – block diagram of the designed controller in closed-loop with the dynamics, used for the post-grasp phase, where $\boldsymbol{V}_s = (\boldsymbol{v}_b, \dot{\boldsymbol{q}})$.

To summarize, the controller in (3.8) is composed of three terms, namely $\boldsymbol{\Gamma}_{\text{T1}}$, which damps the end-effector velocity, $\boldsymbol{\Gamma}_{\text{T2}}$ for the reconfiguration of the manipulator in the nullspace, and $\boldsymbol{\Gamma}_\mu$ to decouple the end-effector from nullspace dynamics. Note that the terms $\boldsymbol{\Gamma}_{\text{T1}}$ and $\boldsymbol{\Gamma}_{\text{T2}}$ are completely independent of the client inertia parameters, whereas $\boldsymbol{\Gamma}_\mu$ has a dependency through the Coriolis coupling between the end-effector task and nullspace. The dependency on servicer's inertia parameters in (3.8) are seen only via the nullspace inverse[1] $\boldsymbol{N}_e^{T_{M\dagger}}$. A block diagram of the controller law (3.8) in closed-loop with the post-grasp dynamics is shown in Figure 3.2.

3.3.2 Stability of the controller

Proposition 1. *Consider the dynamics in* (3.4) *with the control law in* (3.6), (3.7). *The stiffness and damping gains* $\boldsymbol{K}_{Pm}$, $\boldsymbol{K}_{Dm}$, $\boldsymbol{K}_{Db}$ *and* $\boldsymbol{K}_{De}$ *are symmetric and positive-definite. Then, the control law results in the equilibrium* $\boldsymbol{v}_e, \boldsymbol{v}_n, \Delta\boldsymbol{q} = \boldsymbol{0}$ *being asymptotically stable.*

The stability of the controller can be analyzed similar to [Ott08] using the theory of semi-definite Lyapunov functions in [IKO96] and [VdS00] (refer Section 2.3). First, considering $V_e = \frac{1}{2}\boldsymbol{v}_e^T \boldsymbol{\Lambda}_{ee} \boldsymbol{v}_e$ as the positive semi-definite Lyapunov function, and using the task dynamics in (3.4) with the chosen $\boldsymbol{F}_e$ in (3.6), leads to

$$\dot{V}_e = \boldsymbol{v}_e^T \boldsymbol{F}_{De} = -\boldsymbol{v}_e^T \boldsymbol{K}_{De} \boldsymbol{v}_e \preceq 0. \tag{3.9}$$

[1] The uncertainties in inertia parameters of the servicer can be expected to have minimal influence for a similar controller (see [WOD22]).

Second, consider $V_n = \frac{1}{2}\boldsymbol{v}_n^T \boldsymbol{\Lambda}_{nn} \boldsymbol{v}_n + \frac{1}{2}\Delta\boldsymbol{q}^T \boldsymbol{K}_{Pm}\Delta\boldsymbol{q}$, in the set where the first task T1 is converged, i.e. end-effector velocity, $\boldsymbol{v}_e = \boldsymbol{0}$. Using the task dynamics in (3.4), leads to the derivative,

$$\dot{V}_n = \boldsymbol{v}_n^T \boldsymbol{F}_n - \dot{\boldsymbol{q}}^T \boldsymbol{K}_{Pm}\Delta\boldsymbol{q} \tag{3.10}$$

The joint velocities $\dot{\boldsymbol{q}}$ can be obtained in terms of the nullspace velocity $\boldsymbol{v}_n$ as follows.

$$\underbrace{\begin{bmatrix}\boldsymbol{v}_b \\ \dot{\boldsymbol{q}}\end{bmatrix}}_{\boldsymbol{V}_s} = \underbrace{\begin{bmatrix}\boldsymbol{J}_e^{M+} & \boldsymbol{N}_e\end{bmatrix}}_{\boldsymbol{J}_N^{-1}} \begin{bmatrix}\boldsymbol{v}_e \\ \boldsymbol{v}_n\end{bmatrix} \qquad \Rightarrow \dot{\boldsymbol{q}} = \begin{bmatrix}\boldsymbol{0} & \boldsymbol{I}\end{bmatrix} \boldsymbol{N}_e \boldsymbol{v}_n \qquad \text{in the set } \boldsymbol{v}_e = \boldsymbol{0}$$

Therefore, (3.10) becomes,

$$\dot{V}_n = \boldsymbol{v}_n^T \left(\boldsymbol{F}_n - \boldsymbol{N}_e^T \begin{bmatrix}\boldsymbol{0} \\ \boldsymbol{K}_{Pm}\Delta\boldsymbol{q}\end{bmatrix} \right) \tag{3.11}$$

Choosing $\boldsymbol{F}_n$ in (3.7), results in

$$\dot{V}_n = -\boldsymbol{v}_n^T \boldsymbol{N}_e^T \begin{bmatrix}\boldsymbol{K}_{Db} & \boldsymbol{0} \\ \boldsymbol{0} & \boldsymbol{K}_{Dm}\end{bmatrix} \boldsymbol{N}_e \boldsymbol{v}_n \preceq 0 \tag{3.12}$$

which shows conditional stability to the set $\boldsymbol{v}_e = \boldsymbol{0}$. Finally, stability is concluded using the theory of semi-definite Lyapunov functions in [IKO96] and [VdS00] and $\boldsymbol{v}_e, \boldsymbol{v}_n \rightarrow \boldsymbol{0}$ (for more details on hierarchical stability of nullspace control, refer [Ott08]). The convergence of the joint task to its equilibrium $\Delta\boldsymbol{q} = \boldsymbol{0}$ in the nullspace of the end-effector can be shown by the detailed analysis ahead.

Convergence of the task in the nullspace

The advantage of the particular choice of $\boldsymbol{F}_n$ in (3.4), using only a joint stiffness for achieving a global equilibrium, can be highlighted by an analysis of the different cases when the stiffness may be applied to a combination of base and joints. Consider the general case when, in the set $\boldsymbol{v}_e = \boldsymbol{0}$, the spring potential in V_n may be chosen as $V_K = \frac{1}{2}\Delta\boldsymbol{x}_b^T \boldsymbol{K}_{Pb}\Delta\boldsymbol{x}_b + \frac{1}{2}\Delta\boldsymbol{q}^T \boldsymbol{K}_{Pm}\Delta\boldsymbol{q}$, with $\Delta\boldsymbol{x}_b$ the error in position and orientation of the base. The derivative of the potential $\dot{V}_K$ for small angles yields

$$\dot{V}_K = -\boldsymbol{v}_n^T \boldsymbol{N}_e^T \begin{bmatrix}\boldsymbol{K}_{Pb}\Delta\boldsymbol{x}_b \\ \boldsymbol{K}_{Pm}\Delta\boldsymbol{q}\end{bmatrix} \tag{3.13}$$

- Case i) *When $\boldsymbol{K}_{Pb} \neq \boldsymbol{0}$ and $\boldsymbol{K}_{Pm} \neq \boldsymbol{0}$:* In this scenario, a desired equilibrium is imposed on the base pose in addition to the manipulator pose in the nullspace of the end-effector. Using (3.13), the minimum of the potential V_K is obtained when,

$$\underbrace{\begin{bmatrix}-\boldsymbol{J}_m^T \boldsymbol{J}_b^{-T} & \boldsymbol{I}\end{bmatrix}}_{\boldsymbol{N}_e^T} \begin{bmatrix}\boldsymbol{K}_{Pb}\Delta\boldsymbol{x}_b \\ \boldsymbol{K}_{Pm}\Delta\boldsymbol{q}\end{bmatrix} = \boldsymbol{0}, \quad \text{which can occur when, } \begin{bmatrix}\Delta\boldsymbol{x}_b \\ \Delta\boldsymbol{q}\end{bmatrix} \neq \boldsymbol{0}$$

$$\Rightarrow \boldsymbol{J}_m^T \boldsymbol{J}_b^{-T} \boldsymbol{K}_{Pb}\Delta\boldsymbol{x}_b = \boldsymbol{K}_{Pm}\Delta\boldsymbol{q}.$$

In this scenario, the base and joint tasks cancel each other, reaching a displaced equilibrium, and reconfiguration of the arm in the nullspace is not guaranteed. Therefore, choosing an $\boldsymbol{F}_n$ with a potential on the base and joints does not guarantee the desired equilibrium $\Delta\boldsymbol{x}_b, \Delta\boldsymbol{q} = \boldsymbol{0}$, and can instead converge to a local minimum of the potential V_n.

- Case ii) *When $\boldsymbol{K}_{Pb} \neq \boldsymbol{0}$ and $\boldsymbol{K}_{Pm} = \boldsymbol{0}$:* In this scenario, a desired equilibrium is imposed only on the base pose, and not on the manipulator pose, in the nullspace of the end-effector. Using (3.13), the minimum of the potential V_K is obtained when,

$$\underbrace{\begin{bmatrix} -\boldsymbol{J}_m^T \boldsymbol{J}_b^{-T} & \boldsymbol{I} \end{bmatrix}}_{\boldsymbol{N}_e^T} \begin{bmatrix} \boldsymbol{K}_{Pb}\Delta\boldsymbol{x}_b \\ \boldsymbol{0} \end{bmatrix} = \boldsymbol{0}, \quad \text{which can occur when, } \Delta\boldsymbol{x}_b \neq \boldsymbol{0}$$

$$\Rightarrow \boldsymbol{J}_m^T \boldsymbol{J}_b^{-T} \boldsymbol{K}_{Pb}\Delta\boldsymbol{x}_b = \boldsymbol{0}.$$

  This can occur when the manipulator Jacobian $\boldsymbol{J}_m$ is singular. Therefore, choosing an $\boldsymbol{F}_n$ with a potential only on the base does not guarantee the desired equilibrium $\Delta\boldsymbol{x}_b = \boldsymbol{0}$, and can instead converge to a local minimum of the potential V_n.

- Case iii) *When $\boldsymbol{K}_{Pb} = \boldsymbol{0}$ and $\boldsymbol{K}_{Pm} \neq \boldsymbol{0}$:* This case corresponds to the proposed controller in (3.7). In this scenario, a desired equilibrium is imposed only on the manipulator pose in the nullspace of the end-effector. As in (3.11), the minimum of the potential V_K occurs when,

$$\underbrace{\begin{bmatrix} -\boldsymbol{J}_m^T \boldsymbol{J}_b^{-T} & \boldsymbol{I} \end{bmatrix}}_{\boldsymbol{N}_e^T} \begin{bmatrix} \boldsymbol{0} \\ \boldsymbol{K}_{Pm}\Delta\boldsymbol{q} \end{bmatrix} = \boldsymbol{0}, \quad \text{which can occur only when, } \Delta\boldsymbol{q} = \boldsymbol{0}.$$

  Due to the full row rank of $\boldsymbol{N}_e^T$ given by $\boldsymbol{I}$, the invertibility of $\boldsymbol{J}_b$, and $\boldsymbol{K}_{Pm}$ being positive-definite, the minimum occurs only when $\Delta\boldsymbol{q} = \boldsymbol{0}$. In this scenario, the manipulator joints implicitly control the base pose relative to the client without conflicting potentials. Therefore, choosing an $\boldsymbol{F}_n$ with a potential only on the joints guarantees the desired equilibrium $\Delta\boldsymbol{q} = \boldsymbol{0}$ and convergence to the global minimum of the potential V_n.

Validity of controller under kinematic singularities of the manipulator

Observe in Case iii) above that the minimum of joint error potential in the nullspace of the whole-body end-effector is independent of the rank of the manipulator Jacobian $\boldsymbol{J}_m$. This implies that the controller designed in (3.8) can also operate in kinematically singular configurations of the manipulator arm. This follows from the existence of the nullspace matrix, $\boldsymbol{N}_e^{M\dagger}$, which was shown in (3.2) to have rank n independent of the rank of the manipulator Jacobian $\boldsymbol{J}_m$. A physical intuition to this lies in the observation that the restriction on the motion directions, imposed by the arm in a singular configuration, can be overcome by an appropriate 6-DoF actuation of the base.

3.4 Optimal QP-based control

The controller described in Section 3.3 reconfigures the arm while stabilizing the motion of both the servicer and client. However, it does not guarantee that the interaction forces at the grasp remain within acceptable thresholds. Adhering to interaction force limits is essential in space missions to prevent mechanical damage to the grasp interface and to avoid loss of the client from the servicer's grasp [Agh09]. First, the interaction force computation is presented and later used as a constraint for the QP-based control.

Computation of the interaction wrench

The interaction wrench is the force and torque, which acts during the post-grasp phase between the servicer's end-effector and the client's grasping point. Figure 3.3 shows a close up of the client's grasp and servicer's end-effector frame in the post-grasp phase. This is computed as a function of the control applied to the base and joints (see [MLS94]) by using the velocity constraint in (2.9), recalled below.

$$\text{Grasp velocity constraint}: \qquad \boldsymbol{v}_e = \boldsymbol{J}_e \boldsymbol{V}_s = \boldsymbol{J}_c \boldsymbol{v}_c$$

Specifically, the velocity constraint is reformulated as $\boldsymbol{A}\begin{bmatrix}\boldsymbol{V}_s^T & \boldsymbol{v}_c^T\end{bmatrix}^T = \boldsymbol{0}$, where $\boldsymbol{A} = \begin{bmatrix}-\boldsymbol{J}_e & \boldsymbol{J}_c\end{bmatrix}$, Taking its time-derivative combined with $\begin{bmatrix}\dot{\boldsymbol{V}}_s^T & \dot{\boldsymbol{v}}_c{}^T\end{bmatrix}^T$ from the servicer and client dynamics in (2.7) and (2.8), the interaction wrench is obtained as follows:

$$\text{Interaction wrench}: \qquad \boldsymbol{F}_c = \left(\boldsymbol{A}\boldsymbol{M}^{-1}\boldsymbol{A}^T\right)^{-1}\left[\boldsymbol{A}\boldsymbol{M}^{-1}\left(\begin{bmatrix}\boldsymbol{\Gamma}\\ \boldsymbol{0}\end{bmatrix} - \boldsymbol{C}\begin{bmatrix}\boldsymbol{V}_s\\ \boldsymbol{v}_c\end{bmatrix}\right) + \dot{\boldsymbol{A}}\begin{bmatrix}\boldsymbol{V}_s\\ \boldsymbol{v}_c\end{bmatrix}\right], \tag{3.14}$$

where,

$$\boldsymbol{M} = \begin{bmatrix}\boldsymbol{M}_s & \boldsymbol{0}\\ \boldsymbol{0} & \boldsymbol{M}_c\end{bmatrix} \qquad\qquad \boldsymbol{C} = \begin{bmatrix}\boldsymbol{C}_s & \boldsymbol{0}\\ \boldsymbol{0} & \boldsymbol{C}_c\end{bmatrix}.$$

Note here the term $\boldsymbol{A}\boldsymbol{M}^{-1}\boldsymbol{A}^T$ is invertible since $\boldsymbol{A}$ has full rank as both $\boldsymbol{J}_e$ and $\boldsymbol{J}_c$ have full rank, and the client velocity is computed from the grasp constraint in (2.9) as $\boldsymbol{v}_c = \boldsymbol{J}_c^{-1}\boldsymbol{J}_e\boldsymbol{V}_s$.

QP Optimization of the virtual control

This section presents a quadratic programming (QP)-based optimization of the controller described in Section 3.3. The primary objective is to optimally limit the interaction wrench in (3.14) through the control effort, while maintaining the structure of the controller defined in (3.8). To achieve this, the control variables in (3.8) are first analyzed to identify which variables should be optimized.

To maintain the decoupling between the nullspace and the end-effector, the control effort $\boldsymbol{\Gamma}_\mu$ is retained without modification. The variable $\boldsymbol{\Gamma}_{T2}$ in (3.8) may be modified by optimizing $\boldsymbol{\Gamma}_0$ and

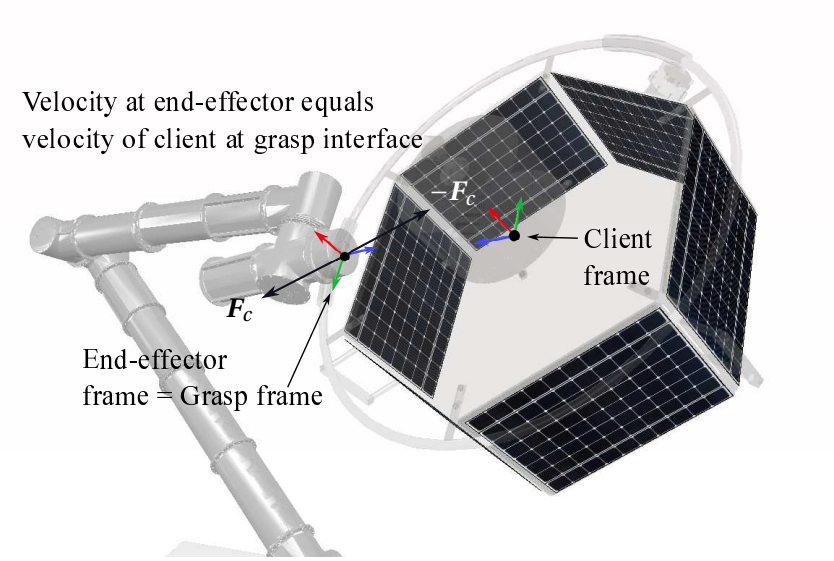

Figure 3.3: *EE-client grasp interface* – close-up of the end-effector and client frames (RGB≡XYZ). For a rigid grasp, the velocity of the end-effector equals the velocity of the client's grasp interface.

projecting it into the nullspace. Before proceeding, the contribution of the nullspace term $\mathbf{\Gamma}_{\mathrm{T2}}$ to the interaction force is determined by examining (3.14). The relevant part of the expression in (3.14) that multiplies with $\mathbf{\Gamma}_{\mathrm{T2}}$ is analyzed as follows:

$$\boldsymbol{A}\boldsymbol{M}^{-1}\begin{bmatrix}\mathbf{\Gamma}_{\mathrm{T2}}\\ \mathbf{0}\end{bmatrix} = -\boldsymbol{J}_e\boldsymbol{M}_s^{-1}\boldsymbol{N}_e^{T_{M\dagger}}\boldsymbol{N}_e^T\mathbf{\Gamma}_0$$

Substituting for $\boldsymbol{N}_e^{M\dagger}$ from (3.3), results in

$$\text{Wrench decoupled from nullspace}: \qquad \boldsymbol{J}_e\boldsymbol{N}_e(\boldsymbol{N}_e^T\boldsymbol{M}_s\boldsymbol{N}_e)^{-1}\boldsymbol{N}_e^T\mathbf{\Gamma}_0 = \mathbf{0},$$

where the relation between the servicer's Jacobian and its nullspace, $\boldsymbol{J}_e\boldsymbol{N}_e = \mathbf{0}$ is used. Hence, the nullspace control has no influence on the interaction force $\boldsymbol{F}_c$. This is consistent with the knowledge that the dynamically consistent nullspace projection does not directly produce a wrench at the end-effector. Therefore, the control effort $\mathbf{\Gamma}_{\mathrm{T2}}$, which reconfigures the arm in the nullspace, is retained without modification.

Lastly, while retaining the term $\mathbf{\Gamma}_\mu$ for nullspace decoupling, the control effort $\mathbf{\Gamma}_{\mathrm{T1}}$ can be optimized to limit the interaction wrench. Furthermore, optimizing $\boldsymbol{F}_{De}$ rather than $\mathbf{\Gamma}_{\mathrm{T1}}$ directly preserves the Jacobian-transposed structure of the controller described in (3.8). While it is possible to reduce $\boldsymbol{F}_{De}$—and consequently $\boldsymbol{F}_c$—by lowering the gain $\boldsymbol{K}_{De}$, this method does not ensure adherence to interaction force limits as effectively as a rigorous constrained optimization of $\boldsymbol{F}_{De}$.

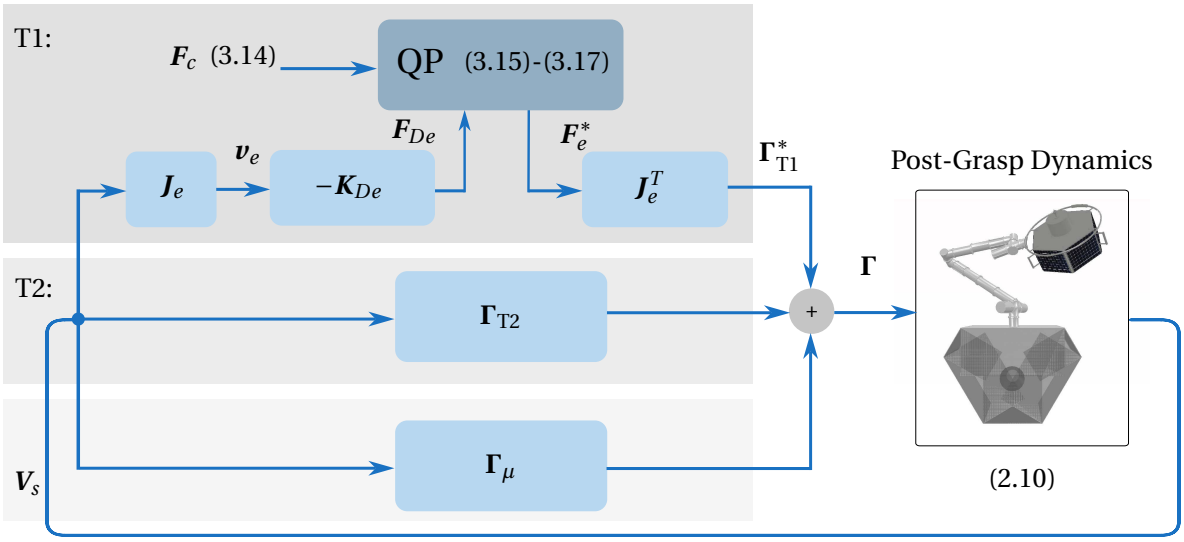

Figure 3.4: *QP-augmented controller* – block diagram of the controller in Figure 3.2 augmented with QP. The main differences are highlighted in blue. An open source solver like qpOASES [FKP+14b] may be used for real-time implementation, which has already proven successful in robot control methods focusing on interaction force limitations [HRO16].

Therefore, the following QP problem optimizes the proposed controller to limit the interaction forces:

(3.15)	Optimizing end-effector control :	$\min_{F_e^*} \quad \frac{1}{2}(F_e^* - F_{De})^T Q_c (F_e^* - F_{De})$
(3.16)	Interaction wrench constraint :	s.t. $\lvert F_c \rvert_i \leq F_{c,max_i}$
(3.17)	Stability constraint :	$v_e^T F_e^* \leq 0.$

$Q_c \in \mathbb{R}^{6\times 6}$ is a positive definite weighting matrix and F_e^* is the optimized control wrench, which will modify Γ_{T1} in (3.8) with $\Gamma_{T1}^* = J_e^T F_e^*$. The selected cost function minimizes the distance between the optimal wrench and the desired wrench F_{De}.

To comply with interaction force limits specified by space mission requirements, the constraint in (3.16) is incorporated. This constraint ensures that the optimized control effort F_e^* does not produce an interaction force F_c at the client's grasp interface that exceeds the component-wise threshold i of the allowable maximum interaction wrench $F_{c,max}$.

The second constraint in (3.17) is introduced to ensure controller convergence as required by the stability condition in (3.9). Physically, this guarantees that the rate of change in the energy of the end-effector motion does not increase as a result of the optimization. Therefore, the controller structure can be augmented with quadratic programming (QP) optimization, as illustrated in Figure 3.4.

3.5 Controller for post-stabilization phase

Up to this point, a controller has been designed that tackles the objectives of the first phase (post-grasp) as outlined in Table 3.1. To tackle the objectives of the second phase (post-stabilization)—to manipulate the client to initialize berthing under ground observation—requires a control design that prioritizes spacecraft attitude maintenance. The controller thus far designed in (3.8) cannot be used for this phase, since the primary task was designed at the end-effector level rather than the base attitude, given detumbling objectives. Further, the stabilization strategy for the grasped client utilized both the manipulator and the full 6-DoF external actuation capabilities of the servicer to dampen momentum. In contrast, since the post-stabilization phase has zero momentum, it is sufficient to control the servicer using only reaction wheels.

Therefore, we shall explicitly consider the modeling of three reaction wheels and use a reduced dynamic model for designing the controller. A reduced dynamic model also allows the use of a reduced Jacobian for representing the servicer's attitude. These are described in the following sections and will be used for designing the hierarchical control for the post-stabilization strategy.

3.5.1 Reduced dynamic model

Using the servicer dynamics in (2.7) with the orbital manipulator dynamics, which include reaction wheels as described in (2.6), yields the post-grasp model presented in (2.10). When only reaction wheels are employed and external actuation like thrusters are not used, the reduced control input $\bar{\boldsymbol{\tau}} = \begin{bmatrix}\boldsymbol{\tau}_m^T & \boldsymbol{\tau}_r^T\end{bmatrix}^T \in \mathbb{R}^{n+r}$ can be mapped to the dynamics of the combined servicer-client system using a selector matrix $\boldsymbol{T}$, as shown below.

$$\boldsymbol{M}_{sc}\dot{\boldsymbol{V}}_s + \boldsymbol{C}_{sc}\boldsymbol{V}_s = \boldsymbol{T}^T\bar{\boldsymbol{\tau}} \tag{3.18}$$

Here, $\boldsymbol{T} = [\boldsymbol{0} \quad \boldsymbol{I}_n \quad \boldsymbol{I}_r]$ and the servicer-client system operates under the condition where external forces and momentum are zero. In order to reduce the model to the DoF of the control, let us define reduced coordinates $\dot{\bar{\boldsymbol{q}}} = \begin{bmatrix}\dot{\boldsymbol{q}}^T & \dot{\boldsymbol{r}}^T\end{bmatrix}^T$ corresponding to the reduced control inputs,

$$\dot{\bar{\boldsymbol{q}}} = \boldsymbol{T}\boldsymbol{V}_s. \tag{3.19}$$

Further, let us define $\boldsymbol{\xi} = \begin{bmatrix}\boldsymbol{M}_{bb} & \boldsymbol{M}_{bm} & \boldsymbol{M}_{br}\end{bmatrix}\boldsymbol{V}_s$, the generalized momentum (linear and angular) and $\boldsymbol{T}^{\mathcal{M}+} = \boldsymbol{M}_{sc}^{-1}\boldsymbol{T}^T(\boldsymbol{T}\boldsymbol{M}^{-1}\boldsymbol{T}^T)^{-1}$, generalized-inverse of $\boldsymbol{T}$, where

$$\boldsymbol{M}_{sc} = \begin{bmatrix}\boldsymbol{M}_{bb} & \boldsymbol{M}_{bm} & \boldsymbol{M}_{br}\\ \boldsymbol{M}_{bm}^T & \boldsymbol{M}_{mm} & \boldsymbol{0}\\ \boldsymbol{M}_{br}^T & \boldsymbol{0}^T & \boldsymbol{M}_{rr}\end{bmatrix}, \qquad \boldsymbol{T}^{T_{\mathcal{M}+}} = \begin{bmatrix}-\boldsymbol{M}_{bm}^T\boldsymbol{M}_{bb}^{-1} & \boldsymbol{I}_n & \boldsymbol{0}\\ -\boldsymbol{M}_{br}^T\boldsymbol{M}_{bb}^{-1} & \boldsymbol{0} & \boldsymbol{I}_r\end{bmatrix}. \tag{3.20}$$

$\boldsymbol{M}_{bb} \in \mathbb{R}^{6\times6}, \boldsymbol{M}_{mm} \in \mathbb{R}^{n\times n}, \boldsymbol{M}_{rr} \in \mathbb{R}^{3\times3}$ are the base, manipulator and reaction wheel inertia matrices and, $\boldsymbol{M}_{bm} \in \mathbb{R}^{6\times n}, \boldsymbol{M}_{br} \in \mathbb{R}^{6\times3}$ are the base-manipulator and, base-reaction-wheel inertia coupling matrices (including grasped client in the post-grasp phase), respectively.

The servicer states can be retrieved from the reduced coordinates and the generalized momentum of the system as,

$$\boldsymbol{V}_s = \begin{bmatrix} & \boldsymbol{T} & \\ \boldsymbol{M}_{bb} & \boldsymbol{M}_{bm} & \boldsymbol{M}_{br} \end{bmatrix}^{-1} \begin{bmatrix} \dot{\boldsymbol{q}} \\ \boldsymbol{\xi} \end{bmatrix} \tag{3.21}$$

Considering a free-floating system without any external momentum i.e. $\boldsymbol{\xi} = \boldsymbol{0}$, the zero-momentum is conserved when no external forces act on the base. In this case, the servicer states in (3.21) are given by $\boldsymbol{V}_s = \boldsymbol{T}^{M+}\dot{\boldsymbol{q}}$.

Finally, the post-grasp dynamics of the system in (3.18) can be reduced using a coordinate transformation via (3.19) and substituting for service states from (3.21), resulting in,

$$\text{Post-grasp reduced dynamics}: \quad \bar{\boldsymbol{M}}\ddot{\boldsymbol{q}} + \bar{\boldsymbol{C}} = \bar{\boldsymbol{\tau}}, \tag{3.22}$$

where,

$$\begin{aligned} \bar{\boldsymbol{M}} &= (\boldsymbol{T}\boldsymbol{M}_{sc}^{-1}\boldsymbol{T}^T)^{-1} = \boldsymbol{T}^{T_{M+}}\boldsymbol{M}_{sc}\boldsymbol{T}^{M+}, \\ \bar{\boldsymbol{C}} &= \bar{\boldsymbol{M}}\boldsymbol{T}\boldsymbol{M}_{sc}^{-1}\boldsymbol{C}_{sc}\boldsymbol{V}_s - \bar{\boldsymbol{M}}\dot{\boldsymbol{T}}\boldsymbol{V}_s = \bar{\boldsymbol{C}}\dot{\boldsymbol{q}}, \\ \Rightarrow \bar{\boldsymbol{C}} &= \boldsymbol{T}^{T_{M+}}\boldsymbol{C}_{sc}\boldsymbol{T}^{M+} \quad \text{given} \quad \dot{\boldsymbol{T}} = \boldsymbol{0}. \end{aligned}$$

Observe that the reduced dynamics in (3.22) obtained via a coordinate transformation is equivalent to the generalized dynamics for a free-floating system ([UY87]) obtained via the momentum constraint. The model reduction being equivalent to a linear coordinate transformation, it is clear that the passivity property $\dot{\boldsymbol{q}}^T(\dot{\bar{\boldsymbol{M}}} - 2\bar{\boldsymbol{C}})\dot{\boldsymbol{q}} = \boldsymbol{0}$ holds for the reduced model.

The reduced Jacobian for attitude control that shall be consistent with the reduced dynamics in (3.22) is derived ahead and used for the controller design.

3.5.2 Reduced Jacobian

The primary goal of the controller is to maintain the base attitude to ensure communication with the ground. In order to address the task of maintaining the base attitude, we must first express the angular base velocity $\boldsymbol{\omega_b} \in \mathbb{R}^3$ in terms of the reduced states of the system to ensure consistency with the reduced dynamics. Therefore, we can define the base attitude Jacobian from (3.21) and the zero-momentum condition to get,

$$\boldsymbol{\omega}_b = \underbrace{-\begin{bmatrix} \boldsymbol{0} & \boldsymbol{I} \end{bmatrix} \boldsymbol{M}_{bb}^{-1} \begin{bmatrix} & \boldsymbol{M}_{br} \end{bmatrix}}_{\bar{\boldsymbol{J}}_\omega} \dot{\boldsymbol{q}} \tag{3.23}$$

where, $\bar{\boldsymbol{J}}_\omega$ is generalized Jacobian for the angular base velocity. The inertia matrices in (3.23) are further expanded as,

$$\boldsymbol{M}_{bb} = \begin{bmatrix} \boldsymbol{M}_{vv} & \boldsymbol{M}_{v\omega} \\ \boldsymbol{M}_{v\omega}^T & \boldsymbol{M}_{\omega\omega} \end{bmatrix} \qquad \begin{aligned} {}^T &= \begin{bmatrix} \boldsymbol{M}_{vm}^T & \boldsymbol{M}_{\omega m}^T \end{bmatrix} \\ \boldsymbol{M}_{br}^T &= \begin{bmatrix} \boldsymbol{0}^T & \boldsymbol{M}_{\omega r}^T \end{bmatrix} \end{aligned}$$

Here, the inertia matrices include the grasped client in the post-grasp phase with $\boldsymbol{M}_{vv}, \boldsymbol{M}_{\omega\omega} \in \mathbb{R}^{3\times3}$ the translational and rotational base inertia matrices and, $\boldsymbol{M}_{v\omega} \in \mathbb{R}^{3\times3}, \boldsymbol{M}_{vm} \in \mathbb{R}^{3\times n}, \boldsymbol{M}_{\omega m} \in \mathbb{R}^{3\times n}, \boldsymbol{M}_{\omega r} \in \mathbb{R}^{3\times3}$ the inertia coupling matrices between the linear base to angular motion, linear base to manipulator motion, angular base to manipulator motion and, angular base to reaction wheel motion respectively. Using the structure of the inertia matrices above, $\bar{\boldsymbol{J}}_\omega$ in (3.23) is simplified as,

$$\text{Reduced attitude Jacobian}: \qquad \bar{\boldsymbol{J}}_\omega = -\bar{\boldsymbol{M}}_{\omega\omega}^{-1}\begin{bmatrix}\bar{\boldsymbol{M}}_{\omega m} & \boldsymbol{M}_{\omega r}\end{bmatrix} \tag{3.24}$$

where, the inertia terms are given by $\bar{\boldsymbol{M}}_{\omega\omega} = \boldsymbol{M}_{\omega\omega} - \boldsymbol{M}_{v\omega}^T\boldsymbol{M}_v^{-1}\boldsymbol{M}_{v\omega}$ and $\bar{\boldsymbol{M}}_{\omega m} = \boldsymbol{M}_{\omega m} - \boldsymbol{M}_{v\omega}^T\boldsymbol{M}_{vv}^{-1}\boldsymbol{M}_{vm}$.

When $r = 3$ reaction wheels are mounted in mutually orthogonal directions, $\boldsymbol{M}_{\omega r}$ attains full rank. Further, the matrix $\bar{\boldsymbol{M}}_{\omega\omega}$ is invertible in the absence of dynamic singularities [PD93]. In this chapter, we shall explicitly assume $r = 3$ reaction wheels in mutually orthogonal directions and the absence of dynamic singularities.

3.5.3 Hierarchical control law

To facilitate the design of the control objectives in Table 3.1 for the post-stabilization phase, the angular base velocity $\boldsymbol{\omega_b}$ and nullspace coordinates $\boldsymbol{v}_{\bar{n}}$ are introduced as augmented task coordinates.

$$\text{Augmented task coordinates}: \quad \begin{matrix}\text{T1:}\\ \text{T2:}\end{matrix}\begin{bmatrix}\boldsymbol{\omega}_b\\ \boldsymbol{v}_{\bar{n}}\end{bmatrix} = \boldsymbol{J}_N\dot{\boldsymbol{q}}, \quad \boldsymbol{J}_N = \begin{bmatrix}\bar{\boldsymbol{J}}_\omega\\ \boldsymbol{N}_\omega^{\bar{M}\dagger}\end{bmatrix}. \tag{3.25}$$

$\boldsymbol{N}_\omega^{\bar{M}\dagger} = (\boldsymbol{N}_\omega^T\bar{\boldsymbol{M}}\boldsymbol{N}_\omega)^{-1}\boldsymbol{N}_\omega^T\bar{\boldsymbol{M}} \in \mathbb{R}^{n\times n+3}$ is the transposed generalized-inverse of $\boldsymbol{N}_\omega^T = \begin{bmatrix}\boldsymbol{I} & -\bar{\boldsymbol{M}}_{\omega m}^T\boldsymbol{M}_{\omega r}^{-T}\end{bmatrix}$. $\boldsymbol{N}_\omega$ represents the nullspace basis matrix of $\bar{\boldsymbol{J}}_\omega$ and the property $\bar{\boldsymbol{J}}_\omega\boldsymbol{N}_\omega = \boldsymbol{0}$ holds true. Given the assumption $\boldsymbol{M}_{\omega r}$ is invertible, the nullspace coordinates, $\boldsymbol{v}_{\bar{n}} \in \mathbb{R}^n$ has dimension n.

To design the controller at a task level as proposed in Table 3.1, the dynamics in (3.22) is transformed to the augmented task velocity coordinates in (3.25) to obtain inertially decoupled dynamics,

$$\begin{matrix}\text{Inertially-decoupled}\\ \text{nullspace dynamics}:\end{matrix}\quad \begin{matrix}\text{T1:}\\ \text{T2:}\end{matrix}\quad \underbrace{\begin{bmatrix}\boldsymbol{\Lambda}_{bb} & \boldsymbol{0}\\ \boldsymbol{0} & \boldsymbol{\Lambda}_{\bar{n}\bar{n}}\end{bmatrix}}_{\boldsymbol{\Lambda}}\begin{bmatrix}\dot{\boldsymbol{\omega}}_b\\ \dot{\boldsymbol{v}}_{\bar{n}}\end{bmatrix} + \underbrace{\begin{bmatrix}\boldsymbol{\mu}_{bb} & \boldsymbol{\mu}_{b\bar{n}}\\ \boldsymbol{\mu}_{\bar{n}b} & \boldsymbol{\mu}_{\bar{n}\bar{n}}\end{bmatrix}}_{\boldsymbol{\mu}}\begin{bmatrix}\boldsymbol{\omega}_b\\ \boldsymbol{v}_{\bar{n}}\end{bmatrix} = \underbrace{\begin{bmatrix}\boldsymbol{\tau}_\omega\\ \boldsymbol{\tau}_{\bar{n}}\end{bmatrix}}_{\boldsymbol{\tau}_N}, \tag{3.26}$$

where,

$$\begin{aligned}\boldsymbol{\Lambda} &= \boldsymbol{J}_N^{-T}\bar{\boldsymbol{M}}\boldsymbol{J}_N^{-1}, & \boldsymbol{\mu} &= \boldsymbol{J}_N^{-T}\bar{\boldsymbol{M}}\frac{d}{dt}(\boldsymbol{J}_N^{-1}) + \boldsymbol{J}_N^{-T}\bar{\boldsymbol{C}}\boldsymbol{J}_N^{-1},\\ \boldsymbol{J}_N^{-1} &= \begin{bmatrix}\bar{\boldsymbol{J}}_\omega^{\bar{M}+} & \boldsymbol{N}_\omega\end{bmatrix}, & \boldsymbol{\tau}_N &= \boldsymbol{J}_N^{-T}\boldsymbol{\tau}_\omega.\end{aligned} \tag{3.27}$$

Here $\bar{\boldsymbol{J}}_\omega^{\bar{M}+} = \bar{\boldsymbol{M}}^{-1}\bar{\boldsymbol{J}}_\omega^T(\bar{\boldsymbol{J}}_\omega\bar{\boldsymbol{M}}^{-1}\bar{\boldsymbol{J}}_\omega^T)^{-1}$ is the dynamically consistent generalized-inverse of $\bar{\boldsymbol{J}}_\omega$. The control torques in augmented task coordinates for the dynamics in (3.26) are chosen as,

$$\text{Augmented task control}: \qquad \text{T1:} \quad \boldsymbol{\tau}_\omega = 2\boldsymbol{E}^T\boldsymbol{K}_{P\omega}\Delta\boldsymbol{\epsilon} - \boldsymbol{K}_{D\omega}\boldsymbol{\omega}_b + \boldsymbol{\mu}_{b\bar{n}}\boldsymbol{v}_{\bar{n}}, \tag{3.28}$$

$$\text{T2:} \quad \boldsymbol{\tau}_{\bar{n}} = \boldsymbol{N}_\omega^T\begin{bmatrix}\boldsymbol{K}_{Pm}\Delta\boldsymbol{q}\\ \boldsymbol{0}\end{bmatrix} - \boldsymbol{N}_\omega^T\begin{bmatrix}\boldsymbol{K}_{Dm}\dot{\boldsymbol{q}}\\ \boldsymbol{K}_{Dr}\dot{\boldsymbol{r}}\end{bmatrix} \tag{3.29}$$

where$\Delta\boldsymbol{\epsilon} = \eta\boldsymbol{\epsilon}^d - \eta^d\boldsymbol{\epsilon} - \boldsymbol{\epsilon}\times\boldsymbol{\epsilon}^d$ is the vector part of the base error quaternion and $(\eta,\boldsymbol{\epsilon})$, $(\eta^d,\boldsymbol{\epsilon}^d)$ are the measured and desired base quaternions respectively. The matrix $\boldsymbol{E} = \Delta\eta\boldsymbol{I} + \boldsymbol{S}(\Delta\boldsymbol{\epsilon})$ where $\Delta\eta = \eta\eta^d + \boldsymbol{\epsilon}^T\boldsymbol{\epsilon}^d$ and $\boldsymbol{S}(\cdot)$ is the skew-symmetric cross-product operator. $\boldsymbol{K}_{D\omega}\in\mathbb{R}^{3\times3}, \boldsymbol{K}_{Dm}\in\mathbb{R}^{n\times n}$ and $\boldsymbol{K}_{Dr}\in\mathbb{R}^{3\times3}$ are positive-definite damping gain matrices of the base attitude, manipulator joints and reaction wheels, respectively. $\boldsymbol{K}_{P\omega}\in\mathbb{R}^{3\times3}$, $\boldsymbol{K}_{Pm}\in\mathbb{R}^{n\times n}$ are the positive-definite stiffness matrices for the base attitude and joints respectively.

Finally, the control torques $\boldsymbol{\tau}_\omega$ applied to the manipulator and reaction wheels in the reduced dynamics (3.22) can be obtained using the transposed-Jacobian relation in (3.27) to transform the torques in task coordinates, (3.28) and (3.29).

(3.30) Control in actuator coordinates :
$$\boldsymbol{\tau}_\omega = \underbrace{\bar{\boldsymbol{J}}_\omega^T\boldsymbol{\tau}_{\bar{\omega}}}_{\boldsymbol{\tau}_{\mathrm{T1}}} + \underbrace{\boldsymbol{N}_\omega^{T_{\bar{M}\dagger}}\boldsymbol{N}_\omega^T\boldsymbol{\tau}_0}_{\boldsymbol{\tau}_{\mathrm{T2}}} + \underbrace{\bar{\boldsymbol{J}}_\omega^T\boldsymbol{\mu}_{b\bar{n}}\boldsymbol{v}_{\bar{n}}}_{\boldsymbol{\tau}_\mu},$$

where,
$$\boldsymbol{\tau}_{\bar{\omega}} = 2\boldsymbol{E}^T\boldsymbol{K}_{P\omega}\Delta\boldsymbol{\epsilon} - \boldsymbol{K}_{D\omega}\boldsymbol{\omega}_b$$
$$\boldsymbol{\tau}_{PD} = \boldsymbol{K}_{Pm}\Delta\boldsymbol{q} - \boldsymbol{K}_{Dm}\dot{\boldsymbol{q}} \qquad \text{with, } \boldsymbol{\tau}_0 = \begin{bmatrix}\boldsymbol{\tau}_{PD}\\ -\boldsymbol{K}_{Dr}\dot{\boldsymbol{r}}\end{bmatrix}$$

$\Delta\boldsymbol{q} = \boldsymbol{q}_n^d - \boldsymbol{q}_n$ is the error between the desired manipulator joint angles $\boldsymbol{q}_n^d$ and the measured angles $\boldsymbol{q}_n$. The proposed control law in (3.30) is composed of three terms. The feedback term, $\boldsymbol{\tau}_{\mathrm{T1}}$, allows to maintain the attitude of the base to a desired value. $\boldsymbol{\tau}_{\mathrm{T2}}$ allows to reconfigure the joints in the nullspace of the base attitude, while damping the joint velocities in addition to stabilizing the reaction wheels. The term $\boldsymbol{\tau}_\mu$ compensates for the Coriolis coupling between the base attitude and the nullspace dynamics. The schematic of the proposed controller is shown in Figure 3.5.

It is worth mentioning that, the nullspace $\boldsymbol{N}_\omega^{T_{\bar{M}\dagger}}\boldsymbol{N}_\omega^T$ in (3.30) can be shown to be equivalent to the *angular reaction null space* proposed in [DY04], using the relation $\boldsymbol{N}_\omega^{T_{\bar{M}\dagger}}\boldsymbol{N}_\omega^T = \boldsymbol{I} - \bar{\boldsymbol{J}}_\omega^T\bar{\boldsymbol{J}}_\omega^{T_{\bar{M}}+}$. That is, $\boldsymbol{N}_\omega^{T_{\bar{M}\dagger}}\boldsymbol{N}_\omega^T$ in (3.30) projects the inertia coupling $\begin{bmatrix}\bar{\boldsymbol{M}}_{\omega m} & \boldsymbol{M}_{\omega r}\end{bmatrix}$ orthogonal to the metric $\bar{\boldsymbol{M}}^{-1}$. This is a dynamically consistent nullspace projection ([Kha95]), which ensures that there is no direct feed-through of angular acceleration to the base due to the nullspace task.

3.5.4 Stability of the controller

Proposition 2. *Consider the dynamics in* (3.26) *with the control law in* (3.29). *The stiffness and damping gains* $\boldsymbol{K}_{P\omega}, \boldsymbol{K}_{Pm}, \boldsymbol{K}_{D\omega}, \boldsymbol{K}_{Dm}$ *and* $\boldsymbol{K}_{Dr}$ *are symmetric and positive-definite. Then, given three orthogonal reaction wheels and the absence of dynamic singularities, the controller in* (3.29) *results in the equilibrium* $\Delta\boldsymbol{\epsilon}, \Delta\boldsymbol{q}, \boldsymbol{\omega}_b, \boldsymbol{v}_{\bar{n}} = 0$ *being asymptotically stable.*

The stability of the controller in (3.29) is analysed similar to [Ott08], using the theory of semi-definite Lyapunov functions in [IKO96] and [VdS00] (refer Section 2.3). Towards this end, first, the positive semi-definite Lyapunov function $V_\omega = \frac{1}{2}\boldsymbol{\omega}_b^T\boldsymbol{\Lambda}_{bb}\boldsymbol{\omega}_b + 2\Delta\boldsymbol{\epsilon}^T\boldsymbol{K}_{P\omega}\Delta\boldsymbol{\epsilon}$ is chosen for the main

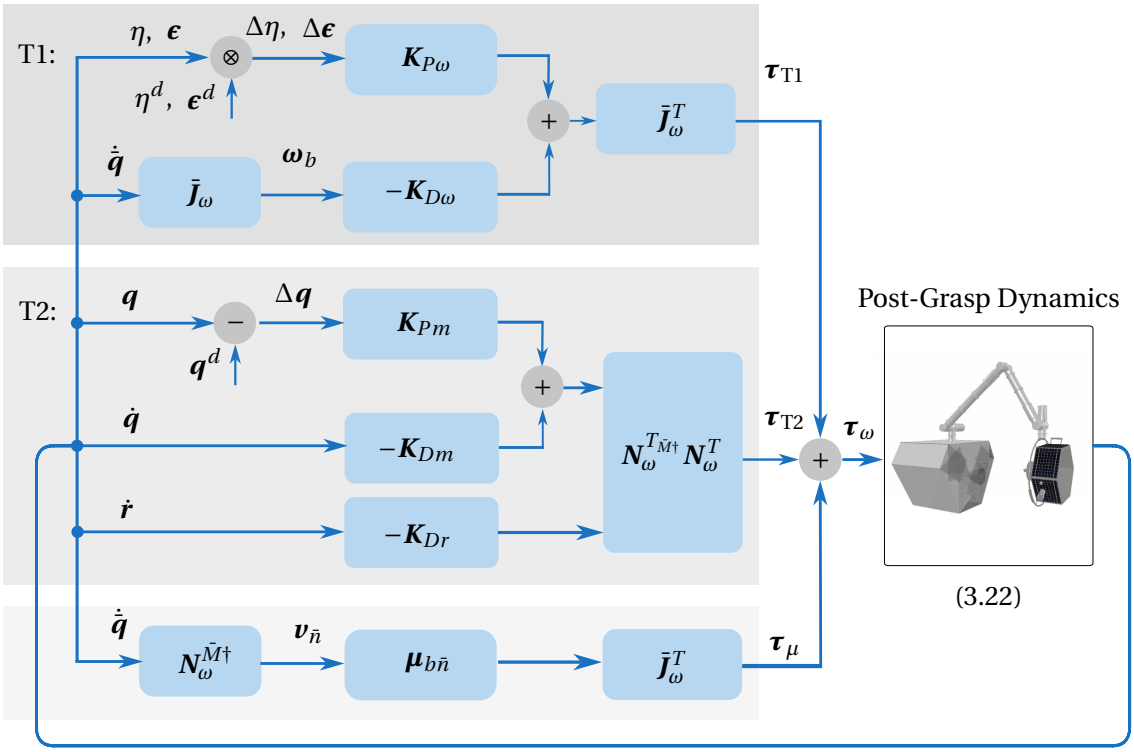

Figure 3.5: *Controller for post-stabilization phase* – block diagram of the proposed controller in closed-loop with the servicer-client dynamics.

task of base attitude control. For the designed control torque $\boldsymbol{\tau}_\omega$ in (3.28), $\dot{V}_\omega = -\boldsymbol{\omega}_b^T \boldsymbol{K}_{D\omega}\boldsymbol{\omega}_b$, which follows from the passivity property retained through the coordinate transformations from (2.10) through (3.22) to (3.26).

Second, the Lyapunov function $V_{\bar{n}} = \frac{1}{2}\boldsymbol{\nu}_{\bar{n}}^T \boldsymbol{\Lambda}_{\bar{n}\bar{n}}\boldsymbol{\nu}_{\bar{n}} + \frac{1}{2}\Delta\boldsymbol{q}^T\boldsymbol{K}_{Pm}\Delta\boldsymbol{q}$ is chosen in the set where the first task T1 is converged, $\Delta\boldsymbol{\epsilon}, \boldsymbol{\omega}_b = \boldsymbol{0}$ and the designed nullspace control torque $\boldsymbol{\tau}_{\bar{n}}$ in (3.29) leads to

$$\dot{V}_{\bar{n}} = -\boldsymbol{\nu}_{\bar{n}}^T \boldsymbol{N}_\omega^T \begin{bmatrix} \boldsymbol{K}_{Dm} & \boldsymbol{0} \\ \boldsymbol{0} & \boldsymbol{K}_{Dr} \end{bmatrix} \boldsymbol{N}_\omega \boldsymbol{\nu}_{\bar{n}}$$

which shows conditional stability to the set $\boldsymbol{\omega}_b = \boldsymbol{0}$. Given three orthogonal reaction wheels, and the absence of dynamic singularities, stability is concluded by invoking LaSalle's invariance principle and using the theory of semi-definite Lyapunov functions in [IKO96] and [VdS00]. This means $\boldsymbol{\omega}_b \to \boldsymbol{0}$ and $\boldsymbol{\nu}_{\bar{n}} \to \boldsymbol{0}$, and $\Delta\boldsymbol{\epsilon}$ converges to an equilibrium where the compliant frame aligns with the desired frame ([CNSV99]).

Further, notice that the stiffness term in (3.29) is responsible for driving the system to, the minimum of the potential $\frac{1}{2}\Delta\boldsymbol{q}^T\boldsymbol{K}_{Pm}\Delta\boldsymbol{q}$. This minimum occurs when,

$$\underbrace{\begin{bmatrix} \boldsymbol{I} & -\bar{\boldsymbol{M}}_{\omega m}^T \boldsymbol{M}_{\omega r}^{-T} \end{bmatrix}}_{\boldsymbol{N}_\omega^T} \begin{bmatrix} \boldsymbol{K}_{Pm}\Delta\boldsymbol{q} \\ \boldsymbol{0} \end{bmatrix} = \boldsymbol{0}, \tag{3.31}$$

i.e. when $\Delta \boldsymbol{q} = \mathbf{0}$. This is evident from the full rank of the identity matrix that multiplies with the stiffness on the joint errors. Hence, the joint task converges to its equilibrium in the nullspace of the base attitude.

3.6 Weighted-damping control

The controller designed in (3.30) may lead to reaction wheels reaching their saturation speeds. To reduce the demand from the reaction wheels, we can investigate which terms can be modified without compromising the primary objectives of the controller.

We see that $\boldsymbol{\tau}_{\mathrm{T1}}$ in (3.30) is necessary for stabilizing and maintaining the attitude of the base for pointing accuracy requirements. It is also desirable to retain the PD term responsible for the secondary task of reconfiguring the arm in $\boldsymbol{\tau}_{\mathrm{T2}}$. The Coriolis compensation $\boldsymbol{\tau}_{\mu}$ decouples the attitude and arm reconfiguration tasks. Therefore, reaction wheel damping in $\boldsymbol{\tau}_{\mathrm{T2}}$ could be modified to alter the rate at which this term drives the system's energy to a stable equilibrium.

Therefore, the control torque $\boldsymbol{\tau}_{\mathrm{T2}}$ in (3.30) is modified with a new damping gain on the reaction wheels $\boldsymbol{K}'_{Dr}$, as follows:

(3.32) Velocity-weighted damping :

$$\boldsymbol{\tau}'_{\mathrm{T2}} = \boldsymbol{N}_{\omega}^{T_{\bar{M}\dagger}} \boldsymbol{N}_{\omega}^{T} \begin{bmatrix} \boldsymbol{\tau}_{PD} \\ -\boldsymbol{K}'_{Dr}\dot{\boldsymbol{r}} \end{bmatrix}$$

$$\text{where,} \quad \boldsymbol{K}'_{Dr} = \boldsymbol{K}_{Dr}\boldsymbol{\sigma}(\dot{\boldsymbol{r}}).$$

Here $\boldsymbol{\sigma}(\dot{\boldsymbol{r}}) = \mathrm{diag}(\sigma(\dot{q}_{r_i}))$, is a weighting function that increases the damping on the reaction wheels as they approach their saturation limits as. The weighting function σ is chosen for the i-th wheel as:

(3.33) Weighting function :

$$\sigma(x) = \begin{cases} \cosh\left(\frac{|x|-L_i}{U_i-L_i}\mathrm{acosh}(u_i)\right), & |x| > L_i \\ 1, & |x| \leq L_i \end{cases}$$

where L_i, U_i and u_i are positive constants with $L_i < U_i$. L_i is the lower bound of the wheel speed from where the weighting factor σ starts to increase above 1 along a cosine hyperbolic curve. U_i is the upper bound on the wheel speed where the damping factor increases to a value equal to u_i. The weighting function is visualized in Figure 3.6

Applying the weighted damping in (3.32) preserves the projection into the nullspace of the base attitude. This approach is essential to prevent disturbances to the base attitude resulting from the modified reaction wheel torques. Accordingly, the controller in (3.30) is modified by incorporating $\boldsymbol{\tau}'_{\mathrm{T2}}$ from (3.32). The updated schematic is presented in Figure 3.7.

The convergence of the modified controller is established when the reaction wheel damping gain $\boldsymbol{K}_{Dr}$ in (3.32) is a diagonal, positive-definite matrix. Since the weighting function $\boldsymbol{\sigma}$ is also diagonal and positive-definite, $\boldsymbol{K}'_{Dr}$ in (3.32) is diagonal and positive-definite. Consequently, stability is ensured by the arguments previously presented in Section 3.5.4.

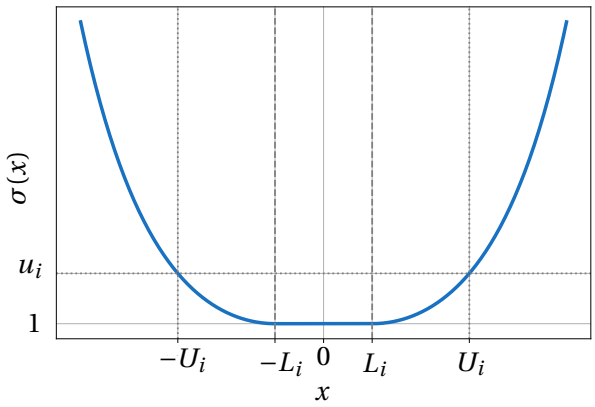

Figure 3.6: Hyperbolic cosine function in (3.33) used to weight the damping gain on the reaction wheels starting from the lower bound L_i.

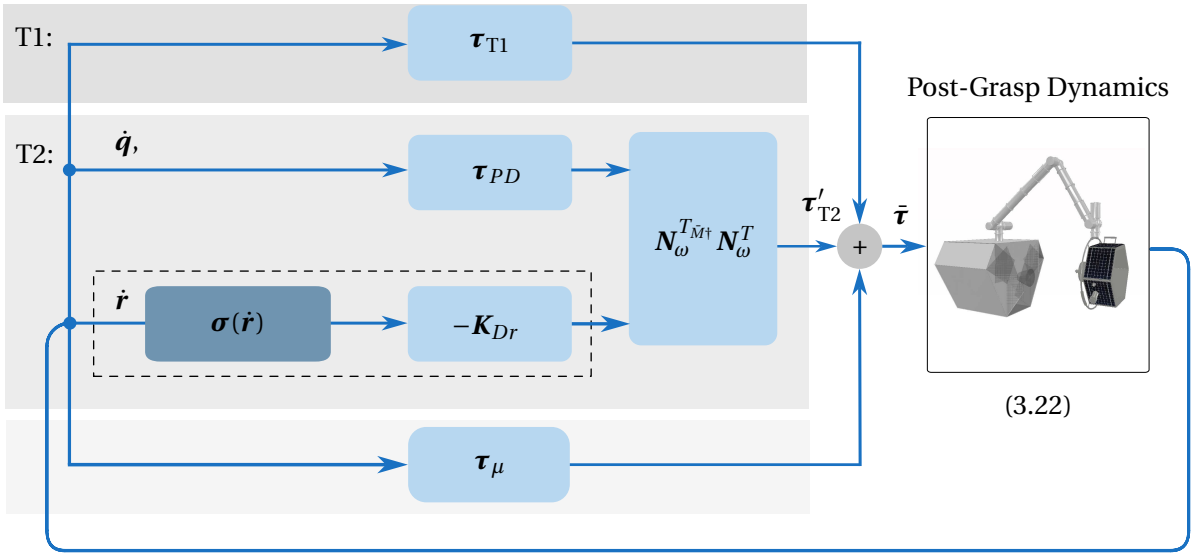

Figure 3.7: *Reaction wheel speed limitation* – block diagram of the modified controller with reaction wheel torque limitation. The dashed box shows the difference to nominal control in Figure 3.5.

3.7 Validation results

The proposed control strategies are validated using a scenario in which the client satellite is initially in a grasped state with the servicer. The simulation is conducted in MATLAB/Simulink with an integration time step of 1 ms. The dynamic/kinematic and control parameters for the servicer and client considered for the simulation of the post-grasp stabilization and post-stabilization reconfiguration are summarized in Table 3.2. The servicer is considered equipped with the 7-DoF DLR CAESAR manipulator arm (see [BGH+18] for details about the arm). The distance from the client satellite's center of mass to its grasping point is 0.5 m. The initial state of the servicer is defined as the final

Table 3.2: Simulation parameters. *Principal moment of inertia.

DYNAMIC/KINEMATIC PARAMETERS		
Parameter	**Post-grasp phase**	**Post-stabilization phase**
Servicer mass & MOI*	700kg, $(400, 450, 400)\mathrm{kg\,m^2}$	
Client mass & MOI*	200kg, $(120, 100, 90)\mathrm{kg\,m^2}$	
Manipulator arm	7-DoF CAESAR robot [BGH+18]	
Initial joint angles	$(-14, 22, 21, 62, 140, -24, -35)$deg	$(0, 20, 0, -45, 0, -45, 0)$deg
Final joint angles	$(0, 20, 0, -45, 0, -45, 0)$deg	$(0, -50, 0, -100, 0, 30, 0)$deg
Spacecraft actuators	6-DoF external actuation	3 orthogonal reaction wheels
Constraints	Interaction wrench: 2N, 2Nm	Reaction wheel speed: 1000rpm

CONTROLLER PARAMETERS			
T#	$\boldsymbol{K_\bullet}$	**Post-grasp phase**	**Post-stabilization phase**
T1	$\boldsymbol{K}_P$	–	$\boldsymbol{K}_{P\omega}: 200\boldsymbol{I}_{3\times3}\mathrm{Nm\,rad^{-1}}$
	$\boldsymbol{K}_D$	$\boldsymbol{K}_{De}: 100\boldsymbol{I}_{3\times3}\mathrm{Nm^{-1}s}, 100\boldsymbol{I}_{3\times3}\mathrm{Nm\,rad^{-1}s}$	$\boldsymbol{K}_{D\omega}: 100\boldsymbol{I}_{3\times3}\mathrm{Nm\,rad^{-1}s}$
T2	$\boldsymbol{K}_{Pm}$	$500\boldsymbol{I}_{7\times7}\mathrm{Nm\,rad^{-1}}$	$4\times10^4\boldsymbol{I}_{7\times7}\mathrm{Nm\,rad^{-1}}$
	$\boldsymbol{K}_{Dm}$	$100\boldsymbol{I}_{7\times7}\mathrm{Nm\,rad^{-1}s}$	$100\boldsymbol{I}_{7\times7}\mathrm{Nm\,rad^{-1}s}$
	$\boldsymbol{K}_D$	$\boldsymbol{K}_{Db}: 500\boldsymbol{I}_{3\times3}\mathrm{Nm^{-1}s}, 500\boldsymbol{I}_{3\times3}\mathrm{Nm\,rad^{-1}s}$	$\boldsymbol{K}_{Dr}: 0.01\boldsymbol{I}_{3\times3}\mathrm{Nm\,rad^{-1}s}$

state at the moment of grasping, with velocity matching at the grasp point. In order to show the effectiveness of the control strategy, a smooth interpolated trajectory from the initial to the final joint configuration is generated, causing the manipulator to approach a kinematic singularity.

3.7.1 Post-grasp phase — Stabilization and reconfiguration

For the post-grasp scenario, the client's initial tumbling velocity is set to $\boldsymbol{v}_c$=(7.071, −7.071, 0)deg/s. The initial and desired final configurations of the manipulator arm are chosen as in Table 3.2. The desired final configuration of the arm is an *elbow-up* configuration, suitable for further manipulation/servicing tasks. The allowable maximum interaction force, $\boldsymbol{F}_{c,max}$, is a configurable parameter determined by mission requirements. For this simulation, it is set to 2N, 2Nm to evaluate an extreme scenario with minimal values. The weighting matrix used in the optimization is defined as $\boldsymbol{Q} = \mathrm{diag}(1/\boldsymbol{F}_{c,max_i}^2)$.

Simulation results for the nominal controller, which excludes the QP solver and is designed as described in (3.8), are presented in Figure 3.8 and Figure 3.9. Although the simulation duration is 70 s, Figure 3.8 displays data from the first 20s to better visualize the results. The client's tumbling motion is fully damped within 10 s, as shown in Figure 3.8(a), whereas the interaction wrench in Figure 3.8(b) exceeds the maximum force $\boldsymbol{F}_{c,max}$.

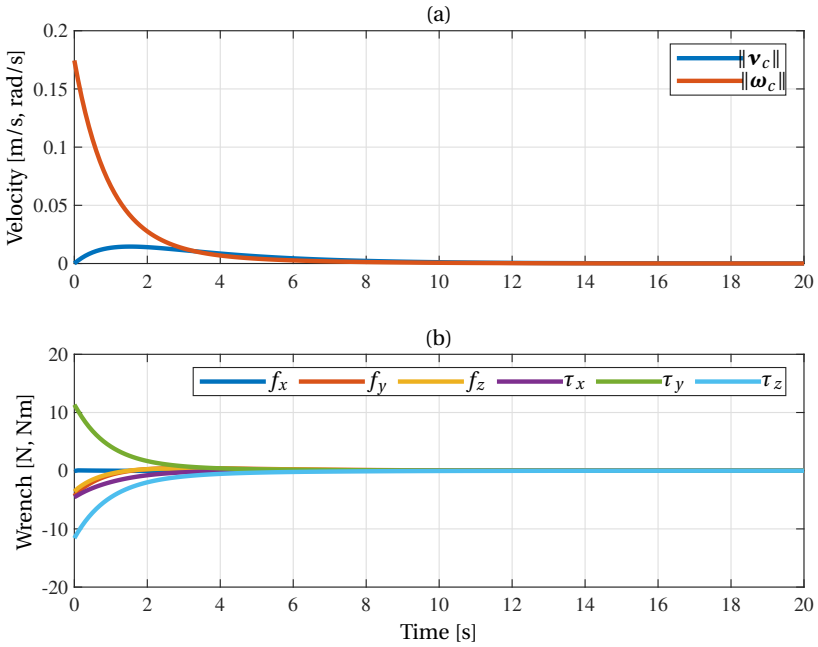

Figure 3.8: *Post-grasp phase* – client detumbling with nominal controller (3.8). (a) Norm of client velocity (b) Interaction Wrench $\boldsymbol{F_c}$.

The base velocity initially increases before being damped, as illustrated in Figure 3.9(a), while the joint errors converge to zero in Figure 3.9(b). This behavior demonstrates that the base is actuated via the nullspace to facilitate arm reconfiguration. After the client's motion is damped, the nullspace control remains active; however, the interaction forces remain near zero during the 10-20 s interval (refer to Figure 3.8 and Figure 3.9).

Kinematic singularity of the arm is quantified by $\det(\boldsymbol{J}_m \boldsymbol{J}_m^T)$, with a value of zero indicating a singular configuration. As shown in Figure 3.9(c), the manipulator arm approaches a singular configuration at 12 s. This proximity to singularity does not impede the convergence of the joint task in the nullspace, which aligns with the discussion in Section 3.3.2.

The scenario is considered for the QP-optimized controller constraining the interaction forces, and the results are shown in Figure 3.10 (data for the first 20 s shown for improved visualization). The client's tumbling motion is seen to be damped within 20 s in Figure 3.10(a), while the interaction wrench in Figure 3.10(b) is strictly maintained below $\boldsymbol{F}_{c,max}$, as imposed by the constraint given in (3.16). The slower rate of detumbling in Figure 3.10(a) compared to Figure 3.8(a) is a consequence of the optimization that limits the maximum interaction force.

Figure 3.11(a) shows the rate of change of energy of the end-effector motion $\boldsymbol{v}_e^T \boldsymbol{F}_e^*$, which maintains the strictly decreasing behaviour imposed by the convergence constraint in (3.17). For completeness, the convergence of the joint angle errors is shown in Figure 3.11(b). As can be seen, these evolve similarly to those in Figure 3.9 (b) since the joint task is achieved in the nullspace of the end-effector. Figure 3.12 illustrates the various configuration stages of the servicer-client system during the simulated detumbling strategy, from the initial to the final pose, including the approach to a

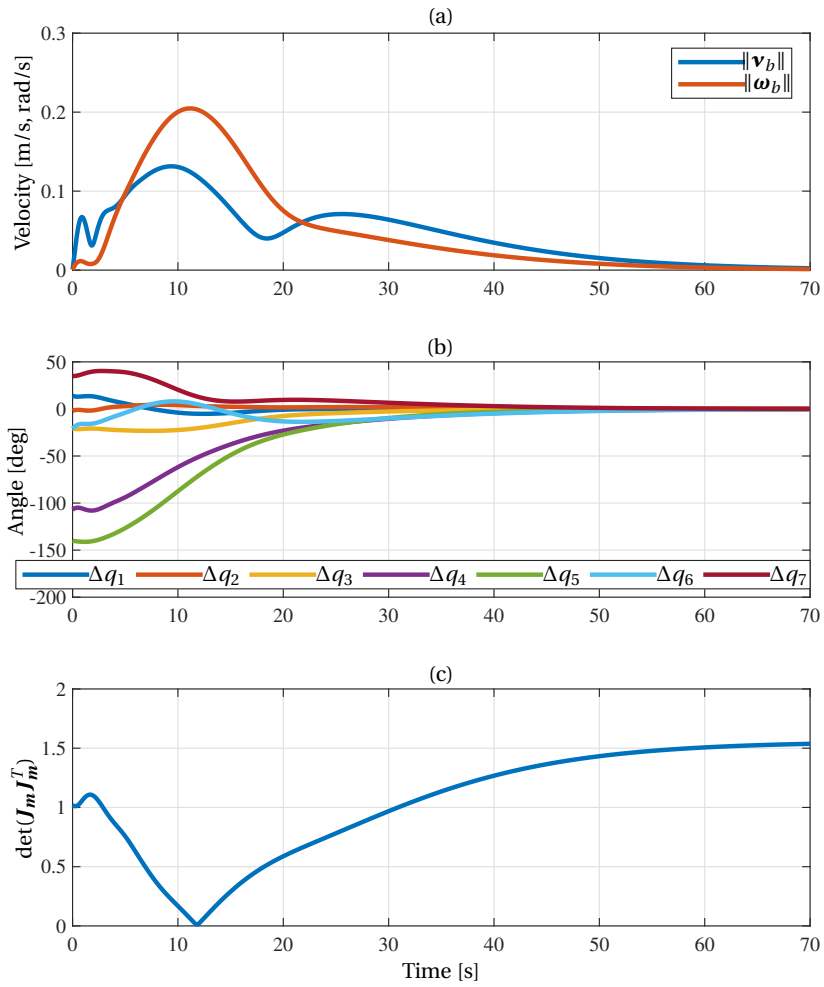

Figure 3.9: *Post-grasp phase* – arm reconfiguration with nominal controller (3.8). (a) Norm of base velocity (b) Joint angle errors (c) Measure of kinematic singularity of the manipulator arm.

singular arm configuration at $t = 12$ s.

A robustness analysis is conducted for the same detumbling scenario. This analysis incorporates uncertainties in the client parameters, sampled from a uniform distribution with bounds of ±20% for mass, ±20% for inertia parameters, and a sphere of radius 0-5 cm for the center of mass.

The maximum error between the allowable wrench $\boldsymbol{F}_{c,max}$ and the developed interaction wrench $\boldsymbol{F}_c$ is calculated. The corresponding results are shown in a scatter plot in Figure 3.13 for 30 simulation runs. The maximum error in any force component is $\Delta f = 0.02$ N, and in any torque component is $\Delta\tau = 0.01$ Nm, corresponding to less than 1% and 0.5% of the maximum threshold, respectively. These results confirm the controller's robustness to uncertainties in the client parameters.

3.7.2 Post-stabilization phase — Preparation for berthing

For attitude stabilization, the servicer spacecraft considers three reaction wheels, each with a mass of 2 kg, and inertia parameters $I_x = 0.0225$, $I_y = 0.0225$, $I_z = 0.045$, and $I_{xy} = I_{xz} = I_{yz} = 0$ kgm^2. The

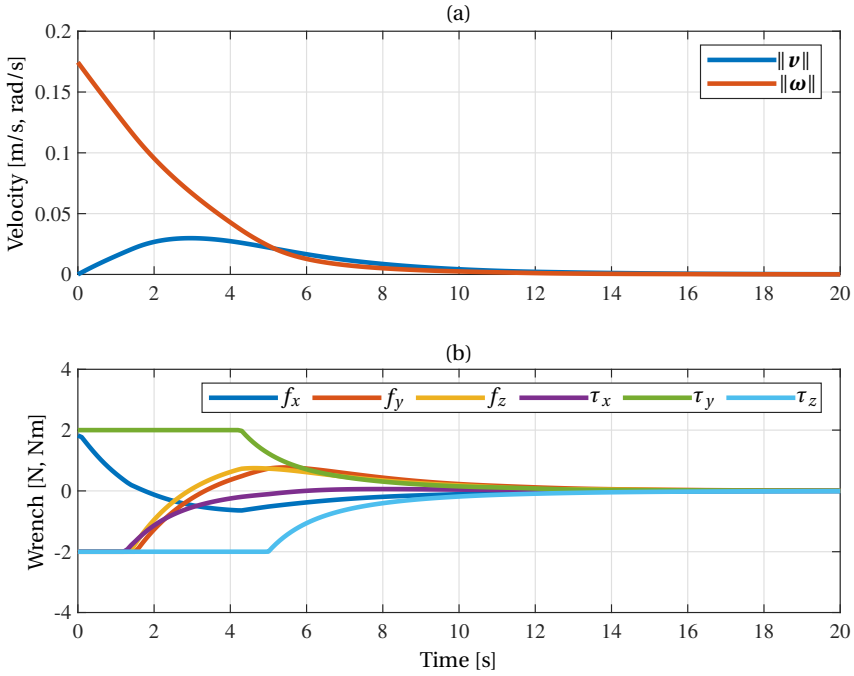

Figure 3.10: *Post-grasp phase* – QP-based client detumbling. (a) Norm of client velocity (b) Interaction Wrench $\boldsymbol{F_c}$.

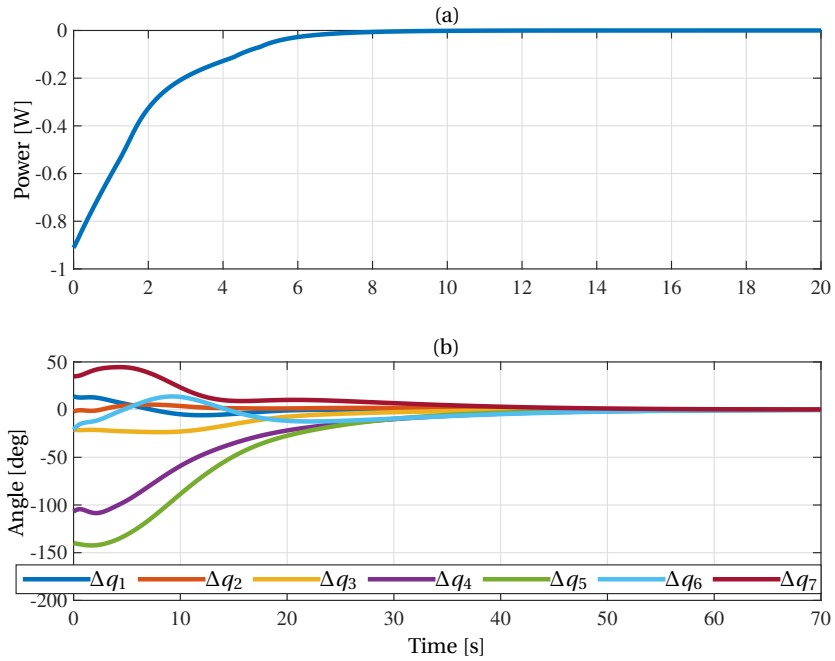

Figure 3.11: *Post-grasp phase* – energy rate and reconfiguration with QP-control. (a) Energy rate constraint $\boldsymbol{v}_e^T \boldsymbol{F}_e^*$ (b) Joint angle errors for arm reconfiguration.

initial velocity of the servicer-client system is zero after momentum is damped in the post-grasp stabilization phase. The weighting function parameters in (3.33) are defined by the wheel speed bounds $L_i = 0.7U_i$, $U_i = 1000$ rpm, and $u_i = 10$.

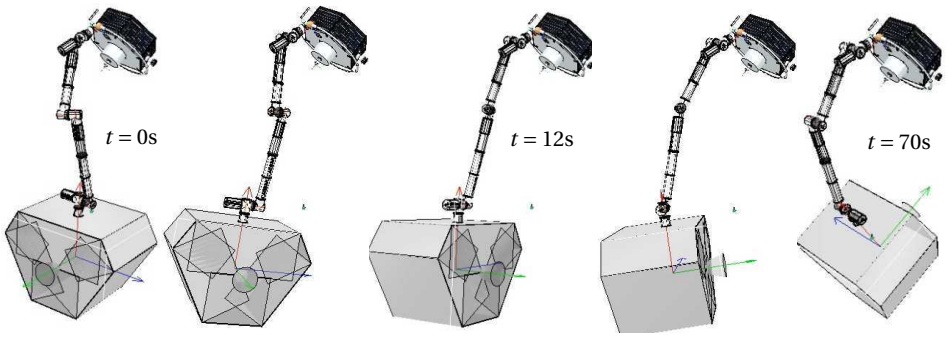

Figure 3.12: Stills from an animated motion of the servicer-client system reconfiguring the manipulator arm while stabilizing the client. A link to the simulation video is given in Appendix G, Table G.1.

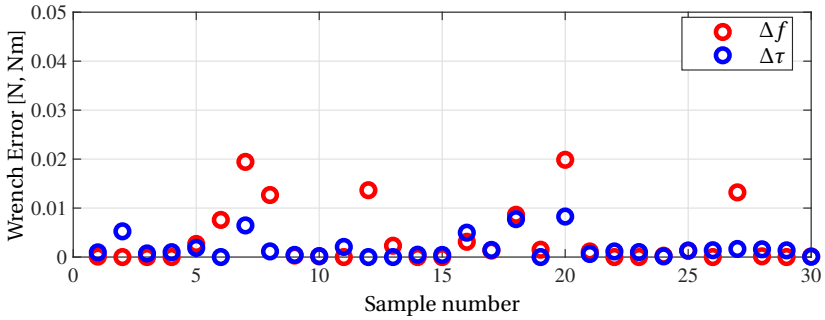

Figure 3.13: *Post-grasp phase* – maximum deviation of interaction wrench calculated for 30 simulations (samples) with client parameter uncertainties.

Results obtained with the nominal controller, which does not include reaction wheel torque modification, are presented in Figure 3.14 and Figure 3.15. Manipulator reconfiguration and reaction wheel speeds over a simulation duration of 400 s are illustrated in Figure 3.14. As shown in Figure 3.14 (a), the joint errors converge, indicating stabilization of the rigidly grasped client's motion. The arm approaches a kinematic singularity at approximately 13 s, as depicted in Figure 3.14 (c), where the singularity measure approaches zero.

The reaction wheel speeds are presented in Figure 3.14 (b). The wheels accelerate in response to the arm's motion to maintain the base attitude, with peak wheel speeds exceeding 1000 rpm. The base attitude stabilization results using the nominal controller in Figure 3.15 show the angular velocity of the base undisturbed due to the nullspace reconfiguration of the manipulator. The linear velocity of the base corresponds to the motion of the base due to conservation of momentum.

The results for the same scenario simulated with the modified controller that weights the damping on the reaction wheels is shown in Figure 3.16. The evolution of joint errors in Figure 3.16 (a) is similar to those in Figure 3.14 (a), but upon closer observation, one sees minor delay in convergence. The corresponding results of the reaction wheel speed in Figure 3.16 (b) show the wheel speeds limited within 1000 rpm. The plots for the base stabilization are omitted since they show no discernible difference in comparison to the results from the nominal controller. This is anticipated since the

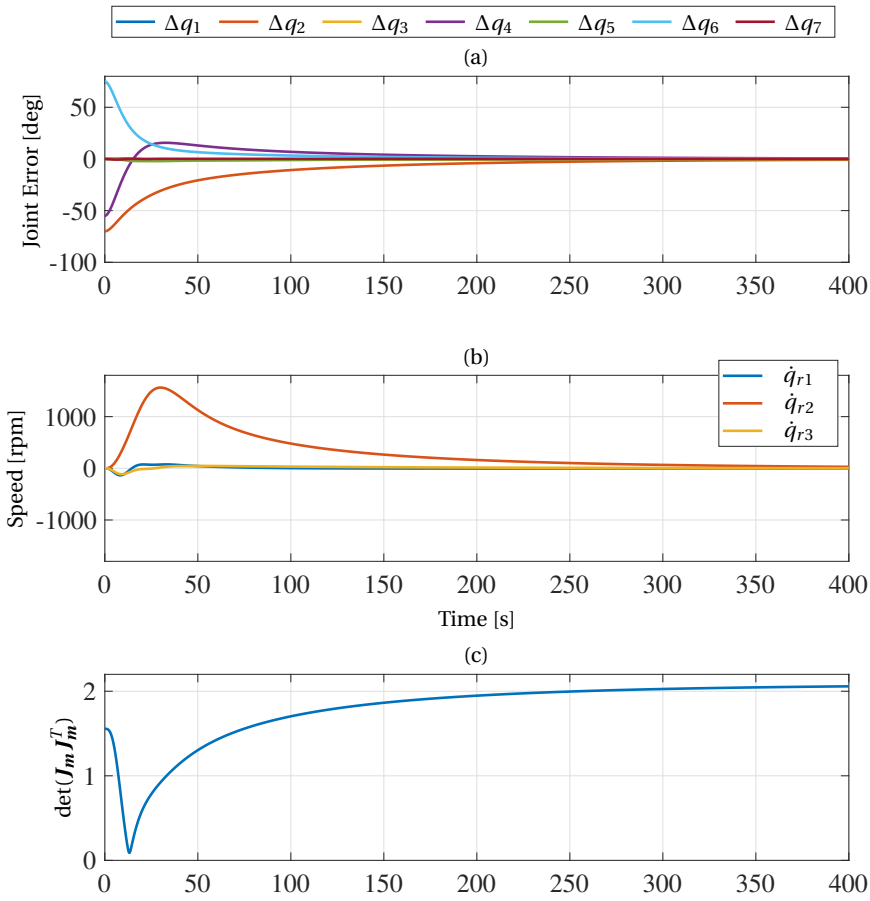

Figure 3.14: *Post-stabilization phase* – arm reconfiguration in attitude nullspace with nominal controller (3.30). (a) Convergent joint errors (b) Excessive reaction wheel speed (c) Measure of kinematic singularity of the manipulator arm.

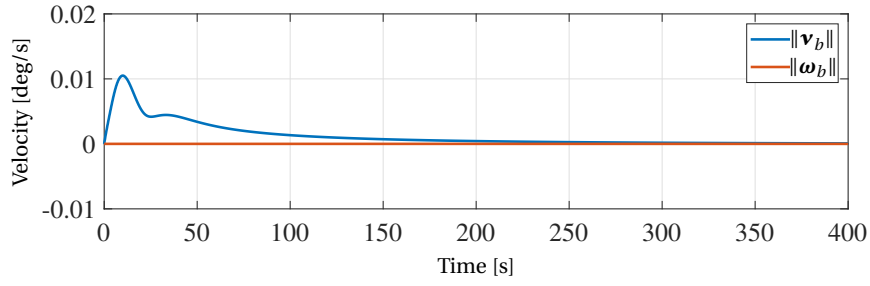

Figure 3.15: *Post-stabilization phase* – attitude maintenance with nominal controller in (3.30) showing angular velocity undisturbed, while base translates and stabilizes during arm reconfiguration.

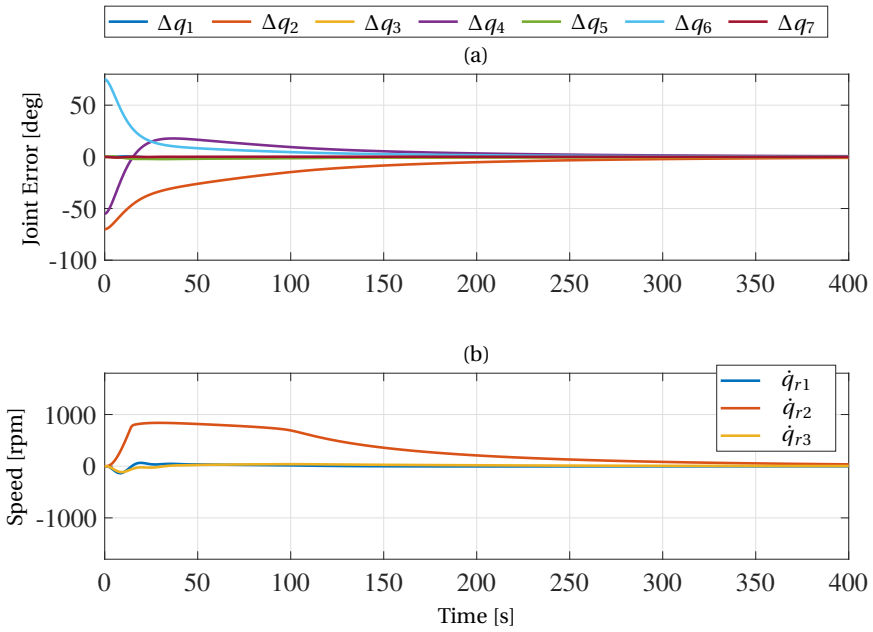

Figure 3.16: *Post-stabilization phase* – arm reconfiguration in attitude nullspace using velocity-weighted reaction wheel damping. (a) Convergent joint errors (b) Limited reaction wheel speed.

modifications to the controller are made in the nullspace of the base attitude and therefore the base stabilization motion is expected to be largely unaffected by the minor changes of the system configuration. These results validate the effectiveness of the designed controller in reconfiguring the arm without disturbing the base attitude while reducing reaction wheel speeds.

3.8 Discussion and summary

This chapter introduced a control strategy for post-grasp motion stabilization of a tumbling non-cooperative client satellite, addressing space mission requirements including maximum allowable interaction force and manipulator reconfiguration. The interaction force constraint was enforced by augmenting the controller with a quadratic programming (QP) algorithm. Reconfiguration of the orbital manipulator was accomplished entirely within the end-effector's null space, using a fully actuated servicer spacecraft.

Designing a joint-space potential in the nullspace, rather than a Cartesian potential on the base, offers three key benefits. First, it indirectly stabilizes the base pose relative to the client. Second, it maintains a desirable manipulator pose for all joints of the redundant manipulator while stabilizing the base. Third, it ensures the convergence of the desired pose in the nullspace unlike the Cartesian potential on the base that can converge to a local minimum when the manipulator Jacobian drops rank (see Section 3.3.2). Stabilizing the servicer in the nullspace of the fully-actuated end-effector also decouples interaction forces at the grasp interface, separating client stabilization from manipulator stabilization.

Furthermore, a control strategy was proposed for the post-stabilization phase using a servicer satellite equipped with reaction wheels. This control strategy is designed for operations requiring strict attitude pointing, such as tasks under ground observation. Unlike the previous stabilization approach, the primary task shifts from the end-effector to the base attitude, while the joint-space potential remains in the nullspace as previously discussed. Since attitude control requires only 3-DoF, compared to the 6-DoF needed for end-effector control, reaction wheels can effectively complement manipulator torques to achieve the desired arm reconfiguration without disturbing the attitude. This approach leverages the redundancy provided by the reaction wheels' rotational degrees of freedom, enabling manipulator reconfiguration within the null space of the servicer base attitude.

The effectiveness of the post-grasp stabilization controller was demonstrated in a post-grasp scenario involving a client spinning at an initial velocity of 10 deg/s, using a servicer equipped with a 7-DoF manipulator. Joint convergence was achieved even as the manipulator arm approached a kinematically singular configuration. As the end-effector's nullspace projector was shown to be independent of the client parameters (see (3.3)), the controller demonstrated robustness to significant client parameter uncertainties given the couplings in the Coriolis terms and the computation of interaction forces (see Figure 3.13).

The effectiveness of the post-stabilization controller was demonstrated in a post-grasp scenario involving a servicer-client system with zero momentum. Validation results show the controller achieving manipulator reconfiguration while approaching a kinematic singularity of the manipulator arm. A variation of the damping torques was used to prevent the reaction wheels from reaching speed limits using a weighting function dependent on the wheel speed. In summary, the control strategies presented in this chapter demonstrate how to design a singularity-free two-level task hierarchy for an actuated floating-base with a manipulator during the post-grasp phase, while incorporating constraints.

CHAPTER 4

UNIFIED CONTROL FRAMEWORK FOR PRE- AND POST-GRASP PHASES

In this chapter, the control methodology developed in Chapter 3 is extended to focus not solely on the post-grasp phase but to create a unified framework that transitions from the pre-grasp or approach phase, through the grasping event, and into the post-grasp stabilization phase. Since the autonomous part of the robotic capture sequence begins with the approach phase and extends through to post-grasp stabilization, the unification is useful to allow a smooth transition of control between the phases. Switching from one control scheme to another between phases can lead to spikes in control inputs, therefore, a unique control framework allows smooth modification of control parameters, easing implementation and reducing energy injection due to control switching.

The *approach* phase or pre-grasp phase is defined as the phase from where the motion towards capture/grasp is initiated with the client in the close vicinity of the servicing manipulator's workspace (as in Figure 4.1). The end of the approach phase is the *grasp phase* and following the capture we enter the *post-grasp* stabilization phase. Stabilization refers to the damping of the client's momentum post-capture. Against this background, a unified control framework that encompasses the approach, grasp, and post-grasp phases is proposed for an orbital manipulator. The controller is structured hierarchically to address the specific requirements of each phase.

The structure of the chapter is as follows. Section 4.1 provides background on combined control methods for capture and post-capture, and highlights the contributions. Section 4.2 describes the mission scenario and its challenges, and proposes the unified control strategy for the approach phase to post-grasp phase. Section 4.3 presents the design of the unified controller for the proposed strategies in the approach phase and post-grasp phase. Section 4.4 presents the results of simulation and experiment performed on the HIL facility, OOS-Sim, at DLR [A+15] (see Figure 4.1). Section 4.5 discusses the benefits of unified control and gives perspective on mission implementation.

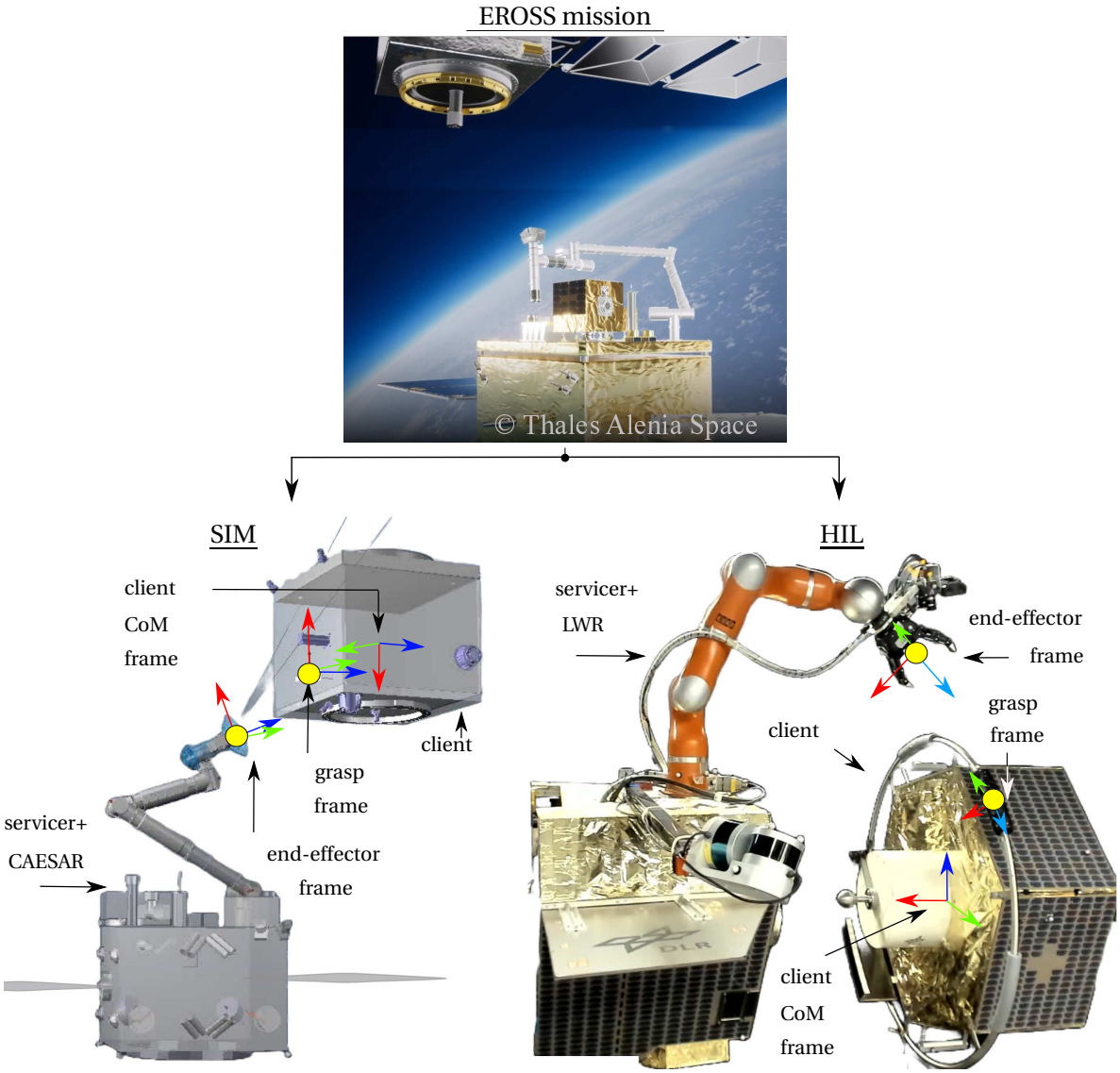

Figure 4.1: Simulation (SIM) and hardware-in-the-loop (HIL) setup with relevant frames (RGB≡XYZ) used for the analysis/experiments. Both setups show a servicer satellite equipped with a manipulator (CAESAR/LWR) and a client satellite with a grasping interface.

4.1 Relevant work and contributions

Robotic solutions for on-orbit servicing (OOS) tasks have been demonstrated in recent mission studies, including the e.Deorbit and DEOS missions [HCT+19, RMNL11], the COMRADE project [CSS+20], and a comprehensive survey on space robotics [PAML21b]. Defunct satellites typically retain a residual spin velocity, such as 1 deg/s as reported in [J+18], which results in momentum transfer to the servicer during capture. Consequently, a post-grasp stabilization strategy is necessary prior to conducting servicing operations [CSS+20]. The primary challenge in the post-grasp

phase is to limit interaction forces at the manipulator's end-effector interface. This limitation is essential to ensure gentle momentum transfer [PAML21b, Agh20] and to prevent mechanical damage during stabilization [GLdR19, M$^+$15, OANY11]. While methods, such as those described in [S$^+$18, GLdR19, OANY11], utilize force/torque measurements for direct force control, the QP optimization presented in Section 3.4 shall be further incorporated into the unified control framework from approach to post-grasp phase.

The effectiveness of coordinated control, which involves managing both manipulator and base motion, for the approach phase of space robots has been demonstrated in several studies (see [J$^+$16, H$^+$16, DS$^+$19]; for comprehensive reviews, refer to [FAMPU14, PAML21b, AZ24]). Coordinated control of the manipulator and spacecraft enhances the flexibility of orbital servicing operations [DP93, MP07]. Control strategies for multi-arm orbital manipulators during approach and capture phases have been developed [PM94]. The work of [GGAS17] decouples the internal dynamics of the manipulator and reaction wheels from the external center-of-mass motion, coordinating thrusters for external motion and joint motors and reaction wheels for internal motion. The strategy in [MBDSO21] proposes a shared control that integrates teleoperation and autonomous control to achieve a primary task at the end-effector and a secondary task at the base. In [SBR22], the approach of a servicer tangential to the grasping point trajectory is analyzed.

Combined control methods applied to the approach phase and capture have been studied in some works. Robust control methods are used in [BPB$^+$24] to develop a combined control approach based on extensions of the computed torque controller, to manage the uncertain, nonlinear dynamics of the system during both the capture and post-capture phases. Two sequential submanoeuvres—a precapturing manoeuvre and a postcapturing manoeuvre—using a single optimal control framework that enables real-time switching is studied in [Agh23]. A cascaded position-velocity controller is presented in [BST$^+$17] for translation that can be used for both fine position control during the robotic capture phase and velocity control during phases like de-orbiting. Two control strategies are presented in [GP15] for use in the approaching and post-grasping phases, with the first focusing on flexibility compensation applied to the robotic arm joints and the second relegating the compensation task to the base platform thrusters. A dual-arm control framework is presented in [YXHL19] where virtual base reactionless control is used for pre-capture, dual-arm hybrid force control for contact and post-capture phase.

The above works do not directly allow a prioritization of control objectives, and do not address the optimal distribution of actuation between thrusters and reaction wheels. Therefore, a unified control strategy that can tackle multiple objectives with a hierarchical prioritization is needed to fulfill the mission objectives of each phase is proposed. Further, complementing thrusters with reaction wheels presents a pragmatic solution to minimize thrust utilization in the approach phase and partially dump and transfer momentum incurred during the grasp phase.

Contributions

This chapter proposes a unified coordinated control strategy for both the approach-to-grasp and post-grasp phases, utilizing a hierarchical control framework based on nullspace projections. While Chapter 3 focused exclusively on the post-grasp phase with a regulation controller, the present work unifies control across the approach, contact, and post-grasp phases through the design of a tracking controller. In Chapter 3, a controller employing only thrusters was developed for the post-grasp phase to dissipate momentum while limiting applied forces. In contrast, the current approach leverages the redundant degrees of freedom (DoF) provided by the servicer's reaction wheels to conserve thruster energy during the approach phase and to supplement thruster limitations in the post-grasp phase. This is achieved by adapting the optimization-based algorithm from [HS87] to perform torque redistribution in nullspace coordinates rather than generalized coordinates, thereby reducing the optimization problem to only the redundant DoF. The post-grasp stabilization task is formulated to avoid influencing interaction forces by exploiting the end-effector's nullspace. The contributions of this work are summarized as follows:

- A control framework which allows the inclusion of constraints through quadratic-programming (QP) based adaptations within the nullspace projection-based control paradigm.
- A unified controller using the above framework, for the approach phase and post-grasp phase, that respects multiple space mission constraints. In addition to limiting the interaction forces at the manipulator's end-effector, thruster limits are tackled through redistribution of reaction wheel torques within the nullspace.
- Experimental validation on a hardware-in-the-loop robotic facility.

This chapter is based on the work published in [VDSDO25], which was a finalist of the *Best Paper Award* among papers published in 2025 in the IEEE/ASME Transactions on Mechatronics (TMECH).

4.2 Unified control strategy

The scenario under consideration involves the approach and capture of a client satellite that spins along its major axis using an orbital manipulator. In this context, joint limits, manipulator singularities, or undesirable base displacement [SB08], [MB17] may compromise both the approach-to-grasp and post-grasp stabilization phases, potentially resulting in mission failure. This issue is demonstrated through simulation and hardware analysis as illustrated in Figure 4.2. Employing a free-floating (unactuated base) strategy with a spinning satellite can cause the manipulator arm to lose manipulability during the approach phase (Figure 4.2 left) and may lead to base collision with the client during the post-grasp phase (Figure 4.2 right).

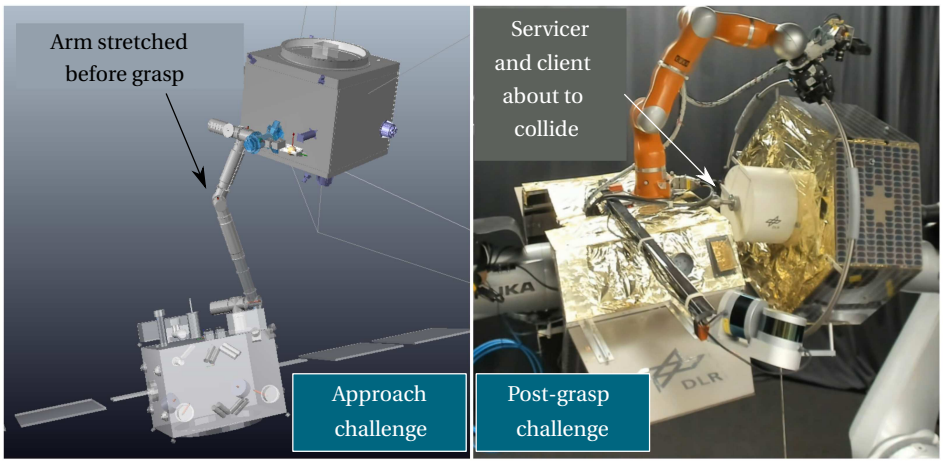

Figure 4.2: *Problem statement* – (left) arm with low manipulability before approaching grasp, (right) servicer and client in an unsafe configuration during post-grasp stabilization.

To address these challenges, a free-flying (actuated base) control strategy during the approach phase may be implemented, incorporating two Cartesian tasks: one at the end-effector for grasping and another at the base for configuration safety. However, for redundant manipulators utilizing nullspace-based potentials, this approach does not always yield an optimal manipulator configuration (see discussion in Section 3.3.2). An alternative is to assign a Cartesian task to the end-effector and a secondary task to the joint pose within the nullspace. The desired joint pose can be selected to enhance manipulability and satisfy workspace constraints, such as joint limits and self-collision avoidance [X$^+$20, L$^+$18].

The challenge of configuration safety is also relevant in the post-grasp phase. To mitigate the risk of collision described in Figure 4.2 right, applying a potential to the joints or base in parallel with the Cartesian potential at the end-effector results in increased interaction forces at the grasp interface of the captured client. High interaction forces at the grasp interface must be avoided [GLdR19, OANY11]. To address this, the secondary potential is applied in the end-effector's nullspace, effectively isolating the interaction forces from the configuration task. Specifying a particular manipulator configuration in the nullspace ensures that the servicer's base remains at a safe distance from the client. Additionally, the interaction forces arising from the Cartesian stabilization task at the end-effector are explicitly limited by augmenting the controller with a quadratic programming (QP)-based algorithm.

Furthermore, consideration of thruster limitations is a critical requirement for space missions. This challenge is addressed by employing reaction wheels to complement thrusters and by designing a QP-based optimal torque distribution strategy for each operational phase.

Based on these considerations, Table 4.1 summarizes the task hierarchy corresponding to the proposed objectives for the controller during the approach and post-grasp phases. During the approach phase, the strategy is to track the Cartesian pose of the grasp point on the client while si-

Table 4.1: *Proposed strategy* – for unification of task hierarchy for proposed control objectives of pre- and post-grasp phases in decreasing order of priority.

Left: **Approach phase**	Middle: **Grasp phase**	Right: **Post-grasp phase**

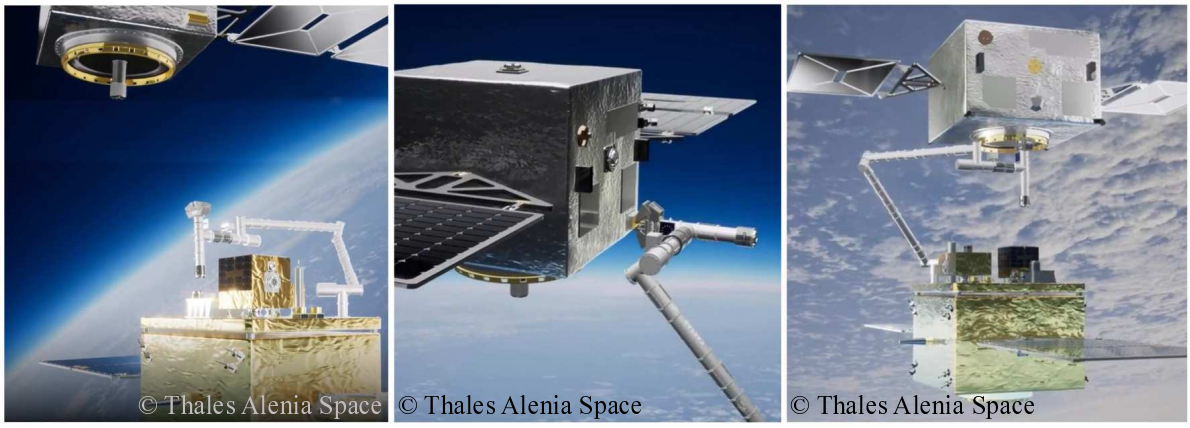

Task (subsystem)	**Approach-to-grasp phase**	**Post-grasp phase**
T1 (end-effector)	Track client grasping point with end-effector	Stabilize client while limiting interaction forces at end-effector
T2 (manipulator joints)	Follow joint trajectory for desirable pose at grasp	Damp out joint velocities and reach a safe configuration
T3 (reaction wheels)	Use reaction wheels to minimize thruster actuation	Dissipate gained external momentum with thruster actuation

multaneously following a joint-space trajectory in the nullspace to achieve an optimal servicer pose for grasping. In the post-grasp phase, the controller stabilizes the client with limited interaction forces and guides the servicer to a safe configuration relative to the client. The unified controller reallocates torques between thrusters and reaction wheels to conserve thruster energy during the approach phase and to minimize external momentum in the post-grasp phase.

Compared to the control strategy seen previously in Table 3.1 the control strategy in Table 4.1 extends the post-grasp strategy to a third hierarchy T3 to accommodate reaction wheels, while also unifying the task hierarchy to meet the objectives of the approach phase. The tasks defined in Table 4.1 will thus allow a safe approach and capture of a spinning satellite while tackling the problems in Figure 4.2.

4.3 Unified control framework

This section details the design of the unified control framework, outlining the tasks required to achieve the objectives of both the approach and post-grasp phases (see Table 4.1). Initially, a nominal controller, defined as one without constraints, is developed. Subsequently, its convergence prop-

erties are analyzed, and the controller is then adapted to incorporate relevant constraints.

The objectives of both the approach and post-grasp phases are defined by a primary task and several subtasks (see Table 4.1). Consequently, a hierarchical task-based controller is employed, where tasks are fulfilled simultaneously rather than sequentially. The control strategy incorporates dynamic decoupling through nullspace projections. The unified control design for both phases assigns the primary Cartesian task to the end-effector for client tracking and subsequent stabilization. The secondary task is formulated at the joint level of the manipulator to ensure manipulability and, later, configuration safety of the base. For floating robots, the Cartesian and joint tasks are not conflicting, as base actuation enables simultaneous positioning of the end-effector and joint angles, unlike fixed-base robots. A third task leverages the redundancy in base actuation to redistribute control between thrusters and reaction wheels.

The steps ahead for designing the unified controller for the approach phase and post-grasp phase are summarized below:

i Define task coordinates, followed by nullspace-projected coordinates required to design the decoupled controller.

ii Hierarchically decouple dynamics in nullspace-projected task coordinates to design a nominal impedance controller.

iii Adapt the nominal control inputs in the nullspace-projected task coordinates to account for constraints.

The controller is designed for a servicer spacecraft equipped with r reaction wheels and a n-degree-of-freedom (DoF) manipulator. The client is modeled as an unactuated floating satellite with known dynamic parameters (as in [Agh09]). At the start of the approach phase, the servicer's initial velocity is assumed to be zero. The dynamics of the servicer and client are described by (2.7) and (2.8), respectively, with the servicer dynamics incorporating reaction wheels as specified in (2.6). The term $\boldsymbol{F}_c \in \mathbb{R}^6$ in (2.7) and (2.8) represents the external wrench at the end-effector, corresponding to the constraint interaction force during the capture phase. For the controller in the approach phase, the dynamics in (2.7) are used with $\boldsymbol{F}_c = \boldsymbol{0}$. The structure of the inertia matrix in (2.6) will be utilized in the analysis in Section 4.3.4 to redistribute control between thrusters and reaction wheels. Notably, this inertia matrix structure also applies to the post-grasp phase dynamics in (2.10) for the combined servicer-client system.

4.3.1 Definition of coordinates

The objectives of the approach phase and post-grasp phase are summarized in Table 4.1 as tasks to be achieved hierarchically. These can be defined by their task coordinates $\boldsymbol{V}_T$, and corresponding

task Jacobian matrices $\boldsymbol{J}_T$ as

$$\text{(4.1)} \qquad \text{Task coordinates}: \qquad \begin{matrix}\text{T1:}\\ \text{T2:}\\ \text{T3:}\end{matrix} \underbrace{\begin{bmatrix}\boldsymbol{v}_e\\ \dot{\boldsymbol{q}}\\ \dot{\boldsymbol{r}}\end{bmatrix}}_{\boldsymbol{V}_T} = \underbrace{\begin{bmatrix}\boldsymbol{J}_e\\ \boldsymbol{J}_q\\ \boldsymbol{J}_r\end{bmatrix}}_{\boldsymbol{J}_T} \boldsymbol{V}_s \quad \text{with} \quad \underbrace{\begin{bmatrix}\boldsymbol{J}_e\\ \boldsymbol{J}_q\\ \boldsymbol{J}_r\end{bmatrix}}_{\boldsymbol{J}_T} = \begin{bmatrix}\boldsymbol{J}_b & \boldsymbol{J}_m & \boldsymbol{0}\\ \boldsymbol{0} & \boldsymbol{I}_n & \boldsymbol{0}\\ \boldsymbol{0} & \boldsymbol{0} & \boldsymbol{I}_r\end{bmatrix},$$

where, $\boldsymbol{I}_\bullet$ is a square identity matrix. Notice here that the end-effector Jacobian of the servicer $\boldsymbol{J}_e = [\boldsymbol{J}_b \;\; \boldsymbol{J}_m \;\; \boldsymbol{0}] \in \mathbb{R}^{6\times(6+n+r)}$ maps the servicer states including reaction wheels $\boldsymbol{V}_s = \begin{bmatrix}\boldsymbol{v}_b^T & \dot{\boldsymbol{q}}^T & \dot{\boldsymbol{r}}^T\end{bmatrix}^T \in \mathbb{R}^{6+n+r}$ to the end-effector Cartesian velocity $\boldsymbol{v}_e \in \mathbb{R}^6$. The $\boldsymbol{0}$ in $\boldsymbol{J}_e$ indicates that the reaction wheels are in a separate kinematic chain from the arm. The base Jacobian $\boldsymbol{J}_b \in \mathbb{R}^{6\times6}$ is an invertible adjoint transformation, and $\boldsymbol{J}_m \in \mathbb{R}^{6\times(n+r)}$ is the manipulator Jacobian. The nullspace bases $\boldsymbol{N}_\bullet$ can be deduced[1] from observing the structure in (4.1) as

$$\text{(4.2)} \qquad \text{Nullspace bases}: \qquad \begin{matrix}\text{T2: } \boldsymbol{N}_1^T\\ \text{T3: } \boldsymbol{N}_2^T\end{matrix} = \begin{bmatrix}-\boldsymbol{J}_m^T\boldsymbol{J}_b^{-T} & \boldsymbol{I}_n & \boldsymbol{0}\\ \boldsymbol{0} & \boldsymbol{0} & \boldsymbol{I}_r\end{bmatrix} \text{ s.t.} \begin{matrix}\boldsymbol{J}_e\boldsymbol{N}_1 = \boldsymbol{0}\\ \begin{bmatrix}\boldsymbol{J}_e\\ \boldsymbol{J}_q\end{bmatrix}\boldsymbol{N}_2 = \boldsymbol{0}.\end{matrix}$$

The matrix $\boldsymbol{N}_1$ is the nullspace basis for the end-effector Jacobian, and $\boldsymbol{N}_2$ for the end-effector and joints' task Jacobians combined. Note that all nullspaces $\boldsymbol{N}_\bullet^T$ defined in (4.2) have full row-rank, evident from the identity matrices therein. This means they are well-defined and independent of kinematic singularities of the manipulator related to $\boldsymbol{J}_m$ appearing in (4.2). Redefining the task coordinates $\boldsymbol{V}_T$ in (4.1) using (4.2), as projected coordinates $\boldsymbol{V}_N$ with the extended Jacobian matrix $\boldsymbol{J}_N$ (see [DOAS15],[DO20] for details) gives

$$\text{(4.3)} \qquad \begin{matrix}\text{Augmented}\\ \text{task coordinates}:\end{matrix} \qquad \begin{matrix}\text{T1:}\\ \text{T2:}\\ \text{T3:}\end{matrix} \underbrace{\begin{bmatrix}\boldsymbol{v}_e\\ \boldsymbol{v}_m\\ \boldsymbol{v}_r\end{bmatrix}}_{\boldsymbol{V}_N} = \underbrace{\begin{bmatrix}\boldsymbol{J}_e\\ \bar{\boldsymbol{J}}_q\\ \bar{\boldsymbol{J}}_r\end{bmatrix}}_{\boldsymbol{J}_N} \boldsymbol{V}_s \;\; \text{where,} \;\; \begin{bmatrix}\bar{\boldsymbol{J}}_q\\ \bar{\boldsymbol{J}}_r\end{bmatrix} = \begin{bmatrix}\boldsymbol{J}_q\boldsymbol{N}_1\boldsymbol{N}_1^{M\dagger}\\ \boldsymbol{J}_r\boldsymbol{N}_2\boldsymbol{N}_2^{M\dagger}\end{bmatrix}$$
$$\boldsymbol{J}_N^{-1} = \begin{bmatrix}\boldsymbol{J}_e^{M+} & \bar{\boldsymbol{J}}_q^{\bar{M}+} & \bar{\boldsymbol{J}}_r^{\bar{M}+}\end{bmatrix}.$$

It is worth pointing out that the nullspace projection matrix $\boldsymbol{N}_\bullet\boldsymbol{N}_\bullet^{M\dagger}$ is equivalent to

$$\boldsymbol{N}_\bullet\boldsymbol{N}_\bullet^{M\dagger} = \boldsymbol{I} - \boldsymbol{J}_\bullet^{M\dagger}\boldsymbol{J}_\bullet$$

which is a common form of the nullspace projection [Kha95], where,

$$\text{(4.4)} \qquad \begin{aligned}\boldsymbol{N}_\bullet^{M\dagger} &= (\boldsymbol{N}_\bullet^T\boldsymbol{M}_s\boldsymbol{N}_\bullet)^{-1}\boldsymbol{N}_\bullet^T\boldsymbol{M}_s,\\ \boldsymbol{J}_\bullet^{M\dagger} &= \boldsymbol{M}_s^{-1}\boldsymbol{J}_\bullet^T(\boldsymbol{J}_\bullet\boldsymbol{M}_s^{-1}\boldsymbol{J}_\bullet^T)^{-1}.\end{aligned}$$

Further note that regardless of the approach phase or post-grasp phase, the dynamically consistent nullspaces depend only on $\boldsymbol{M}_s$, and not on $\boldsymbol{M}_c$. This can be shown since $\boldsymbol{N}_\bullet^T\boldsymbol{M}_{sc} = \boldsymbol{N}_\bullet^T\boldsymbol{M}_s$ in (2.10)

[1] For the general case of a task Jacobian whose nullspace basis may not be deducible analytically, it may be computed using methods such as [CW93]. Alternatively, a method based on eigen decomposition is given in Appendix C.

using the property $\boldsymbol{N}_{\bullet}^{T}\boldsymbol{J}_{e}^{T}=\boldsymbol{0}$. This is consistent with the load-independence property of nullspaces [FK97]. Thus, (4.3) implies that $\boldsymbol{v}_m$ for task T2 is defined in the nullspace of $\boldsymbol{v}_e$, while $\boldsymbol{v}_r$ for task T3 is in the nullspace of $\boldsymbol{v}_e$ and $\boldsymbol{v}_m$.

Remark: It is worth comparing the nullspace coordinate $\boldsymbol{v}_m$ in (4.3) versus the nullspace coordinate $\boldsymbol{v}_n$ in (3.1) in Chapter 3, both of which are designed for reconfiguring the manipulator in the nullspace of the end-effector.

$$\text{In (3.1)} : \boldsymbol{v}_n = \boldsymbol{N}_e^{M\dagger}\boldsymbol{V}_s$$
$$\text{In (4.3)} : \boldsymbol{v}_m = \boldsymbol{J}_q\boldsymbol{N}_1\boldsymbol{N}_1^{M\dagger}\boldsymbol{V}_s$$

In (4.3), the nullspace is partitioned specifically to address the manipulator joint task via the manipulator task Jacobian $\boldsymbol{J}_q$. Whereas, in (3.1) the nullspace coordinate could be used for applying an impedance on either the manipulator or base (see discussion in Section 3.3.2). Further, (3.1) only considered a two-level hierarchy, thus, not necessitating a partitioning of the nullspace. In (4.3) such a partitioning of the nullspace $\boldsymbol{v}_m$ for the manipulator task, allows for a third-level in the nullspace hierarchy $\boldsymbol{v}_r$ for the reaction wheels. Incidentally, the last nullspace coordinate $\boldsymbol{v}_r = \boldsymbol{J}_r\boldsymbol{N}_2\boldsymbol{N}_2^{M\dagger}\boldsymbol{V}_s$ in the hierarchy in (4.3) is equivalent to $\boldsymbol{v}_r = \boldsymbol{N}_2^{M\dagger}\boldsymbol{V}_s$ (as $\boldsymbol{J}_r\boldsymbol{N}_2 = \boldsymbol{I}$), making it analogous in definition to the last hierarchy level in (3.1).

4.3.2 Dynamic decoupling and nominal control design

Designing the control inputs in the nullspace-projected coordinates in (4.3) will ensure the desired prioritization. In order to do this, the dynamics in (2.7) for approach phase (or (2.10) for post-grasp) are transformed, using (4.3) to get:

Inertially-decoupled nullspace dynamics :

$$\underbrace{\begin{bmatrix}\boldsymbol{\Lambda}_{ee} & \boldsymbol{0} & \boldsymbol{0}\\ \boldsymbol{0} & \boldsymbol{\Lambda}_{mm} & \boldsymbol{0}\\ \boldsymbol{0} & \boldsymbol{0} & \boldsymbol{\Lambda}_{rr}\end{bmatrix}}_{\boldsymbol{\Lambda}}\underbrace{\begin{bmatrix}\dot{\boldsymbol{v}}_e\\ \dot{\boldsymbol{v}}_m\\ \dot{\boldsymbol{v}}_r\end{bmatrix}}_{\dot{\boldsymbol{V}}_N} + \underbrace{\begin{bmatrix}\boldsymbol{\mu}_{ee} & \boldsymbol{\mu}_{em} & \boldsymbol{\mu}_{er}\\ \boldsymbol{\mu}_{me} & \boldsymbol{\mu}_{mm} & \boldsymbol{\mu}_{mr}\\ \boldsymbol{\mu}_{re} & \boldsymbol{\mu}_{rm} & \boldsymbol{\mu}_{rr}\end{bmatrix}}_{\boldsymbol{\mu}}\underbrace{\begin{bmatrix}\boldsymbol{v}_e\\ \boldsymbol{v}_m\\ \boldsymbol{v}_r\end{bmatrix}}_{\boldsymbol{V}_N} = \underbrace{\begin{bmatrix}\boldsymbol{F}_e\\ \boldsymbol{F}_m\\ \boldsymbol{F}_r\end{bmatrix}}_{\boldsymbol{F}},$$

$$\boldsymbol{\Lambda} = \boldsymbol{J}_N^{-T}\boldsymbol{M}_{\bullet}\boldsymbol{J}_N^{-1}, \qquad \boldsymbol{F} = \boldsymbol{J}_N^{-T}\boldsymbol{\Gamma}$$
$$\boldsymbol{\mu} = \boldsymbol{J}_N^{-T}\boldsymbol{M}_{\bullet}\frac{d}{dt}(\boldsymbol{J}_N^{-1}) + \boldsymbol{J}_N^{-T}\boldsymbol{C}_{\bullet}\boldsymbol{J}_N^{-1}. \tag{4.5}$$

Here $\bullet$ adapts to the dynamic parameters of the approach phase and post-grasp phase in (2.7) and (2.10), respectively. It can be seen that the dynamics in nullspace-projected coordinates in (4.5), although inertially decoupled, still have Coriolis couplings. To ensure the decoupling of tasks, the Coriolis couplings are first compensated by choosing

$$\boldsymbol{F} = \boldsymbol{F}' + (\boldsymbol{\mu} - \bar{\boldsymbol{\mu}})\boldsymbol{V}_N, \tag{4.6}$$

with, $\bar{\boldsymbol{\mu}} = \text{diag}(\boldsymbol{\mu}_{ee}, \boldsymbol{\mu}_{mm}, \boldsymbol{\mu}_{rr})$. Note that, compensating purely the Coriolis cross-coupling terms as in (4.6) is a power-preserving action [OKN08]. The remaining control input to be designed is $\boldsymbol{F}'$. Then, (4.6) in closed loop with (4.5) results in the following dynamics:

$$\boldsymbol{\Lambda}\dot{\boldsymbol{V}}_N + \bar{\boldsymbol{\mu}}\boldsymbol{V}_N = \boldsymbol{F}' \,. \tag{4.7}$$

To design a control input for tracking a desired time-dependent task trajectory in the nullspace, the projected velocities, $\boldsymbol{V}_N$ are substituted by task velocities, $\boldsymbol{V}_T$ in (4.7) using the relation $\boldsymbol{V}_N = \boldsymbol{J}_N\boldsymbol{J}_T^{-1}\boldsymbol{V}_T$. This results in the following dynamics:

$$\text{Nullspace-projected task dynamics :} \quad \underbrace{\begin{bmatrix} \boldsymbol{\Lambda}_{ee} & \boldsymbol{0} & \boldsymbol{0} \\ \boldsymbol{\Lambda}_{me} & \boldsymbol{\Lambda}_{mm} & \boldsymbol{0} \\ \boldsymbol{\Lambda}_{re} & \boldsymbol{\Lambda}_{rm} & \boldsymbol{\Lambda}_{rr} \end{bmatrix}}_{\boldsymbol{\Lambda}'} \underbrace{\begin{bmatrix} \dot{\boldsymbol{v}}_e \\ \ddot{\boldsymbol{q}} \\ \ddot{\boldsymbol{r}} \end{bmatrix}}_{\dot{\boldsymbol{V}}_T} + \underbrace{\begin{bmatrix} \boldsymbol{\mu}_{ee} & \boldsymbol{0} & \boldsymbol{0} \\ \boldsymbol{\mu}'_{me} & \boldsymbol{\mu}_{mm} & \boldsymbol{0} \\ \boldsymbol{\mu}'_{re} & \boldsymbol{\mu}'_{rm} & \boldsymbol{\mu}_{rr} \end{bmatrix}}_{\boldsymbol{\mu}'} \underbrace{\begin{bmatrix} \boldsymbol{v}_e \\ \dot{\boldsymbol{q}} \\ \dot{\boldsymbol{r}} \end{bmatrix}}_{\boldsymbol{V}_T} = \underbrace{\begin{bmatrix} \boldsymbol{F}'_e \\ \boldsymbol{F}'_m \\ \boldsymbol{F}'_r \end{bmatrix}}_{\boldsymbol{F}'}, \tag{4.8}$$

$$\text{where,} \qquad \boldsymbol{\Lambda}' = \boldsymbol{\Lambda}\boldsymbol{J}_N\boldsymbol{J}_T^{-1}, \qquad\qquad \boldsymbol{\mu}' = \bar{\boldsymbol{\mu}}\boldsymbol{J}_N\boldsymbol{J}_T^{-1} + \boldsymbol{\Lambda}\frac{d}{dt}(\boldsymbol{J}_N\boldsymbol{J}_T^{-1}).$$

The sequential transformation to projected task coordinates $\boldsymbol{V}_N$ in (4.5), followed by substitution with the original task coordinates $\boldsymbol{V}_T$ in (4.8), reveals how the original task velocities influence the nullspace-projected dynamics [DO20]. While the dynamics in projected coordinates $\boldsymbol{V}_N$ in (4.7) are inertially decoupled, the dynamics expressed in task coordinates $\boldsymbol{V}_T$ in (4.8) exhibit a top-down coupling, as indicated by the lower-triangular structure of the dynamics in (4.8). Thus, it can be seen that the lower-priority tasks do not influence the higher-priority tasks. This property is leveraged in the proposed control design to fulfill the objectives outlined in Table 4.1.

The dynamics in (4.8) can be used to design a tracking controller for the desired task trajectories in the nullspace. A nominal control $\boldsymbol{F}'$ is designed in nullspace-projected task coordinates as follows,

$$\text{Nullspace-projected task control :} \quad \underbrace{\begin{bmatrix} \boldsymbol{F}'_e \\ \boldsymbol{F}'_m \\ \boldsymbol{F}'_r \end{bmatrix}}_{\boldsymbol{F}'} = \boldsymbol{\Lambda}' \begin{bmatrix} \dot{\boldsymbol{v}}_e{}^d \\ \ddot{\boldsymbol{q}}^d \\ \boldsymbol{0} \end{bmatrix} + \boldsymbol{\mu}' \begin{bmatrix} \boldsymbol{v}_e^d \\ \dot{\boldsymbol{q}}^d \\ \boldsymbol{0} \end{bmatrix} + \begin{bmatrix} \boldsymbol{E}\boldsymbol{K}_{Pe}\Delta\boldsymbol{x}_e + \boldsymbol{K}_{De}\Delta\boldsymbol{v}_e \\ \boldsymbol{K}_{Pm}\Delta\boldsymbol{q} + \boldsymbol{K}_{Dm}\Delta\dot{\boldsymbol{q}} \\ \boldsymbol{0} \end{bmatrix} \tag{4.9}$$

Here $\boldsymbol{v}_e^d$ is the desired Cartesian end-effector velocity and $\Delta\boldsymbol{v}_e = \boldsymbol{v}_e^d - \boldsymbol{v}_e$ is the velocity error. The end-effector's pose error is $\Delta\boldsymbol{x}_e = \begin{bmatrix} \Delta\boldsymbol{x}^T & \Delta\boldsymbol{\epsilon}^T \end{bmatrix}^T \in \mathbb{R}^6$ with position error, $\Delta\boldsymbol{x}$ and the vector part of the quaternion error, $\Delta\boldsymbol{\epsilon}$. The matrix $\boldsymbol{E} = \text{diag}(\boldsymbol{I}_3, \Delta\eta\boldsymbol{I}_3 + \boldsymbol{S}(\Delta\boldsymbol{\epsilon}))$, where, $\Delta\eta$ is the scalar part of the quaternion error and $\boldsymbol{S}(\cdot)$ is the skew-symmetric cross-product operator [CNSV99]. Further, $\boldsymbol{q}^d, \dot{\boldsymbol{q}}^d$ are the desired joint position and velocity, $\Delta\boldsymbol{q} = \boldsymbol{q}^d - \boldsymbol{q}$ and $\Delta\dot{\boldsymbol{q}} = \dot{\boldsymbol{q}}^d - \dot{\boldsymbol{q}}$. The proportional-derivative gains for the end-effector and joints are $\boldsymbol{K}_{Pe}, \boldsymbol{K}_{De} \in \mathbb{R}^{6\times6}$ and $\boldsymbol{K}_{Pm}, \boldsymbol{K}_{Dm} \in \mathbb{R}^{n\times n}$, respectively.

Thus, the control $\boldsymbol{F}_e'$ in (4.10) tracks an end-effector trajectory, while $\boldsymbol{F}_m'$ tracks a joint-level trajectory in accordance with the objectives defined in Table 4.1 for T1 and T2. Notice that for the nominal control in (4.9), $\boldsymbol{F}_r'$ does not track an explicit trajectory because the desired task (T3 in Table 4.1) does not have position tracking requirements. The convergence implications will be discussed in the next section.

The corresponding nominal control $\boldsymbol{\Gamma}$ input to the servicer in (2.7) and (2.10) is obtained from the Jacobian-transpose relation in (4.5), expanded using (4.3) as

(4.10) Control in actuator coordinates :
$$\boldsymbol{\Gamma} = \underbrace{\boldsymbol{J}_e^T \boldsymbol{F}_e'}_{\boldsymbol{\Gamma}_{\mathrm{T1}}} + \underbrace{\bar{\boldsymbol{J}}_q^T \boldsymbol{F}_m'}_{\boldsymbol{\Gamma}_{\mathrm{T2}}} + \underbrace{\bar{\boldsymbol{J}}_r^T \boldsymbol{F}_r'}_{\boldsymbol{\Gamma}_{\mathrm{T3}}} + \boldsymbol{\Gamma}_\mu,$$

where, $\boldsymbol{\Gamma}_\mu = \boldsymbol{J}_N^T(\boldsymbol{\mu} - \bar{\boldsymbol{\mu}})\boldsymbol{V}_N$ is the Coriolis decoupling term and $\boldsymbol{\Gamma}_{\mathrm{T}\bullet}$ are related to the three tasks. This concludes the design of the nominal controller (i.e. excluding constraints) for the approach phase and post-grasp phase.

The block diagram in Figure 4.3 summarizes the sequence of computations for dynamic decoupling starting from (4.1) to obtain the final control input to the system in (4.10). Finally, Figure 4.4 gives a broader overview of the control (4.10) in closed loop with the dynamics (2.7) and (2.10) of the servicer-client system, along with the measured states and desired trajectories. Section 4.3.4 will address the interaction force limit in T1 and actuator limits in T3.

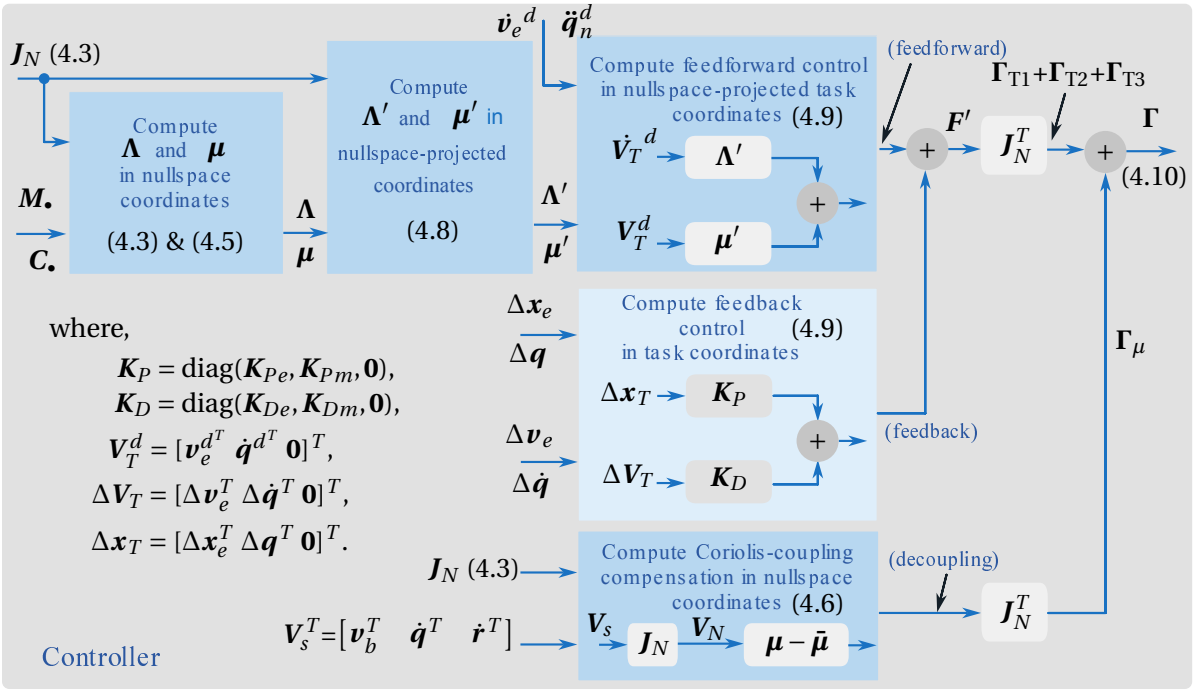

Figure 4.3: *Nominal controller* – block diagram showing the sequence of computations for dynamic decoupling, to arrive at the hierarchical controller in (4.10).

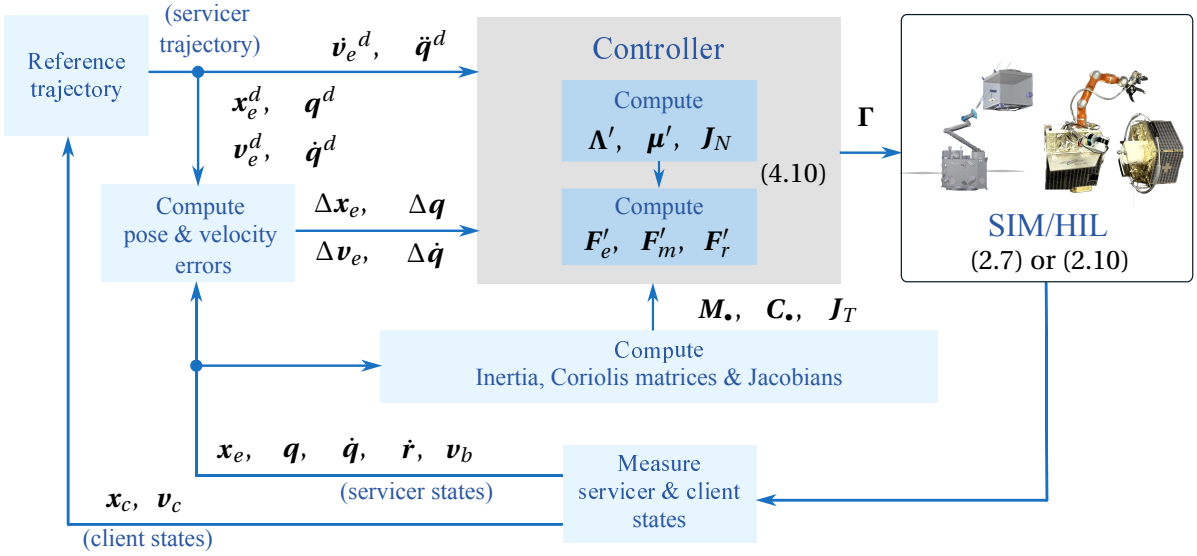

Figure 4.4: *Closed-loop overview* – controller (4.10), detailed in Figure 4.3, in closed loop with the dynamics (2.7) and (2.10) of the servicer-client system.

4.3.3 Stability of the controller

Equation (4.9) indicates that, for tasks T1 and T2, the reaction wheels constitute redundant DoF, i.e. T1 and T2 can be fulfilled even without reaction wheels. Therefore, the convergence analysis is divided into two parts. The first part examines the convergence of the tracking controller for tasks T1 and T2 under the condition that the reaction wheels are not utilized, meaning they are locked and task T3 is omitted. The second part extends the analysis to include the use of reaction wheels and task T3, specifically for the regulation scenario in which the controller operates during the final stabilization phase. This analysis relies on stability theorems for time-varying systems using semi-definite Lyapunov functions [W+08] (refer Section 2.3).

The desired trajectories for all tasks are assumed to be bounded. In the initial stage of the analysis, the reaction wheels are considered locked. The stability analysis follows a bottom-up approach, as described in [DO20]. The semi-definite Lyapunov function V_m is considered for task T2 within the set where the state errors of T1 are zero ($\Delta \boldsymbol{v}_e, \Delta \boldsymbol{x}_e = \boldsymbol{0}$).

$$V_m = \frac{1}{2} \begin{bmatrix} \Delta \dot{\boldsymbol{q}} \\ \Delta \boldsymbol{q} \end{bmatrix}^T \begin{bmatrix} \boldsymbol{\Lambda}_{mm} & \varepsilon_n \boldsymbol{\Lambda}_{mm}^T \\ \varepsilon_n \boldsymbol{\Lambda}_{mm} & \boldsymbol{K}_{Pm} \end{bmatrix} \begin{bmatrix} \Delta \dot{\boldsymbol{q}} \\ \Delta \boldsymbol{q} \end{bmatrix}. \tag{4.11}$$

where, ε_n is a small non-negative scalar. With $\boldsymbol{F}'_m$ in (4.9) and $\varepsilon_n = 0$, $\dot{V}_m = -\Delta \dot{\boldsymbol{q}}^T \boldsymbol{K}_{Dm} \Delta \dot{\boldsymbol{q}}$. This shows boundedness of involved states in the considered set. Given this boundedness, for $\varepsilon_n > 0$, $\dot{V}_m$ results as follows:

$$\dot{V}_m = -\begin{bmatrix} \Delta \dot{\boldsymbol{q}} \\ \Delta \boldsymbol{q} \end{bmatrix}^T \begin{bmatrix} \boldsymbol{K}_{Dm} - \varepsilon_n \boldsymbol{\Lambda}_{mm} & \frac{1}{2}\varepsilon_n (\boldsymbol{K}_{Dm} - \boldsymbol{\mu}_{mm}^T)^T \\ \frac{1}{2}\varepsilon_n (\boldsymbol{K}_{Dm} - \boldsymbol{\mu}_{mm}^T) & \varepsilon_n \boldsymbol{K}_{Pm} \end{bmatrix} \begin{bmatrix} \Delta \dot{\boldsymbol{q}} \\ \Delta \boldsymbol{q} \end{bmatrix}.$$

The negative-definiteness of $\dot{V}_m$ depends on the block matrix being positive-definite. This condition is satisfied when [DO20]

$$\varepsilon_n \boldsymbol{K}_{Pm} \succ \mathbf{0}$$
$$\boldsymbol{K}_{Dm} - \varepsilon_n \left(\boldsymbol{\Lambda}_{mm} + \frac{1}{4} (\boldsymbol{K}_{Dm} - \boldsymbol{\mu}_{mm}^T)^T \boldsymbol{K}_{Pm}^{-1} (\boldsymbol{K}_{Dm} - \boldsymbol{\mu}_{mm}^T) \right) \succ \mathbf{0}$$

The second condition above is the Schur complement of $\varepsilon_n \boldsymbol{K}_{Pm}$. Given the boundedness of $\dot{\boldsymbol{q}}$ obtained from $\dot{V}_m \prec 0$ using $\varepsilon_n = 0$, the matrix $\boldsymbol{\mu}_{mm}$ is concluded to be bounded. Further, given $\boldsymbol{K}_{Pm}$, $\boldsymbol{K}_{Dm}$, $\boldsymbol{\Lambda}_{mm}$ are symmetric, positive-definite and bounded, for a sufficiently small $\varepsilon_n > 0$, the Schur complement is positive-definite, and $\dot{V}_m \prec 0$. This implies the states of T2 are uniformly asymptotically stable in the set where errors of states of T1 are zero.

Further, consider the following semi-definite Lyapunov function V_e for task T1:

$$V_e = \frac{1}{2} \begin{bmatrix} \Delta \boldsymbol{v}_e \\ \Delta \boldsymbol{x}_e \end{bmatrix}^T \begin{bmatrix} \boldsymbol{\Lambda}_{ee} & \varepsilon_e \boldsymbol{\Lambda}_{ee}^T \\ \varepsilon_e \boldsymbol{\Lambda}_{ee} & \boldsymbol{K}_{Pe} \end{bmatrix} \begin{bmatrix} \Delta \boldsymbol{v}_e \\ \Delta \boldsymbol{x}_e \end{bmatrix}. \tag{4.12}$$

where, ε_e is a small non-negative scalar. With $\boldsymbol{F}_e'$ in (4.9) and $\varepsilon_e = 0$, the derivative equals $\dot{V}_e = -\Delta \boldsymbol{v}_e^T \boldsymbol{K}_{De} \Delta \boldsymbol{v}_e$. This shows boundedness of all involved states, cascaded with the boundedness of states in the set where T1 errors are zero. Given boundedness, for a sufficiently small $\varepsilon_e > 0$, $\dot{V}_e$ can be shown to be negative-definite similar to the line of argumentation for $\dot{V}_m$ above. Invoking the stability theorem for time-varying systems using semi-definite Lyapunov functions [W+08], the negative-definiteness of $\dot{V}_e$ and $\dot{V}_m$ allows to conclude the equilibrium $(\Delta \boldsymbol{v}_e, \Delta \boldsymbol{x}_e, \Delta \dot{\boldsymbol{q}}, \Delta \boldsymbol{q} = \mathbf{0})$ to be uniformly asymptotically stable. Note that the convergence of joint errors in task T2 (in the nullspace of the end-effector) is independent of manipulator singularities. This is due to the nullspaces in (4.2) being well-defined for the fully-actuated (6-DoF) base that compensates for any loss of DoF due to singularities (see [VDSO22] for details). The proof of stability here does not imply sequential convergence, rather it is a simultaneous convergence of hierarchical tasks.

In the second stage of the analysis, the reaction wheels are assumed to be unlocked, and task T3 is included. Since task T3 is the lowest in the hierarchy, the candidate Lyapunov function $V_r = \dot{\boldsymbol{r}}^T \boldsymbol{\Lambda}_{rr} \dot{\boldsymbol{r}}$ is considered in the set where the errors of states for T1 and T2 are zero $(\Delta \boldsymbol{v}_e, \Delta \boldsymbol{x}_e, \Delta \dot{\boldsymbol{q}}, \Delta \boldsymbol{q} = \mathbf{0})$. It is important to note that $\boldsymbol{r}$ is not a relevant state of the system, as the angular position of the rotationally symmetric reaction wheels does not influence the inertia in (2.7) or (2.10). Under the regulation scenario for tasks T1 and T2, the nominal $\boldsymbol{F}_r'$ in (4.9) results in $\dot{V}_r = 0$ within the considered set. This shows that the reaction wheels converge to a constant residual velocity in the nullspace at the end of the stabilization phase. This outcome is intentional, as reaction wheels, unlike manipulator links, are actuators that work on the principle of exchanging momentum with the base to generate torques. The wheel velocities are not damped, since damping would require thrusters to balance the control torque requirements of tasks T1 and T2, undermining the purpose of using reaction wheels. In the tracking scenario during the approach phase, trajectories with bounded velocities for tasks T1 and T2 ensure that the reaction wheel velocities remain bounded.

4.3.4 Optimizing nominal controller for constraints

The nominal controller in (4.10) does not guarantee respecting interaction force limits or thruster limits, dictated by space mission requirements. The following sections show how the nominal controller can be adapted to meet these requirements.

Optimizing F_e' for interaction force limits in the post-grasp phase

In Chapter 3 Section 3.4, the influence of the end-effector wrench was deduced step-by-step by investigating each term of the hierarchical control law. We can instead arrive at a similar result in a more direct way by substituting $\boldsymbol{\Gamma}$ from (4.10) into (3.14), which gives us a more direct relation between $\boldsymbol{F}_e'$ and $\boldsymbol{F}_c$ as compared to (3.14).

$$\text{Interaction wrench :} \qquad \boldsymbol{F}_c = (\boldsymbol{I} + \boldsymbol{\Lambda}_{ee}\boldsymbol{\Lambda}_{cc}^{-1})^{-1}\boldsymbol{F}_e' + \boldsymbol{f}(\boldsymbol{V}_s, \boldsymbol{v}_c), \tag{4.13}$$

$$\text{where,} \qquad \boldsymbol{\Lambda}_{cc} = (\boldsymbol{J}_c\boldsymbol{M}_c^{-1}\boldsymbol{J}_c^T)^{-1}, \qquad \boldsymbol{\Lambda}_{ee} = (\boldsymbol{J}_e\boldsymbol{M}_s^{-1}\boldsymbol{J}_e^T)^{-1}.$$

The quantities $\boldsymbol{\Lambda}_{cc}, \boldsymbol{\Lambda}_{ee} \in \mathbb{R}^{6\times 6}$ describe the Cartesian inertia of the client and servicer at the end-effector, respectively. For brevity, the remaining terms in (3.14) arising from Coriolis/centrifugal effects are depicted as $\boldsymbol{f}(\boldsymbol{V}_s, \boldsymbol{v}_c)$ in (4.13). As anticipated, the terms $\boldsymbol{\Gamma}_{\text{T2}}$ and $\boldsymbol{\Gamma}_{\text{T3}}$ from (4.10) have zero influence on $\boldsymbol{F}_c$. This can be proven by plugging in $\boldsymbol{\Gamma}_{\text{T2}}, \boldsymbol{\Gamma}_{\text{T3}}$ in (3.14) and using the property of dynamic consistency, $\boldsymbol{J}_e\boldsymbol{M}_{sc}^{-1}\boldsymbol{N}_{\bullet}^{T_{M\dagger}} = \boldsymbol{0}$. This is because they lie in the dynamically consistent nullspace of the end-effector task. This also demonstrates the advantage of designing the secondary tasks such as the joint reconfiguration in the nullspace, as it has no influence on the interaction forces during stabilization.

Thus, (4.13) indicates that the interaction force $\boldsymbol{F}_c$ is primarily determined by $\boldsymbol{F}_e'$, scaled by the ratio of the Cartesian inertia of the servicer and client at the end-effector. Typically, $\boldsymbol{\Lambda}_{cc} \gg \boldsymbol{\Lambda}_{ee}$, which may appear counter-intuitive because the client satellite is lighter than the servicer (base plus arm). However, $\boldsymbol{\Lambda}_{ee}$ is governed by the manipulability of the arm, specifically the inertia of the arm rather than the base. In contrast, $\boldsymbol{\Lambda}_{cc}$ represents a large inertia at the end-effector due to the client's rigid-body mass, which is generally heavier than the manipulator arm. Consequently, a first-order approximation of (4.13) is $\boldsymbol{F}_c \approx \boldsymbol{F}_e'$, while $\boldsymbol{f}(\boldsymbol{V}_s, \boldsymbol{v}_c)$ can be neglected for slow motions.

Further, stabilization is to be performed as a regulation task to remove the spin of the combined servicer-client system, which implies $\boldsymbol{v}_e^d = \boldsymbol{0}$. Thus, to limit the interaction forces the optimization of $\boldsymbol{F}_e'$ is formulated as the following QP problem:

$$\text{Optimizing end-effector control :} \qquad \min_{\boldsymbol{F}_e^*} \ \frac{1}{2}(\boldsymbol{F}_e^* - \boldsymbol{F}_e')^T\boldsymbol{Q}_c(\boldsymbol{F}_e^* - \boldsymbol{F}_e') \tag{4.14}$$

$$\text{Interaction wrench constraint :} \qquad \text{s.t. } |\boldsymbol{F}_c|_i \le \boldsymbol{F}_{c,max_i} \tag{4.15}$$

$$\text{Stability constraint :} \qquad \boldsymbol{v}_e^T(\boldsymbol{F}_e^* - \boldsymbol{E}\boldsymbol{K}_{Pe}\Delta\boldsymbol{x}_e) < 0 \tag{4.16}$$

with, the weighting matrix, $\boldsymbol{Q}_c \in \mathbb{R}^{6\times6}$, and $\boldsymbol{F}_e^*$ is the optimized control wrench. The constraint (4.15) limits the interaction forces, according to space mission requirements, where, $\boldsymbol{F}_{c,max_i}$ is the component wise threshold of the allowable maximum interaction wrench. The constraint (4.16) ensures that the stability requirements are met by the optimized wrench. Taking the time-derivative of the candidate Lyapunov function V_1 in (4.12) with $\varepsilon_e = 0$ results in $\dot{V}_1 = \Delta\boldsymbol{\nu}_e^T(\boldsymbol{F}_e' - \boldsymbol{E}\boldsymbol{K}_{Pe}\Delta\boldsymbol{x}_e)$ for the regulation case. Therefore, the constraint (4.16) replaces $\boldsymbol{F}_e'$ with $\boldsymbol{F}_e^*$ to ensure boundedness of the optimized solution. In contrast to the optimization in (3.17), the constraint (4.16) allows to accommodate a spring potential on the end-effector while ensuring boundedness. Finally, $\boldsymbol{F}_e^*$ replaces $\boldsymbol{F}_e'$ in (4.10) and Figure 4.4.

Optimizing F_r' for thruster capacity limits

$\boldsymbol{F}_r'$ maps to the actuation $\boldsymbol{\Gamma}_{\mathrm{T3}}$ on the servicer through the Jacobian-transpose $\bar{\boldsymbol{J}}_r^T$ as seen in (4.10). A closer look at $\bar{\boldsymbol{J}}_r$ using the definition in (4.3) and the structure of the inertia matrix in (2.6) reveals:

$$\bar{\boldsymbol{J}}_r = \begin{bmatrix} \boldsymbol{M}_{rr}^{-1}\boldsymbol{M}_{br}^T & \boldsymbol{0} & \boldsymbol{I}_r \end{bmatrix} \tag{4.17}$$

with, $\boldsymbol{M}_{br}^T = \begin{bmatrix} \boldsymbol{0} & \boldsymbol{M}_{\omega r}^T \end{bmatrix}$. Here $\boldsymbol{M}_{\omega r}$ is the inertia coupling of reaction wheels to the base's angular velocity. From (4.17) and through $\boldsymbol{\Gamma}_{\mathrm{T3}} = \bar{\boldsymbol{J}}_r^T\boldsymbol{F}_r'$ we observe that $\boldsymbol{F}_r'$ cannot influence the linear force on the base or the manipulator torques. However, the base torques can be modified by redesigning $\boldsymbol{F}_r'$. The optimization of $\boldsymbol{F}_r'$ [HS87] is formulated as a QP problem:

$$\text{Optimizing reaction wheel control :} \quad \min_{\boldsymbol{F}_r^*} \ \frac{1}{2}(\bar{\boldsymbol{\Gamma}} + \bar{\boldsymbol{J}}_r^T\boldsymbol{F}_r^*)^T\boldsymbol{Q}_{\boldsymbol{\Gamma}}(\bar{\boldsymbol{\Gamma}} + \bar{\boldsymbol{J}}_r^T\boldsymbol{F}_r^*) \tag{4.18}$$

$$\text{External torque constraint :} \quad \text{s.t. } |\boldsymbol{\tau}_b|_i \leq \boldsymbol{\tau}_{b,max_i} \tag{4.19}$$

During the approach phase, $\bar{\boldsymbol{\Gamma}} = \boldsymbol{\Gamma}_{\mathrm{T1}} + \boldsymbol{\Gamma}_{\mathrm{T2}} + \boldsymbol{\Gamma}_\mu$, as defined in (4.10). In the post-grasp phase, $\bar{\boldsymbol{\Gamma}} = \boldsymbol{\Gamma}_{\mathrm{T1}}^* + \boldsymbol{\Gamma}_{\mathrm{T2}} + \boldsymbol{\Gamma}_\mu$, which incorporates the optimized end-effector wrench from (4.14) to limit interaction forces, where $\boldsymbol{\Gamma}_{\mathrm{T1}}^* = \boldsymbol{J}_e^T\boldsymbol{F}_e^*$. The formulation in (4.14) restricts the optimization dimension to the redundant DoFs, in contrast to optimizing over all system DoFs as in [HS87].

The cost function in (4.18) penalizes actuation based on the weight $\boldsymbol{Q}_{\boldsymbol{\Gamma}} \in \mathbb{R}^{(6+n+r)\times(6+n+r)}$. The constraint in (4.19) limits the final torques distributed to the thrusters, $\boldsymbol{\tau}_b$. Here, $\boldsymbol{\tau}_{b,max_i}$ denotes the component-wise threshold for the maximum allowable thruster torque, as determined by thruster limits. The variable $\boldsymbol{F}_r^*$ represents the optimized allocation of torques between the thrusters and reaction wheels. Hence, $\boldsymbol{F}_r^*$ replaces $\boldsymbol{F}_r'$ in (4.10) and Figure 4.4. Appropriate tuning of the weights enables adaptation of the torque distribution to the operational phase requirements. The optimized result does not affect the convergence analysis, since in the set where tasks T1 and T2 have converged, $\boldsymbol{F}_r^* = \boldsymbol{0}$ for the regulation case at the end of the post-grasp phase.

Finally, Algorithm 1 complements the block diagrams in Figure 4.3 and Figure 4.4 to compute the unified control law. Further, the update to the controller in Figure 4.4 is also shown in the block diagram Figure 4.5 where the nominal control inputs are optimized for constraints.

Algorithm 1 Computing Unified Control Law

Require: Kinematics ($\boldsymbol{J}_e, \boldsymbol{J}_c$) and dynamics ($\boldsymbol{M}_\bullet, \boldsymbol{C}_\bullet$) from (2.7),(2.10) in generalized coordinates

1: Compute kinematics ($\boldsymbol{J}_N$ from (4.3)) and dynamics ($\boldsymbol{\Lambda}, \boldsymbol{\mu}$ from (4.5)) in nullspace coordinates
2: Compute Coriolis decoupling $(\boldsymbol{\mu} - \bar{\boldsymbol{\mu}})\boldsymbol{\nu}_N$ from (4.6)
3: Compute dynamics ($\boldsymbol{\Lambda}', \boldsymbol{\mu}'$ from (4.8)) in nullspace-projected task coordinates
4: Compute nominal control law $\boldsymbol{F}'$, $\boldsymbol{\Gamma}$ from (4.9), (4.10)
5: **if** phase = post-grasp **then**
6: Optimize end-effector wrench ($\boldsymbol{F}_e^*$ from (4.14)-(4.16)) for limiting interaction forces
7: **end if**
8: Optimize torque distribution between reaction wheels and thrusters ($\boldsymbol{F}_r^*$ from (4.18)-(4.19))
9: Compute optimized control law in actuator coordinates (replace $\boldsymbol{F}_e', \boldsymbol{F}_r'$ with $\boldsymbol{F}_e^*, \boldsymbol{F}_r^*$ in (4.10))

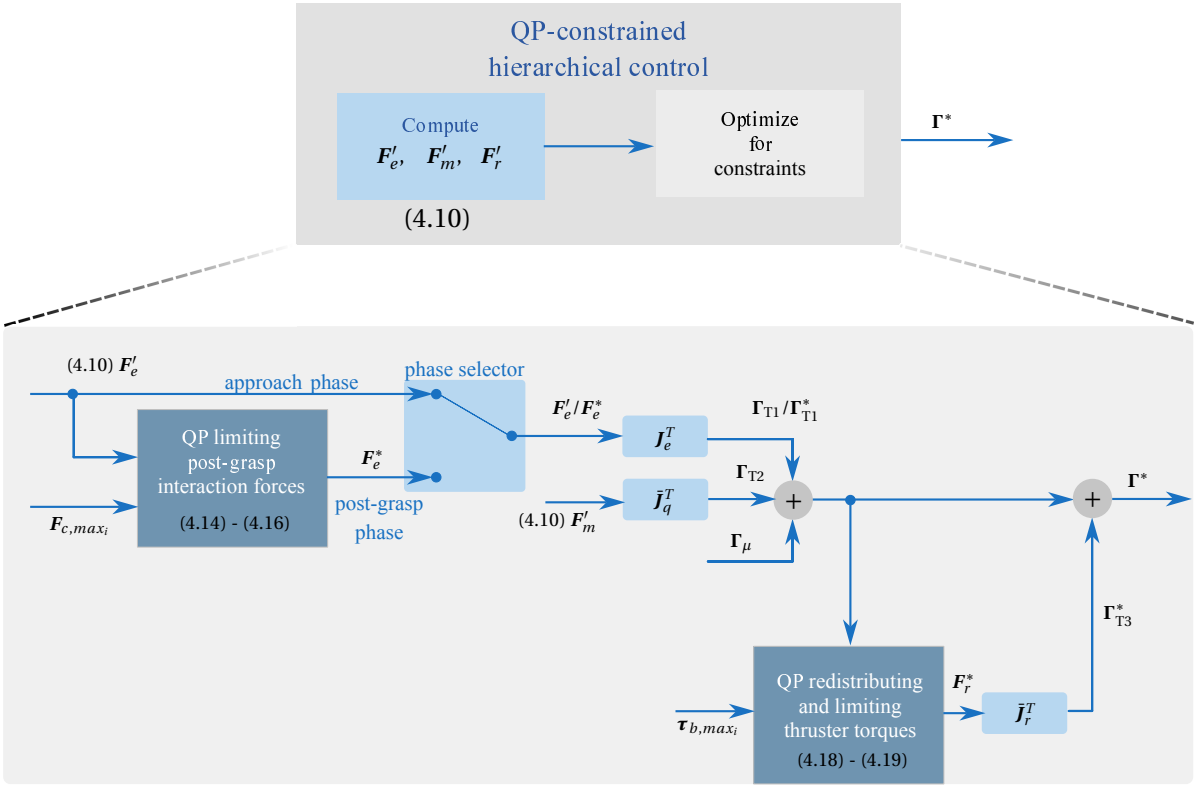

Figure 4.5: *QP-adapted controller* – constraints inclusion. The constraint on interaction forces applies only in the post-grasp phase, shown by the phase selector. Finally, $\boldsymbol{\Gamma}^*$ replaces $\boldsymbol{\Gamma}$ in Figure 4.4

.

4.4 Validation results

This section presents the validation of the proposed control strategy using two setups – i) simulation (SIM) using the EROSS IOD[R$^+$] mission setup and, ii) HIL experiments using the COMRADE[CSS$^+$20] mission setup on the OOS-Sim at DLR [A$^+$15]. Both setups are shown in Figure 4.1. The dynamic, kinematic and control parameters for the SIM and HIL setups are summarized in Table 4.2.

Table 4.2: SIM and HIL parameters. *Moment of inertia, **Euler angles (XYZ), †Double-Diagonalization [AS+03] with damping ratio 0.7, ††$\boldsymbol{Q}_\Gamma$=[$\boldsymbol{0}_3, \boldsymbol{Q}_{\tau_b}, \boldsymbol{0}_n, \boldsymbol{Q}_{\tau_r}$], #Magnitudes as in [GLdR19].

DYNAMIC/KINEMATIC PARAMETERS		
Parameter	**SIM**	**HIL**
Client mass & MOI*	350kg, $(58.33, 58.33, 58.33)\mathrm{kgm}^2$	400kg, $(360, 362.95, 264.94)\mathrm{kgm}^2$
Servicer mass & MOI*	360kg, $(210.9, 77.9, 212.1)\mathrm{kgm}^2$	1000kg, $(700, 600, 500)\mathrm{kgm}^2$
Reaction wheels	4	3
Manipulator arm	7-DoF CAESAR robot [BGH+18]	7-DoF Light Weight Robot (LWR)
Initial joint angles	$(90, 60, 0, 132, 90, -90, 50)$deg	$(-7, 14, 4, 91, 2, -54, -3)$deg
Initial pose** of end-effector	$(0.84, -0.30, 1.65)$m, $(62, 0, 90)$deg	$(1.27, -0.01, 0.89)$m, $(-173, 53, -175)$deg
Initial pose** of client grasp	$(0.95, -0.91, 2.16)$m, $(90, 5, 90)$deg	$(1.33, -0.41, 0.47)$m, $(-136, 47, -178)$deg
Initial client velocity norm	$2.865\mathrm{degs}^{-1}$	$0.5\mathrm{degs}^{-1}$

SIM: CONTROLLER PARAMETERS			
T#	K/Q	**Approach phase**	**Post-Grasp phase**
T1	$\boldsymbol{K}_{Pe}$	$[250, 250, 250]\mathrm{Nm}^{-1}$, $[50, 50, 50]\mathrm{Nmrad}^{-1}$	$[10, 10, 10]\mathrm{Nm}^{-1}$, $[5, 5, 5]\mathrm{Nmrad}^{-1}$
	$\boldsymbol{K}_{De}$	$[200, 200, 200]\mathrm{Nm}^{-1}\mathrm{s}$, $[125, 125, 125]\mathrm{Nmrad}^{-1}\mathrm{s}$	$[400, 400, 400]\mathrm{Nm}^{-1}\mathrm{s}$, $[250, 250, 250]\mathrm{Nmrad}^{-1}\mathrm{s}$
	$\boldsymbol{Q}_c$	-	$[1/f_{c,max}^2, 1/\tau_{c,max}^2]^\#$, f_{c,max_i}=10N, τ_{c,max_i}=7Nm
T2	$\boldsymbol{K}_{Pm}$	$[120, 120, 100, 100, 50, 40, 40]\mathrm{Nmrad}^{-1}$	$[120, 120, 100, 100, 50, 40, 40]\mathrm{Nmrad}^{-1}$
	$\boldsymbol{K}_{Dm}$	variable damping using DD†	DD† scaled by $(5, 5, 5, 10, 25, 12.5, 22.5)$
T3	$\boldsymbol{Q}_\Gamma^{\dagger\dagger}$	$\boldsymbol{Q}_{\tau_b}$=$\boldsymbol{I}_3$, $\boldsymbol{Q}_{\tau_r}$=$\boldsymbol{0}_r$, τ_{b,max_i}=15Nm	$\boldsymbol{Q}_{\tau_b}$=$\boldsymbol{0}_3$, $\boldsymbol{Q}_{\tau_r}$=$\boldsymbol{I}_r$, τ_{b,max_i}=15Nm

HIL: CONTROLLER PARAMETERS			
T#	K/Q	**Approach phase**	**Post-Grasp phase**
T1	$\boldsymbol{K}_{Pe}$	$[700, 500, 500]\mathrm{Nm}^{-1}$, $[40, 60, 40]\mathrm{Nmrad}^{-1}$	$[50, 50, 50]\mathrm{Nm}^{-1}$, $[30, 30, 30]\mathrm{Nmrad}^{-1}$
	$\boldsymbol{K}_{De}$	$[100, 100, 100]\mathrm{Nm}^{-1}\mathrm{s}$, $[24, 24, 24]\mathrm{Nmrad}^{-1}\mathrm{s}$	$[100, 100, 100]\mathrm{Nm}^{-1}\mathrm{s}$, $[24, 24, 24]\mathrm{Nmrad}^{-1}\mathrm{s}$
	$\boldsymbol{Q}_c$	-	$[1/f_{c,max}^2, 1/\tau_{c,max}^2]^\#$, f_{c,max_i}=12N, τ_{c,max_i}=8Nm
T2	$\boldsymbol{K}_{Pm}$	$[60, 60, 60, 40, 35, 25, 30]\mathrm{Nmrad}^{-1}$	$[2, 30, 1, 10, 1, 10, 0.5]\mathrm{Nmrad}^{-1}$
	$\boldsymbol{K}_{Dm}$	variable damping using DD†	$[20, 60, 10, 60, 10, 60, 7]\mathrm{Nmrad}^{-1}\mathrm{s}$
T3	$\boldsymbol{Q}_\Gamma^{\dagger\dagger}$	$\boldsymbol{Q}_{\tau_b}$=$\boldsymbol{I}_3$, $\boldsymbol{Q}_{\tau_r}$=$\boldsymbol{0}_r$, τ_{b,max_i}=15Nm	$\boldsymbol{Q}_{\tau_b}$=$\boldsymbol{0}_3$, $\boldsymbol{Q}_{\tau_r}$=$\boldsymbol{I}_r$, τ_{b,max_i}=15Nm

The controller gains are chosen as per the desired performance in tracking (for approach phase) and compliance (for post-grasp phase). Initial estimates of the gains are obtained from a frequency-domain analysis using the linearized closed-loop dynamics about the initial and final configurations of the servicer. As the impedance gains are only relevant to tasks T1 and T2, the linearization for the sake of gain tuning can be simplified by eliminating task T3 on the redundant reaction wheels.

The initial gains can thus be tuned against step responses for tracking performance, and against impulse responses for compliance performance. These estimates form the basis for further tuning and validation in a nonlinear dynamic environment. A detailed procedure for the linearization and analysis with step and impulse responses can be found in the Appendix D. The controller gains from the approach to grasp phase are updated to be more compliant to impact, yet more dissipative for stabilization.

Snapshots visualizing the SIM and HIL scenarios at different stages of the approach and post-grasp stabilization are provided in Figure 4.6. The graphical results in Figure 4.7-4.10 show the most relevant states, control, and forces recorded for the SIM and HIL experiments. The SIM and HIL results are summarized graphically in Figure 4.7-4.10 and quantitatively in Table 4.3, validating the

(a) SIM

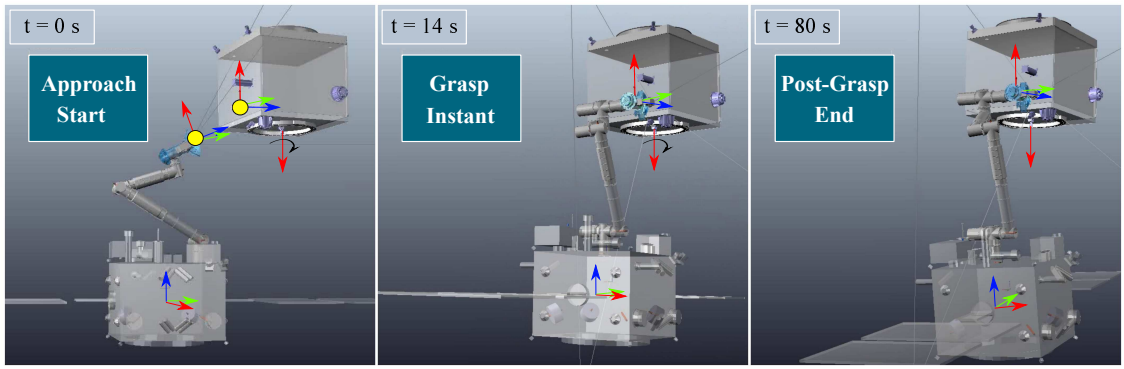

(b) HIL

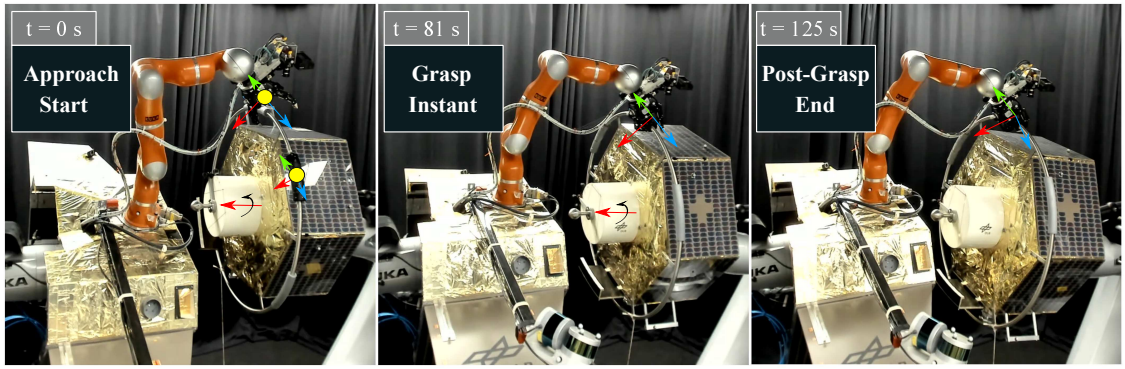

Figure 4.6: (a) SIM and (b) HIL scenarios from approach to post-grasp phase. A link to the experimental videos is given in Appendix G, Table G.1.

proposed control objectives in Table 4.1. The columns a and b in Figure 4.7-4.8 show the results of the SIM experiment for the approach and post-grasp phases, respectively, while the columns c and d in Figure 4.9-4.10 show the results of the HIL experiment for the approach and post-grasp phases, respectively. The moment of grasp (contact) in SIM and HIL results can be recognized from the characteristic spike at the beginning of the graphs presented for the post-grasp phase.

4.4.1 Simulation (SIM) results

The SIM setup uses the Open Dynamics Engine [S+05] in CoppeliaSim for simulating the servicer and client dynamics. The manipulator used in simulation is the CAESAR space robot [BGH+18], a 7-DoF redundant robot. The grasping dynamics between manipulator's end-effector and capture point is modeled as an inelastic contact. A force-torque sensor at the end-effector measures the interaction forces as ground truth.

The SIM analysis in Figure 4.6 (a) shows the start of the approach phase, the grasp instant, and the end of the post-grasp stabilization. In contrast to the issue presented in Figure 4.2, the proposed control strategy enables the system to approach the spinning client with a safe pose and improved manipulability as the end-effector grasps the client. Consequently, the base synchronizes its rotation with the client while maintaining a safe relative pose. This is evident when comparing the base orientation in the SIM snapshots at the grasp instant, and the approach start in Figure 4.6 (a). During the post-grasp phase, the strategy further dissipates the client's spin with increased compliance, while still achieving a safe and desirable pose for both the manipulator and the base. The SIM snapshot at the end of the post-grasp phase in Figure 4.6 (a) demonstrates that the servicer attains a pose suitable for subsequent manipulation of the stabilized client.

Figure 4.7 a.i and a.ii show the end-effector tracking a smooth trajectory to align with the client grasp pose at the end of the approach phase, shown in a.iii and a.iv and highlighted in blue. Figure 4.7 b.i and b.ii show the effect of constraints that limit the interaction forces and torques in the post-grasp phase to their respective thresholds. Figure 4.7 b.iii and b.iv show the stabilization of the spinning client (initial spin of 2.86deg/s) as the linear and angular body velocities get damped.

Figure 4.8 a.v shows the tracking of a joint pose in the nullspace to arrive at a manipulable configuration at the end of the approach phase. It is this simultaneous tracking of a joint trajectory in addition to the end-effector pose that results in the base synchronizing its spin to that of the client before capture. Figure 4.8 b.v shows the arm stabilizing during the post-grasp phase as the joint velocities get damped. Figure 4.8 a.vi shows the complete redistribution of base torques to the four reaction wheels in the approach phase. On the other hand, Figure 4.8 b.vi shows the torque distribution to the thrusters being maximized for damping the acquired momentum in the grasp phase. The SIM results are quantitatively summarized in terms of performance metrics in Table 4.3.

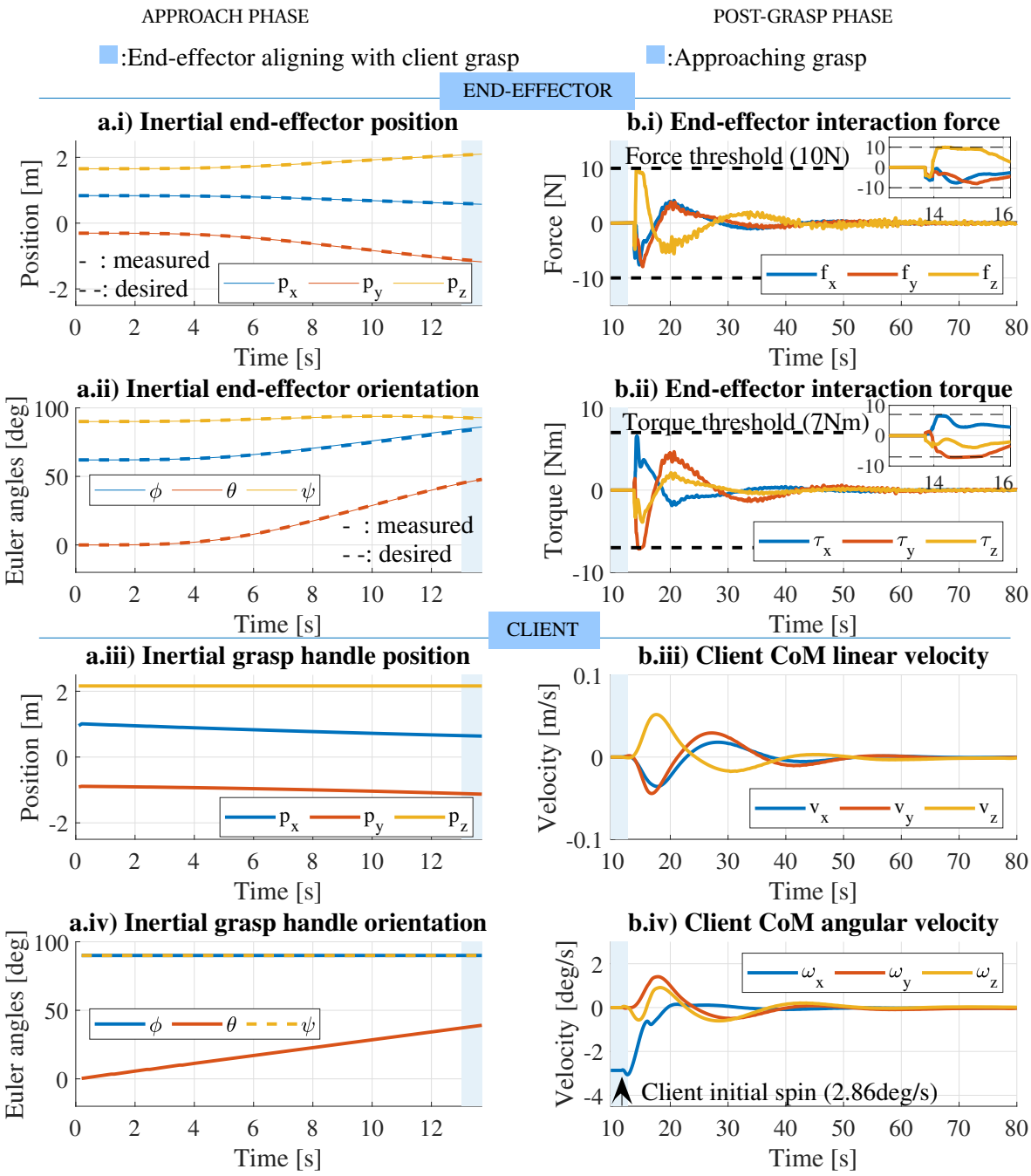

Figure 4.7: *SIM results* – task T1 (end-effector) showing fulfillment of proposed control objectives in Table 4.1. For ease of presentation, Euler angles (ϕ, θ, ψ in the XYZ convention) are reported here.

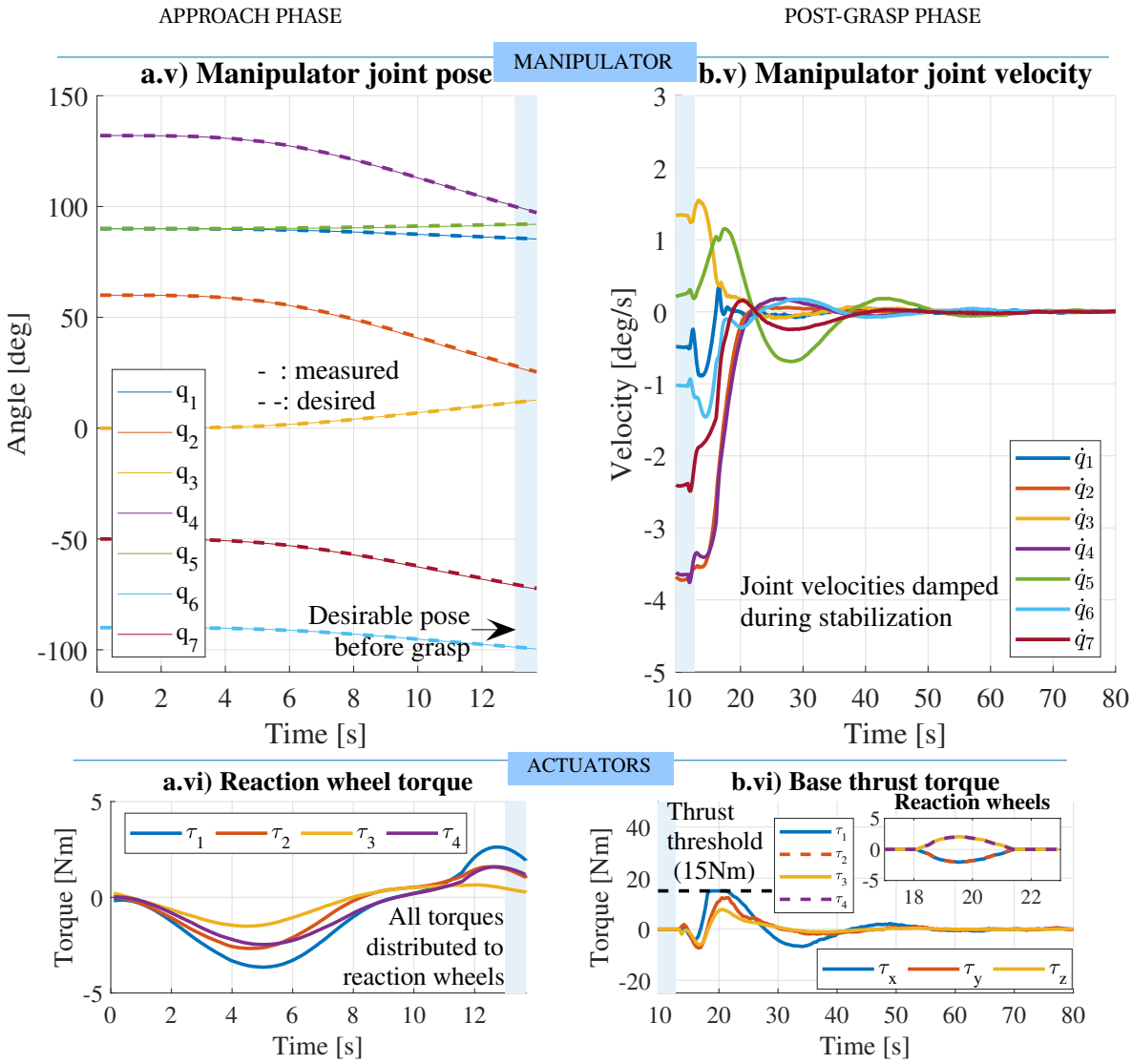

Figure 4.8: *SIM results* – tasks T2 (manipulator) and T3 (actuators) showing fulfillment of proposed control objectives in Table 4.1.

Table 4.3: SIM and HIL performance – quantitative metrics. † Euclidean norm, *Absolute error along any axes, **Time for absolute joint velocity to reach below 0.1deg/s along all axes after grasp.

Performance metric	**SIM**	**HIL**
Maximum end-effector position error† (m)	$1.9e{-}5$	$1.1e{-}2$
Maximum end-effector orientation error† (deg)	$2.3e{-}2$	1.5
Maximum joint tracking error* (deg)	$6.7e{-}2$	2.95
Settling time for post-grasp stabilization** (s)	45	43

4.4.2 Experimental (HIL) results

The HIL setup uses the OOS-Sim facility described in Chapter 2 Section 2.1.1. The torque distribution to reaction wheels is simulated while considering its dynamics parameters. The first-order approximation of the interaction force in (4.13) is used to limit post-grasp forces in the experiment.

Consistent with the SIM results, the HIL experiment snapshots in Figure 4.6 (b) depict the initiation of the approach phase, the grasp event, and the conclusion of post-grasp stabilization. The proposed method again enables the base to synchronize its rotation with that of the client during the approach phase, positioning the manipulator in an optimal configuration for capture. This synchronization is evident when comparing the base orientation and manipulator configuration in the HIL snapshots at the grasp instant and at the approach start in Figure 4.6 (b). Notably, in contrast to the issue identified in Figure 4.2, the proposed control strategy safely stabilizes the client by leveraging the nullspace potential of the manipulator joints, thereby preventing collisions between the base and the client. This outcome is demonstrated in the HIL snapshot at the end of the post-grasp phase in Figure 4.6 (b).

The HIL results can be correlated with the SIM results described in Section 4.4.1. Figure 4.9 c.i and c.ii show the end-effector tracking and Figure 4.9 d.i and d.ii show the interaction forces and torques being limited in the post-grasp phase, while the spinning client (initial spin of 0.5deg/s) stabilizes, seen from the body velocities being damped in Figure 4.9 d.iii and d.iv.

Figure 4.10 c.v. shows the nullspace joint tracking in the approach phase and the joints stabilize in the post-grasp phase, see Figure 4.10 d.v. For faster energy dissipation within the workspace limits of the HIL facility, stabilization is performed with an additional damping gain on the base velocity applied in the nullspace of the end-effector task. Further, the stiffness in the post-grasp phase is emphasized on the joints that ensure the safe relative configuration between servicer and client, while the remaining are relaxed to increase compliance during stabilization (see Table 4.2).

Similar to SIM results, Figure 4.10 c.vi shows the redistribution of base torques to the three reaction wheels in the approach phase whereas Figure 4.10 d.vi shows the maximization of thruster utilization in the post-grasp phase. The activation of the limit on the base thrust can be seen resulting in the co-utilization of reaction wheels. The control input demanded from the servicer in the grasp phase is greater than the approach phase, as expected due to the momentum injected during the grasp of the client satellite. The HIL results are quantitatively summarized in terms of performance metrics in Table 4.3.

Further, emphasis is made on the configuration safety achieved in the post-grasp phase evidenced by the result of the HIL experiment in Figure 4.6 (right) which mitigated the collision risk shown in Figure 4.2 (right). The nullspace potential on the joints responsible for this, not only achieved safety, but also did so while staying decoupled from the interaction forces (see (4.13)). This highlights the advantage of the hierarchical controller.

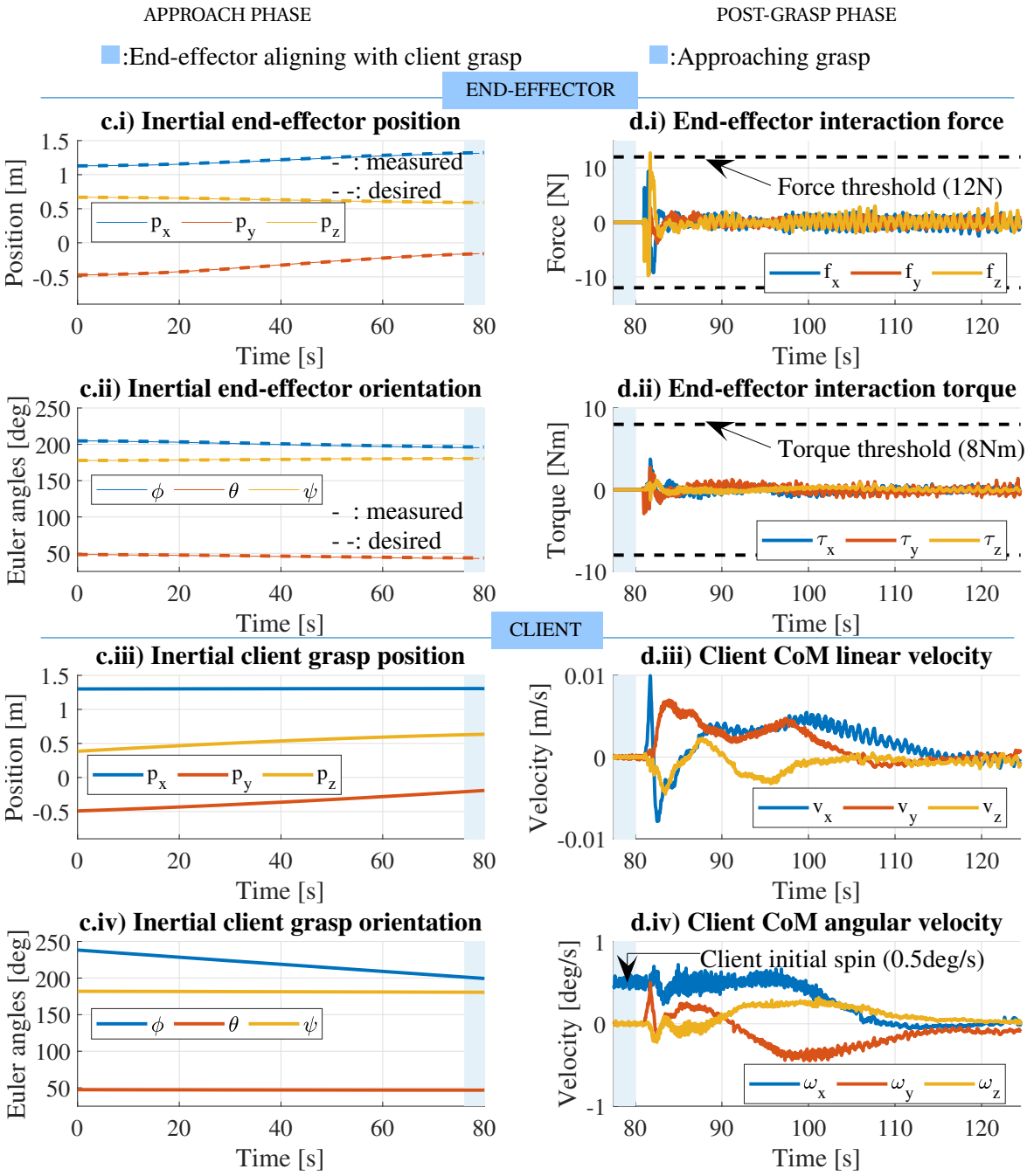

Figure 4.9: *HIL results* – task T1 (end-effector) showing fulfillment of proposed control objectives in Table 4.1. For ease of presentation, Euler angles (ϕ, θ, ψ in the XYZ convention) are reported here.

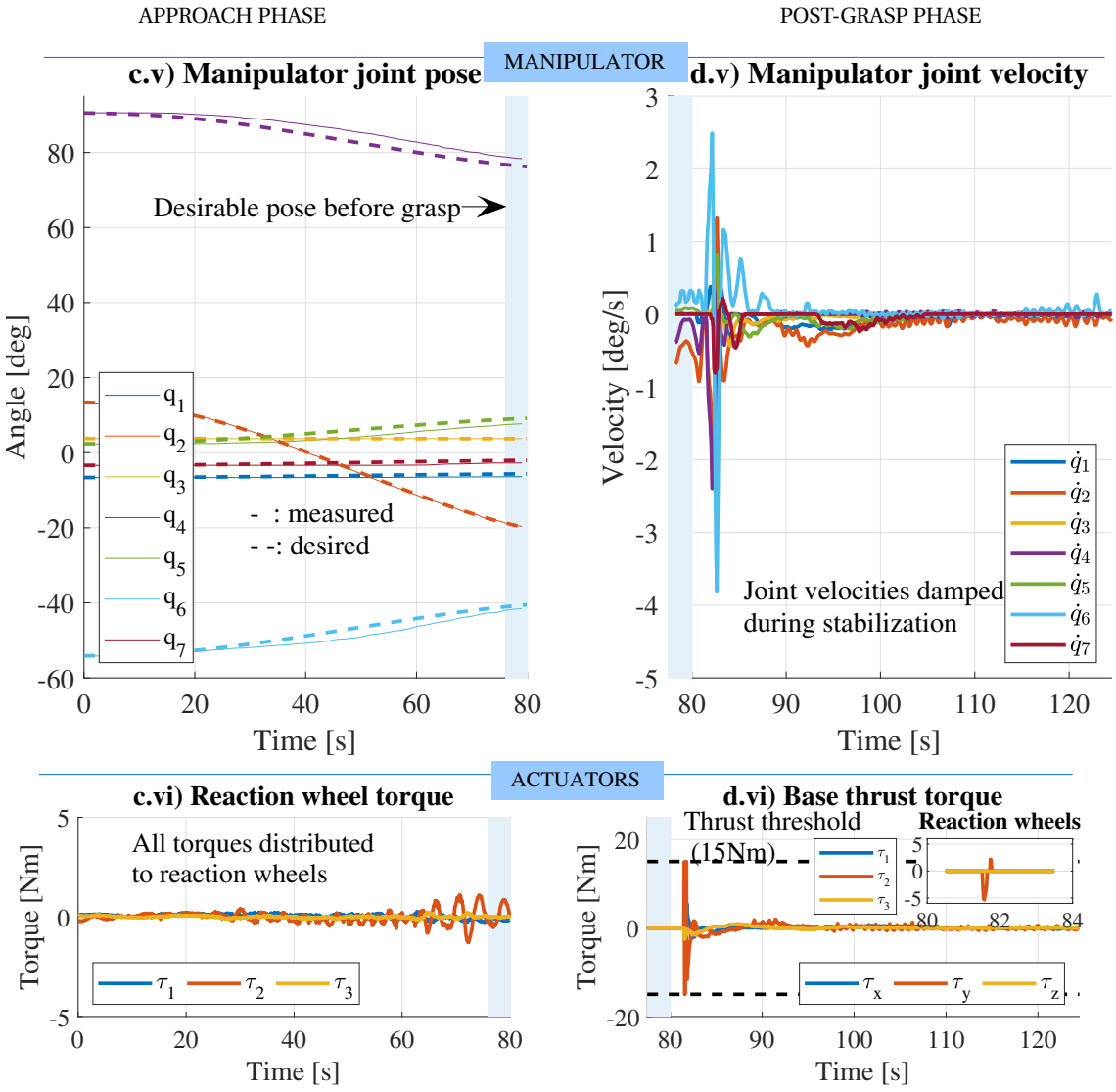

Figure 4.10: *HIL results* – tasks T2 (manipulator) and T3 (actuators) showing fulfillment of proposed control objectives in Table 4.1.

4.4.3 Momentum and interaction constraint

For the SIM experiment, the profile of angular momentum is shown in Figure 4.11. The residual momentum at the end corresponds to the momentum accumulated from the approach phase to stabilization. This results from the distribution of torques between reaction wheels and thrusters in Figure 4.8, thus effectively reducing the use of thrusters under torque limits. Further, the improvement in performance by using the QP-based limit on the interaction forces versus not is shown in Figure 4.12. A comparison of the performance of the controller was performed without the QP optimization for interaction forces, and it was found that the threshold was violated by 93.8% in force and 65.87% in torque in this scenario.

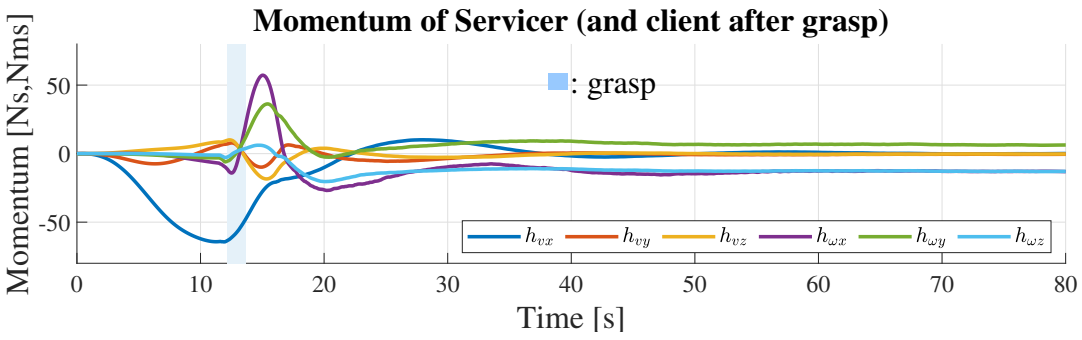

Figure 4.11: *SIM results* – momentum of servicer (and client after grasp). Linear momentum damped while residual angular momentum stored in wheels under thruster torque limits.

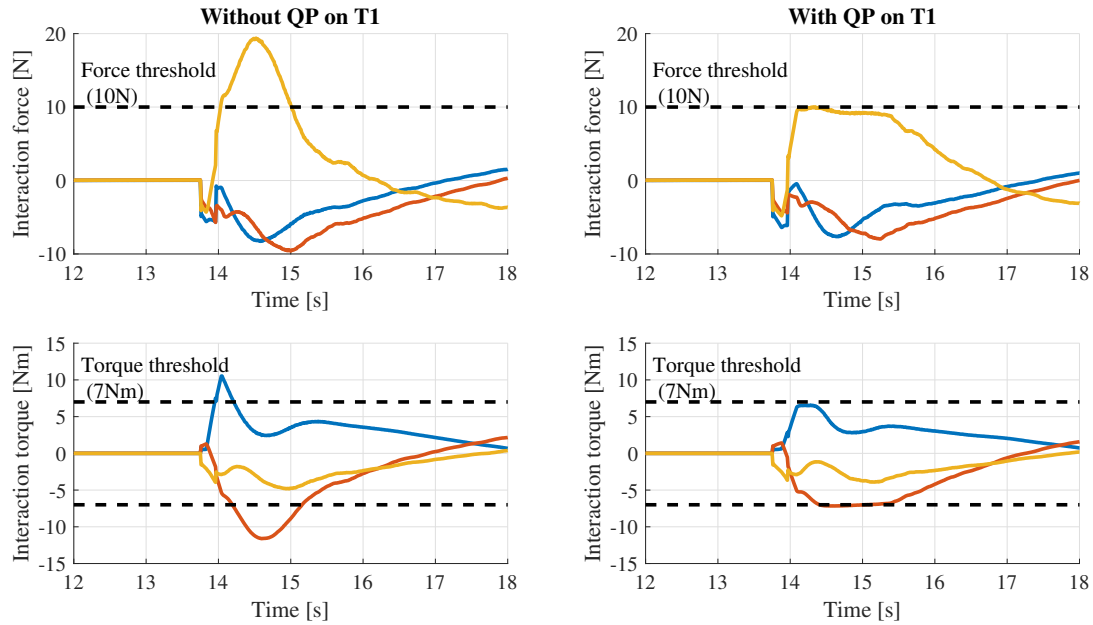

Figure 4.12: *SIM results* – comparison of the interaction force and torque with (right) and without (left) QP optimization for simulation in Figure 4.7 b.i and b.ii.

4.4.4 Robustness and sensitivity analysis

To evaluate the robustness of the controller, its sensitivity to both gain variation and client parameter uncertainties is analysed through simulation. Gain sensitivity is assessed by varying the gains from 30% to 120% of the nominal values specified in Table 4.2. During the approach phase (see Figure 4.13 a), the maximum Euclidean error in end-effector tracking remains below 1e-4 m for position and 1e-2 deg for orientation. Additionally, the manipulator tracking error for any joint does not exceed 1e-2 deg. In the post-grasp phase (see Figure 4.13 b), the percentage of settling time for stabilization increases as gains decrease and decreases as gains increase.

Further assessment of the robustness is performed by introducing simultaneous uncertainties

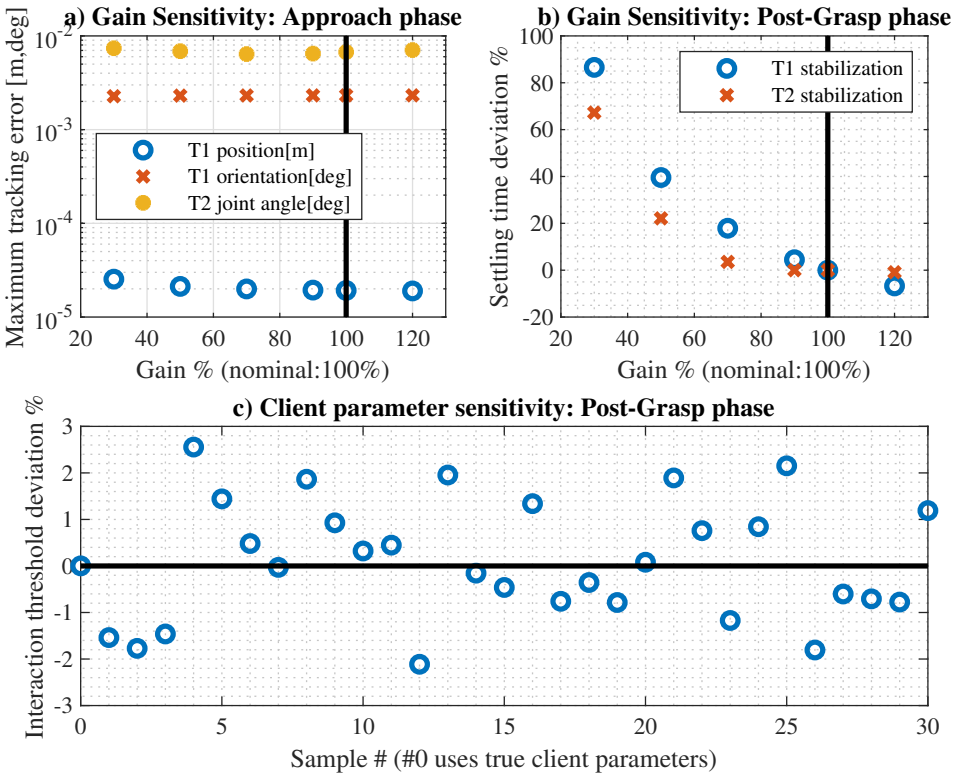

Figure 4.13: *Robustness analysis* – parameter sensitivity to control performance.

of up to 20% in the client's mass, inertia, and center-of-mass. In 30 simulations with uniformly distributed samples of client parameter uncertainties, the violation of the interaction force threshold does not exceed 3% (see Figure 4.13 c). The forces are constrained to higher or lower thresholds depending on whether the optimizer under- or over-compensates for the client's dynamics. These results demonstrate the controller's robustness across a broad range of gain and client parameter uncertainties.

The controller's robustness to client parameter uncertainties arises from the terms $\boldsymbol{\Gamma}_{T1}, \boldsymbol{\Gamma}_{T2}, \boldsymbol{\Gamma}_{T3}$ in (4.10), which are independent of the client's inertia parameters during the post-grasp phase. This independence results from the regulation scheme for T1 and the load-independence of the nullspace tasks T2 and T3. The only dependency on client parameters occurs through the Coriolis coupling $\boldsymbol{\Gamma}_{\mu}$ and the optimized $\boldsymbol{F}_e^*$ via the interaction force limitation with (4.13).

4.4.5 Joint reconfiguration in whole-body nullspace

The concept of whole-body nullspace of the end-effector with a fully-actuated base is demonstrated using HIL experiments on the OOS-Sim. In order to demonstrate the end-effector nullspace, the base actuation is sufficient, and therefore the reaction wheels are considered locked in this experiment. To distinguish the motion clearly, a joint-by-joint displacement of ±5deg is executed on in-

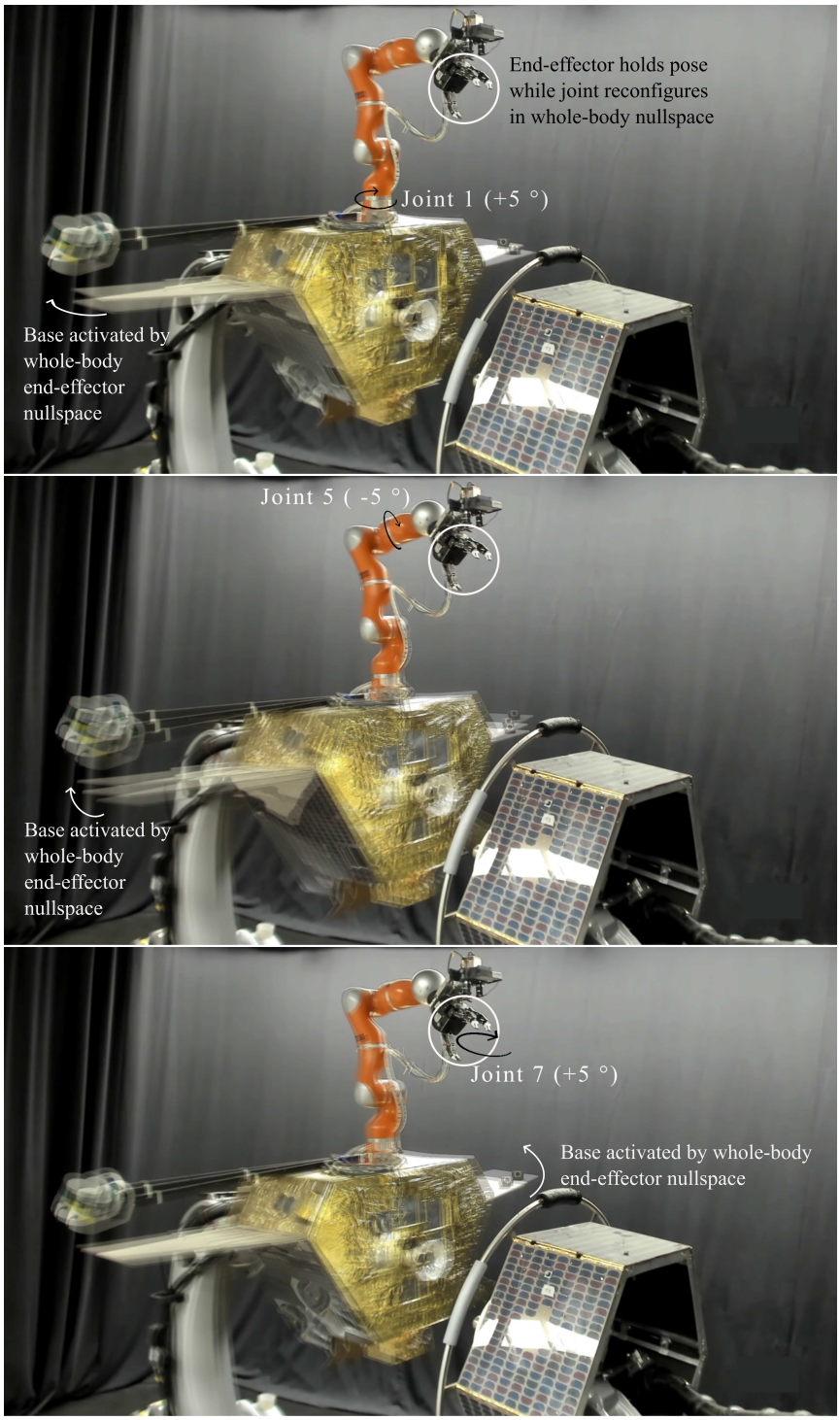

Figure 4.14: *Whole-body nullspace* – overlay of servicer's motion showing end-effector holding pose (white circle) while joint 1 (top), 5 (middle) and 7 (bottom) of the LWR reconfigure via nullspace activation of the base. A link to the experimental videos is given in Appendix G, Table G.1.

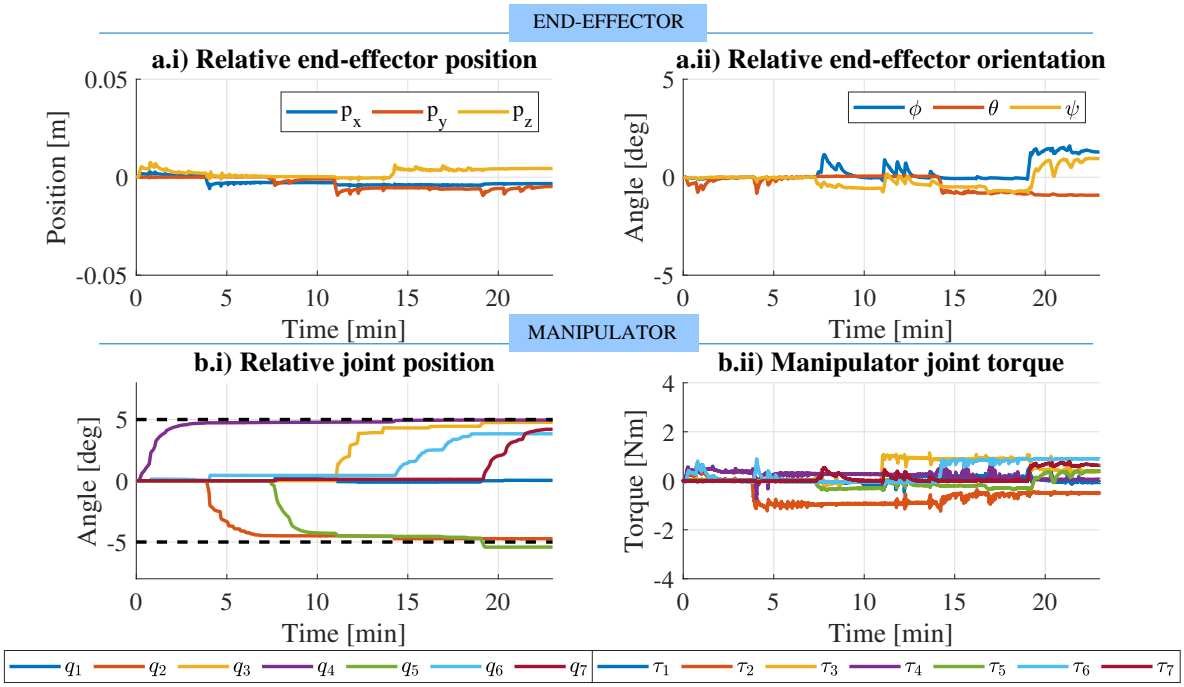

Figure 4.15: *Whole-body nullspace* – HIL results for joint-by-joint arm reconfiguration in the end-effector's nullspace.

dividual joints while the end-effector holds pose. Examples of joint 1, 5, and 7 reconfiguring in the nullspace are visualized in Figure 4.14. The snapshots show an overlay of the servicer's motion over the duration of joint reconfiguration maneuvers. The sharp focus on the end-effector as compared to the motion blur induced by the overlay of the servicer's motion during the joint reconfiguration verifies that the end-effector maintains its pose while the joints rotate using the nullspace activation of the base.

Further experiments show the consecutive reconfiguration of joints in Figure 4.15. The experiments show the influence of the coupling from the Coriolis compensation terms when omitted. The end-effector is seen to hold its pose to an accuracy of 6.5×10^{-3}m and 1.6deg in norm (see Figure 4.15 a.i and a.ii). The joints reconfigure with a maximum error of 1.2deg on joint 6 (see Figure 4.15 b.i), attributed to the friction evidenced by the residual torques in Figure 4.15 b.ii.

4.4.6 Stabilizing external disturbances

The effectiveness of the control in stabilizing external disturbances besides that anticipated from contact in the grasp phase, is demonstrated using further HIL experiments. The experiments consider a rope attached to the servicer's end-effector, which is pulled by a human operator to induce an arbitrary external disturbance into the system.

Snapshots of the experiment are visualized in Figure 4.16, where panel (a) shows the initial configuration when the rope is pulled downward. The horizontal guideline serves to compare the move-

ment of the servicer base during the experiment.

Upon release of the rope, the end-effector exhibits the behaviour of the virtual spring dictated by the control gains on the end-effector. Panel (b) shows the dynamic coupling of the servicer base

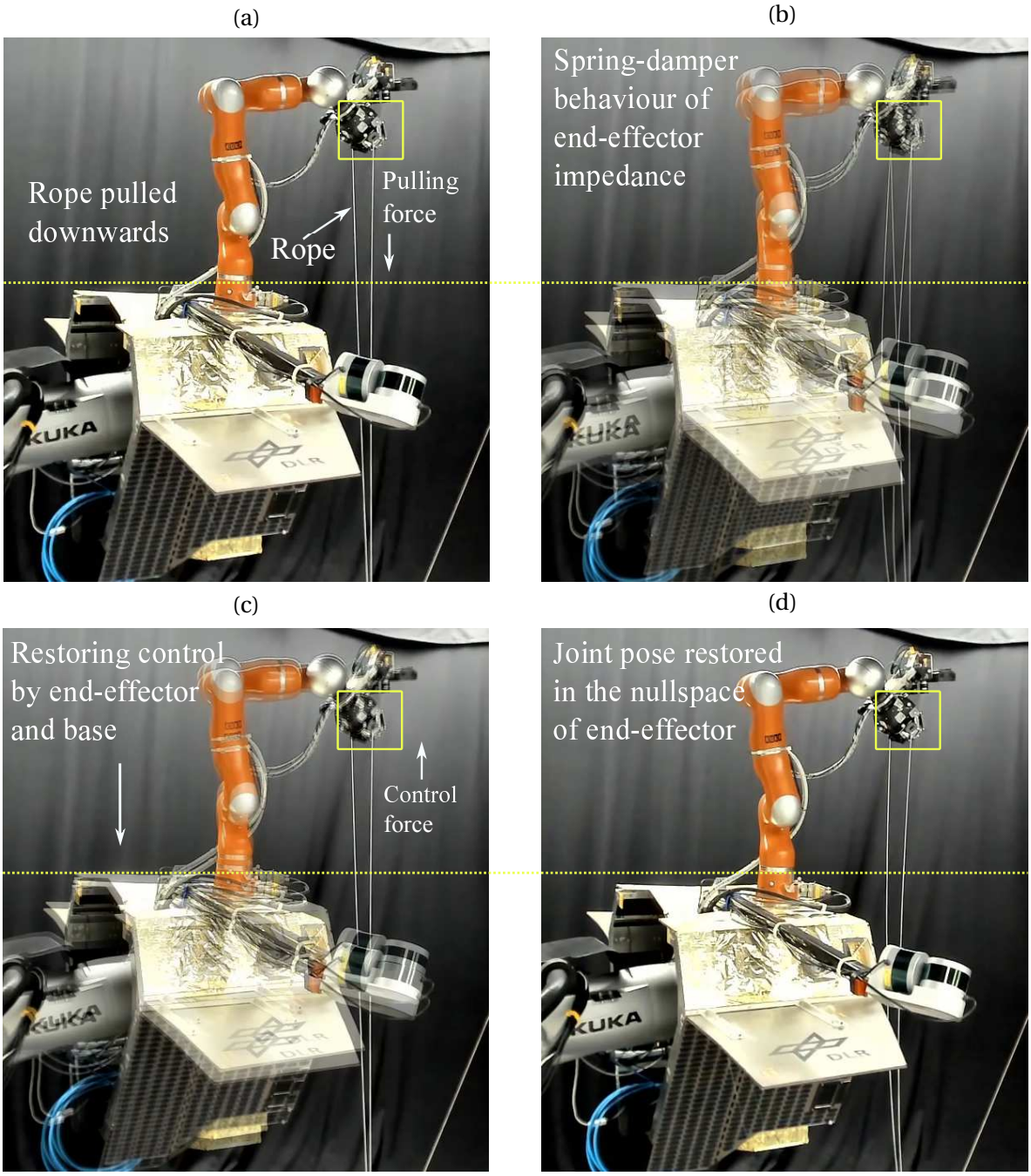

Figure 4.16: *Stabilizing disturbances* – external disturbance induced by pulling end-effector with a rope. The proposed controller restores the end-effector pose (yellow box) and the initial joint pose in its nullspace. A link to the experimental videos is given in Appendix G, Table G.1.

which results in a reaction force causing the base to move upwards. Panel (c) shows the restoring control via the nullspace activation of the base that exhibits the behaviour of the virtual spring dictated by the gains on the joints. Panel (d) shows the stabilization of the end-effector along with the joints, and thereby the servicer base.

The corresponding results for the end-effector velocity, joint velocity and base actuation are shown in Figure 4.17. Reaction wheels are considered locked in this demonstration experiment. The highlighted region in blue indicates the duration of the rope being pulled. The release of the rope is seen from the reversal in directions of end-effector and joint velocities in Figure 4.17. The end-effector and joint motions are subsequently damped by the manipulator torques and nullspace activation of the base wrench.

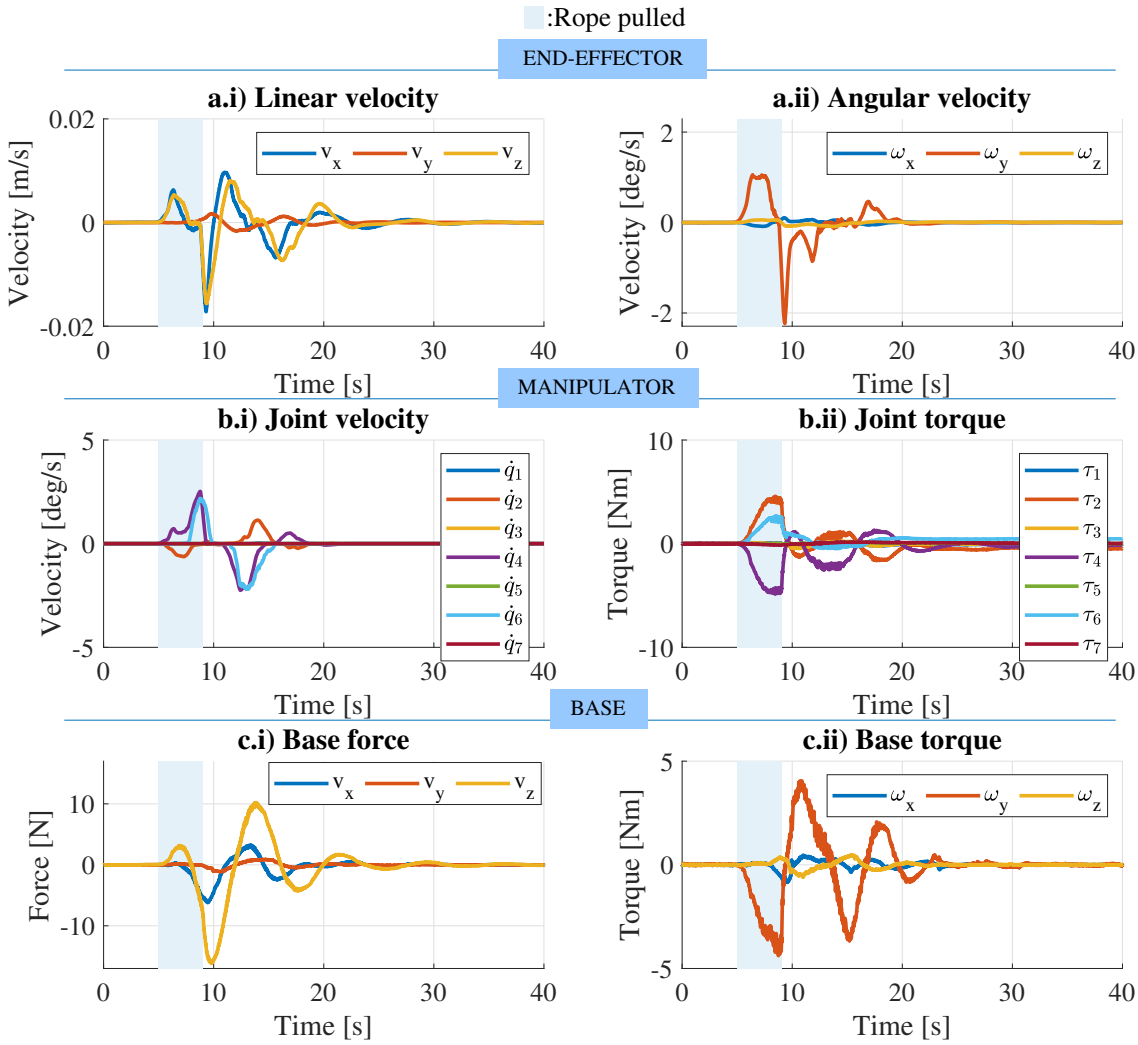

Figure 4.17: *Stabilizing disturbances* – HIL results showing stability to external forces induced by a rope pulled at the end-effector, highlighted by the duration in light blue.

4.5 Discussion and summary

This chapter details the design and experimental validation of a unified control strategy for the approach and stabilization of a spinning satellite. The strategy is formulated within a three-level task hierarchy based on nullspace projections, enabling systematic incorporation of mission-specific constraints. Beneficially, the analytical expressions for nullspace bases are provided in (4.2), therefore avoiding the need for their empirical determination via methods like the Gaussian elimination or singular value decomposition.

Addressing the challenges identified in Table 4.1, the proposed approach ensures manipulability by maintaining the manipulator in a desired configuration and implicitly achieves a desirable relative poses between the servicer and client during the post-grasp phase. Both objectives are achieved through a single nullspace task that dictates a desirable manipulator pose. The concept of the whole-body end-effector nullspace was demonstrated through hardware-in-the-loop experiments, as shown in Figure 4.14, highlighting the agility of the fully-actuated servicer in achieving joint reconfiguration in the nullspace. This intrinsic property is actively exploited to mitigate the practical challenges of maintaining manipulable and safe servicer poses throughout the mission.

This scheme addresses two primary challenges in the post-grasp phase: (i) ensuring a safe configuration between the servicer and client, and (ii) limiting high interaction forces at the end-effector. Challenge (i) is addressed through a potential function on the manipulator (see Table 4.1, task T2 for the post-grasp phase), which is designed so that the desired manipulator configuration leads to a unique, safe pose of the servicer base relative to the client. When executed in the nullspace, this task does not contribute to interaction forces at the end-effector, thereby not aggravating challenge (ii). However, the nullspace potential does not directly limit interaction forces. To address challenge (ii), the nominal control was augmented with a quadratic programming (QP)-based algorithm to explicitly limit interaction forces, in addition to the configuration safety task in the nullspace. Simulation results support robustness to varying gains and client parameter uncertainties. Experimental validation confirmed stability under various external disturbances by applying a pulling force to the end-effector with a rope.

The unified framework enables continuous operation in compliance mode and facilitates a smooth transition into the contact and stabilization phase while avoiding high interaction forces. Unlike conventional implementations that require switching between controllers for the approach and grasping phases, the proposed method requires only gain updates, enabling uninterrupted operation of the impedance control scheme. Typically, position control is used during approach for high tracking accuracy, followed by a switch to impedance control near contact. In contrast, the unified tracking impedance control, augmented with interaction force limitation, eliminates the need for such switching. The optimization for interaction forces can be activated prior to anticipated contact without affecting tracking performance, as the interaction force threshold is generally higher than the virtual control force required for trajectory tracking. This approach increases tolerance to navigation inaccuracies that could lead to premature contact, compared to a stiff, position-

controlled robot lacking compliance.

The method is validated through hardware-in-the-loop (HIL) results (see Figure 4.9 d.i and d.ii, interaction forces), where the exact moment of contact depends on sensing and hardware conditions that vary between experiments. This variability demonstrates the method's robustness in transitioning to post-grasp stabilization via compliant contact, even without force-sensing. Similarly, simulation (SIM) results in Figure 4.7 b.i and b.ii further validate the proposed method by confirming adherence to interaction force limits.

Therefore, the unified impedance control also streamlines hardware implementation, validation, traceability, troubleshooting, and software qualification for space missions. For implementation in a mission, the controller could be deployed on the robotic on-board computer (OBC), which interfaces with the spacecraft OBC via a dedicated connection. This interface would facilitate the exchange of navigation and control information with the spacecraft's guidance, navigation, and control (GNC) subsystem. Consequently, manipulator torques and base wrench can be computed on the robotic OBC, and the spacecraft wrench commanded to be executed using its existing GNC.

In summary, this chapter proposed a unified control framework to address mission requirements during the approach and grasp/post-grasp phases. The method utilized a hierarchical nullspace projection-based controller that prioritizes the servicer's end-effector task for tracking and stabilizing the client satellite in the respective phases. Within the end-effector's nullspace, a planned joint trajectory is tracked with support from base actuation. The designed control strategy was extensively tested both using simulation and hardware-in-the-loop experiments. The proposed method further enables modification of terms within the nullspace projection-based control scheme to incorporate mission constraints on interaction forces during the stabilization phase and to account for thruster torque limits using reaction wheels. The controller demonstrates convergence for tasks designed across three hierarchy levels, considering the end-effector, manipulator, and reaction wheels of the servicer.

CHAPTER 5

SAMPLING-AWARE MULTI-RATE CONTROL

In the context of on-orbit servicing (OOS), certain challenging scenarios (e.g., synchronized approach to a drifting client) require active control of both the servicer and manipulator, called *combined control*, coordinated control or free-flying control in the literature. The control strategies presented for different mission phases in Chapter 3 and Chapter 4 illustrate scenarios where combined control is beneficial. This chapter examines combined control in scenarios where spacecraft control operates at a significantly lower frequency than manipulator control, whereas previous chapters considered the same control frequency, which may not always be the case.

The complexity of combined control is compounded when the servicer satellite and its manipulator arm are controlled at different frequencies (see Figure 5.1). Traditional spacecraft control typically operates at a relatively low frequency below 10Hz, while the manipulator arm, which requires precise movements, is controlled at a much higher rate of approximately 1kHz [C+18]. This disparity in control frequencies means that the servicer's control is discrete, whereas the manipulator's control is quasi-continuous. This is referred to as *multi-rate* control in the scope of this work for combined control of an orbital manipulator. If not carefully designed, the low sampling and actuation rate of the servicer satellite can cause instabilities due to energy leaks from the time-delays introduced by a sampled-data system [DNBS06], as demonstrated on hardware in [DSBS20]. Therefore, the reduced frequency of the spacecraft controller relative to the manipulator may compromise the stability margin of the combined control system.

In this chapter, a combined control strategy is developed to decouple the high-frequency manipulator control from the spacecraft's low-frequency control. Additionally, a novel discrete controller is introduced to address the first-order effects of the servicer's low sampling rate by augmenting a classical proportional-derivative (PD) control scheme. The operational bounds of the discrete controller are initially benchmarked on a single-degree-of-freedom (DoF) system and subsequently evaluated

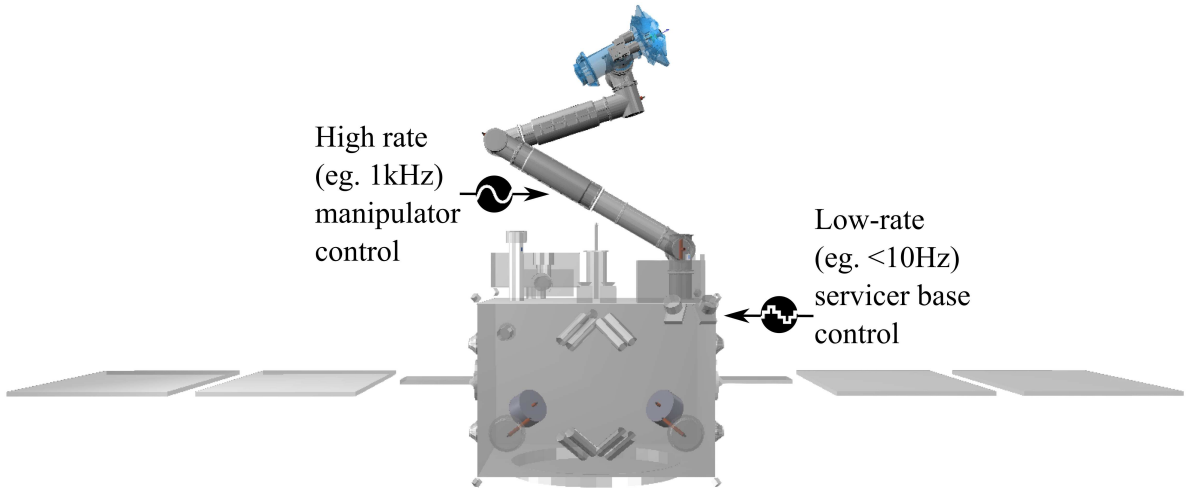

Figure 5.1: *Multi-rate control problem* – Traditional spacecraft control typically operates at a relatively low frequency below 10Hz, while the manipulator arm, which requires precise movements, is controlled at a much higher rate of approximately 1kHz.

for performance using a multi-DoF orbital manipulator. The findings identify regions of improved performance in terms of stability and efficiency. Simulation results and hardware-in-the-loop experiments are conducted to validate the proposed method.

The structure of the chapter is as follows. Section 5.1 surveys multi-rate approaches and outlines this work's contributions. Section 5.2 describes the mission scenario, the problem statement, and proposes a control strategy. Section 5.3 presents the design of the multi-rate hierarchical controller. Section 5.4 benchmarks the discrete controller on a low-dimensional system. Section 5.5 compares simulation results of the proposed multi-rate control vs. a baseline of zero-order control and a passivity-based controller from the literature. Experiments performed on the HIL facility, OOS-Sim, are also presented to validate the method. Section 5.6 summarizes the main takeaways of the results.

5.1 Related work and contributions

Low-rate control has been investigated within the framework of sampled-data systems. In [TMNC16], the design of sampled-data controllers is addressed through Lyapunov function matching at sampling instants to stabilize a backstepping controller. The stability of haptic rendering under discretization, quantization, time delay, and Coulomb effects is analyzed for the one degree-of-freedom (DoF) case in [DNBS06]. Variable sampling strategies have been introduced in [CWG23] to stabilize nonholonomic systems linearized about their equilibrium points. In [M$^+$21], a feedback passivation controller is implemented in discrete time to match energy consumption at all sampling instants along the closed-loop system. Sampled-data control based on discrete-time equivalent models is

proposed for a class of nonlinear time-delay systems in [JDLY19]. A variable-rate digital feedback control algorithm employing a series expansion is developed in [JCD17] to preserve the stability of continuous-time controllers at sampling instants. In [MMMANC22], a passivating and stabilizing controller is introduced for discrete-time nonlinear systems via energy balancing by assigning a target energy profile at all sampling instants. The combination of discrete- and continuous-time elements is utilized in [HASH14] to analyze passivity and stability of a one DoF discrete system with time delay.

Discrete-time controllers have also been explored in spacecraft control applications. In [NP22], a guidance algorithm based on feedback linearization is developed, incorporating a modulation scheme with adaptive control gains for discrete-variable actuation. An adaptive robust control approach utilizing disturbance estimation as feed-forward to attenuate disturbance effects is presented in [Hom22]. In [PP23], a saturated feedback law for propulsion is designed with quasi-global analytical stability properties for nonlinear orbit control. A discrete-time nonlinear attitude tracking controller achieving semiglobal practical asymptotic stability, while accounting for sampling effects of digital control, is introduced in [Ike17]. An adaptive sliding mode controller ensuring uniformly ultimately bounded stability in the presence of actuator faults and disturbances is demonstrated in [W$^+$23]. In [C$^+$16], a discrete-time sliding mode control method is proposed to suppress chattering for finite-time attitude tracking of spacecraft with flexible structures. Model predictive control with discontinuities and constraints is designed for the attitude dynamics of underactuated spacecraft and shown to be asymptotically stable in [PLK17]. In [TMSL24], a model predictive controller is proposed to incorporate deadband constraints, utilizing convex optimization techniques to address the discrete nature of actuators in rendezvous missions. A passivity-based multi-rate control was designed in [DS$^+$19] to tackle stability issues arising from different sampling rates of the manipulator and the spacecraft controllers.

Contributions

This chapter examines the design and analysis of a multi-rate combined control strategy for a multi-DoF system. Unlike previous studies, this work explicitly addresses the coupling between subsystems operating at different control rates. The study focuses on an orbital manipulator in which the spacecraft base is actuated at a low rate (e.g., below 10 Hz) and the manipulator at a high rate (e.g., 1 kHz). In contrast to the passivity-based approach in [DS$^+$19], which dissipates active energy identified by a passivity observer, the proposed method employs theoretical deduction to proactively reduce system activity. The methodology consists of two principal components. First, a combined control strategy is developed to decouple the high-rate manipulator control from the discrete control of the spacecraft. Second, a discrete controller is designed to compensate for the first-order effects resulting from the servicer's low sampling rate. This compensation is achieved by augmenting a classical proportional-derivative (PD) control scheme derived from a discrete Lyapunov analysis. The proposed controller is initially evaluated on a one-DoF system, followed by an assessment of its

operational limits for the multi-DoF orbital manipulator.

The contributions of this chapter can be summarized as:

- A novel combined control strategy applied to an orbital manipulator operated under a multi-rate control scheme. This considers low-rate (e.g., below 10 Hz) control of spacecraft and high-rate (e.g., 1 kHz) control of manipulator.
- A novel sampling-aware discrete control that accounts for first-order sampling effects due to low-rate spacecraft control.
- Validation and analysis in simulation of the performance of the proposed multi-rate combined controller compared to different baselines.
- Validation of the proposed multi-rate combined controller using HIL experiments.

This chapter is based on the work published in [VDSO26b].

5.2 Control strategy

This study addresses a regulation task in which a classical proportional-derivative (PD) control law is applied to both the manipulator joints, operating at 1 kHz, and the spacecraft base, operating at 3 Hz. The scenario illustrated in Figure 5.2 demonstrates that, in comparison to the quasi-continuous case (row I. of Figure 5.2), the system exhibits instability under multi-rate operation (row II. of Figure 5.2). The low-rate discrete actuation of the base induces instability in the spacecraft, which subsequently affects the manipulator. The scenario considers the multi-rate control of an orbital manipulator under the following assumptions.

A1. The manipulator is controlled at a high sampling frequency (e.g., 1 kHz) and, therefore, can be considered quasi-continuous in nature.

A2. The servicer spacecraft is controlled at a low sampling rate (e.g., below 10 Hz) and, therefore, can be considered discrete in nature.

A3. The manipulator has a significantly lower mass and higher control gain compared to the spacecraft, thus resulting in fast and slow dynamic time-scales, respectively.

The objective of this work is to design and analyze the operational limits of a sampling-aware, multi-rate combined control strategy to address such instabilities. The control strategy employs a two-level hierarchy to address the multi-rate control problem:

i A high-rate manipulator controller actively compensates for disturbances induced by the spacecraft's discrete control actions.

ii A low-rate spacecraft based on discrete Lyapunov analysis to counteract first-order energy leaks from low sampling rates.

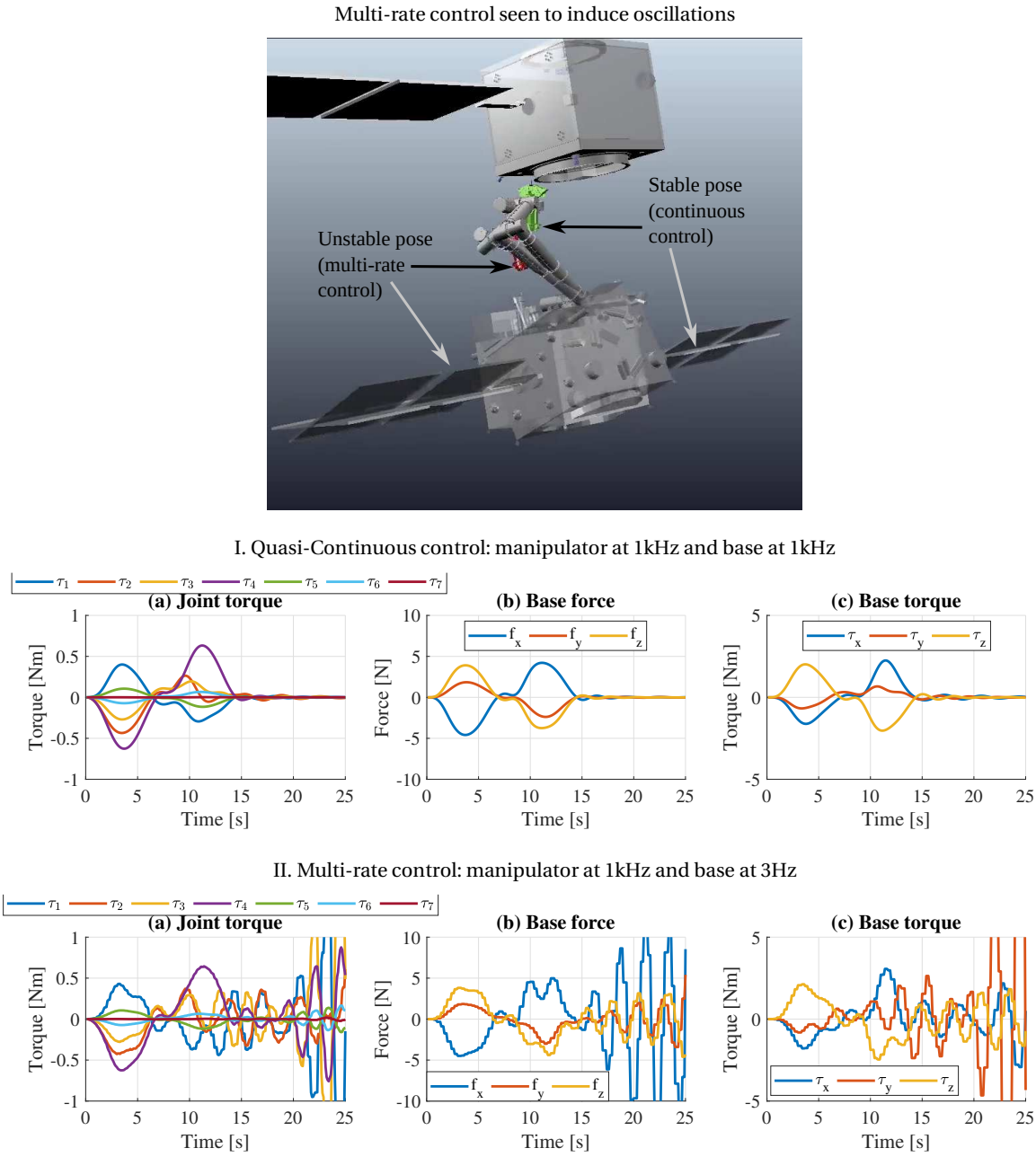

Figure 5.2: *Problem statement* – exemplary scenario showing stable vs. unstable behaviour using quasi-continuous (row I.) vs. multi-rate (row II.) control of an orbital manipulator with 7 joints. Actuator profiles compared for (a) joint torques (b) base forces and (c) base torques.

By partitioning the control design between fast (manipulator) and slow (spacecraft) subsystems, the strategy isolates dynamic interactions while addressing control rate disparities. The proposed control strategy for multi-rate combined control is summarized in Table 5.1 showing the hierarchy that shall be used to enhance performance. The nonlinear coupled dynamics of a spacecraft base equipped with an n-DoF manipulator is considered as in (2.5).

Table 5.1: *Proposed strategy* – for multi-rate combined control in decreasing order of priority.

Task		**Multi-rate strategy**
T1:	*Subsystem*	*Manipulator joints*
	Objective	High-rate control of manipulator joints decoupled from spacecraft
T2:	*Subsystem*	*Spacecraft base*
	Objective	Low-rate control of spacecraft pose compensating for energy-leaks

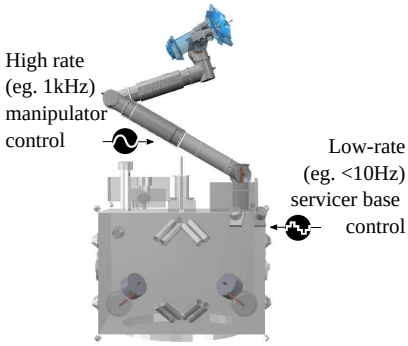

5.3 Controller design

This section first presents the high-rate control of the manipulator in the continuous domain, followed by the low-rate control of the spacecraft base in the discrete domain. Given the hybrid nature of the control domains, the control laws are explicitly formulated for each respective domain. The control strategy prioritizes manipulator control for high-precision tasks by decoupling acceleration from spacecraft actuation. Finally, the low-rate control of the spacecraft is designed using decoupled dynamics based on discrete Lyapunov analysis. The control hierarchy is shown to be equivalent to that obtained via the augmented task-based approach seen in Chapter 3 and Chapter 4.

5.3.1 High-rate manipulator control

Given that the manipulator is controlled at a high rate (e.g., 1 kHz), it is appropriate to model the system in continuous time. For designing the high-rate manipulator control, the manipulator dynamics shall first be decoupled from the base acceleration. This decoupling is achieved by substituting $\dot{\boldsymbol{\nu}}_b$ from the top row into the manipulator dynamics in the bottom row of (2.5) to obtain:

$$\text{(5.1)} \qquad \text{Manipulator dynamics :} \qquad \text{T1 :} \quad \boldsymbol{\Lambda}_{qq}\ddot{\boldsymbol{q}} + \boldsymbol{\mu}_{qq}\dot{\boldsymbol{q}} + \boldsymbol{\mu}_{qb}\boldsymbol{\nu}_b = \boldsymbol{\tau}_m - \boldsymbol{M}_{bm}^T\boldsymbol{M}_{bb}^{-1}\boldsymbol{F}_b$$

where,

$$\begin{aligned}\boldsymbol{\Lambda}_{qq} &= \boldsymbol{M}_{mm} - \boldsymbol{M}_{bm}^T\boldsymbol{M}_{bb}^{-1}\boldsymbol{M}_{bm},\\ \boldsymbol{\mu}_{qq} &= \boldsymbol{C}_{mm} - \boldsymbol{M}_{bm}^T\boldsymbol{M}_{bb}^{-1}\boldsymbol{C}_{bm},\\ \boldsymbol{\mu}_{qb} &= \boldsymbol{C}_{mb} - \boldsymbol{M}_{bm}^T\boldsymbol{M}_{bb}^{-1}\boldsymbol{C}_{bb}.\end{aligned}$$

Here, the passivity property, $\dot{\boldsymbol{\Lambda}}_{qq} = \boldsymbol{\mu}_{qq} + \boldsymbol{\mu}_{qq}^T$ holds. The dynamics described in (5.1) are analogous to the generalized dynamics of a floating-base manipulator [UY87], except for the presence of non-zero momentum resulting from base actuation. Analysis of (5.1) indicates that the disturbance torque on the manipulator due to base actuation is represented by $\boldsymbol{M}_{bm}^T\boldsymbol{M}_{bb}^{-1}\boldsymbol{F}_b$, whereas the

coupling torque arising from floating base motion is attributed to the Coriolis acceleration terms dependent on $\boldsymbol{v}_b$. Based on these observations, a control law is formulated to achieve dynamic decoupling [MDSGO20] of the manipulator's control task from the base by selecting,

$$\text{High-rate : manipulator control} \qquad \boldsymbol{\tau}_m = \underbrace{\boldsymbol{K}_{Pm}\Delta\boldsymbol{q} - \boldsymbol{K}_{Dm}\dot{\boldsymbol{q}}}_{\boldsymbol{\tau}_{PD}} + \underbrace{\boldsymbol{M}_{bm}^T\boldsymbol{M}_{bb}^{-1}\boldsymbol{F}_b}_{\boldsymbol{\tau}_F} + \underbrace{\boldsymbol{\mu}_{qb}\boldsymbol{v}_b}_{\boldsymbol{\tau}_v} \tag{5.2}$$

Here, $\boldsymbol{K}_{Pm}, \boldsymbol{K}_{Dm} \in \mathrm{R}^{n\times n}$ are the proportional and derivative (PD) gains, respectively, while $\Delta\boldsymbol{q} = \boldsymbol{q}^d - \boldsymbol{q} \in \mathrm{R}^n$ represents the joint errors of the manipulator relative to the desired joint angles $\boldsymbol{q}^d$. The control law in (5.2) achieves decoupling of the manipulator from the base dynamics through the terms $\boldsymbol{\tau}_F$ and $\boldsymbol{\tau}_v$. Notably, the control law in (5.2) is consistent with prioritizing the manipulator task by projecting the base control task into its nullspace (details discussed in Section 5.3.6).

5.3.2 Stability of the high-rate control

Proposition 3. *Consider the system* (2.5) *with the control law* (5.2)*. Assume that the stiffness and damping gains* $\boldsymbol{K}_{Pm}$ *and* $\boldsymbol{K}_{Dm}$ *are symmetric and positive-definite. Then, the control law in* (5.2) *results in the equilibrium* $\Delta\boldsymbol{q}, \dot{\boldsymbol{q}} = \boldsymbol{0}$ *being asymptotically stable.*

Proof. Consider the continuous-time positive definite candidate Lyapunov function,

$$V_q = \frac{1}{2}\dot{\boldsymbol{q}}^T\boldsymbol{\Lambda}_{qq}\dot{\boldsymbol{q}} + \frac{1}{2}\Delta\boldsymbol{q}^T\boldsymbol{K}_{Pm}\Delta\boldsymbol{q} \tag{5.3}$$

Its time-derivative along a trajectory governed by the dynamics in (5.1) results in,

$$\dot{V}_q = \dot{\boldsymbol{q}}^T\left(\boldsymbol{\tau}_m - \boldsymbol{K}_{Pm}\Delta\boldsymbol{q} - \boldsymbol{M}_{bm}^T\boldsymbol{M}_{bb}^{-1}\boldsymbol{F}_b - \boldsymbol{\mu}_{qb}\boldsymbol{v}_b\right) \tag{5.4}$$

where, the passivity property $\dot{\boldsymbol{\Lambda}}_{qq} = \boldsymbol{\mu}_{qq} + \boldsymbol{\mu}_{qq}^T$ is used. Therefore, substituting the control law (5.2) results in $\dot{V}_q = -\dot{\boldsymbol{q}}^T\boldsymbol{K}_{Dm}\dot{\boldsymbol{q}}$ which is negative semi-definite. This allows to conclude stability and boundedness of the manipulator states. Furthermore, application of LaSalle's invariance principle establishes the asymptotic stability of the equilibrium $\Delta\boldsymbol{q}, \dot{\boldsymbol{q}} = \boldsymbol{0}$. □

5.3.3 Low-rate base control

The proposed approach begins by discretizing the base dynamics within the set where manipulator errors have converged. A sample-and-hold discrete controller, when designed using these discretized dynamics, can result in energy leaks [SSVdSF05] due to mismatches between the physical and virtual energies of the continuous plant and the discrete controller at sampling instants. To address these sampling effects up to the first order, a discrete Lyapunov-based controller is developed.

The base dynamics from (2.5) are considered under the condition that the manipulator states have converged, specifically when $\Delta\boldsymbol{q}, \dot{\boldsymbol{q}} = \boldsymbol{0}$.

(5.5) $$\text{Base dynamics}: \quad \text{T2}: \quad \boldsymbol{M}_{bb}\dot{\boldsymbol{v}}_b + \boldsymbol{C}_{bb}\boldsymbol{v}_b = \boldsymbol{F}_b$$

Note that the passivity property, $\dot{\boldsymbol{M}}_{bb} = \boldsymbol{C}_{bb} + \boldsymbol{C}_{bb}^T$ holds. The base dynamics in (5.5), when subject to a zero-order-hold (ZOH) on the control input, can be discretized using a Taylor series expansion [KK99] as follows:

(5.6) $$\boldsymbol{v}_b[k+1] = \boldsymbol{v}_b[k] + h\dot{\boldsymbol{v}}_b[k] + \frac{1}{2!}h^2\ddot{\boldsymbol{v}}_b[k] + \ldots$$

Here, h denotes the sampling time corresponding to the actuation rate of the base, and $\dot{\boldsymbol{v}}_b[k]$, along with its higher derivatives, are computed from (5.5). To compensate for sampling effects up to the first order of h, the low-rate base control law is designed by considering $\boldsymbol{F}_b$ of the form.

(5.7) $$\boldsymbol{F}_b[k] = \boldsymbol{F}_{b0}[k] + h\boldsymbol{F}_{b1}[k]$$

where, $\boldsymbol{F}_{b0}$ represents the zero-order state-feedback control, while $\boldsymbol{F}_{b1}$ denotes the first-order control law that compensates for first-order sampling effects. The following control law is chosen:

(5.8) $$\begin{aligned}\boldsymbol{F}_{b0}[k] =& \ \boldsymbol{E}\boldsymbol{K}_{Pb}\Delta\boldsymbol{x}_b - \boldsymbol{K}_{Db}\boldsymbol{v}_b \\ \boldsymbol{F}_{b1}[k] =& -\frac{1}{2}\boldsymbol{K}_{Db}^T\boldsymbol{M}_{bb}^{-1}\boldsymbol{E}\boldsymbol{K}_{Pb}\Delta\boldsymbol{x}_b + \frac{1}{2}\dot{\boldsymbol{E}}\boldsymbol{K}_{Pb}\Delta\boldsymbol{x}_b \\ & -\frac{1}{2}(\boldsymbol{E}\boldsymbol{K}_{Pb}\boldsymbol{E}^T - \boldsymbol{K}_{Db}^T\boldsymbol{M}_{bb}^{-1}\boldsymbol{C}_{bb} - \boldsymbol{K}_{Db}^T\boldsymbol{M}_{bb}^{-1}\boldsymbol{K}_{Db})\boldsymbol{v}_b\end{aligned}$$

where $[k]$ has been omitted for all quantities on the right-hand-side for brevity. Here, $\boldsymbol{K}_{Pb}, \boldsymbol{K}_{Db} \in \mathrm{R}^{6\times 6}$ are the zero-order PD gains. The Cartesian pose error (position and orientation) of the base is $\Delta\boldsymbol{x}_b \in \mathrm{R}^6$, such that $\Delta\dot{\boldsymbol{x}}_b = -\boldsymbol{E}^T\boldsymbol{v}_b$ [1]. The design of $\boldsymbol{F}_{b0}$ and $\boldsymbol{F}_{b1}$ as in (5.8) is a consequence of discrete-Lyapunov analysis (detailed in the proof of Proposition 4 ahead) that reduces the sampling effects to the order of $\mathcal{O}(h^2)$. Finally, (5.7) with (5.8) can be equivalently re-arranged as

(5.9) Low-rate : base control

$$\begin{aligned}\boldsymbol{F}_b[k] =& \underbrace{(\boldsymbol{E}\boldsymbol{K}_{Pb} + h\boldsymbol{K}_{Pb1})}_{\bar{\boldsymbol{K}}_{Pb}}\Delta\boldsymbol{x}_b - \underbrace{(\boldsymbol{K}_{Db} + h\boldsymbol{K}_{Db1})}_{\bar{\boldsymbol{K}}_{Db}}\boldsymbol{v}_b, \\ \boldsymbol{K}_{Pb1} =& \frac{1}{2}(\dot{\boldsymbol{E}}\boldsymbol{K}_{Pb} - \boldsymbol{K}_{Db}\boldsymbol{M}_{bb}^{-1}\boldsymbol{E}\boldsymbol{K}_{Pb}), \\ \boldsymbol{K}_{Db1} =& \frac{1}{2}(\boldsymbol{E}\boldsymbol{K}_{Pb}\boldsymbol{E}^T - \boldsymbol{K}_{Db}\boldsymbol{M}_{bb}^{-1}\boldsymbol{C}_{bb} - \boldsymbol{K}_{Db}\boldsymbol{M}_{bb}^{-1}\boldsymbol{K}_{Db}).\end{aligned}$$

Note that $\bar{\boldsymbol{K}}_{Pb}$ and $\bar{\boldsymbol{K}}_{Db}$ are the sampling-aware PD gains that tend to the classical continuous-time PD gains when $h \to 0$. A schematic of the multi-rate combined controller is summarized in Figure 5.4, and a comparison can be made with the zero-order combined control in Figure 5.3, which leads to the problem of instability, as shown in Figure 5.2. The particular structures of $\boldsymbol{F}_{b0}$ and $\boldsymbol{F}_{b1}$ in (5.8) are dictated by discrete-Lyapunov analysis and the detailed argument is given in the proof of Proposition 4 ahead.

[1] Here, $\boldsymbol{E} = \mathrm{diag}(\boldsymbol{I}_3, \frac{1}{2}(\Delta\eta\boldsymbol{I}_3 + S(\Delta\boldsymbol{\epsilon})))$, where $\Delta\eta, \Delta\boldsymbol{\epsilon}$ are the scalar, vector parts of the error quaternion and $S(\cdot)$ is the skew-symmetric cross-product operator [CNSV99].

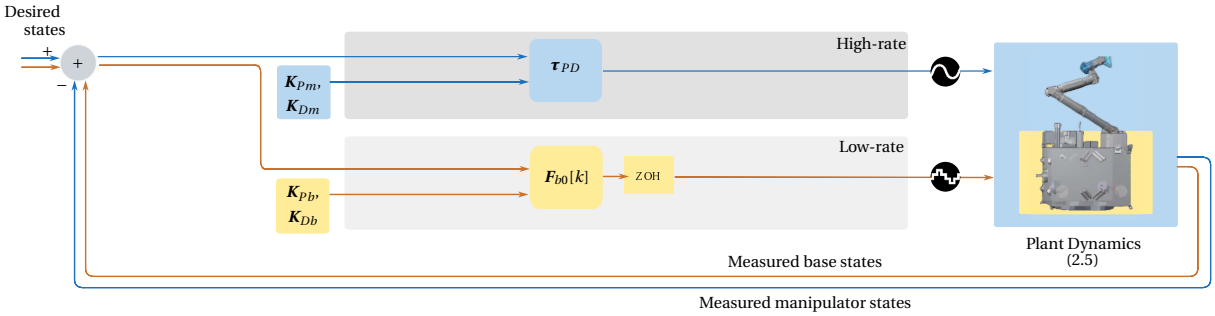

Figure 5.3: *0th-order multi-rate control* – block diagram of the combined control used for problem statement in Figure 5.2 can be compared against the proposed controller in Figure 5.4. The blocks/signals in blue and yellow associate with high- and low-rate control, respectively.

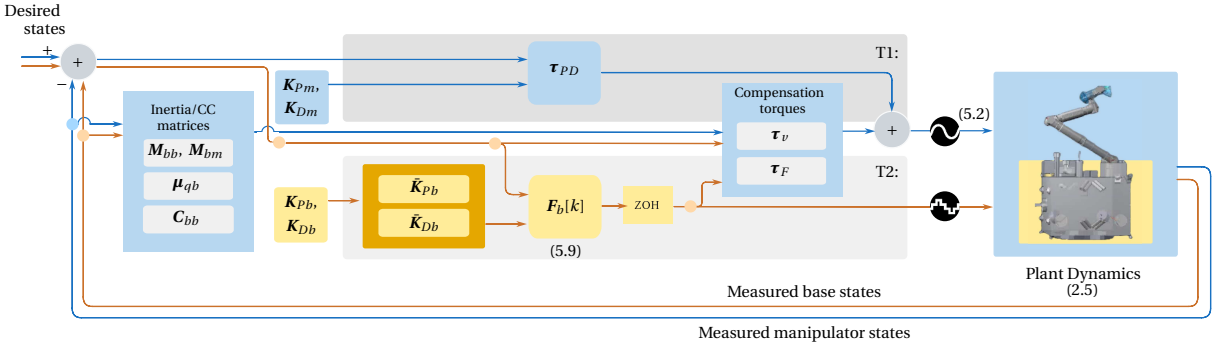

Figure 5.4: *1st-order (sample-aware) multi-rate control* – block diagram of the proposed high-rate manipulator control (5.2) and low-rate base control (5.9).

5.3.4 Stability of the low-rate control

Proposition 4. *Consider the dynamics in* (5.5) *in the set* $\Delta\boldsymbol{q}, \dot{\boldsymbol{q}} = \mathbf{0}$ *discretized using the Taylor series as per* (5.6) *with the control law in* (5.9). *The stiffness and damping gains* $\boldsymbol{K}_{Pb}$ *and* $\boldsymbol{K}_{Db}$ *are symmetric and positive-definite. Then, neglecting higher-order terms, the control law in* (5.9) *results in the equilibrium* $\Delta\boldsymbol{x}_b, \boldsymbol{v}_b = 0$ *being asymptotically stable conditionally to the set* $\Delta\boldsymbol{q}, \dot{\boldsymbol{q}} = \mathbf{0}$.

Proof. Consider the following positive definite candidate Lyapunov function

$$V_b = \frac{1}{2h}\boldsymbol{v}_b^T \boldsymbol{M}_{bb}\boldsymbol{v}_b + \frac{1}{2h}\Delta\boldsymbol{x}_b^T \boldsymbol{K}_{Pb}\Delta\boldsymbol{x}_b \tag{5.10}$$

in the set of the manipulator errors converged i.e. $\Delta\boldsymbol{q}, \dot{\boldsymbol{q}} = \mathbf{0}$. The Lyapunov difference equation of (5.10) in discrete-time can be written as,

$$\begin{aligned} V_b[k+1] - V_b[k] = &+ \frac{1}{2h}\boldsymbol{v}_b^T[k+1]\boldsymbol{M}_{bb}[k+1]\boldsymbol{v}_b[k+1] - \frac{1}{2h}\boldsymbol{v}_b^T[k]\boldsymbol{M}_{bb}[k]\boldsymbol{v}_b[k] \\ &+ \frac{1}{2h}\Delta\boldsymbol{x}_b^T[k+1]\boldsymbol{K}_{Pb}\Delta\boldsymbol{x}_b[k+1] - \frac{1}{2h}\Delta\boldsymbol{x}_b^T[k]\boldsymbol{K}_{Pb}\Delta\boldsymbol{x}_b[k] \end{aligned} \tag{5.11}$$

Further, consider the expansions $\boldsymbol{M}_{bb}[k+1] = \boldsymbol{M}_{bb}[k] + h\dot{\boldsymbol{M}}_{bb}[k] + \frac{1}{2!}h^2\ddot{\boldsymbol{M}}_{bb}[k] + \ldots$ and $\Delta\boldsymbol{x}_b[k+1] = \Delta\boldsymbol{x}_b[k] + h\Delta\dot{\boldsymbol{x}}_b[k] + \frac{1}{2!}h^2\Delta\ddot{\boldsymbol{x}}_b[k] + \ldots$ Applying (5.5)-(5.6) and the above expansions to (5.11), followed

by some tedious but straightforward simplifications (see Appendix E for details) result in

$$V_b[k+1] - V_b[k] = \left(\boldsymbol{v}_b - \frac{h}{2}\boldsymbol{M}_{bb}^{-1}\boldsymbol{C}_{bb}\boldsymbol{v}_b + \frac{h}{2}\boldsymbol{M}_{bb}^{-1}\boldsymbol{F}_b\right)^T (\boldsymbol{F}_b - \boldsymbol{E}\boldsymbol{K}_{Pb}\Delta\boldsymbol{x}_b)$$
$$+\frac{h}{2}\boldsymbol{v}_b^T\boldsymbol{E}\boldsymbol{K}_{Pb}\boldsymbol{E}^T\boldsymbol{v}_b - \frac{h}{2}\boldsymbol{v}_b^T\dot{\boldsymbol{E}}\boldsymbol{K}_{Pb}\Delta\boldsymbol{x}_b + \mathcal{O}(h^2) \tag{5.12}$$

where the passivity property $\dot{\boldsymbol{M}}_{bb} = \boldsymbol{C}_{bb} + \boldsymbol{C}_{bb}^T$ has been used. Considering $\boldsymbol{F}_b$ as in (5.7) and $\boldsymbol{F}_{b0}$ as in (5.8), $\boldsymbol{F}_{b1}$ can be obtained as in (5.8) to yield,

$$V_b[k+1] - V_b[k] = -\bar{\boldsymbol{v}}_b{}^T\boldsymbol{K}_{Db}\bar{\boldsymbol{v}}_b + \mathcal{O}(h^2) \tag{5.13}$$

where, $\bar{\boldsymbol{v}}_b = \boldsymbol{v}_b - \frac{h}{2}\boldsymbol{M}_{bb}^{-1}\boldsymbol{C}_{bb}\boldsymbol{v}_b + \frac{h}{2}\boldsymbol{M}_{bb}^{-1}\boldsymbol{F}_{b0}$. Neglecting higher order terms, the control law (5.9) for $\boldsymbol{F}_b$ yields (5.13) negative semi-definite, showing boundedness of the considered states. Further, applying LaSalles's invariance principle for discrete systems [LS76] it can be shown that all trajectories in the set $\Delta\boldsymbol{q}, \dot{\boldsymbol{q}} = \boldsymbol{0}$ will converge to the equilibrium $\Delta\boldsymbol{x}_b, \boldsymbol{v}_b = \boldsymbol{0}$. This allows to conclude that the equilibrium $\Delta\boldsymbol{x}_b, \boldsymbol{v}_b = \boldsymbol{0}$ is conditionally stable in the set $\Delta\boldsymbol{q}, \dot{\boldsymbol{q}} = \boldsymbol{0}$, neglecting higher order terms. □

Note that for combined stability, V_q can be considered as in (5.3) to be the semi-definite Lyapunov function of the complete system. In addition, using the conditional stability analysis in Proposition 4 and neglecting higher-order terms, the combined stability can be concluded similarly to [GK01] for discrete-time systems. Note that the proof of stability here does not imply sequential convergence; rather, it shows simultaneous convergence of hierarchical tasks [DO20]. In other words, the hierarchy is not referring to the time of convergence but the decoupling via the nullspace of the base disturbance on the manipulator.

5.3.5 Interpretation of the sample-aware control

All terms in (5.12) except $\boldsymbol{v}_b^T(\boldsymbol{F}_b - \boldsymbol{E}\boldsymbol{K}_{Pb}\Delta\boldsymbol{x}_b)$ represent sampling effects in discrete time of the continuous time plant. This phenomenon corresponds to the energy leak described in [SSVdSF05], which arises from the discrete controller's inability to respond between sampling instants. The discrete controller proposed in (5.9) reduces this energy leak to the negligible order of $\mathcal{O}(h^2)$.

The rationale for targeting the Lyapunov difference equation in (5.13) is based on the key observation that (5.12) can alternatively be interpreted as follows:

$$V_b[k+1] - V_b[k] = (\underbrace{\boldsymbol{v}_b + \frac{h}{2}\dot{\boldsymbol{v}}_b}_{\approx\boldsymbol{v}_b[k+\frac{1}{2}]})^T(\boldsymbol{F}_b - (\underbrace{\boldsymbol{E} + \frac{h}{2}\dot{\boldsymbol{E}}}_{\approx\boldsymbol{E}[k+\frac{1}{2}]})\boldsymbol{K}_{Pb}(\underbrace{\Delta\boldsymbol{x}_b - \frac{h}{2}\boldsymbol{E}^T\boldsymbol{v}_b}_{\approx\Delta\boldsymbol{x}_b[k+\frac{1}{2}]})) + \mathcal{O}(h^2) \tag{5.14}$$

while neglecting higher-order terms. With a slight abuse of notation, here the continuous time instant $t = h(k+\frac{1}{2})$ is denoted as the discrete time instant $[k+\frac{1}{2}]$, although discrete time does not strictly permit noninteger values. From (5.14) it is seen that the first-order approximation of the Lyapunov difference equation can be captured by the first-order approximation of the states at mid-sampling instant $[k+\frac{1}{2}]$. The control law in (5.9) is equivalent to $\boldsymbol{F}_b = \boldsymbol{F}_{b0} + \frac{h}{2}\dot{\boldsymbol{F}}_{b0} \approx \boldsymbol{F}_b[k+\frac{1}{2}]$,

the first-order approximation of the continuous-domain controller at mid-sampling instant, where $\boldsymbol{F}_{b1} = \frac{1}{2}\dot{\boldsymbol{F}}_{b0}$.

To summarize, the first-order discrete control law can equivalently be interpreted in the following different ways.

$$
\begin{aligned}
&\text{i)} \quad \boldsymbol{F}_b[k] = \boldsymbol{F}_{b0} + h\boldsymbol{F}_{b1} \\
&\text{ii)} \quad \boldsymbol{F}_b[k] = \boldsymbol{F}_{b0} + \frac{h}{2}\dot{\boldsymbol{F}}_{b0} \approx \boldsymbol{F}_b[k+\frac{1}{2}] \\
&\text{iii)} \quad \boldsymbol{F}_b[k] = (\boldsymbol{E}\boldsymbol{K}_{Pb} + h\boldsymbol{K}_{Pb1})\Delta\boldsymbol{x}_b - (\boldsymbol{K}_{Db} + h\boldsymbol{K}_{Db1})\boldsymbol{v}_b \\
&\text{iv)} \quad \boldsymbol{F}_b[k] = \underbrace{(\boldsymbol{E} + \frac{h}{2}\dot{\boldsymbol{E}})}_{\approx \boldsymbol{E}[k+\frac{1}{2}]}\boldsymbol{K}_{Pb}\underbrace{(\Delta\boldsymbol{x}_b + \frac{h}{2}\Delta\dot{\boldsymbol{x}})}_{\approx \Delta\boldsymbol{x}_b[k+\frac{1}{2}]} - \boldsymbol{K}_{Db}\underbrace{(\boldsymbol{v}_b + \frac{h}{2}\dot{\boldsymbol{v}}_b)}_{\approx \boldsymbol{v}_b[k+\frac{1}{2}]}
\end{aligned}
$$

The first interpretation represents the sum of zero-order and sampling-aware first-order control inputs. The second interpretation corresponds to the first-order truncation of the control signal at the mid-sampling instant $[k+\frac{1}{2}]$. The third interpretation involves the sum of zero-order and sampling-aware first-order proportional-derivative (PD) gains applied to the states at the sampling instant $[k]$. The fourth interpretation applies a PD law to the first-order truncation of the states at the mid-sampling instant.

A visual comparison of the differences between the zero-order and first-order PD laws is presented in Figure 5.5. The visualization demonstrates that the zero-order PD law both lags and leads the continuous control signal, while the first-order PD law improves this effect by approximating the control signal at the mid-sampling instant using the $h\boldsymbol{F}_{b1}$ term. A zoomed inset of the first-order PD law is further visualized in Figure 5.6 showing the projection of the gradient at the k-th instant to the mid-sampling instant $k+\frac{1}{2}$.

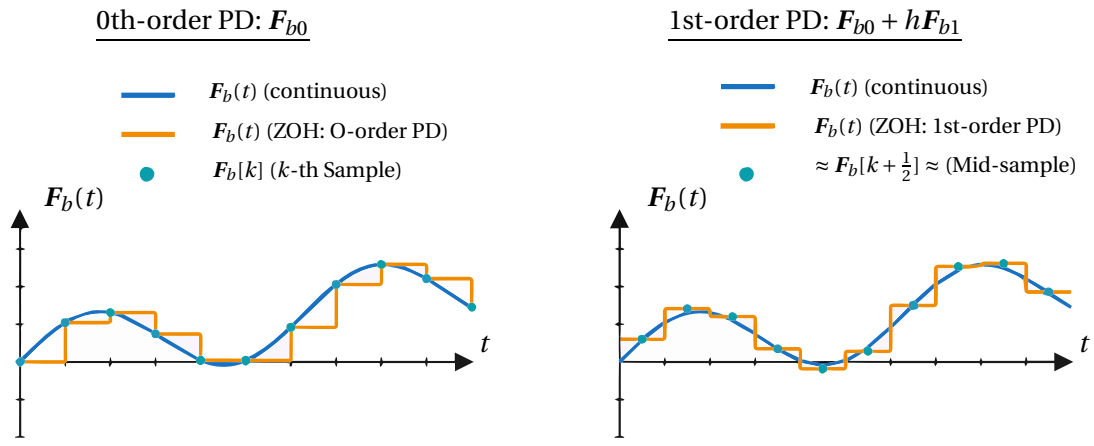

Figure 5.5: *0th- vs. 1st-order control* – visualization of 0th-order and 1st-order discrete control.

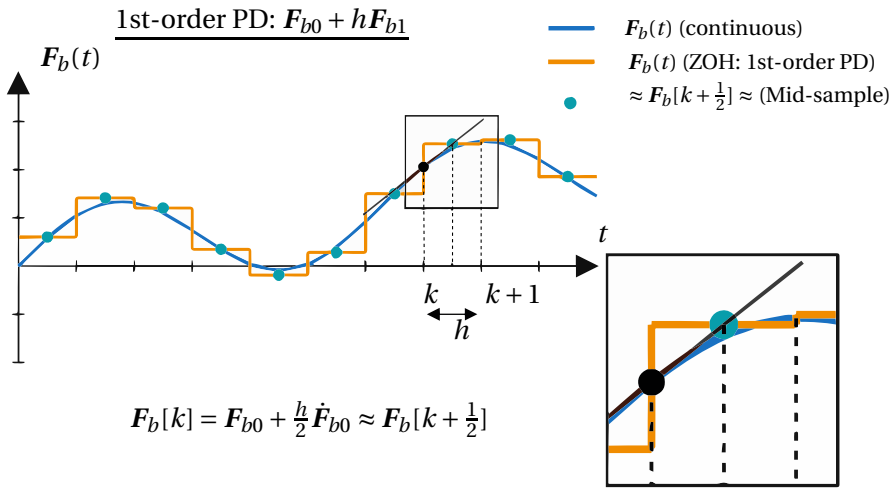

Figure 5.6: A zoomed inset of the 1st-order signal shows the projection of the gradient (solid black line) at the k-th instant (black dot) to the mid-sampling instant $k+\frac{1}{2}$ (green dot).

5.3.6 Interpretation as a hierarchical controller

The overall combined control law for the manipulator and spacecraft can be equivalently interpreted as a hierarchical control law that respects the priority defined in Table 5.1. The primary task is the manipulator joint control and the spacecraft control is relegated to its nullspace. This equivalence is demonstrated by first defining a task Jacobian $\boldsymbol{J}_T$ and the augmented Jacobian $\boldsymbol{J}_N$ [DO20] as follows:

$$\text{(5.15)} \qquad \begin{matrix}\text{T1:}\\ \text{T2:}\end{matrix} \underbrace{\begin{bmatrix}\dot{\boldsymbol{q}}\\ \boldsymbol{v}_b\end{bmatrix}}_{\boldsymbol{V}_T} = \boldsymbol{J}_T \underbrace{\begin{bmatrix}\boldsymbol{v}_b\\ \dot{\boldsymbol{q}}\end{bmatrix}}_{\boldsymbol{V}_s}, \qquad \boldsymbol{J}_T = \begin{bmatrix}\boldsymbol{J}_q\\ \boldsymbol{J}_s\end{bmatrix} = \begin{bmatrix}\boldsymbol{0}_{n\times 6} & \boldsymbol{I}_{n\times n}\\ \boldsymbol{I}_{6\times 6} & \boldsymbol{0}_{6\times n}\end{bmatrix}, \qquad \underbrace{\boldsymbol{V}_N = \begin{bmatrix}\boldsymbol{J}_q\\ \boldsymbol{J}_s\boldsymbol{N}_q\boldsymbol{N}_q^{M\dagger}\end{bmatrix}}_{\boldsymbol{J}_N}\boldsymbol{V}_s$$

The nullspace projection matrix $\boldsymbol{N}_q\boldsymbol{N}_q^{M\dagger} = \boldsymbol{I} - \boldsymbol{J}_q^{M+}\boldsymbol{J}_q$ and, the nullspace basis $\boldsymbol{N}_q$ is given by,

$$\begin{aligned}\boldsymbol{N}_q^T &= \begin{bmatrix}\boldsymbol{I}_{6\times 6} & \boldsymbol{0}_{n\times 6}\end{bmatrix}, \quad \text{such that } \boldsymbol{J}_s\boldsymbol{N}_q = \boldsymbol{0},\\ \boldsymbol{N}_q^{M\dagger} &= (\boldsymbol{N}_q^T\boldsymbol{M}\boldsymbol{N}_q)^{-1}\boldsymbol{N}_q^T\boldsymbol{M} = \begin{bmatrix}\boldsymbol{I}_{6\times 6} & \boldsymbol{M}_{bb}^{-1}\boldsymbol{M}_{bm}\end{bmatrix}\\ \boldsymbol{J}_N^{-1} &= \begin{bmatrix}\boldsymbol{J}_q^{M+} & \boldsymbol{N}_q\end{bmatrix}, \qquad \boldsymbol{J}_q^{M+} = \begin{bmatrix}-\boldsymbol{M}_{bm}^T\boldsymbol{M}_{bb}^{-1} & \boldsymbol{I}_{n\times n}\end{bmatrix}.\end{aligned}$$

The dynamics in nullspace-projected task coordinates can then be obtained by transforming the dynamics in (2.7) using $\boldsymbol{J}_N$ and $\boldsymbol{J}_T$ from (5.15) to get:

$$\text{(5.16)} \qquad \begin{matrix}\text{Nullspace-projected}\\ \text{task dynamics :}\end{matrix} \quad \begin{matrix}\text{T1:}\\ \text{T2:}\end{matrix} \underbrace{\begin{bmatrix}\boldsymbol{\Lambda}_{qq} & \boldsymbol{0}\\ \boldsymbol{M}_{bm} & \boldsymbol{M}_{bb}\end{bmatrix}}_{\boldsymbol{\Lambda}'} \underbrace{\begin{bmatrix}\ddot{\boldsymbol{q}}\\ \dot{\boldsymbol{v}}_b\end{bmatrix}}_{\dot{\boldsymbol{V}}_T} + \underbrace{\begin{bmatrix}\boldsymbol{\mu}_{qq} & \boldsymbol{\mu}_{qb}\\ \boldsymbol{C}_{bm} & \boldsymbol{C}_{bb}\end{bmatrix}}_{\boldsymbol{\mu}'} \underbrace{\begin{bmatrix}\dot{\boldsymbol{q}}\\ \boldsymbol{v}_b\end{bmatrix}}_{\boldsymbol{V}_T} = \underbrace{\begin{bmatrix}\boldsymbol{\tau}_m - \boldsymbol{M}_{bm}^T\boldsymbol{M}_{bb}^{-1}\boldsymbol{F}_b\\ \boldsymbol{F}_b\end{bmatrix}}_{\boldsymbol{J}_N^{-T}\boldsymbol{\Gamma}}$$

$$\text{where,} \qquad \boldsymbol{\Lambda}' = \boldsymbol{J}_N^{-T}\boldsymbol{M}\boldsymbol{J}_T^{-1}, \qquad \boldsymbol{\mu}' = \boldsymbol{J}_N^{-T}\boldsymbol{C}\boldsymbol{J}_T^{-1} + \boldsymbol{J}_N^{-T}\boldsymbol{M}\frac{d}{dt}(\boldsymbol{J}_T^{-1}).$$

Notably, it can be observed that the dynamics of the hierarchically prioritized task T1 in (5.16) is identical to the decoupled manipulator dynamics in (5.1). Further, the dynamics of the spacecraft T2, in the set where the manipulator states are converged, reduces to the dynamics used in (5.5).

Furthermore, the manipulator control law in (5.2) is equivalent to the augmented Jacobian-transpose $\boldsymbol{J}_N^T$ control designed for task convergence of the hierarchical dynamics in (5.16). This can be shown by comparing (5.2) with a decoupled impedance control law for T1 designed as follows:

(5.17) Control in actuator coordinates :
$$\boldsymbol{\Gamma} = \underbrace{\boldsymbol{J}_q^T \boldsymbol{\tau}_{PD}}_{\boldsymbol{\Gamma}_{\mathrm{T1}}} + \underbrace{\boldsymbol{N}_q^{T_{M\dagger}} \boldsymbol{N}_q^T \boldsymbol{J}_s^T \boldsymbol{F}_b}_{\boldsymbol{\Gamma}_{\mathrm{T2}}} + \underbrace{\boldsymbol{J}_q^T \boldsymbol{\mu}_{qb} \boldsymbol{\nu}_b}_{\boldsymbol{\Gamma}_{\mu}}$$
$$\boldsymbol{\Gamma}_{\mathrm{T2}} = \begin{bmatrix} \boldsymbol{F}_b \\ \boldsymbol{M}_{bm}^T \boldsymbol{M}_{bb}^{-1} \boldsymbol{F}_b \end{bmatrix} = \begin{bmatrix} \boldsymbol{F}_b \\ \boldsymbol{\tau}_F \end{bmatrix}, \text{ and } \boldsymbol{\Gamma}_{\mu} = \boldsymbol{J}_q^T \boldsymbol{\tau}_v$$

This formulation is identical to the control law derived in (5.2) using the elimination and substitution method. From (5.17), it is evident that the decoupling term $\boldsymbol{\tau}_F$ in (5.2) corresponds to the spacecraft wrench $\boldsymbol{F}_b$ designed in the second hierarchy (T2) by projecting it into the nullspace of task T1, namely the manipulator joints. The spacecraft control $\boldsymbol{F}_b$ in the continous domain is the input with a Zero-Order Hold (ZOH) applied to the low-rate control law designed in (5.9).

It is important to note that hierarchical stability does not imply sequential or accelerated convergence to the equilibrium point for both the manipulator and the base. Instead, it ensures simultaneous convergence of the hierarchical tasks, as demonstrated in [DO20] for a comparable scenario. In the manipulator controller design presented in (5.2), $\boldsymbol{\tau}_F$ and $\boldsymbol{\tau}_v$ serve to decouple the manipulator from the base dynamics, thereby establishing a hierarchy that prioritizes the manipulator task. The PD term applied to the manipulator and $\boldsymbol{\tau}_F$ operate at a high rate, effectively decoupling the dominant disturbance from the spacecraft on the manipulator, regardless of the base sampling period. The $\boldsymbol{\tau}_v$ term provides Coriolis compensation based on low-rate measurements of $\boldsymbol{\nu}_b$, which results in minor Coriolis couplings. Consequently, $\boldsymbol{\tau}_F$ and $\boldsymbol{\tau}_v$ make the manipulator convergence independent of the base sampling period. Thus, the hierarchy is defined not by the rate of convergence, but by the mitigation of coupling disturbances within its nullspace [DO20].

5.4 Low-dimensional benchmark of sampled-data controller

This section presents the validation of the novel discrete controller applied to a one-degree-of-freedom (1-DoF) double-integrator plant for simplicity and clarity. This approach provides insight into the operational bounds of the discrete controller, which has been enhanced to address first-order sampling effects. The results establish a baseline for anticipating the controller's performance in nonlinear multi-degree-of-freedom (multi-DoF) scenarios.

The results of the discrete controller in (5.9) applied to a 1-DoF case are presented for an exemplary plant with mass $M = 5\mathrm{kg}$ and stiffness $K_P = 25\mathrm{N/m}$ (see Appendix F for details). Stability in response to a step input is compared between the 0th-order ($\boldsymbol{F}_{b0}$) and 1st-order ($\boldsymbol{F}_{b0} + h\boldsymbol{F}_{b1}$)

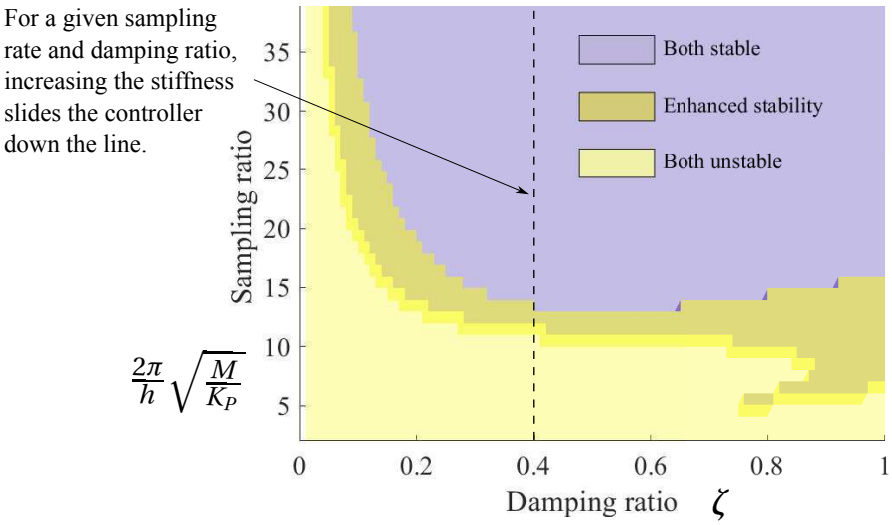

Figure 5.7: *1-DoF plant* – region of stability for the 0th-order and 1st-order PD control law.

proportional-derivative (PD) control laws, evaluated over 4000 data points across a grid of damping and sampling ratios. Stability is assessed by the location of the poles within the unit circle. The damping ratio is defined as $\zeta = K_D/(2\sqrt{K_P M})$, and the sampling ratio is ω_s/ω_n, where $\omega_s = 2\pi/h$ is the sampling frequency[2] and $\omega_n = \sqrt{K_P/M}$ is the natural frequency. The sampling frequency is normalized by the natural frequency to ensure the results are independent of the specific mass and stiffness values chosen.

The expansion of the stability boundary is illustrated in Figure 5.7 by the overlapping area between the violet and yellow regions. Within this region, the first-order PD controller stabilizes cases that are unstable under the zeroth-order PD controller. Regions characterized by very low sampling ratios or very low damping ratios are more susceptible to instability. This evaluation facilitates the a priori tuning of control gains and enables the anticipation of stability boundaries.

5.5 Validation results

This section presents simulation (SIM) and hardware-in-the-loop (HIL) results for the proposed multi-rate combined controller applied to the multi-degree-of-freedom (multi-DoF) case of an orbital manipulator. The simulation setup in Figure 5.8 (a) uses an orbital manipulator from the EROSS IOD mission [R$^+$]. The manipulator considered is the 7-DoF CAESAR arm. The hardware-in-the-loop (HIL) setup utilizes the OOS-Sim facility, as described in Section 2.1.1, which is equipped with a 7-degree-of-freedom (DoF) LWR manipulator. The DLR servicer robot, OOS-Sim, operates at 250 Hz, is capable of simulating zero-gravity dynamics at 1 kHz, and has an intrinsic facility time delay of 4 ms [A$^+$15]. The relevant dynamic/kinematic and control parameters of the two setups are summarized in Table 5.2.

[2]To avoid signal aliasing, the lower limit for sampling is known to be twice the natural frequency.

Table 5.2: SIM and HIL parameters. *Principal moment of inertia,**Euler angles in XYZ convention, †Control rate.

DYNAMIC/KINEMATIC PARAMETERS		
Parameter	**SIM**	**HIL**
Servicer mass & MOI*	360kg, $(210,77,212)\mathrm{kg\,m^2}$	200kg, $(100,100,100)\mathrm{kg\,m^2}$
Manipulator arm	7-DoF CAESAR robot [BGH+18]	7-DoF Light Weight Robot (LWR)
Manipulator rate†	1kHz	1kHz
Base rate†	3Hz	5Hz
Initial joint angles	$(90,75,0,160,0,0,120)$deg	$(-6,62,0,120,4,-38-7)$deg
Delta arm pose**	$(10,-25,10,-45,10,25,10)$deg	$(0,-47,4,-28,-1,-15,3)$deg
Delta base pose**	$(-0.3,0.1,0.2)$m, $(-8,4,12)$deg	$(0.1,0.0,-0.1)$m, $(-10,0,0)$deg

CONTROLLER PARAMETERS			
T#	$\boldsymbol{K}$.	**SIM**	**HIL**
T1	$\boldsymbol{K}_{Pm}$	$[400,800,400,400,100,100,40]\mathrm{Nm\,rad^{-1}}$	$[150,150,135,100,50,50,50]\mathrm{Nm\,rad^{-1}}$
	$\boldsymbol{K}_{Dm}$	$[300,300,200,200,20,20,10]\mathrm{Nm\,rad^{-1}s}$	$[20,30,1,1,1,1,1]\mathrm{Nm\,rad^{-1}s}$
T2	$\boldsymbol{K}_{Pb}$	$[2500,2500,2500]\mathrm{Nm^{-1}}$, $[1000,1000,1000]\mathrm{Nm\,rad^{-1}}$	$[220,220,220]\mathrm{Nm^{-1}}$, $[120,120,120]\mathrm{Nm\,rad^{-1}}$
	$\boldsymbol{K}_{Db}$	$[250,250,250]\mathrm{Nm^{-1}s}$, $[100,100,100]\mathrm{Nm\,rad^{-1}s}$	$[305,305,305]\mathrm{Nm^{-1}s}$, $[170,170,170]\mathrm{Nm\,rad^{-1}s}$

The SIM results first demonstrate the effectiveness of the proposed multi-rate combined control in addressing the instability described in the problem statement (Figure 5.2). Next, HIL results using the OOS-Sim setup in Figure 5.8 (b) are presented for an exemplary maneuver. Further results in simulation test the robustness and sensitivity of the designed control across different manipulator poses against the zero-order control scheme for a range of damping and sampling ratios. The 1st-order approximation of the energy leaks used in the derivation of the discrete control law is evaluated empirically for the SIM scenario. The significance of the compensation torques designed for high-rate manipulator control is examined. Lastly, the performance of the proposed first-order multi-rate combined control is compared to a passivity-based control scheme in [DS+19].

5.5.1 Simulation (SIM) results

The result of applying the low-rate 0th-order PD control on the base and high-rate PD control on the manipulator without any decoupling was shown in the problem statement in Figure 5.2. The manipulator is controlled at a high-rate of 1kHz and the servicer spacecraft is controlled at a low-rate of 3Hz, i.e. $h = 0.33$s. The initial and final poses of this maneuver are shown in Figure 5.8 (a). The result with the proposed multi-rate combined control laws in (5.2) and (5.9) is presented in Figure 5.9 for

(a) SIM

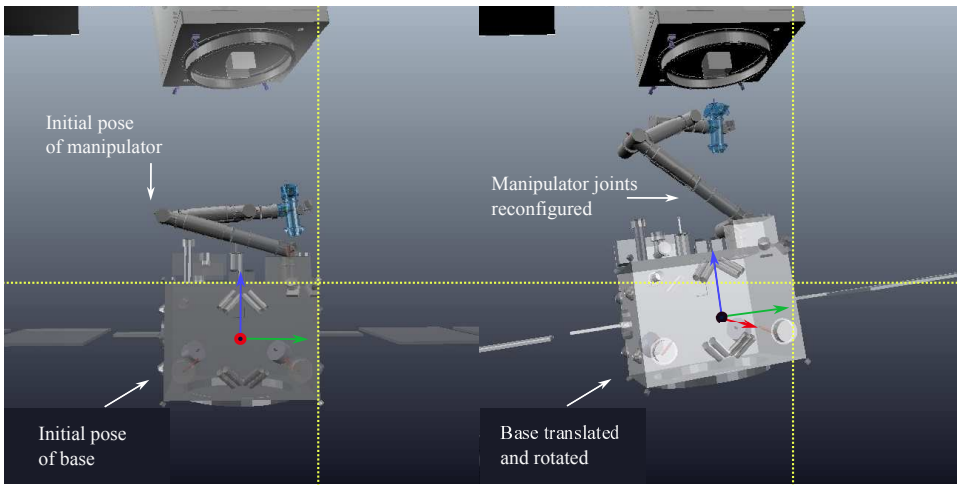

(b) HIL

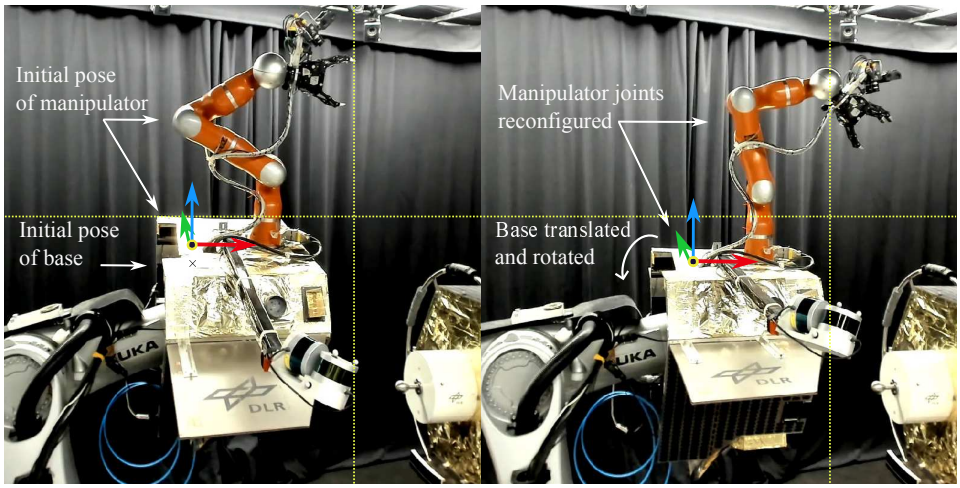

Figure 5.8: Exemplary maneuvers showing initial and final poses in (a) simulation and (b) with hardware-in-the-loop (DLR, OOS-Sim) using 7-DoF manipulators. Dotted lines serve as reference for base and manipulator motion. A link to experimental videos is given in Appendix G, Table G.1.

comparison. It can be seen from Figure 5.9 that the proposed method stabilizes the scenario in the problem statement in a region of low sampling ratio (≈7.5) and damping ratio (≈0.12).

5.5.2 Experimental (HIL) results

The manipulator is controlled at a high-rate of 1kHz and the servicer spacecraft is controlled at a low-rate of 5Hz(h = 0.2s). For the gains of the low-rate base control in Table 5.2, a control rate of 5Hz results in a sampling ratio ≈ 31. The scenario considers an exemplary maneuver of the servicer spacecraft along with the manipulator. The initial and final poses of this maneuver are shown in Figure 5.8 (b).

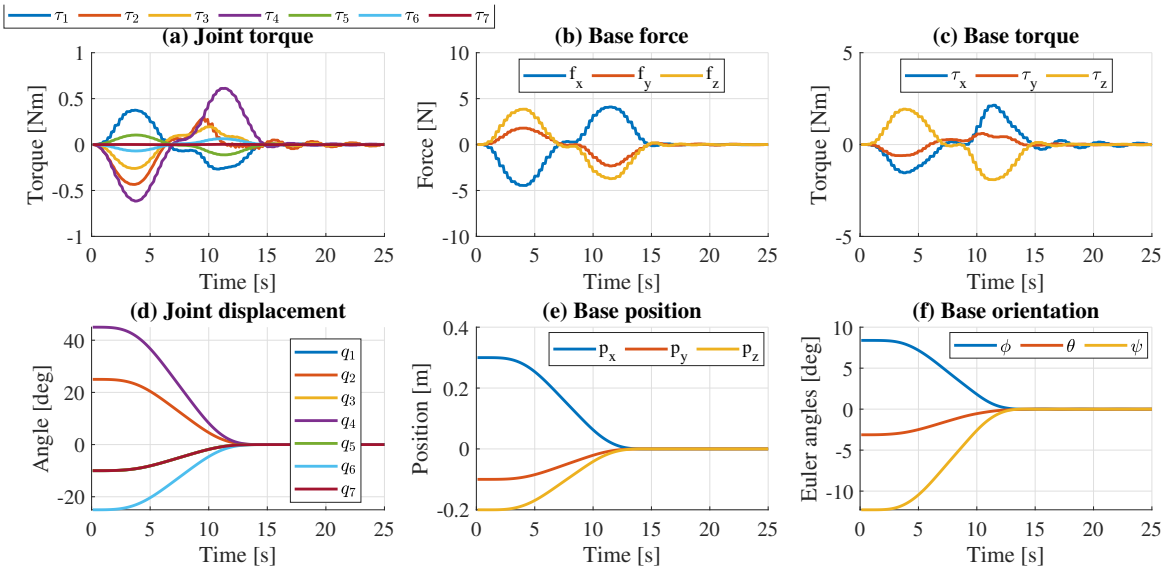

Figure 5.9: *SIM results* – stabilized actuation profiles and trajectories using proposed method for scenario in problem statement, Figure 5.2. For ease of presentation, Euler angles (ϕ, θ, ψ in the XYZ convention) are reported.

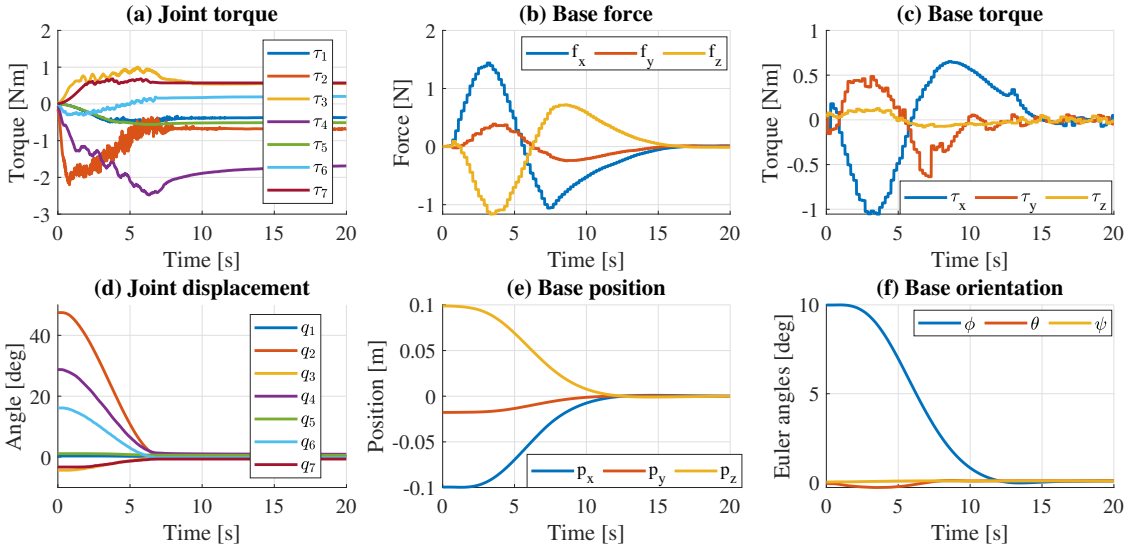

Figure 5.10: *HIL results* – actuation profiles and trajectories for exemplary maneuver performed using proposed method with low-rate (5Hz) base control and high-rate (1kHz) manipulator control.

The application of the proposed multi-rate combined control laws in (5.2) and (5.9) to the scenario is illustrated in Figure 5.10. The multi-rate control approach stabilizes the combined motion of the spacecraft base and manipulator, achieving the desired setpoint with a maximum error of 0.9deg per joint and 10^{-4}m and 0.1deg in norm for the base. The steady-state residual torques ob-

Table 5.3: *HIL results* – efficiency of base actuation at different sampling rates with damping ratio of 0.7. *Percentage reduction in impulse compared using the 1st-order versus 0th-order PD.

Base rate	Sampling ratio	Linear* [%]	Angular* [%]
5 Hz	31	-1	-4
3 Hz	19	-7	-11
2 Hz	13	-3	-7
1 Hz	6	-21	-34

served in Figure 5.10 (a) are attributed to joint friction. The discrete actuation of the base at 5 Hz is evident from the staggered profiles of force and torque in Figure 5.10 (b) and (c). The proposed method reduces the final linear and angular impulses by 1% and 4%, respectively, compared to the 0th-order PD control.

The maneuver was repeated using lower sampling rates of 3Hz, 2Hz, and 1Hz for the base control. The corresponding impulse reductions are reported in Table 5.3, which compares the proposed first-order PD control to the 0th-order control. The results indicate that the proposed method demonstrates greater efficiency in the conducted experiments. Furthermore, the nonlinear reduction of impulse across different base control rates highlights the nonlinear nature of the system dynamics.

5.5.3 Robustness and sensitivity analysis

To cover a broader range of dynamic motions a set of simulations were performed for randomized poses sampled from a uniform distribution across a grid of damping [AS$^+$03] and sampling ratios for the base controller. The parameter grid includes damping ratios from $[0.1, 0.9]$ in increments of 0.1 and sampling ratios from $[3, 33]$ in increments of 3. With a natural frequency of $\omega_n = \pi$rad/s, this corresponds to a frequency range of $[1.5, 16.5]$ Hz in increments of 1.5 Hz for base control. The initial manipulator pose was sampled within $\pm[130, 40, 130, 130, 130, 130, 130]$ deg, and joint displacements were randomly selected as ± 50 deg per joint. Base displacements were sampled along the surfaces of spheres with radii 0.5m and 30 deg. To ensure a fair comparison of the impulse required by different maneuvers, the norms of manipulator and base displacements were standardized, independent of initial pose and displacement direction. Selected snapshots from the grid search simulations in Figure 5.12 show the range of manipulator and base poses tested across different simulations.

For sensitivity analysis, model parameters were perturbed by up to 20% in mass, inertia, and center-of-mass. The 0th-order stiffness gain of the base controller is chosen as $\boldsymbol{K}_{Pb} = \omega_n^2 / \boldsymbol{M}_{bb}(\boldsymbol{q}(0))$ using the initial pose $\boldsymbol{q}(0)$. The manipulator gains are similarly tuned as $\boldsymbol{K}_{Pm} = \omega_n^2 / \boldsymbol{M}_{mm}(\boldsymbol{q}(0))$ and $\boldsymbol{K}_{Dm}$ set to a damping ratio of 0.7, which must not be confused with the range of damping ratios of the base controller considered for the analysis.

Among the data points generated, 80 out of 99 were stable for both controllers. A comparison of the impulse utilized for the maneuvers is presented in Figure 5.11. Notably, 93% and 89% of the

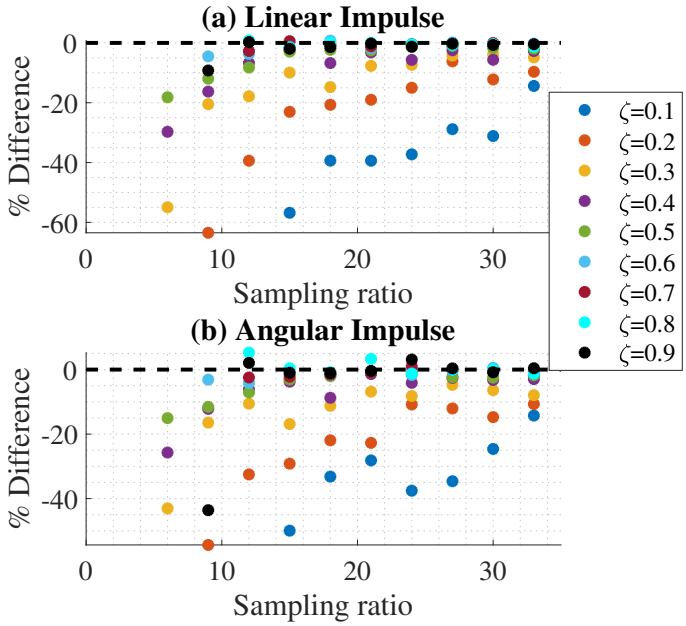

Figure 5.11: *Efficiency* – difference in (a) linear and (b) angular impulse utilized by the 0th-order vs. proposed 1st-order multi-rate control shown across increasing sampling and damping ratios.

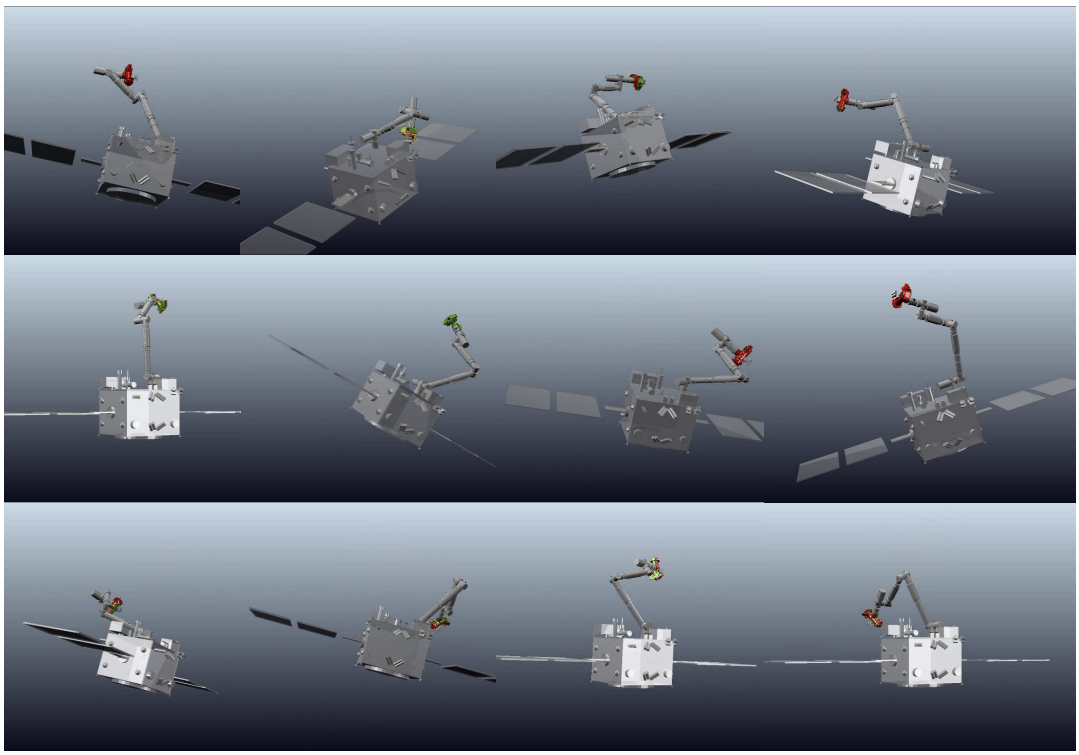

Figure 5.12: *Robustness & sensitivity analysis* – snapshots of a few examples from the grid search simulations illustrating the diversity in manipulator and base poses covered.

stable data points resulted in a reduction in linear and angular impulse consumption, respectively. The mean and standard deviation of the reduction were 9.6 Ns and 14.22 Ns for linear impulse, and 9.22 Nms and 13.21 Nms for angular impulse, respectively. The remaining stable data points, characterized by a high damping ratio ($\zeta > 0.6$), exhibited a comparable or marginal increase in impulse consumption. Therefore, the proposed method demonstrates improved performance, particularly in regions with low damping ratios.

5.5.4 Evaluation of the first-order approximation

An empirical evaluation of the 1st-order approximation has been considered using the simulation scenario in Section 5.5.1 to demonstrate the robustness of the discrete stability analysis. Figure 5.13 shows a comparison between the total Lyapunov difference equation as defined in (5.11) versus its 1st-order approximation in (5.14). The maximum error recorded in this scenario was 4.18 J/s (see Figure 5.13, left), an order of magnitude below a total of 34.68 J/s. As a measure of the cumulative error, the mean absolute error (see Figure 5.13, right) was recorded to be bounded below 0.25 J/s. This shows robust approximation by 1st-order terms in this scenario with sampling ratio of 7.5.

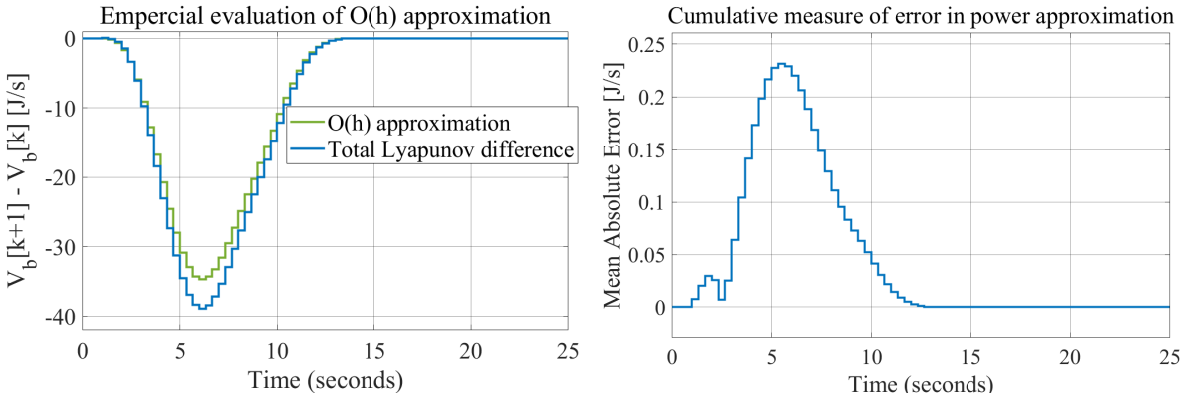

Figure 5.13: *1st-order approximation* – (left) total Lyapunov difference compared to 1st-order approximation, (right) mean absolute error between (5.11) and (5.14) bounded below 0.25 J/s.

5.5.5 Significance of manipulator compensation torques

Using identical control parameters, the effect of compensation torques ($\boldsymbol{\tau}_F$ and $\boldsymbol{\tau}_v$) in (5.2) is examined while the manipulator maintains its pose during discrete actuation of the base. As shown in Figure 5.14 (a), omitting both compensation terms leads to small joint vibrations resulting from the discrete control of the base. In contrast, Figure 5.14 (b) demonstrates that omitting only the Coriolis compensation torques yields smooth joint coupling velocities, which are two orders of magnitude lower than those observed in Figure 5.14 (a). These results indicate that the compensation torques $\boldsymbol{\tau}_F$ and $\boldsymbol{\tau}_v$ in the control law (5.2) serve to decouple the actuation and motion of the base from the manipulator.

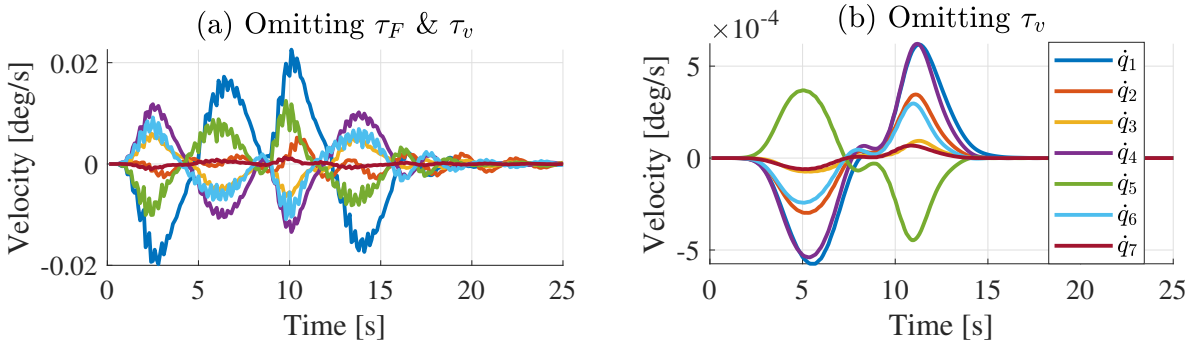

Figure 5.14: *Compensation torques* – manipulator joint velocities resulting from discrete base control while omitting (a) all compensation torques (b) only Coriolis compensation torques.

5.5.6 Comparison to a passivity-based controller

The proposed method was compared with the passivity-based multi-rate control presented in [DS+19] under identical conditions at 8 Hz. The approach in [DS+19] introduces a tracking controller equipped with a passivity observer and a passivity controller to address the energy introduced by the multi-rate process. The Passivity Observer (PO) monitors the energy flow through the system's power ports, while the Passivity Controller (PC) dissipates the necessary amount of energy, as measured by the PO, and operates as a time-varying element. When the PO detects negative energy, indicating potential instability or system activity, the PC dissipates this energy. Subsequently, the PC commands an additional force to the base controller to restore system passivity.

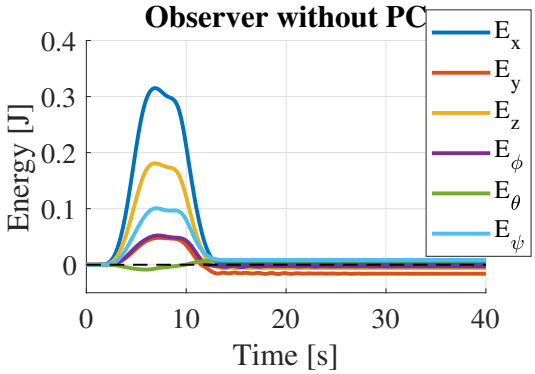

Figure 5.15: *Passivity-based control [DS+19]* – monitoring system activity via the Passivity Observer (PO). Negative values indicate system activity.

The passivity observer described in [DS+19] was implemented to monitor system activity, as illustrated in Figure 5.15. Negative energy values indicate increased system activity and potential instability (see Figure 5.15). When the passivity controller from [DS+19] is enabled for the base controller, it computes a variable damper and commands an additional force to the system to restore

passivity (see Figure 5.16 (a)). The combined operation of the passivity observer and the PC is depicted in Figure 5.16 (b). A positive energy trend indicates that the system remains passive and that all active energy has been dissipated.

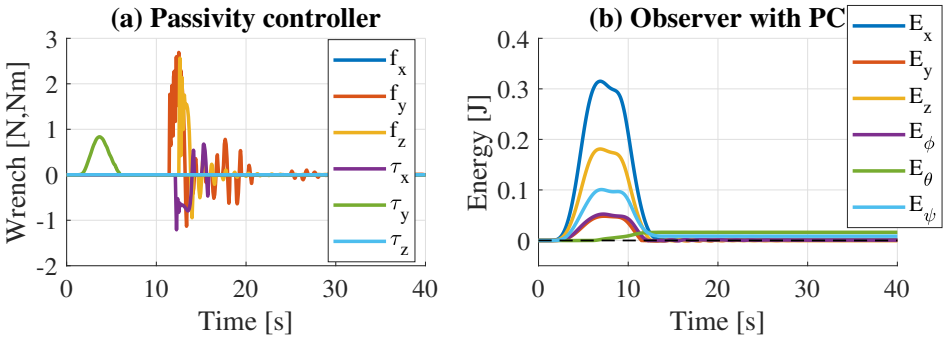

Figure 5.16: *Passivity-based control [DS+19]* – (a) Passivity Controller (PC), (b) Passivity Observer (PO) with PC. Compare PO here versus PO in Figure 5.15. Positive values of the PO indicate passivity of the system is restored.

A comparison of the impulse, defined as the integral of force and torque to measure efficiency, is shown in Figure 5.17. The method in [DS+19] exhibits maximum values of 74 Ns and 33 Nms at the end of the maneuver, whereas the proposed method achieves lower values of 46 Ns and 20 Nms. The approach in [DS+19] first observes energy and subsequently dissipates active energy via passivity control, resulting in greater impulse consumption by the system. In contrast, the proposed method acts a priori, based on theoretical deduction, to reduce system activity.

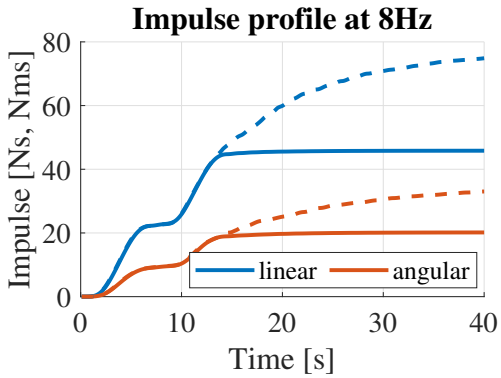

Figure 5.17: *Comparison* – impulse profile of [DS+19] (in dashed lines) versus proposed 1st-order PD (in solid lines).

5.6 Discussion and summary

This chapter proposed a multi-rate control framework to address the combined control challenges encountered during the operation of an orbital manipulator, introducing two principal innovations: the design of a discrete controller that explicitly accounts for the servicer's low sampling rate, and a unified control strategy that separates the manipulator's high-rate control from the spacecraft's discrete control. Specifically, the high-rate manipulator control is formulated in the continuous domain and decoupled from the low-rate spacecraft actuation, thereby effectively relegating the spacecraft control to the nullspace, whereas the low-rate spacecraft control is designed in the discrete domain using discrete Lyapunov analysis, thus establishing a method for hybrid control design.

The presented stability analysis further provided unique insight into the structure of the first-order sample-aware control law, revealing its relation to the first-order approximation of continuous-time states employed in a PD regulation scheme. The first-order truncation of the Lyapunov difference equation was also empirically evaluated for a low sampling ratio in Figure 5.13, corroborating the negligibility of the higher-order terms considered in the stability analysis. The proposed concept was initially validated in simulation using a one-degree-of-freedom benchmark, which demonstrated an enhanced stability boundary, Figure 5.7. Subsequent assessment with a multi-degree-of-freedom orbital manipulator using grid search simulations indicated an overall performance improvement of the sample-aware multi-rate controller compared to the zero-order PD control law in terms of impulse efficiency, Figure 5.11.

The main takeaway from the analysis and results is the insight into the performance of the multi-rate control law across different sampling rates and damping ratios. The parameterization of the results is cautiously done using the sampling ratio, i.e. the ratio between the natural frequency about the equilibrium and the sampling frequency, instead of the absolute sampling rate. This makes the analysis more meaningful, since it puts the performance in perspective with respect to the stiffness gains that dictate the natural frequency of the system. The results are consistent with the knowledge that gains and sampling rates characterized by very low sampling ratios or very low damping ratios are more susceptible to instability. The proposed method helps to enlarge the boundary of stability, given higher-order energy leaks are negligible while augmenting performance in terms of efficiency in the control effort expended.

Improvement was also shown relative to a passivity-based approach, Figure 5.17, which highlights the advantage of applying sample-aware terms a priori, based on theoretical deduction, rather than a posteriori, as in passivity-observer-based methods. The approach was further validated using a hardware-in-the-loop setup, as summarized in Table 5.3. Extensions to Cartesian control, quantized input, and time delay, which rely on power ports and energy measurements as discussed in [DSBS20] and [ABDS+16], may be considered for future work.

CHAPTER 6

GRAVITY COMPENSATION STRATEGY FOR ON-GROUND VALIDATION

The on-ground validation seen thus far used the Hardware-in-the-Loop robotic facility, OOS-Sim. Although OOS-Sim provides a versatile platform for testing six DoF floating-base dynamics with the LWR robot, the on-ground testing of space manipulators such as the CAESAR robot necessitates a different platform capable of supporting its actuators, which do not allow for testing under terrestrial gravitational loads. The torque limitations of these motors result from mission requirements that drive the design of space manipulators to prioritize reduced weight and operation in zero-gravity environments. Specifically, during on-ground operation, the manipulator must actively compensate for gravitational forces while remaining within its joint torque limits. Consequently, the manipulator's effective workspace is reduced by gravitational effects. This chapter primarily addresses gravity-compensation rather than floating dynamics in the context of on-ground testing. Previous studies, such as [MGDS+20], describe methods for emulating floating-base dynamics on fixed-base robots, which can serve as complementary to the method presented here.

This chapter proposes an optimization-based strategy for achieving gravity compensation of a space manipulator arm during on-ground testing. The approach formulates an optimization problem to minimize the motor torques acting on the manipulator arm while enabling an external carrier to track a specified force, thereby achieving full gravity compensation. The method is designed for general applicability to any robot utilizing a generic admittance-controlled carrier. Experimental results demonstrate the effectiveness of the proposed method on the DLR CAESAR space robot (see Figure 6.1), which employs a cable-suspended system to track the desired force as determined by the strategy.

The structure of the chapter is as follows. Section 6.1 reviews gravity offloading methods and highlights the contributions of the chapter. Section 6.2 outlines the challenges and the proposed strategy. Section 6.3 presents the design and analysis of an optimal gravity-compensation strategy.

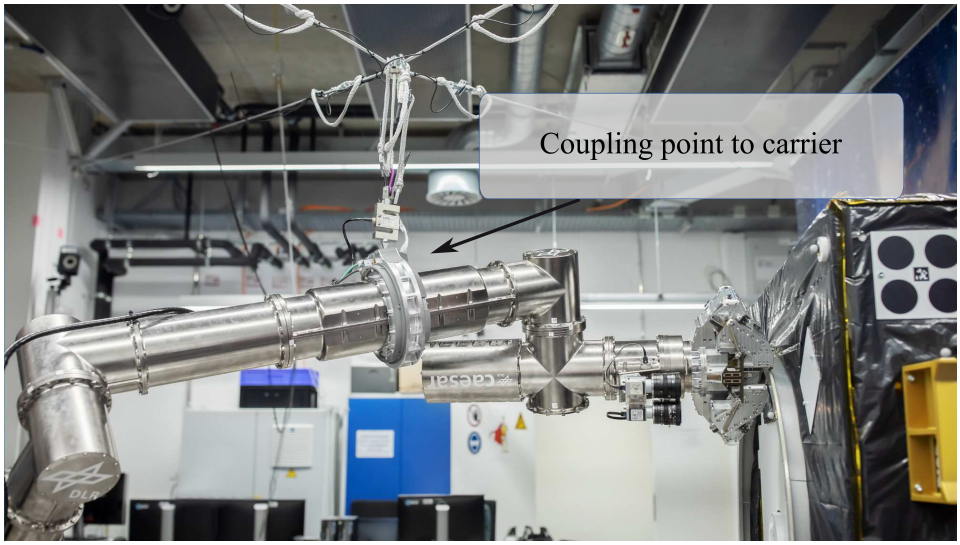

Figure 6.1: On-ground validation of a 7-DoF orbital manipulator arm (CAESAR in [BGH+18]) with an external carrier (described in Section 2.1.2) for gravity compensation.

Section 6.4 validates the method with experimental results using the CAESAR arm and a cable-suspended platform, MSS (see Section 2.1.2). Section 6.5 summarizes the results and highlights its success in the EROSS mission.

6.1 Related work and contributions

Before launch, on-ground validation of control algorithms for the orbital manipulator is necessary. However, the manipulator on the ground is subject to gravitational force, which must be actively compensated. Direct compensation at the motor level can adversely affect the manipulator's workspace during on-ground testing. Specifically, the manipulator is limited to configurations where the required joint torques do not exceed the limits established for zero-gravity operations.

Various technologies can be employed to recreate zero-gravity conditions on the ground for validating an orbital manipulator [SPH03, CJGM17]. These technologies include air bearing systems, zero-gravity parabolic flights, neutral buoyancy, hardware-in-the-loop simulators, and cable-suspended systems. Air bearing systems utilize floating platforms on a flat floor (see [UY89, MAB01, Yos94]). Pressurized air creates a thin film between the floor and the platform, compensating for the weight of moving sections such as robotic arm links. This approach has been used to test control algorithms for the Japanese free-floating robot [Yos03], the Canadarm, and the European Robotic Arm (ERA). However, air bearing systems can only simulate zero-gravity conditions in two dimensions, which include one rotational and two translational degrees of freedom [MBC+07]. In zero-gravity parabolic flights, an aircraft follows a parabolic trajectory to achieve microgravity conditions.

In [SUM+04], experiments were conducted using a zero-gravity parabolic flight for a four degree-

of-freedom robot, achieving $0.02g$ for only 20 seconds. This duration is insufficient for comprehensive validation of complex operations. Another approach for zero-gravity simulation utilizes a water pool to achieve neutral buoyancy, allowing the submerged body to float similarly to conditions in orbit. The primary advantage is the ability to achieve six-dimensional motion without time constraints [CA00]. However, fluid-induced drag forces generate hydrodynamic effects that distort the system dynamics [FAMPU14]. Hardware-in-the-loop technologies use dynamic models to reproduce desired behaviors, such as floating dynamics, on physical hardware. Typically, admittance-controlled robots equipped with force-torque sensors are employed [DSMG+21, MIG16].

In cable-suspended systems, gravity is compensated by cables that generate forces equal in magnitude but opposite in direction to the gravitational force vector [BD94]. This approach is used for on-ground demonstrations of orbital assembly tasks in an ESA project [D+22]. While [WX94] proposes a controller for modulating tension in the cable connected to a robot's counterweight, it operates only in the vertical direction. Another method for gravity compensation computes the required torques using the manipulator's dynamic model and actively commands it to the joints [SSVO08].

Contributions

Recently, the CAESAR manipulator arm was introduced as a robotic solution for performing servicing tasks in orbit [BGH+18]. The CAESAR arm features seven degrees of freedom and is specifically designed for space operations. However, during on-ground validation, its workspace is constrained by gravitational forces, which, if directly compensated at the joint level, could exceed the arm's torque limits. Therefore, a carrier system based on cable suspension is used to support the gravitational force acting on CAESAR, as illustrated in Figure 6.1.

Although cable-suspended systems are documented in the literature, they are typically utilized in scenarios involving only rigid bodies (see e.g. [BLHB20], [PMK+13], [WX94]). In these applications, the primary function of such systems is to position the rigid body within the workspace and support its weight to replicate free-floating dynamics. In contrast, an orbital manipulator constitutes a multi-body system whose inertia varies according to its configuration. Thus, the gravitational force that must be tracked by an external carrier also varies, necessitating a solution capable of adapting to the configuration-dependent loads.

This chapter proposes a strategy to achieve active gravity compensation to enable on-ground validation of an orbital manipulator. The approach allocates gravity compensation between the manipulator's internal torques and an external wrench that can be tracked by an external carrier. An optimization problem is formulated to distribute the gravitational torques between the manipulator and the carrier system. The method is presented for the general case of an orbital arm equipped with an external admittance-controlled carrier. The existence of a solution is also demonstrated in cases where the carrier lacks capability to apply all external wrench components. For validation, a cable-suspended system is employed to track the force resulting from the proposed method.

The contributions of this chapter can be summarized as:

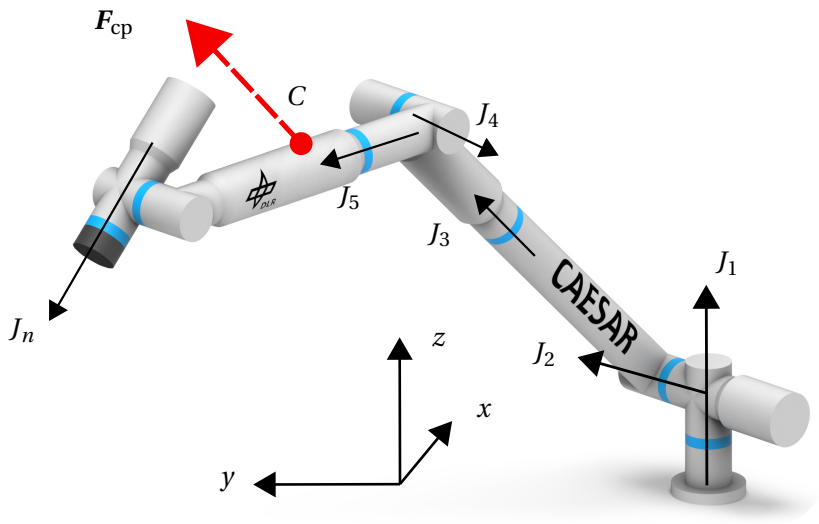

Figure 6.2: A 7-DoF space manipulator arm. C is the coupling point and $\boldsymbol{F}_{cp}$ is the required force/torque wrench which a carrier needs to track. J_i is the rotational axis of the i-th joint.

- A generalization of a gravity-compensation strategy for an external carrier with any DoFs and coupling point for on-ground testing of space manipulators.
- Experimental validation of the gravity compensation strategy with the CAESAR space manipulator using a cable suspended system, MSS.

This chapter is based on the work published in [DSVS+23] and underlying the granted patent [DSOV+23].

6.2 Compensation strategy

The scenario of interest is the on-ground testing of space manipulators under the influence of gravity. A significant limitation in the on-ground validation of space manipulators is that their joint motors are designed to meet operational requirements in a zero-gravity environment. Consequently, these motors are unable to support the torque demands across the entire workspace under terrestrial gravity. This limitation arises in multiple robot configurations when configuration-dependent gravitational torques exceed the torque limits of individual joints. As a result, full gravity compensation cannot be achieved in these configurations, thereby restricting the operational workspace available for on-ground testing.

To clarify the problem statement, the CAESAR arm is considered in a static position as illustrated in Figure 6.2. In order to actively compensate for its weight, the robot must apply torques, with joints J_2 and J_4 experiencing the highest loads at $\tau_2 = 369$ Nm and $\tau_4 = -135$ Nm, respectively. These torque values exceed the manipulator's joint limits of $\pm$ 80 Nm specified for space operation in [BGH+18].

Previous control strategies discussed in Chapter 3 to Chapter 5 incorporated both task-based hierarchy and control input optimization. In contrast, the current objective focuses on control input optimization rather than an explicit task hierarchy. The aim is to develop an optimized control input that maximizes the control input to the primary system (the external carrier) while minimizing the input to the secondary system (the manipulator). The control optimization is done while satisfying the constraint necessary to achieve the desired closed-loop dynamics. The desired closed-loop dynamics correspond to a gravity-compensated manipulator, which can subsequently be utilized for state-feedback control.

In other words, this chapter proposes a general method to deliver a desired Cartesian wrench ($\boldsymbol{F}_{\text{cp}}$ in Figure 6.2) as input to an external carrier, while minimizing the joint torques of the orbital manipulator to ensure compliance with its torque limits. To achieve gravity-compensated dynamics, the external carrier is designed to offload the majority of the gravitational torques acting on the manipulator joints. The manipulator joints then compensate for the remaining gravitational torques not supported by the carrier.

The proposed compensation strategy is summarized in Table 6.1, showing the priority on the control input. It shall be seen that the proposed optimization strategy is equivalent to a hierarchy in the control inputs enforced through the selection of appropriate weighting factors in the optimal problem.

Table 6.1: *Proposed strategy* – for gravity compensation of a space robot by an external carrier.

Control input	Gravity compensation strategy
T1: *Carrier wrench*	Optimize carrier wrench components to distribute gravitational load away from robot joints
T2: *Manipulator torques*	Optimize joint torques to keep residual gravity torques on robot far from manipulator torque limits

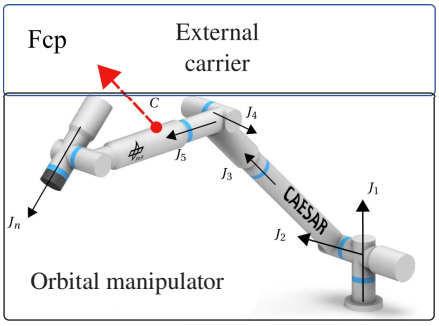

6.3 Compensation design

This section introduces the modeling of the system and outlines methods for compensating gravity forces in a generic manipulator-carrier system. An optimal solution is proposed for distributing gravitational torques between the manipulator and the carrier system.

6.3.1 Dynamics and constraint

For a fixed-base robot, the floating-base states vanish in (2.5), and the gravity vector $\boldsymbol{g}$ appears in the dynamics, which must be compensated for during on-ground testing. The dynamics of a generic

fixed-base manipulator system are governed by the following equations of motion.

(6.1) Manipulator dynamics: $\boldsymbol{M}_{mm}(\boldsymbol{q})\ddot{\boldsymbol{q}} + \boldsymbol{C}_{mm}(\boldsymbol{q},\dot{\boldsymbol{q}})\dot{\boldsymbol{q}} + \boldsymbol{g}(\boldsymbol{q}) = \boldsymbol{\tau}_m + \boldsymbol{J}_{\text{cp}}^T(\boldsymbol{q})\boldsymbol{F}_{\text{cp}}$

Here, $\boldsymbol{q} \in \mathbb{R}^n$ are joint angle positions for a robot with n joints, $\boldsymbol{M}_{mm}(\boldsymbol{q}) \in \mathbb{R}^{n\times n}$ and $\boldsymbol{C}_{mm}(\boldsymbol{q},\dot{\boldsymbol{q}}) \in \mathbb{R}^{n\times n}$ are the robot's inertia and Coriolis matrices, and $\boldsymbol{g}(\boldsymbol{q}) \in \mathbb{R}^n$ is the gravitational torque acting on the robot joints. The torque input to the joints is $\boldsymbol{\tau}_m \in \mathbb{R}^n$. The external wrench $\boldsymbol{F}_{\text{cp}} \in \mathbb{R}^6$ acting on the system at a coupling point C, produces a torque on the joints, transformed with the Jacobian $\boldsymbol{J}_{\text{cp}}(\boldsymbol{q}) \in \mathbb{R}^{6\times n}$ at the coupling point. The torque input $\boldsymbol{\tau}_m$ in (6.1) can be split into $\boldsymbol{\tau}_g$ for gravity compensation and $\boldsymbol{\tau}_c$ to fulfill the desired task-based control tasks, as:

(6.2) Manipulator torques: $\boldsymbol{\tau}_m = \boldsymbol{\tau}_g + \boldsymbol{\tau}_c.$

Traditional on-ground robot control methods employ the gravity-compensation technique to counteract the gravitational torques acting on the joints i.e. by actively applying $\boldsymbol{\tau}_g = \boldsymbol{g}$. Subsequently, a suitable feedback-control input $\boldsymbol{\tau}_m$ is designed in either joint or Cartesian space (e.g. PD+ control [PP88], [ASOH07]) to accomplish the control task. However, configuration-dependent gravitational torques can exceed the individual joint torque limits, implying that active gravity compensation cannot be achieved by the manipulator alone in these configurations.

The objective is to distribute the gravitational load acting on the robot, $\boldsymbol{g}$, between the internal joint torques $\boldsymbol{\tau}_g$ and the components of external wrench $\boldsymbol{F}_{\text{cp}}$, which can be applied by an external carrier system. Then, the following constraint needs to be satisfied, which does not disturb the control task,

(6.3) Desired constraint: $\boldsymbol{J}_{\text{cp}}^T\boldsymbol{F}_{\text{cp}} + \boldsymbol{\tau}_g = \boldsymbol{g}.$

$\boldsymbol{F}_{\text{cp}}$ is the external wrench at the coupling point (e.g. C in Figure 6.2) that a carrier needs to track. This leads to the desired closed-loop dynamics:

(6.4) Closed-loop dynamics: $\boldsymbol{M}_{mm}\ddot{\boldsymbol{q}} + \boldsymbol{C}_{mm}\dot{\boldsymbol{q}} = \boldsymbol{\tau}_c$

Depending on the design of the external carrier and its degrees-of-freedom (DoF), it may be possible to apply only certain components of force and/or torque at the coupling point. Therefore, let $\boldsymbol{\gamma}_c \in \mathbb{R}^m$ be the independent components of the wrench $\boldsymbol{F}_{\text{cp}}$ that can be applied at the coupling point C where $1 \le m \le 6$. Further, let $\boldsymbol{B}^T \in \mathbb{R}^{6\times m}$ be the wrench basis, that maps $\boldsymbol{\gamma}_c$ to the dimension of the full wrench space. Then the resulting wrench $\boldsymbol{F}_{\text{cp}}$ in (6.3) is:

(6.5) Effective external wrench: $\boldsymbol{F}_{\text{cp}} = \boldsymbol{B}^T\boldsymbol{\gamma}_c.$

For example, if the carrier system can only apply a force in the z-direction, then $\boldsymbol{B} = [0\ 0\ 1\ 0\ 0\ 0]$ and $\boldsymbol{\gamma}_c \in \mathbb{R}^1$. Therefore, substituting (6.5) into (6.3) we have,

(6.6) Effective constraint: $\boldsymbol{J}_{\text{cp}}^T\boldsymbol{B}^T\boldsymbol{\gamma}_c + \boldsymbol{\tau}_g = \boldsymbol{g}.$

6.3.2 Influence of coupling point

The coupling point C (see Figure 6.2) between the robot and the external carrier system can be located at different parts of the manipulator, thereby determining which of the joint torques can be influenced by the external wrench. Consider that joints numbered $1, 2, .., i$, where $i \leq n$, lie between the fixed-base and coupling point of the robot chain. Consequently the Jacobian $\boldsymbol{J}_{\text{cp}}^T$ to the coupling point in the constraint equation (6.6) exhibits the following structure:

$$\text{Coupling Jacobian:} \qquad \boldsymbol{J}_{\text{cp}}^T = \begin{bmatrix} \boldsymbol{J}_A^T \\ \boldsymbol{0}_{(n-i)\times 6} \end{bmatrix} \tag{6.7}$$

Here, $\boldsymbol{J}_A \in \mathbb{R}^{6\times i}$ denotes the Jacobian that maps the wrench applied at point C to the joint torques in set $A = \{x \mid x \in \mathbb{N},\ x \leq i\}$. The zero entries in the lower rows of the Jacobian indicate that the applied wrench does not affect the joints in set $B = \{x \mid x \in \mathbb{N},\ i < x \leq n\}$. Since the joints in set B are located between the coupling point and the free end-effector, (6.6) can be further simplified using (6.7) by separating the terms associated with joints in sets A and B as follows:

$$\begin{bmatrix} \boldsymbol{J}_A^T \boldsymbol{B}^T \boldsymbol{\gamma}_c \\ \boldsymbol{0}_{(n-i)\times 1} \end{bmatrix} + \begin{bmatrix} \boldsymbol{\tau}_{gA} \\ \boldsymbol{\tau}_{gB} \end{bmatrix} = \begin{bmatrix} \boldsymbol{g}_A \\ \boldsymbol{g}_B \end{bmatrix} = \boldsymbol{g} \tag{6.8}$$

$\boldsymbol{g}_A$ and $\boldsymbol{g}_B$ represent the gravitational torques for the joints in sets A and B, respectively. Likewise, $\boldsymbol{\tau}_{gA}$ and $\boldsymbol{\tau}_{gB}$ denote the gravity compensation torques for the joints in sets A and B. According to (6.8), the external wrench cannot influence the joints in set B. Therefore, these joints should be actuated using the gravitational torques computed directly from the dynamics model, that is, $\boldsymbol{\tau}_{gB} = \boldsymbol{g}_B$.

The use of sets to define the joint indices that are influenced by the external wrench allows the generalization of the coupling point in the constraint (6.8). From a practical standpoint, the location of C should be selected to ensure that $\boldsymbol{g}_B$ remains within the torque limits for the relevant workspace. This consideration is important during the design phase, as joints closer to the free end-effector typically experience lower gravitational torques.

The remaining joint torques $\boldsymbol{\tau}_{gA}$ and the external wrench components $\boldsymbol{\gamma}_c$ can be allocated to distribute the gravitational load between these two quantities, subject to optimality criteria, such that the following relation from (6.8) is satisfied:

$$\text{Reduced constraint:} \quad \boldsymbol{J}_{cA}^T \boldsymbol{\gamma}_c + \boldsymbol{\tau}_{gA} = \boldsymbol{g}_A \tag{6.9}$$

Here, the coupling Jacobian is defined as $\boldsymbol{J}_{cA}^T = \boldsymbol{J}_A^T \boldsymbol{B}^T$. In general, $\boldsymbol{J}_{cA}^T$ is not a square matrix and is therefore not invertible. As a result, it is not possible to solve directly for $\boldsymbol{\gamma}_c$ by, for instance, setting the torques $\boldsymbol{\tau}_{gA} = \boldsymbol{0}$. Consequently, an optimal solution must be determined for distributing the external forces and joint motor torques.

6.3.3 Optimal distribution of gravity load

To achieve optimal distribution of gravity-compensation torques between the joint motors and the external carrier, the following optimization problem is formulated with (6.9) as a constraint.

$$\min_{(\boldsymbol{\gamma}_c, \boldsymbol{\tau}_{gA})} \quad \frac{1}{2}\begin{bmatrix}\boldsymbol{\gamma}_c^T & \boldsymbol{\tau}_{gA}^T\end{bmatrix}\begin{bmatrix}\boldsymbol{W}_\gamma & \boldsymbol{0}\\ \boldsymbol{0} & \boldsymbol{W}_\tau\end{bmatrix}\begin{bmatrix}\boldsymbol{\gamma}_c\\ \boldsymbol{\tau}_{gA}\end{bmatrix} \tag{6.10}$$

$$\text{subject to,} \qquad \begin{bmatrix}\boldsymbol{J}_{cA}^T & \boldsymbol{I}\end{bmatrix}\begin{bmatrix}\boldsymbol{\gamma}_c\\ \boldsymbol{\tau}_{gA}\end{bmatrix} = \boldsymbol{g}_A \tag{6.11}$$

Here, $\boldsymbol{W}_\tau \in \mathbb{R}^{i\times i}$ and $\boldsymbol{W}_\gamma \in \mathbb{R}^{m\times m}$ denote the weighting matrices for the joint torques and external wrench components, respectively. The inputs from the robot $\boldsymbol{\tau}_{gA}$ and the carrier system $\boldsymbol{\gamma}_c$ are not coupled in the cost function in (6.10) because they originate from two distinct hardware systems.

The optimization problem is addressed using the Lagrange multiplier method, where the objective function is augmented by the constraint equations through a set of non-negative multiplicative Lagrange multipliers, $\boldsymbol{\lambda} \geq 0$, as follows.

$$L = \frac{1}{2}\begin{bmatrix}\boldsymbol{\gamma}_c^T & \boldsymbol{\tau}_{gA}^T\end{bmatrix}\begin{bmatrix}\boldsymbol{W}_\gamma & \boldsymbol{0}\\ \boldsymbol{0} & \boldsymbol{W}_\tau\end{bmatrix}\begin{bmatrix}\boldsymbol{\gamma}_c\\ \boldsymbol{\tau}_{gA}\end{bmatrix} + \boldsymbol{\lambda}^T\left(\boldsymbol{g}_A - \begin{bmatrix}\boldsymbol{J}_{cA}^T & \boldsymbol{I}\end{bmatrix}\begin{bmatrix}\boldsymbol{\gamma}_c\\ \boldsymbol{\tau}_{gA}\end{bmatrix}\right) \tag{6.12}$$

The minimum of the modified function L satisfying the constraint, is computed as

$$\nabla L(\boldsymbol{x}, \boldsymbol{\lambda}) = \boldsymbol{0}, \quad \text{with } \boldsymbol{x} = (\boldsymbol{\tau}_{gA}, \boldsymbol{\gamma}_c) \tag{6.13}$$

which leads to,

$$\frac{\partial L}{\partial \boldsymbol{\gamma}_c} = \boldsymbol{W}_\gamma \boldsymbol{\gamma}_c - \boldsymbol{J}_{cA}\boldsymbol{\lambda} = \boldsymbol{0} \tag{6.14}$$

$$\frac{\partial L}{\partial \boldsymbol{\tau}_{gA}} = \boldsymbol{W}_\tau \boldsymbol{\tau}_{gA} - \boldsymbol{\lambda} = \boldsymbol{0} \tag{6.15}$$

$$\frac{\partial L}{\partial \boldsymbol{\lambda}} = \boldsymbol{g}_A - \boldsymbol{J}_{cA}^T\boldsymbol{\gamma}_c - \boldsymbol{\tau}_{gA} = \boldsymbol{0} \tag{6.16}$$

From (6.15) and (6.16), the Lagrangian multiplier results as:

$$\boldsymbol{\lambda} = \boldsymbol{W}_\tau(\boldsymbol{g}_A - \boldsymbol{J}_{cA}^T\boldsymbol{\gamma}_c) \tag{6.17}$$

and substituting (6.17) in (6.14), the optimal wrench components, $\boldsymbol{\gamma}_c^*$, result in:

$$\text{Optimal carrier compensation :} \quad \boldsymbol{\gamma}_c^* = (\boldsymbol{W}_\gamma + \boldsymbol{J}_{cA}\boldsymbol{W}_\tau\boldsymbol{J}_{cA})^{-1}\boldsymbol{J}_{cA}\boldsymbol{W}_\tau\boldsymbol{g}_A \tag{6.18}$$

The optimized joint torques, $\boldsymbol{\tau}_{gA}^*$, can be obtained by substituting (6.18) in (6.11), resulting in:

$$\text{Optimal robot compensation :} \quad \boldsymbol{\tau}_{gA}^* = \left(\boldsymbol{I} - \boldsymbol{J}_{cA}^T(\boldsymbol{W}_\gamma + \boldsymbol{J}_{cA}\boldsymbol{W}_\tau\boldsymbol{J}_{cA}^T)^{-1}\boldsymbol{J}_{cA}\boldsymbol{W}_\tau\right)\boldsymbol{g}_A \tag{6.19}$$

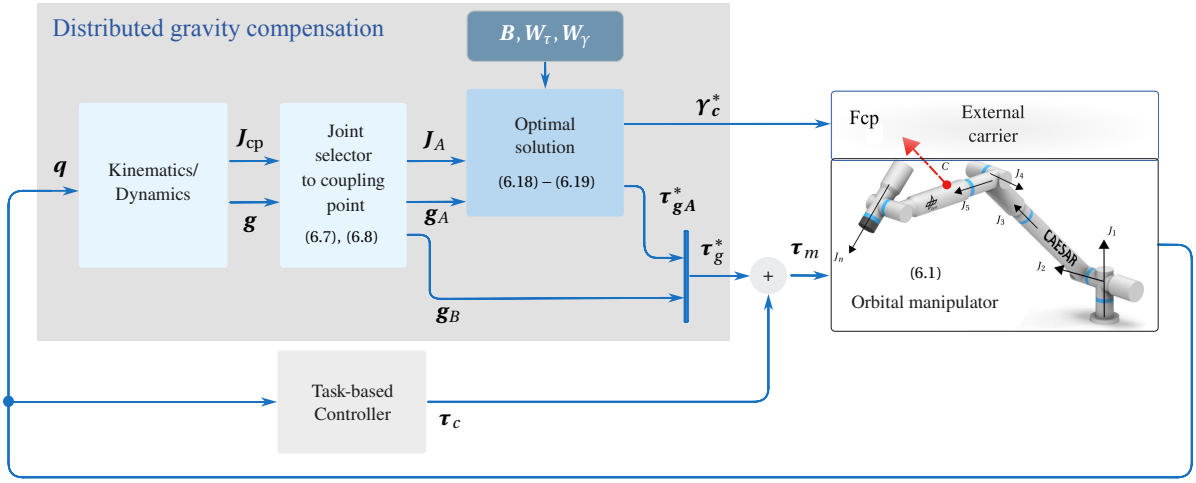

Figure 6.3: *Distributed gravity-compensation* – block diagram of the proposed method.

The solutions in (6.18) and (6.19) provide an optimal distribution of the gravitational torques $\boldsymbol{g}_A$ between $\boldsymbol{\gamma}_c$ and $\boldsymbol{\tau}_{gA}$. Specifically, (6.18) represents the desired force to be tracked by the external carrier, while (6.19) corresponds to the joint torque input for the manipulator joints in set A.

The proposed strategy is summarized with a schematic in Figure 6.3. Using the measured joint positions, $\boldsymbol{q}$, the kinematics and dynamics of the manipulator arm are computed. The Jacobian at the coupling point, $\boldsymbol{J}_{\text{cp}}$ and the vector $\boldsymbol{g}_A$ are the input to the optimizer, whose outputs are sent to the external carrier and the orbital manipulator. Note that the final gravity torque input for the manipulator is $\boldsymbol{\tau}_g^* = [\boldsymbol{\tau}_{gA}^*; \boldsymbol{\tau}_{gB}]$. This includes the optimized torque, $\boldsymbol{\tau}_{gA}^*$ and the gravity torque for the joints in set B (between the coupling point and the free end-effector of the robot chain). From Figure 6.3, it can be seen that the proposed strategy does not interfere with the validation of a task-based controller, i.e. the independent torque input $\boldsymbol{\tau}_c$.

6.3.4 Existence of solution

The existence of solutions (6.18)-(6.19) for different cases of weights and dimensions are discussed ahead and summarized in Table 6.2. Here, $\boldsymbol{W}_\bullet > \boldsymbol{0}$ denotes that the matrix $\boldsymbol{W}_\bullet$ is positive definite.

Case i) Carrier-unweighted : $W_\tau > 0$ and $W_\gamma = 0$

When the carrier is unweighted in the optimization problem, the existence of the solution depends on the dimension of the external wrench of the robot-carrier and the rank of the coupling Jacobian.

- *Coupled joints > Carrier DoF :* When $i > m$, the dimension of the joints i, that can be gravity-compensated via the coupling to the carrier, is greater than the dimension of the external wrench components m. The solution exists only in singularity-free robot configurations. In this case, the joint torques resulting from the optimized external wrench component in (6.18),

Table 6.2: *Existence of solutions* – Optimal solutions of (6.10) and (6.11) are summarized for various cases of weighting matrices, dimensionality and singularity. i: dimension of the joints coupled to the carrier, m: dimension of the external wrench components (carrier).

Case		Dimensionality			Singularity-
		$i > m$	$i = m$	$i < m$	independence
(i)	$\boldsymbol{W}_\tau \succ \mathbf{0}$, $\boldsymbol{W}_\gamma = \mathbf{0}$	$\boldsymbol{\gamma}_c^* = \boldsymbol{J}_{cA}^{T_W\dagger}\boldsymbol{g}_A$ and $\boldsymbol{\tau}_{gA}^* = \left(\boldsymbol{I} - \boldsymbol{J}_{cA}^T\boldsymbol{J}_{cA}^{T_W\dagger}\right)\boldsymbol{g}_A$	$\boldsymbol{\gamma}_c^* = \boldsymbol{J}_{cA}^{-T}\boldsymbol{g}_A$ and $\boldsymbol{\tau}_{gA}^* = \mathbf{0}$	Ill-posed	✗
(ii)	$\boldsymbol{W}_\tau = \mathbf{0}$, $\boldsymbol{W}_\gamma \succ \mathbf{0}$	$\boldsymbol{\gamma}_c^* = \mathbf{0}$ and $\boldsymbol{\tau}_{gA}^* = \boldsymbol{g}_A$			✓
(iii)	$\boldsymbol{W}_\tau \succ \mathbf{0}$, $\boldsymbol{W}_\gamma \succ \mathbf{0}$	$\boldsymbol{\gamma}_c^*$ as in (6.18) and $\boldsymbol{\tau}_{gA}^*$ as in (6.19)			✓

$\boldsymbol{J}_{cA}^T\boldsymbol{\gamma}_c^*$, projects $\boldsymbol{g}_A$ onto the range space (image) of $\boldsymbol{J}_{cA}^T$, and $\boldsymbol{\tau}_{gA}^*$ in (6.19) projects $\boldsymbol{g}_A$ onto the nullspace (kernel) of $\boldsymbol{J}_{cA}^T$. In other words, the joint torques that cannot be generated by the external wrench carrier are actively compensated by the manipulator joint torques. This is consistent with the desired hierarchy of control distribution outlined in Table 6.1, where the primary objective is to prioritize the compensation by the external carrier, which is achieved by not penalizing it in the optimal problem ($\boldsymbol{W}_\gamma = \mathbf{0}$). The resulting optimal solution relegates the compensation by manipulator joints to the nullspace of the coupling Jacobian $\boldsymbol{J}_{cA}^T$. Rewriting the optimized solutions (6.19) and (6.18) in the form of generalized inverses results in the constraint in (6.9) satisfied as:

$$\boldsymbol{g}_A = \underbrace{\boldsymbol{J}_{cA}^T\boldsymbol{J}_{cA}^{T_W\dagger}\boldsymbol{g}_A}_{\boldsymbol{\tau}_{T1}=\boldsymbol{J}_{cA}^T\boldsymbol{\gamma}_c^*} + \underbrace{\left(\boldsymbol{I} - \boldsymbol{J}_{cA}^T\boldsymbol{J}_{cA}^{T_W\dagger}\right)\boldsymbol{g}_A}_{\boldsymbol{\tau}_{T2}=\boldsymbol{\tau}_{gA}^*} \qquad \text{where, } \boldsymbol{J}_{cA}^{W\dagger} = \boldsymbol{W}_\tau\boldsymbol{J}_{cA}^T(\boldsymbol{J}_{cA}\boldsymbol{W}_\tau\boldsymbol{J}_{cA}^T)^{-1}. \tag{6.20}$$

It is evident that the optimized solution prioritizes gravity-compensation by the external carrier (T1) while manipulator torques act in the nullspace of the coupling Jacobian (T2). In the special case when $\boldsymbol{W}_\tau = \boldsymbol{S}_A\boldsymbol{M}_{mm}^{-1}\boldsymbol{S}_A^T$ where, $\boldsymbol{S}_A = [\boldsymbol{I}_i \ \mathbf{0}] \in \mathbb{R}^{i\times n}$ is a selector of joints in set A, the manipulator torques are projected into the dynamically consistent nullspace of the coupling Jacobian, thus inducing zero acceleration at the coupling point.

- *Coupled joints = Carrier DoF :* When $i = m$, the number of joints i that are influenced by the carrier equals the dimension of the external wrench components m. In this case, $\boldsymbol{J}_{cA}^T$ is a square matrix, and for singularity-free robot configurations, $\boldsymbol{\gamma}_c^*$ is determined using the inverse of the transposed Jacobian. Therefore, the carrier system can fully compensate for gravity torques, and no additional joint torques are required.

- *Coupled joints < Carrier DoF:* When $i < m$, the number of joints that can be gravity-compensated is less than the number of external wrench components. In this situation, setting $\boldsymbol{W}_\gamma = \mathbf{0}$

renders the problem ill-posed. This issue arises not from a physical limitation of the carrier system, but from the problem definition, as there is no metric to ensure a unique solution. The minimum cost in (6.10) would be achieved for $\boldsymbol{\tau}^*_{gA} = \mathbf{0}$. Since $\boldsymbol{J}^T_{cA}$ is an $i \times m$ matrix with $i < m$, the problem remains under-constrained, as indicated by (6.11). Therefore, to obtain an optimal solution when $i < m$, it is necessary to assign a non-zero value to the weight $\boldsymbol{W}_\gamma$.

Case ii) Manipulator-unweighted : $W_\tau = 0$ and $W_\gamma > 0$

In this case, there is no external gravity compensation mechanism, and it assumes that the manipulator can already apply sufficient torques on ground to sustain its weight. Therefore, there is no limitation on internal joint motor torques resulting in $\boldsymbol{\gamma}^*_{\boldsymbol{c}} = \mathbf{0}$, $\boldsymbol{\tau}^*_{gA} = \boldsymbol{g}_A$, and the solution is singularity-independent.

Case iii) Both weighted : $W_\tau > 0$ and $W_\gamma > 0$

In this case, an optimal solution always exists, regardless of the rank of the Jacobian or the dimensionality of the external wrench components. The invertibility of the weighted terms in (6.18) and (6.19) is ensured by the positive-definiteness of $\boldsymbol{W}_\gamma$. The solution is consistent with the damped weighted least-squares approach, where $\boldsymbol{W}_\gamma \succ \mathbf{0}$ serves as the damping term to guarantee invertibility. As a result, the interpretation in (6.20) remains valid for singular configurations when using the damped inverse $\boldsymbol{J}^{W\dagger}_{cA} = \boldsymbol{W}_\tau \boldsymbol{J}^T_{cA}(\boldsymbol{J}_{cA}\boldsymbol{W}_\tau \boldsymbol{J}^T_{cA} + \boldsymbol{W}_\gamma)^{-1}$. Additionally, the weight $\boldsymbol{W}_\gamma$ enables selective penalization of carrier wrench components, such as maximizing the z-component by assigning higher penalties to other directions.

6.4 Validation results

This section presents simulation (SIM) and experimental hardware (HW) results obtained using the proposed method. The orbital manipulator under consideration is the CAESAR arm, a torque-controlled robot with seven degrees of freedom and an approximate length of 2.4 m in its fully extended configuration. The arm weighs approximately 60 kg, and the maximum allowable joint torque is ± 80 Nm (see [BGH+18]). The weighting matrices are defined as $\boldsymbol{W}_\tau = \text{diag}(1/\tau^2_{i,max})$, where $\tau_{i,max}$ denotes the maximum torque of the i-th joint, and $\boldsymbol{W}_\gamma = \text{diag}(1/\gamma^2_{i,max})$, where $\gamma_{i,max}$ represents the maximum value of the external component of the wrench. To demonstrate the flexibility of the method, validation in both simulation and experiment considers different points C for force application and different carriers capable of tracking different components of the external wrench. The simulation and hardware parameters are summarized in Table 6.3.

From a practical standpoint, the external carrier may be subject to hardware limitations, such as a minimum force $\boldsymbol{\gamma}_c$. These constraints can be incorporated into the optimal solution by introducing additional inequality constraints in the optimization problem defined in (3.15) and (3.16). In such cases, numerical solvers, such as qpOASES [FKP+14a], may be employed.

Table 6.3: Simulation (SIM) and hardware (HW) parameters.

Parameter	**SIM**	**HW**
Carrier DoF	$m = 5$	$m = 3$
Manipulator DoF	$n = 7$	$n = 7$
Joints before coupling point	$i = 4$, $A = \{1,2,3,4\}$	$i = 5$, $A = \{1,2,3,4\}$
Joints after coupling point	$B = \{5,6,7\}$	$B = \{6,7\}$
Joint torque limits	$\tau_{i,max} = 80$Nm	$\tau_{i,max} = 80$Nm
Carrier wrench limits	$\gamma_{i,max} = 500$N, Nm	$\gamma_{i,max} = 750$N

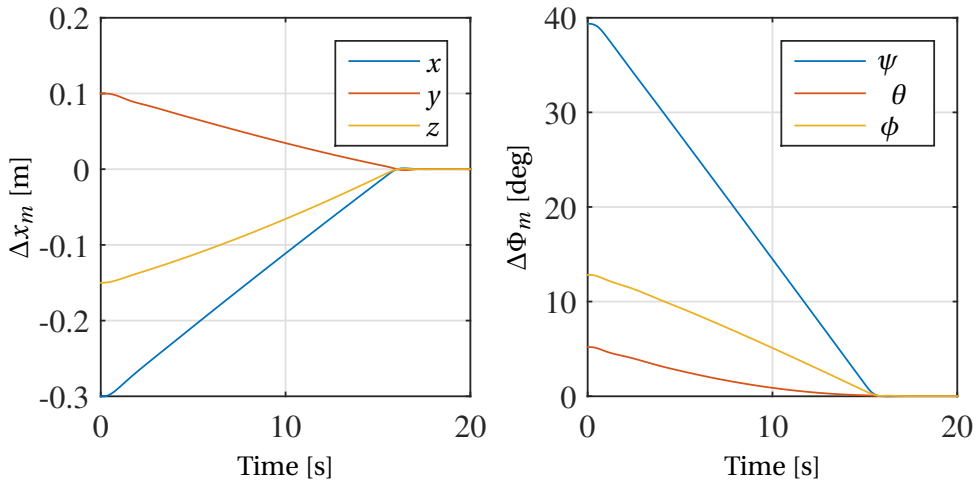

Figure 6.4: *SIM results* – error in position and orientation of end-effector from the initial pose to the final setpoint while following an interpolated trajectory.

6.4.1 Simulation (SIM) results

The simulation scenario considers a different coupling point C than the hardware setup to validate the method's generality. As an example, a more complex coupling mechanism is considered such that the external carrier is capable of tracking forces in the x, y, and z directions, and torques in the x and y directions only. The coupling point is assumed to be located at J_4 (see Figure 6.2). Accordingly, the set A, and B as in Table 6.3 and the wrench basis $\boldsymbol{B}$ of the carrier is given by $\boldsymbol{B} = [\boldsymbol{I}_{5\times5}\ \boldsymbol{0}_{5\times1}]$.

Starting from the initial configuration depicted in Figure 6.2, a relative position of $[-0.3\ 0.1\ -0.15]$ m and a relative orientation of [40 5 12] degrees are commanded to the tool of the CAESAR arm using an impedance Cartesian controller (PD+, see [DS+19, eq. (7)]). The resulting position and orientation errors during the motion are presented in Figure 6.4.

The effectiveness of the proposed method is illustrated in Figure 6.5. Without the application of the proposed method, the gravitational torques required by the arm exceed the limit of ±80 Nm (see Figure 6.5, left), with values reaching 370 Nm and −130 Nm.

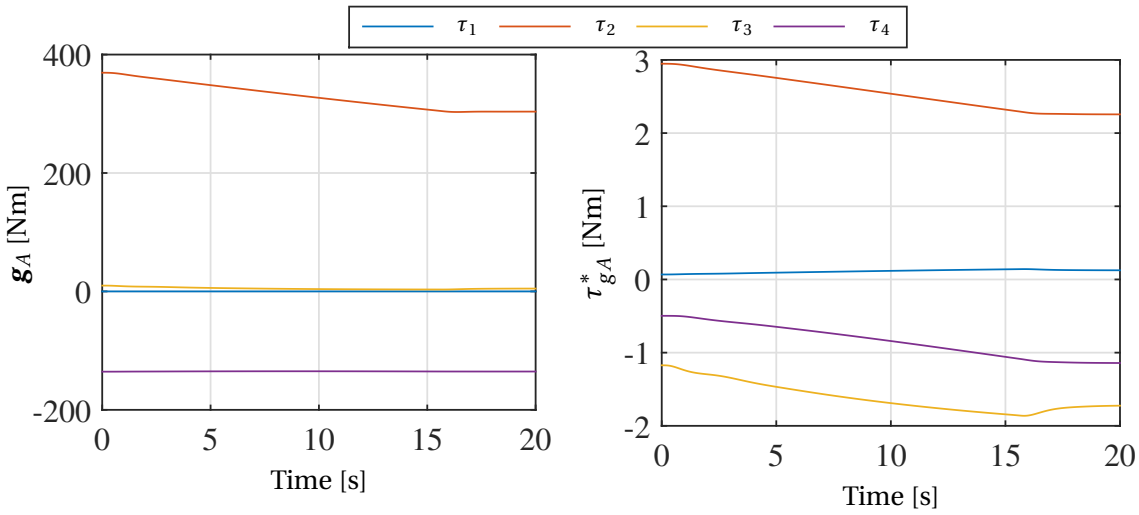

Figure 6.5: *SIM results* – (left) gravity torques required by the arm without the proposed strategy, (right) torques with the proposed method.

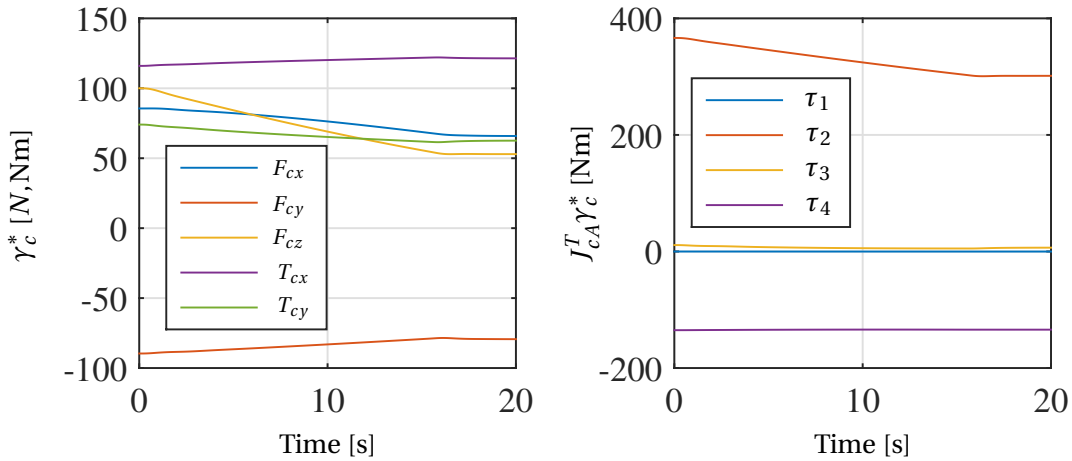

Figure 6.6: *SIM results* – (left) wrench for the carrier resulting from the optimal solution, (right) corresponding wrench transformed in the joint space of manipulator.

Figure 6.5 (right) presents the gravity torque in set A resulting from the proposed method. The maximum torque is now less than 3 Nm. To achieve complete gravity force compensation, the carrier must track a required wrench, which is the output of the proposed method and is shown in Figure 6.6 (left). For validation, Figure 6.6 (right) displays the same force transformed into the manipulator's joint space. Based on Figure 6.5 and Figure 6.6 (right), it can be seen that full gravity compensation of $\boldsymbol{g}_A$ is achieved, and the constraint in (3.16) is satisfied.

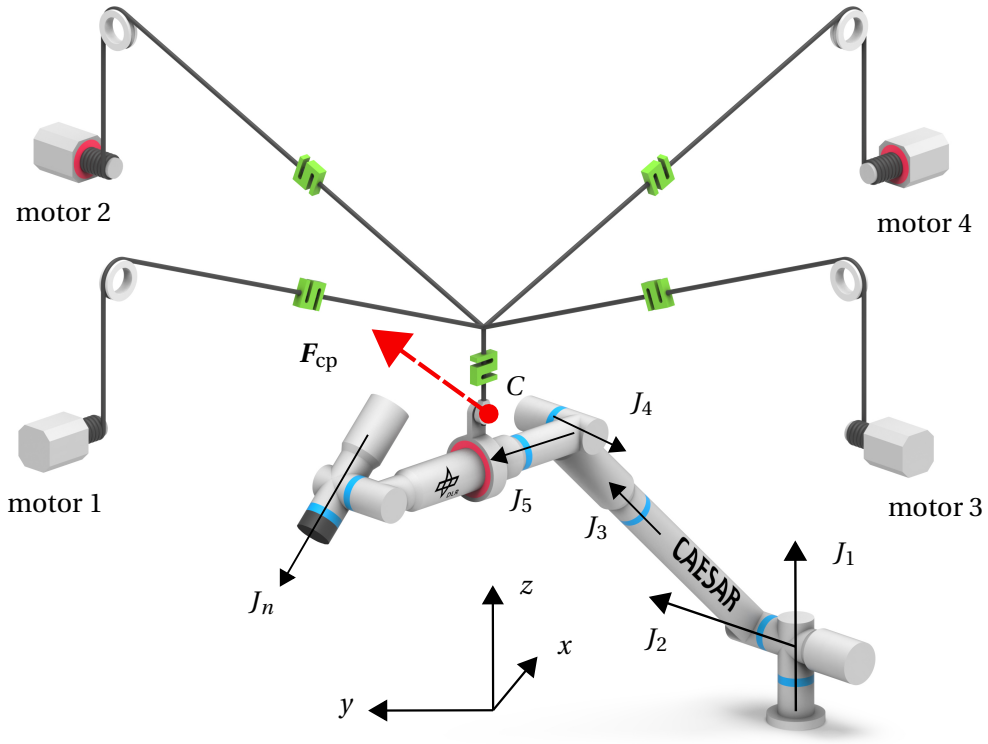

Figure 6.7: *Hardware setup* – a 7-DoF space manipulator coupled with a cable suspended unit as carrier. C is the coupling point between the systems.

6.4.2 Hardware (HW) results

A cable-driven system serves as the external carrier [EBDS+23] and is connected to the CAESAR arm via a coupling mechanism at point C, as illustrated in Figure 6.7. The carrier is controlled at 2 kHz using direct-drive motors, and uses feedback from motor encoder measurements and winch models. The suspension force is reconstructed by using angular and force sensors at the coupling interface between the manipulator and MSS. The carrier is capable of tracking a desired Cartesian force using admittance control [YHKMP15]. The desired force acts as the input to a dynamic model, which computes acceleration and performs discrete integration. Subsequently, a new set-point is provided to the cable-driven system through inverse kinematics [DSBAS17, KAA20].

The carrier depicted in Figure 6.7 is equipped with four motors and is capable of applying and tracking only translational forces along the x, y, and z axes at the coupling point C, without generating torques. The coupling point C was positioned after joint J_5 to ensure that $\boldsymbol{g}_B$ remains within the torque limits for the intended workspace. Therefore, set A and B can be defined as in Table 6.3 and wrench basis $\boldsymbol{B}$ is defined as $\boldsymbol{B} = [\boldsymbol{I}_{3\times3}\ \boldsymbol{0}_{3\times3}]$. As detailed in Section 6.3.2 and (6.8), $\boldsymbol{\tau}_{gB} = \boldsymbol{g}_B$, indicating that the force applied at point C does not affect the joints in set B.

The experiment evaluates the motion of the CAESAR arm from its initial pose, as shown in Figure 6.8 (left), to its final pose (right) using a joint impedance controller [SSVO08] operating at 1 kHz.

The commanded joint position trajectory is presented in Figure 6.9 and compared with the measured data. The optimal gravitational torques computed by the proposed method are illustrated in Figure 6.10 and applied to the CAESAR arm. These torques remain below the specified limit of 80 Nm.

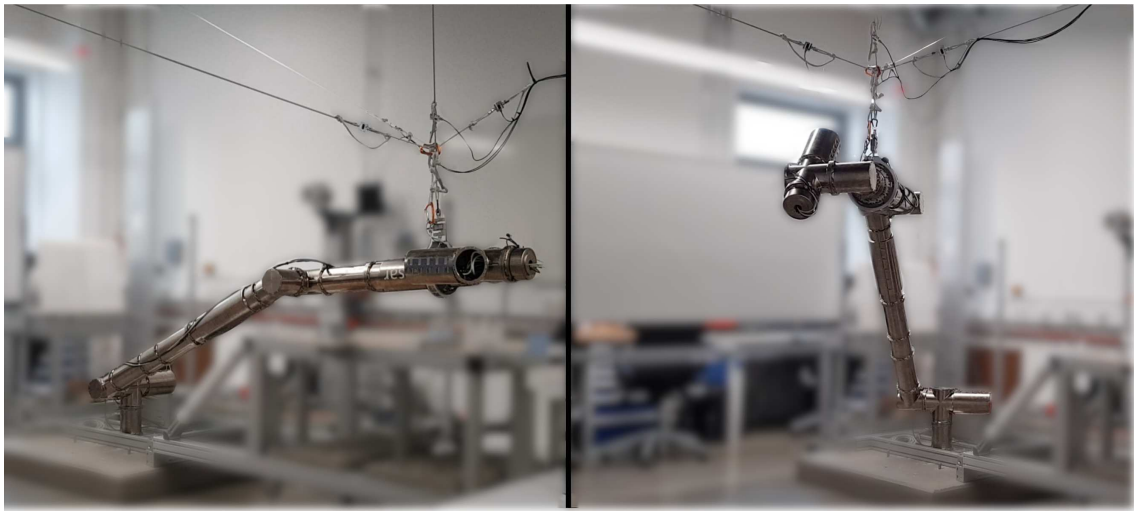

Figure 6.8: *Experimental setup* – motion of CAESAR with the external carrier, MSS, during the experiment between its initial pose (left) to the final one (right). A link to the experimental videos is given in Appendix G, Table G.1.

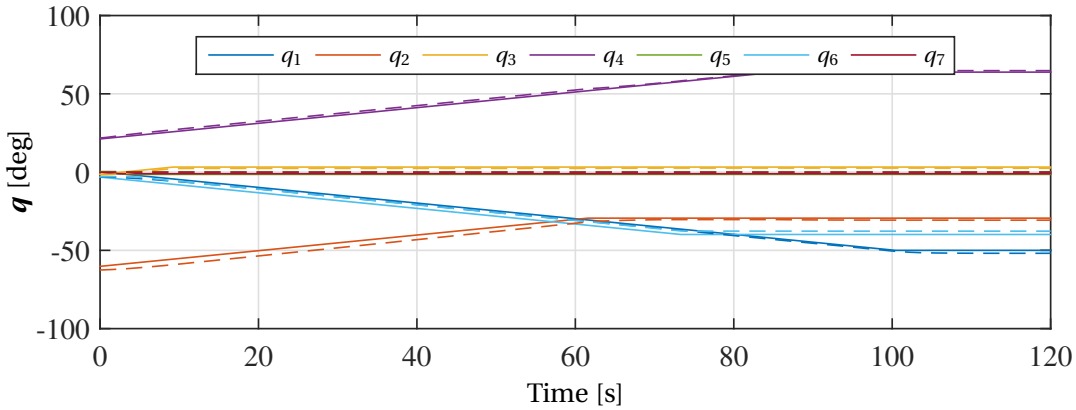

Figure 6.9: *HW results* – desired (dashed line) and measured (solid line) joint positions.

The optimal forces generated by the carrier are presented in Figure 6.11 and compared with the measured values from the carrier system. The force tracking error $\Delta\boldsymbol{\gamma}_c^*$ remains below 4 N and approaches zero in the static pose (see after 100s). For validation, the required gravity torque during motion, $\boldsymbol{g}_A$, is compared with the total forces (internal joint torques and external forces from the carrier) acting on the manipulator. This is calculated as $\bar{\boldsymbol{\tau}}_A = \boldsymbol{\tau}_{msr,A} - \boldsymbol{\tau}_{c,A} + \boldsymbol{J}_{cA}^T \boldsymbol{\gamma}_{c_{msr}}^*$, where $\boldsymbol{\tau}_{msr,A}$ denotes the measured torque and $\boldsymbol{\tau}_{c,A}$, the commanded control torque as per (6.2) in set A. The

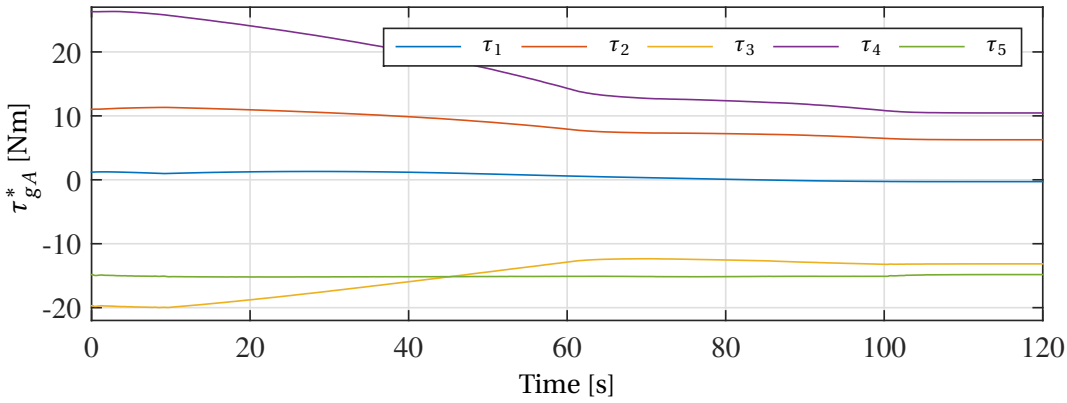

Figure 6.10: *HW results* – optimal joint torques applied to CAESAR.

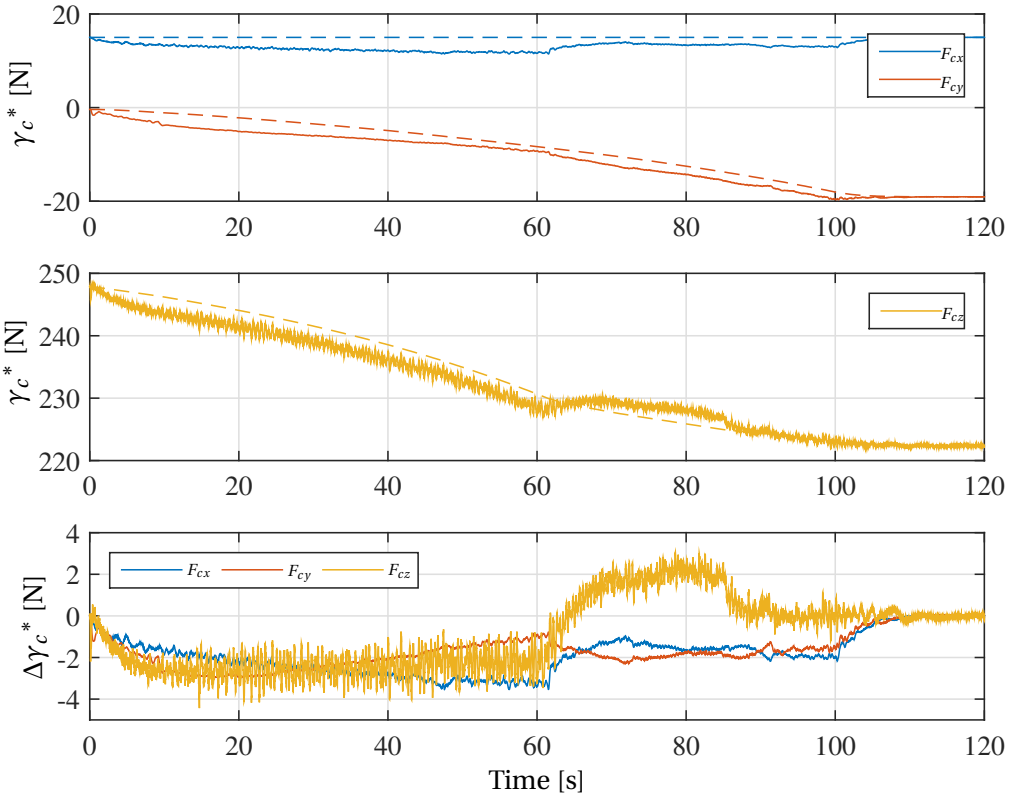

Figure 6.11: *HW results* – optimal force of the external carrier in x-y (top), z (middle), and error (bottom) between commanded (dashed line) and measured (solid line) force of the carrier.

comparison, shown in Figure 6.12, indicates that the largest error occurs at joint 1, attributed to the admittance-controlled carrier during tracking. In the static pose, the error reduces to zero (see after 100s). These results demonstrate that the proposed strategy is effective for on-ground testing of orbital manipulators.

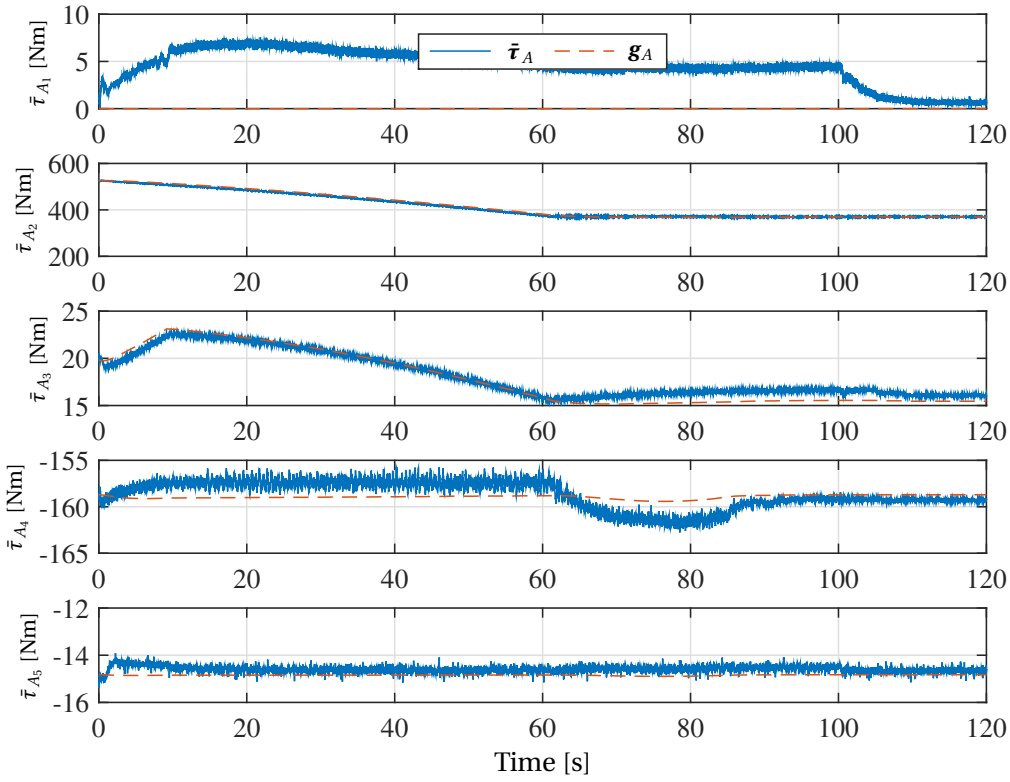

Figure 6.12: *HW results* - comparison between the required gravity torque $\boldsymbol{g}_A$ and the overall gravity torque acting on the manipulator joint space, $\bar{\boldsymbol{\tau}}_A$, (computed from the measured data).

6.5 Discussion and summary

This chapter presented a strategy to compensate for the gravity of a space manipulator during on-ground testing. The proposed approach formulated and solved an optimization problem that minimizes joint torque and outputs a desired force for tracking by an external carrier.

Generalizing the external force and torque components allows this method to be applied to a range of carriers with different designs and degrees of freedom for compensating gravitational loads. In this study, the carrier utilized was a cable-suspended system. However, the same method can be extended to carriers such as cranes or industrial robots, which can deliver the required external wrench according to the proposed optimal solution to offload gravitational torques on the space robot.

Additionally, generalizing the coupling point using the set definition in (6.7) enables clear identification of which joints can be offloaded by a carrier. A further advantage of the method is that, even if the number of joints up to the coupling point is less than the carrier's degrees of freedom — potentially causing the Jacobian to lose rank—the non-zero weighting of both manipulator torques and carrier wrench (case iii of Table 6.2) guarantees the existence of a solution. Detailed analysis of the various cases comparing manipulator and carrier degrees of freedom elucidates the solution space

and informs the selection of appropriate weights for the desired outcome. For instance, case i of Table 6.2 may be preferable when the manipulator is not expected to operate near singular configurations, and when decoupling between manipulator and carrier at the acceleration level is desirable through the specific choice of inertia matrix as the weighting matrix.

Experimental results with the CAESAR arm demonstrate the effectiveness of the method, employing a cable-suspended system as the carrier to track the compensation force. The method has proven highly successful and stable during extensive use of the CAESAR robot with the Motion Suspension System at DLR, particularly in demonstrations for continuous integration of phases B and C of the EROSS SC mission [R$^+$] (see Figure 6.13). The method's transferability is further evidenced by its recent adoption on a different robot and carrier system [CKK$^+$26]. Future research may address the enhancement of robustness under noise and dynamic uncertainties based on performance.

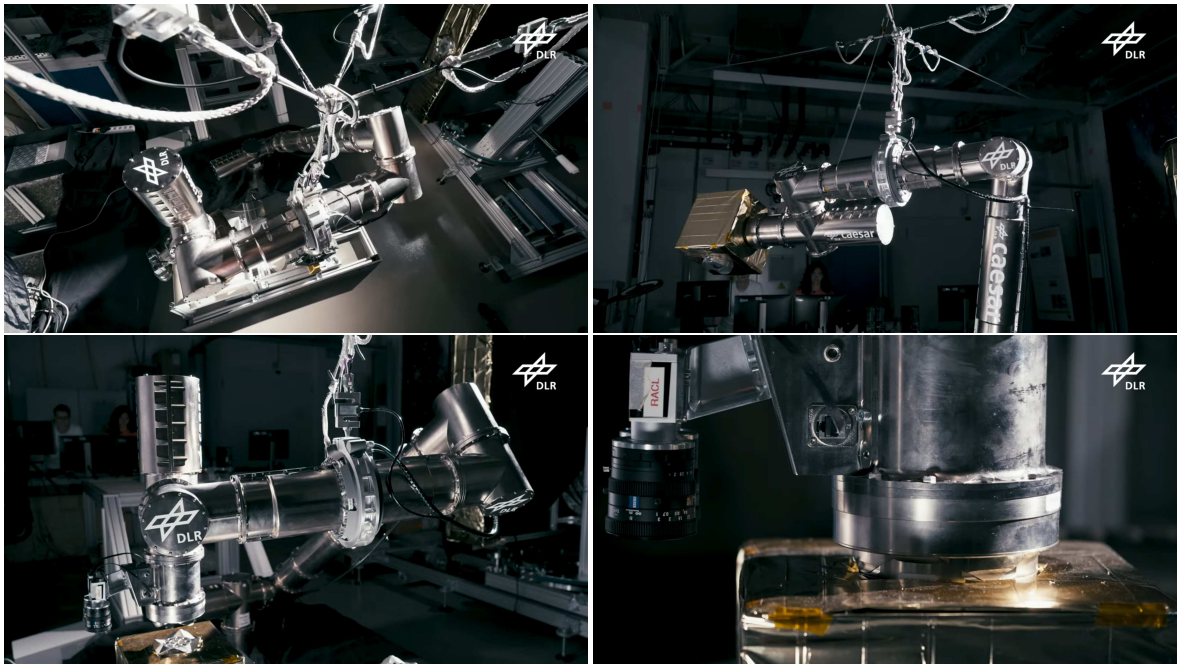

Figure 6.13: Image credits: DLR [RM25]. On-ground testing of space robot CAESAR with the cable-suspended platform. The success of the proposed method demonstrates its robustness across diverse motions, including contact operations with an Orbital Replacement Unit (ORU) mockup (in gold) as shown here. A link to the demonstration video is given in Appendix G, Table G.1.

CHAPTER 7

APPLICATIONS

The methods presented in the previous chapters found application in ongoing OOS mission developments. Among these, applications related to three specific OOS missions: EROSS, an EU initiative, DIANE, a CNES mission study and RISE, an ESA mission development, are discussed in this chapter. The following sections provide an overview of the applications addressed during various phases of each space mission's development.

7.1 EROSS — EU mission

EROSS (European Robotic Orbital Support Services) is a series of EU-funded space robotics initiatives, including EROSS, EROSSplus, and EROSS SC / IOD, designed to research and demonstrate autonomous on-orbit satellite servicing. The project is funded by the European Union's Horizon 2020 and Horizon Europe research programs. It is led by Thales Alenia Space, aimed at developing and demonstrating autonomous on-orbit servicing technologies for satellites in low Earth orbit and geostationary orbit (see Figure 7.1). The project seeks to launch a satellite equipped with a robotic arm that will perform orbital rendezvous between a servicer and a collaborative client satellite. EROSS primarily aims to demonstrate essential in-orbit functions, including the approach and rendezvous of two free-flying spacecraft with comparable mass and inertia, as well as autonomous robotic operations such as capture, refueling, and payload exchange. The project has advanced the Technology Readiness Level (TRL) of several components, notably the robotic arm subsystem developed by DLR, preparing these services for the commercial market in future OOS missions.

In relation to the research presented in this dissertation, the topics examined and developed included the gravity-compensation strategy for on-ground testing of the CAESAR robot, analysis of disturbances affecting robot motion on spacecraft, assessment of spacecraft actuation disturbances on robot joints, and evaluation of achievable end-effector forces to ensure gripper compliance.

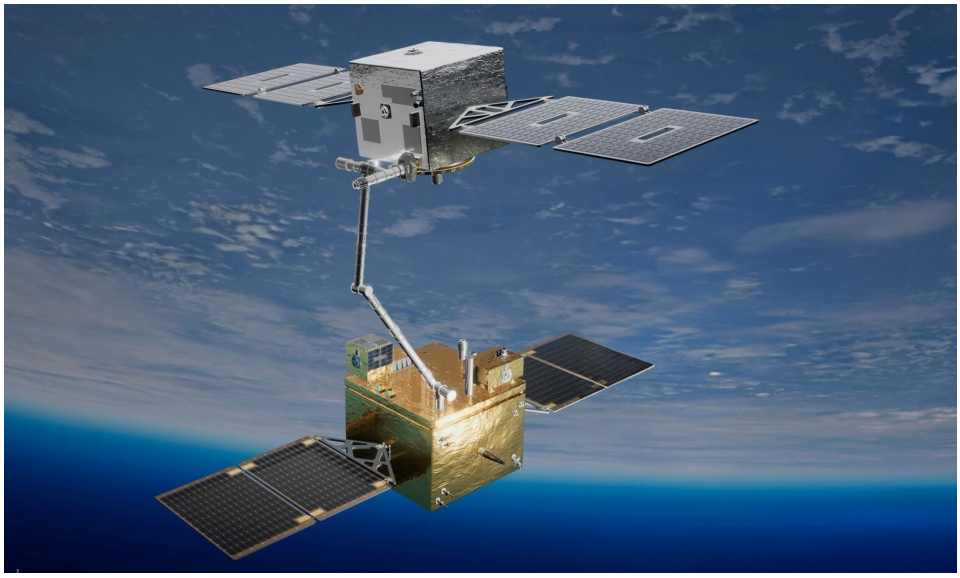

Figure 7.1: Image credit: ©EROSS SC. The EROSS mission is designed to use an orbital manipulator for the capture and docking of a client satellite.

7.1.1 On-ground testing with gravity-compensation

The gravity-compensation strategy for the space robot, CAESAR, was developed and implemented in phase A of the mission using the cable-suspended platform, MSS (described in Section 2.1.2). It has been in operation since, facilitating laboratory demonstrations of grasping, manipulation, and assembly through phases A to C of the mission, as shown in Figure 6.13. The gravity-compensation strategy employs the method detailed in Chapter 6, which has been instrumental in advancing the technology readiness level (TRL) of the robot.

7.1.2 Robot motion disturbance on spacecraft

During phase B of the mission, a study was conducted to determine the disturbance of robotic arm motion on spacecraft attitude de-pointing. The objective was to quantify spacecraft de-pointing under various control strategies and to assess advanced compensation methods using spacecraft control. The modalities of spacecraft attitude control considered were:

- *Free-floating control*: The robotic arm subsystem operates without support or compensation from the spacecraft subsystem, with spacecraft control remaining completely inactive.

- *Decoupled control*: The robotic arm subsystem and spacecraft control operate independently. The spacecraft subsystem corrects its attitude by treating spacecraft de-pointing from arm motion as external disturbances.

- *Parallel control*: The robotic arm subsystem supplies compensation torques to the spacecraft subsystem, which are applied concurrently with robot control to minimize spacecraft depointing. In particular, the method proposed in Section 3.5.3 was analyzed within this control paradigm.

More precisely, free-floating control involves zero torques applied to the spacecraft. In decoupled control, PD control is applied independently to both the spacecraft and the robot. In parallel control, a compensation torque, dependent on robot motion, is applied to the spacecraft in addition to its PD control, while the robot also uses PD control for its motion. Within parallel control, the method from Section 3.5.3 was examined by decomposing the nullspace projection of robot motion into a compensation torque for spacecraft attitude. The analysis results were quantified using linear analysis around several equilibrium robot poses to assess the impact of each joint's motion on each spacecraft attitude direction.

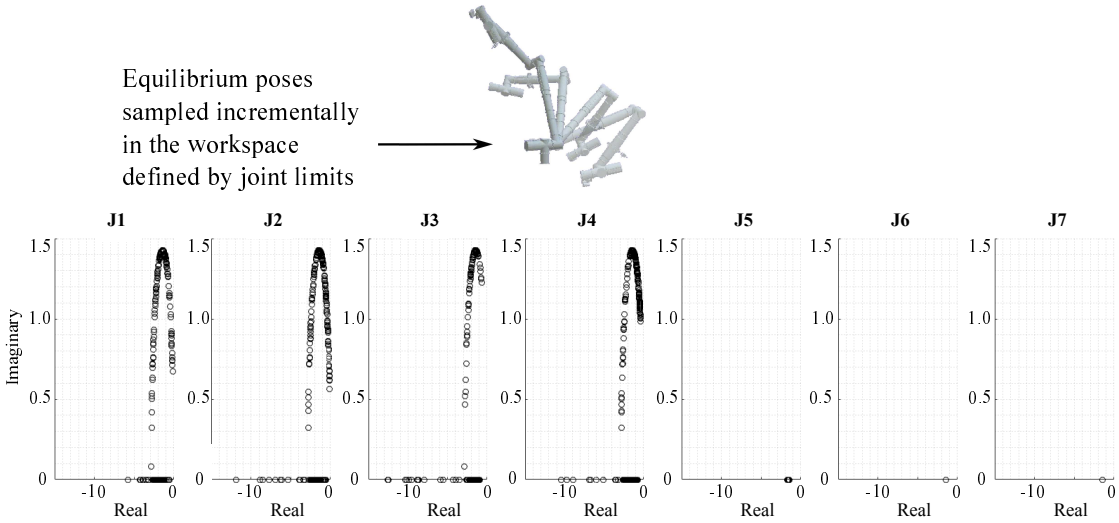

Figure 7.2: Dominant poles traces a curve in the s-plane across the workspace of CAESAR arm for each of the 7 joints (J).

The initial step in linearizing the orbital manipulator dynamics involved an approach analogous to the linearization described in Appendix D for gain tuning. This procedure aimed to characterize expected variations in the system response across the robot's workspace, recognizing that linear analysis quantifies system behavior locally around a selected equilibrium. This is illustrated in Figure 7.2, which depicts the variation of the dominant poles of each joint's closed-loop transfer function across the robot's workspace.

The step response of the closed-loop transfer function from the joints to base attitude was used to quantify the disturbance effects of robot motion on spacecraft roll, pitch, and yaw. This is illustrated in Figure 7.3, where columns represent a step input to the first joint, J1, and rows represent the corresponding responses in spacecraft attitude. Results are presented for the linearized dynamics

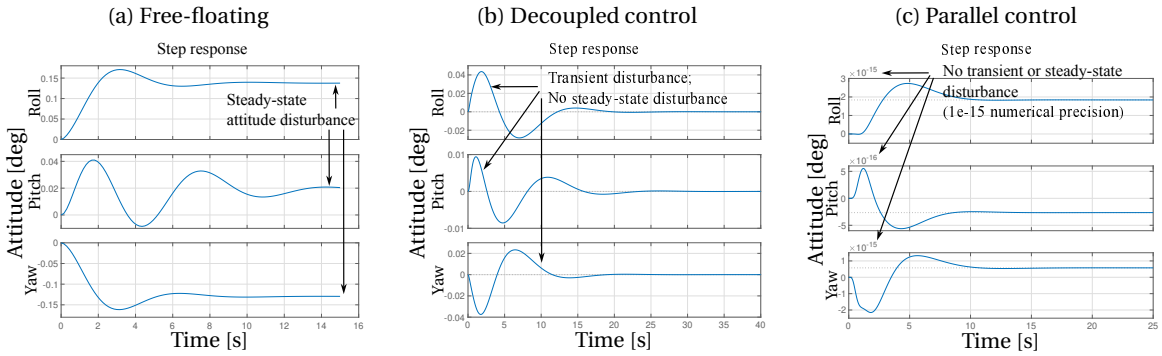

Figure 7.3: *Robot to spacecraft disturbance* – step response of attitude coupling to joint J1 with (a) free-floating control, (b) decoupled control, and (c) parallel control.

about a representative equilibrium pose of the robot under the three control schemes: free-floating, decoupled, and parallel control. Free-floating control produces a non-zero steady-state displacement in attitude. Decoupled control exhibits transient coupling due to robot motion but restores the steady-state attitude to the origin. The parallel control scheme, using the proposed method in Section 3.5.3, demonstrates neither transient nor steady-state disturbances of robot motion on spacecraft attitude, as indicated by step responses that are null to a numerical precision of $1e-15$.

The findings from this study prompted the consideration of parallel control and the development of software interfaces in the mission to facilitate the communication of compensation torques to the spacecraft control system.

7.1.3 Spacecraft actuation disturbance on robot

During phase B of the mission, an analysis was conducted to evaluate the joint torque disturbances on the robot due to spacecraft thrust forces following the commissioning of the arm in the rendezvous phase. Since the robot is specifically designed for space operation without brakes on the joints, the primary objective was to determine whether the small spacecraft thrust forces remain within the static friction limits of the joints, thereby preventing the need for active control and enabling power savings.

The analysis becomes straightforward once the disturbance between spacecraft actuation and the robot is derived from the orbital manipulator dynamics. This relationship was formally established in Section 5.3.1 as the term $\boldsymbol{\tau}_F$, which quantifies the disturbance torques induced on the manipulator arm by low-rate spacecraft actuation.

Within a defined workspace of the robot, 100 poses were randomly sampled. A static analysis was performed in which the instantaneous disturbance torques acting on the joints, resulting from exemplary spacecraft thrust forces, were recorded for each sampled pose.

Snapshots of several representative sampled poses are presented in Figure 7.4 (left), with a histogram of the recorded joint torques shown on the right. As expected, a greater number of

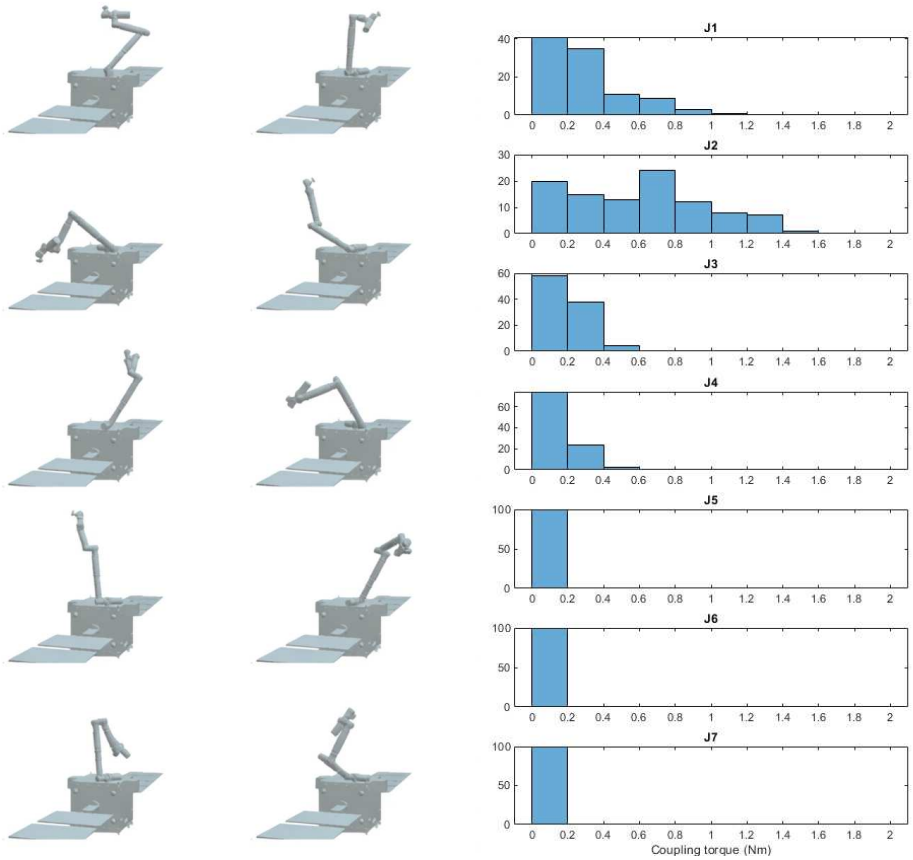

Figure 7.4: *Spacecraft to robot disturbance*– (left) examples of sample poses across workspace, (right) histogram of joint torques generated by spacecraft thruster disturbances.

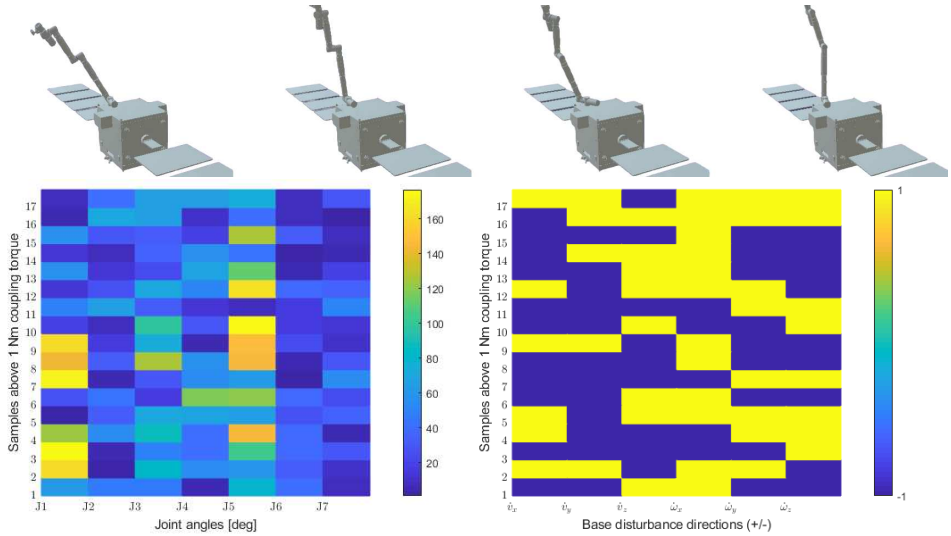

Figure 7.5: *Spacecraft to robot disturbance* – (top) outstretched sample poses with higher joint torques, and heat maps of (bottom left) joint angles, and (bottom right) spacecraft accelerations.

samples fall within intervals of higher torque for the first two joints, which support the majority of the arm's load. Further analysis confirms that most samples resulting in high torques on these joints correspond to nearly outstretched arm configurations. Selected poses from samples with torques exceeding 1 Nm are depicted in Figure 7.5, and the associated heat maps of joint angle distributions align with outstretched arm configurations. In contrast, the heat map of spacecraft acceleration directions does not reveal any clear correlation with the sampled poses.

The preliminary analysis indicated that the static friction margins of the CAESAR arm were sufficient for low thrust forces considered during the rendezvous phase. For combined control strategies involving higher thrust forces, the method described in Section 5.3.1 must be employed to actively compensate for spacecraft-induced disturbances.

7.1.4 Evaluation of achievable end-effector forces

An auxiliary analysis was conducted to determine the maximum force that the robotic arm can achieve at the end-effector to sustain the anticipated gripper loads during contact operations. Considering the joint torque limits, the analysis evaluated the torques required to generate various end-effector forces for a nominal capture configuration of the arm. As discussed in Section 4.3.4, the virtual control force at the end-effector serves as a first-order approximation of the resulting end-effector wrench during slow motions. Consequently, an initial estimate of the required joint torques was obtained by mapping the desired forces using the transposed manipulator Jacobian.

The results are presented in Figure 7.6, where the black dashed line represents the joint torque limit of 80 Nm. The colors of the data points indicate the expected torque values for each joint

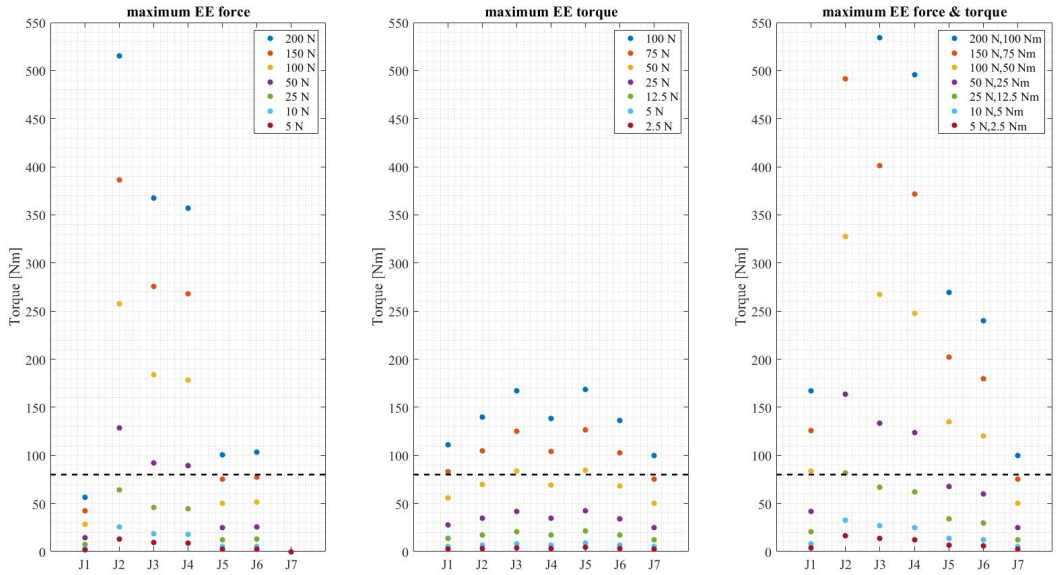

Figure 7.6: *Achievable forces* – joint torques required to generate end-effector forces for a nominal capture configuration of the arm.

corresponding to specific end-effector force or torque values. When all scatter points of a given color are below the dashed line, the arm is capable of achieving the corresponding wrench at the end-effector. This analysis informed one of the considerations for the design of the gripper's mechanical compliance.

7.2 DIANE — CNES mission

DIANE, Démonstration d'Inspection et Amarrage Novatrice Embarquée, a project by the French space agency, CNES, is a sister mission to EROSS (see Figure 7.7), and will utilize a pair of spacecraft scheduled for launch following the EROSS demonstration. The objective of DIANE is to evaluate rendezvous and servicing capabilities in low Earth orbit using a servicer approximately three times the size of the client satellite, equipped with a robotic arm. The mission scenario involves inducing a spin on the client satellite to simulate a target that has lost attitude and orbit control. In addition to inspection, the servicer is designed to reduce the satellite's spin and relocate it to a more suitable position.

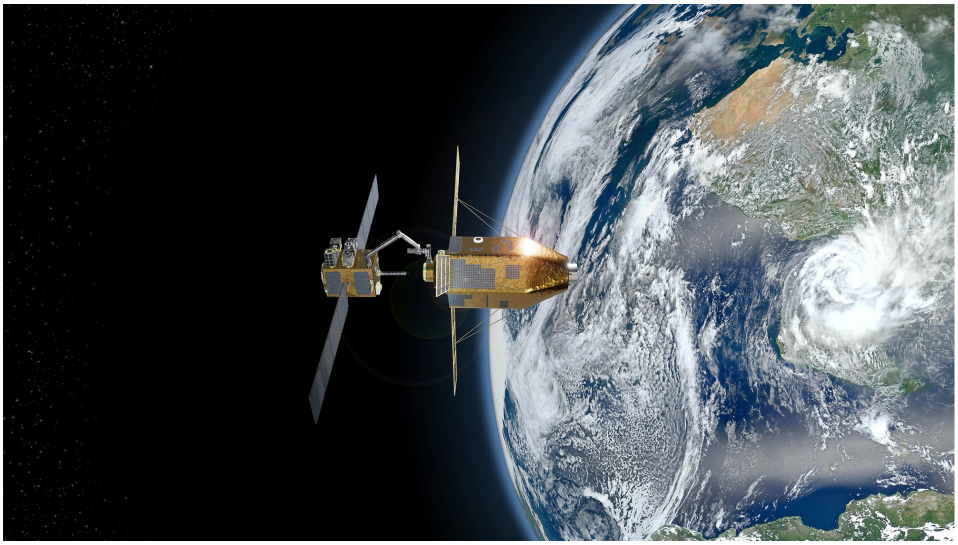

Figure 7.7: Image credit: ©EROSS SC Tipik. The DIANE mission, a sister mission to EROSS, aims to capture and service a spinning client satellite with a robotic arm.

Based on the research conducted in this thesis, a feasibility analysis of control strategies for capturing a spinning satellite, and preliminary results of the on-ground validation of the mission scenario are presented.

7.2.1 Control strategies for spin-synchronized capture

Phase 1 of the DIANE mission aims to comprehensively assess the feasibility of a robotic approach, capture and stabilization of a spinning client satellite. The servicer satellite is assumed to be spin-

synchronized at the beginning of the approach phase. In contrast to the analysis conducted for the EROSS mission in Section 7.1.2, which focused on precise methods for compensating attitude disturbances from the robot using parallel control, the present study constrains attitude de-pointing within a defined pointing budget. Thus, the mission study comprised of:

i) Analyzing limits of free-floating control given the attitude de-pointing budget for robotic approach to a spinning client.

ii) In the limiting cases of free-floating control, analyzing limits of decoupled control, given the reaction wheel budget, for the robotic approach and stabilization.

i) Limits of free-floating control within pointing budget

Multiple approach scenarios were simulated for a spin-synchronized servicer in free-floating control, encompassing various regions of the capture volume as determined by the servicer's positioning accuracy and the client's linear drift velocity. These simulations evaluated the reachability of the client within the manipulator's workspace and quantified the attitude de-pointing incurred during maneuvers relative to allowable thresholds.

The results indicated that both pointing budgets and reachability constraints were violated using free-floating control in several regions of the capture volume, as exemplified in Figure 7.8. As seen in Examples 1 and 2, the robot motion results in severe attitude de-pointing, as the combined inertia of the spacecraft and robot change dynamically with the manipulator motion during approach phase. The attitude de-pointing further adversely affects client reachability within the robot workspace, as seen in Example 1, where the client slips out of reach of the outstretched manipulator. These findings established the limitations of free-floating control during the approach phase in the considered challenging scenario.

ii) Limits of decoupled control within reaction wheel budget

The same scenarios were analyzed using decoupled control to maintain the relative attitude between the servicer and client. This approach significantly improved client reachability within the manipulator's workspace and ensured compliance with the pointing budget during the approach phase, as shown in Figure 7.8, right. However, the entire maneuver from approach phase to post-capture stabilization of the combined servicer and client stack exceeded the reaction wheel momentum capacity, thereby violating the reaction wheel budget. Examples of near and far capture scenarios are presented in Figure 7.9, where decoupled control was used to damp angular momentum while maintaining the relative pose. These maneuvers were observed to utilize spacecraft torques surpassing the total momentum capacity of the reaction wheels.

Additionally, both free-floating and decoupled control methods yield different manipulator poses across variable points in the capture volume, as the spacecraft position remains uncontrolled, result-

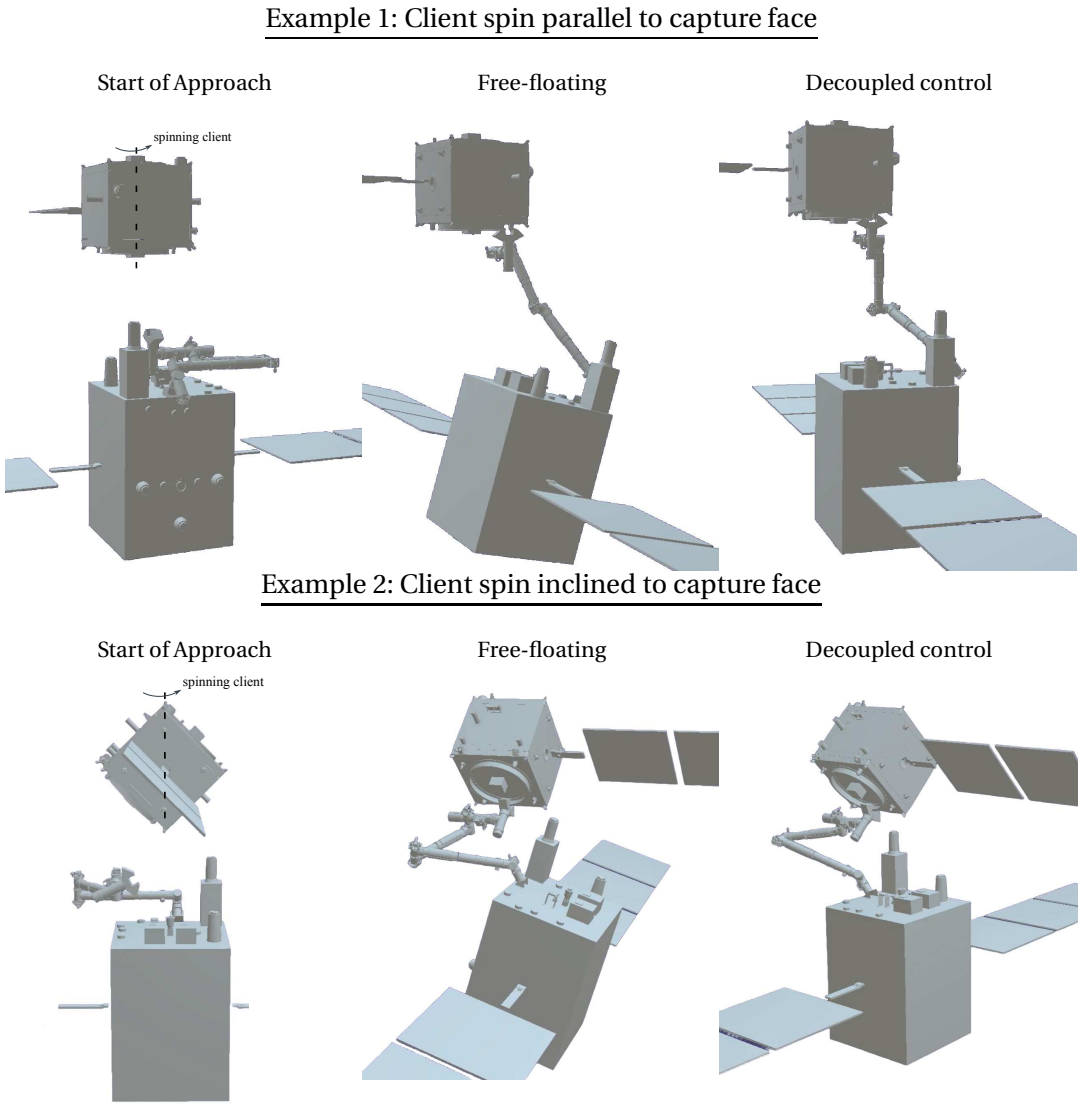

Figure 7.8: *Approach phase* – free-floating vs. decoupled control. Initial poses (left) and grasp poses using free-flying control (middle), violating pointing budgets, versus decoupled control (right), restoring pointing. Free-floating control in Example 1 violates arm's reachable workspace.

ing in varying capture distances and corresponding arm configurations (see far- and near-capture poses in Figure 7.9). Some of these manipulator poses are suboptimal for post-capture client manipulation and for avoiding spacecraft protrusions, as illustrated by the near-capture pose in Figure 7.9, where a spacecraft protrusion is located near the client at the grasp pose.

These limitations underscore the necessity for the unified control strategy proposed in Chapter 4. The strategy employs coupled 6-DoF spacecraft control to achieve a desired manipulator capture pose, accommodating both drifting and spinning clients. Furthermore, challenging scenarios involving spinning clients highlight the importance of the optimized distribution of thruster and

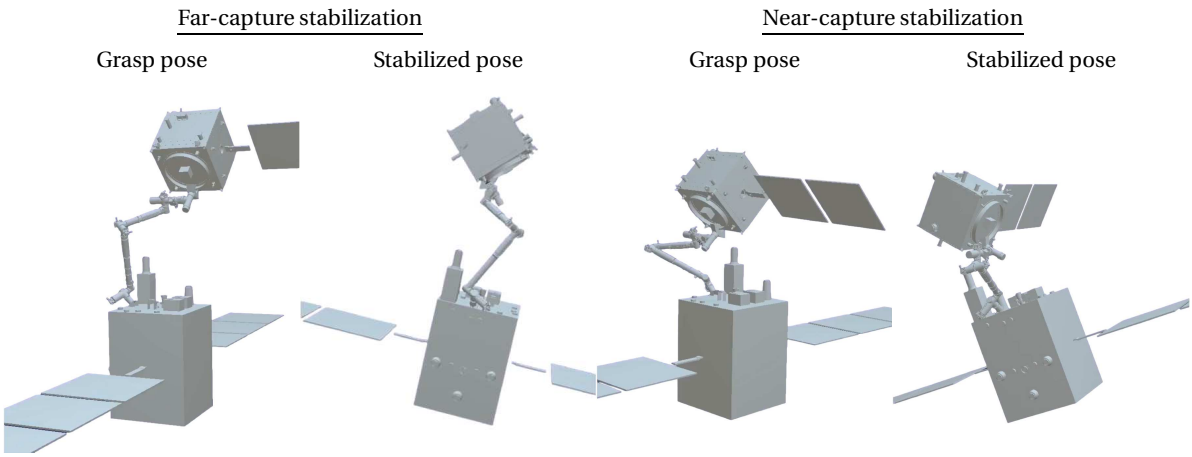

Figure 7.9: *Post-grasp phase* – decoupled control of a far and near capture scenario violates reaction wheel budget during momentum damping of the spinning servicer-client stack.

reaction wheel control, as presented in Chapter 4, to ensure effective momentum dissipation in the post-grasp phase without exceeding the reaction wheel momentum budget. The findings of this study clearly demonstrate the need for advanced combined control strategies, such as the proposed method in Chapter 4, to address the limitations of free-floating and decoupled control.

7.2.2 On-ground validation with impedance-matched robots

On-ground tests for the end of Phase 1 of the DIANE mission assessment aim to demonstrate the floating dynamics of the spin-synchronized scenario for the robotic approach and capture. The on-ground validation of the floating dynamics utilizes the state-of-the-art robotic test facility, OOS-Sim at DLR. Prior to testing the scenario at the OOS-Sim, the DIANE scenario must be adapted to the OOS-Sim workspace, as outlined in Figure 7.10. The OOS-Sim is equipped with an LWR robot, an approximately 1m arm, while the mission scenario considers the CAESAR robot, an approximately 3m arm, requiring a specialized suspended platform (see Section 2.1.2) that cannot be tested in the workspace of the OOS-Sim. Therefore, the on-ground validation of the mission scenario on the OOS-Sim aims to match the dynamics of the LWR robot with the CAESAR robot.

To achieve a dynamic representation of the CAESAR robot on the OOS-Sim using the LWR robot, an impedance matching strategy for the two robots is implemented [DSPO23]. Figure 7.11 presents an experiment validating the impedance matching of the LWR robot to CAESAR, utilizing force-torque sensor measurements during human interaction. The results in Figure 7.12 indicate that the acceleration at the end-effector of the simulated CAESAR robot (dashed lines) responds to measured forces (Figure 7.12 top), while the LWR robot successfully reproduces the impedance behavior of CAESAR at its end-effector (solid lines).

In preparation for the on-ground demonstration concluding Phase 1, ongoing work focuses

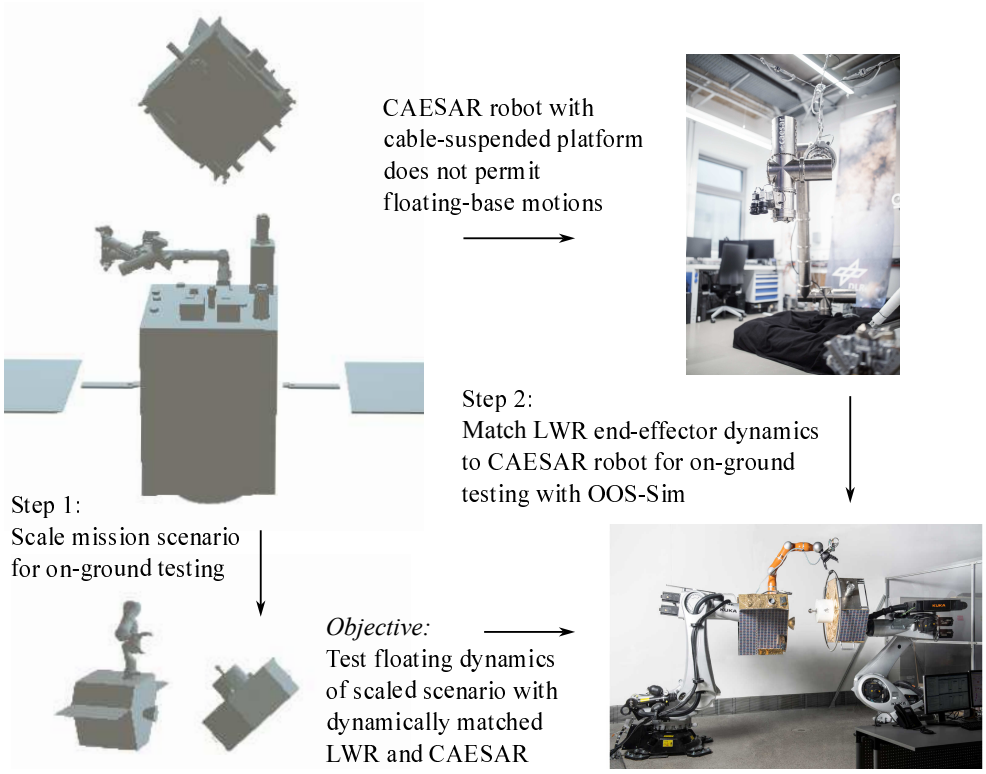

Figure 7.10: Scaling mission scenario to OOS-Sim for HIL validation with impedance matching of LWR to CAESAR, motivated by lack of floating-base servicer-client dynamics using CAESAR and MSS facility.

on transferring the impedance-matched dynamics of CAESAR onto the LWR robot within a scaled mission scenario. This enables robotic capture analysis using different control strategies with spin-synchronized floating dynamics on the OOS-Sim.



Figure 7.11: *Impedance matching experiment* – (left) interacting with impedance-matched LWR and CAESAR, (right) poses of LWR and CAESAR during end-effector impedance matching.

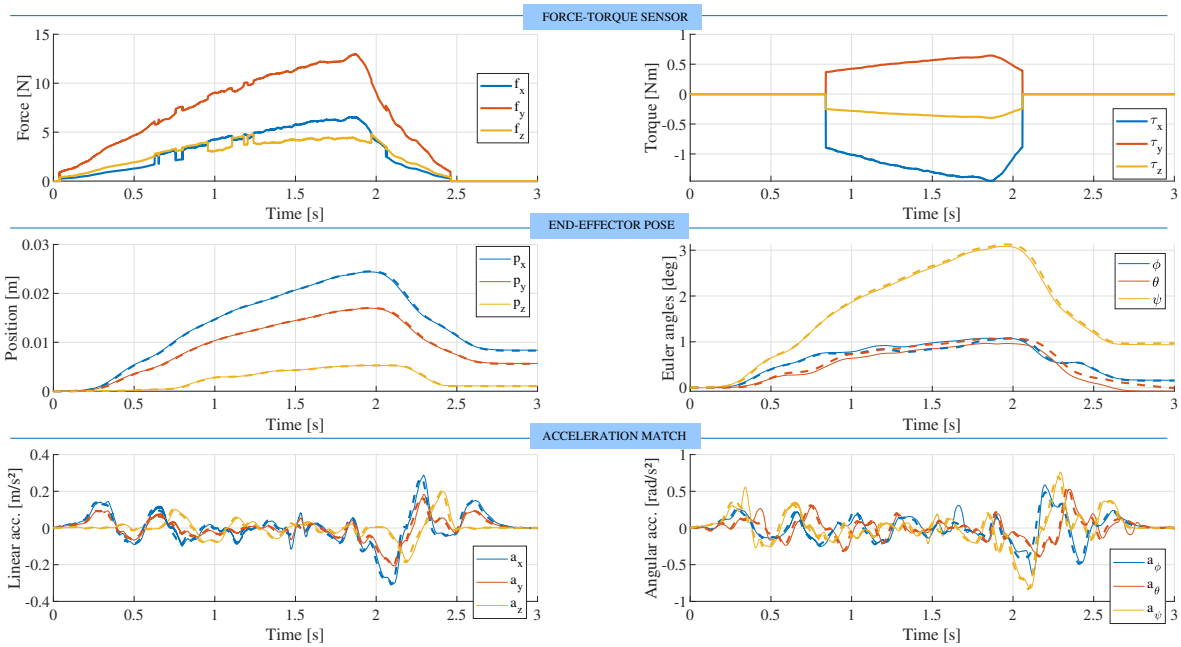

Figure 7.12: *Impedance matching experiment* – LWR to CAESAR. The dashed lines trace the end-effector response of CAESAR to forces measured at the LWR end-effector. The solid lines trace the impedance matched end-effector motion emulated by the LWR robot.

7.3 RISE — ESA mission

The RISE (Resilient In-orbit Servicing for Europe) mission represents ESA's first commercial initiative for in-orbit servicing, developed in collaboration with D-Orbit to demonstrate the extension of geostationary satellite lifespans. RISE is designed to autonomously locate and dock with client satellites, subsequently assuming control of their attitude and orbit (see Figure 7.13). This capability enables satellites that have exhausted their fuel supplies to continue operating. The mission will validate critical technologies for safe proximity operations, autonomous docking, and satellite relocation. RISE is part of ESA's Zero Debris initiative to promote a more sustainable space economy by facilitating satellite life extension and enabling future services such as refueling and repairs.

The mission analysis of Phases A and B of the RISE mission borrowed concepts from this thesis to assess manipulator loads during post-grasp manipulation, tailor end-effector control to align with the client capture plane, and manipulate end-effector forces during tool pick-up.

7.3.1 Client manipulation loads at spacecraft-robot interface

During Phase A of the RISE mission, an analysis was conducted to determine the forces and torques generated at the robot base during post-grasp manipulation of a captured client satellite. Estimating these load profiles informs the sizing of reaction wheels required for attitude stabilization. Sec-



Figure 7.13: Image credit: ESA/D-Orbit. The RISE mission scenario shows the approach of a client satellite using a robotic arm with an end-effector ring.

tion 7.1.2 addressed a similar problem by employing linearization methods to compare various spacecraft control regimes based on disturbance coupling resulting from robot motion across different equilibrium poses. In contrast, the present analysis aims to dynamically estimate the load profiles (forces and torques) at the spacecraft-robot interface during mission-specific manipulation trajectories with the robot attached to the client satellite.

The methodology redefines the interaction forces, previously modeled at the end-effector in (4.13), to represent forces at the spacecraft-robot interface. This modification involves modeling the servicing spacecraft as a floating body constrained by the robotic arm attached to the client satellite. This method was applied in preliminary studies involving post-grasp manipulation of a client satellite with a mass three times greater than that of the servicing spacecraft (see Figure 7.14). The approach was subsequently validated using a force-torque sensor modeled in CoppeliaSim at the arm base to estimate the loads during client satellite manipulation, as shown in Figure 7.15.

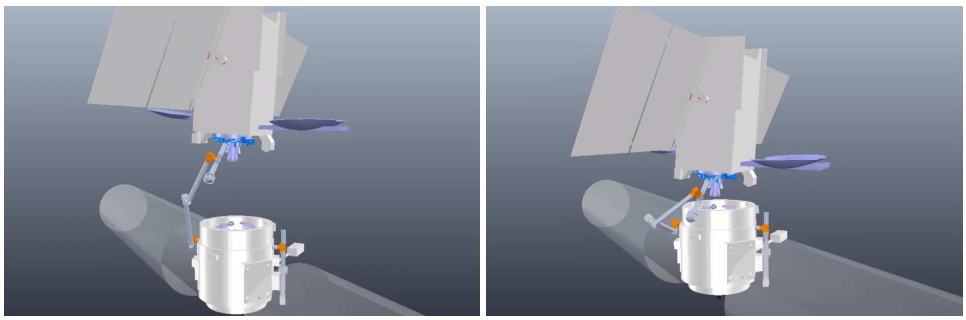

Figure 7.14: *Post-grasp manipulation* – client manipulation maneuver.

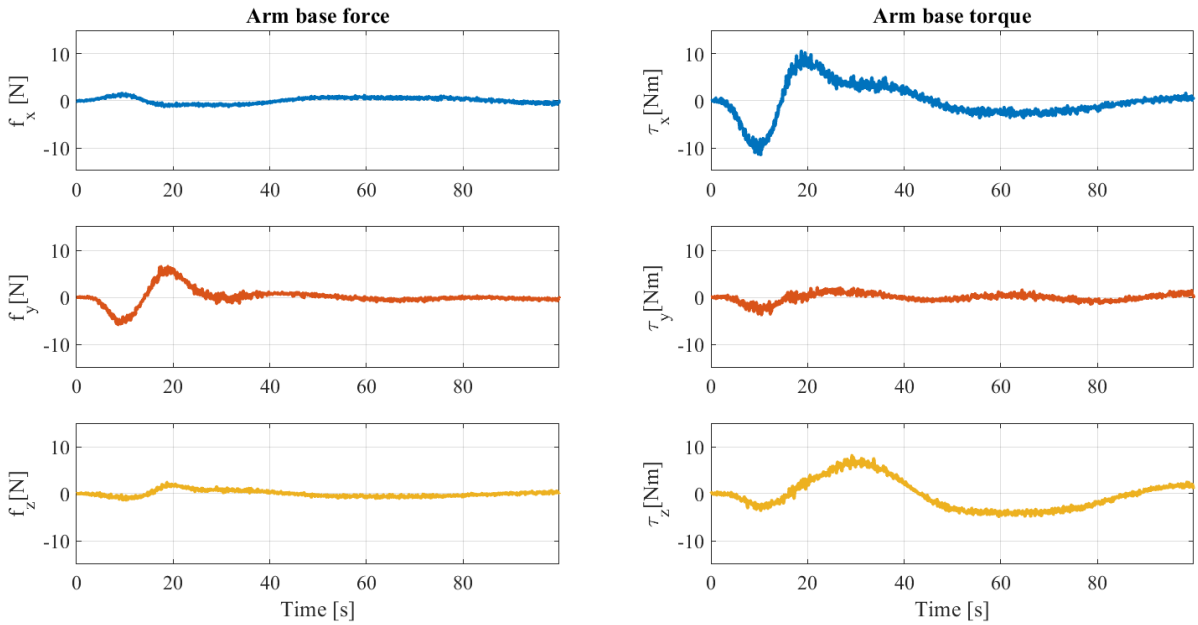

Figure 7.15: *Post-grasp manipulation* – client maneuvering loads on arm base.

7.3.2 End-effector axis alignment control

In Phase A of the RISE mission, a preliminary analysis was conducted to evaluate the control strategy for aligning the end-effector ring with the client Launch Adapter Ring (LAR) during the approach phase. The concentric rings must have parallel planes, meaning their axes must be aligned for successful capture, while the roll about the normal axis to the plane of the ring remains unconstrained.

To achieve alignment with the unconstrained roll angle, the virtual control force at the end-effector, analogous to that defined in (4.9), is applied by relaxing the stiffness about the error quaternion vector aligned with the normal to the ring. This concept is illustrated in Figure 7.16, where the

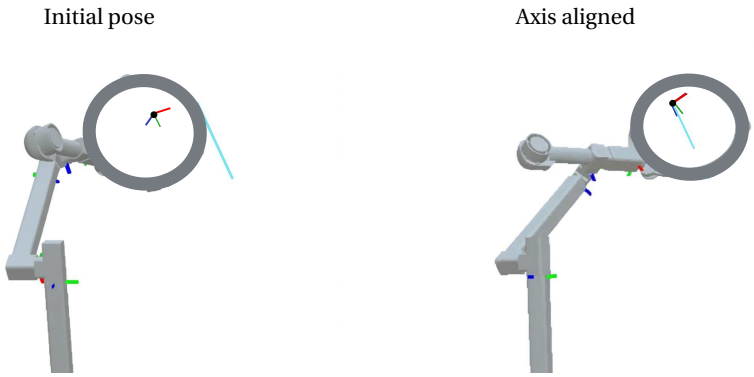

Figure 7.16: *Axis alignment* – alignment control to align normal of ring plane (z-axis in blue) with a desired direction (cyan).

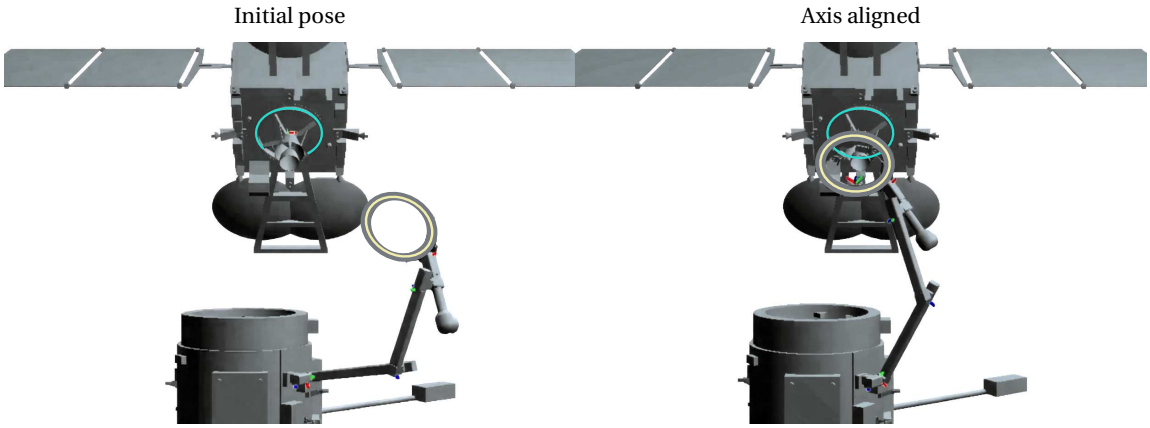

Figure 7.17: *Axis alignment* – alignment control of end-effector ring (yellow) to client LAR (cyan).

z-axis of the ring, in blue, is aligned with the desired axis, depicted in cyan.

This method was subsequently applied in preliminary studies of the approach phase of the RISE mission to assess the ring alignment strategy. The scenario involves a non-spinning client satellite and end-effector alignment using decoupled control to maintain spacecraft attitude. The alignment strategy produces an orientation in which the plane of the end-effector ring aligns with the desired plane of the LAR, as shown in Figure 7.17.

7.3.3 End-effector docking with tool

Previous chapters have extensively discussed and analyzed contact operations involving the client satellite. This section presents the contact operation in which the robotic arm retrieves a tool from the spacecraft. During Phase B of the RISE mission, an analysis was conducted to validate the requirements for the minimum forces that must be applied at the end-effector to engage with a tool prior to retrieval. Once the tool is docked with the end-effector, and before it is disengaged from the spacecraft, the requirements specify that residual forces and torques acting on the manipulator must be relaxed. Figure 7.18 illustrates the homing pose and final pose for tool pick up.

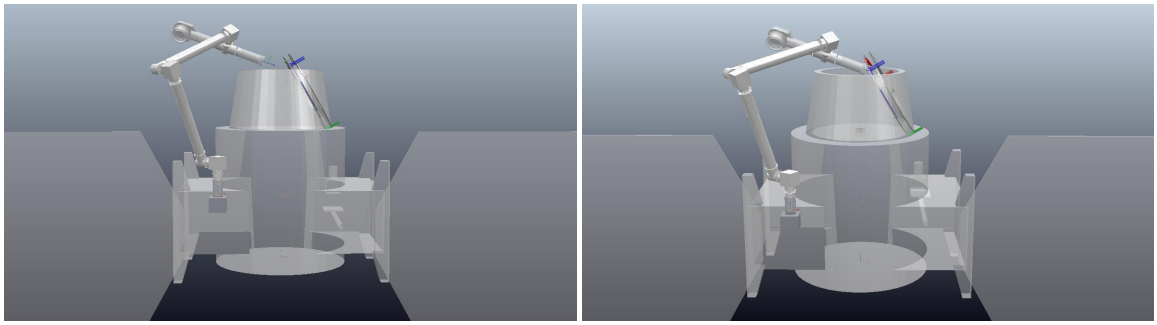

Figure 7.18: *Tool docking* – (a) Homing pose at an offset distance from tool, and (b) docking pose in contact with tool.

For contact operations such as tool pick up, a homing pose is initialized at a short distance from the tool, which can be achieved using either stiff position control or impedance control. From the homing pose, impedance control with soft gains is engaged to follow a slow trajectory for tool engagement. This switching of control modes is feasible for tool pick up because multiple stops can be performed during the approach to a fixed tool on the spacecraft. However, such control switching is not desirable during continuous trajectory execution, such as during approach and contact operations with a drifting or spinning client. Therefore, a unified tracking control is proposed in Chapter 4 for approach, grasp, and stabilization involving spinning client satellites.

For the present application involving a tool pick-up on the spacecraft, the adopted strategy utilizes impedance control to establish a compliant contact, with a penetrative setpoint for indirect force control. While using a virtual end-effector force analogous to (4.9) with decoupled control, a penetrative setpoint within the tool unifies the impedance control for motion tracking to reach the contact point, and enables a smooth transition to indirect force control for applying docking loads. The penetrative setpoint within the tool enables indirect application of end-effector forces by leveraging the spring stiffness of the impedance control law, thereby generating a non-zero error at the contact surface. Gradual interpolation of the penetrative setpoint results in a corresponding application of forces at the contact interface. After tool engagement, the stiffness gains are progressively reduced, and the desired end-effector pose is reset to the current pose. Subsequent arm motion with the attached tool is then performed using a standard impedance controller.

This method was applied in preliminary studies of the robotic Concept of Operations (CONOPS) phases of the RISE mission and Figure 7.19 presents the results showing a penetrative setpoint, subsequent application of exemplary forces and relaxation of contact forces, validated by a force-torque sensor modeled in CoppeliaSim.

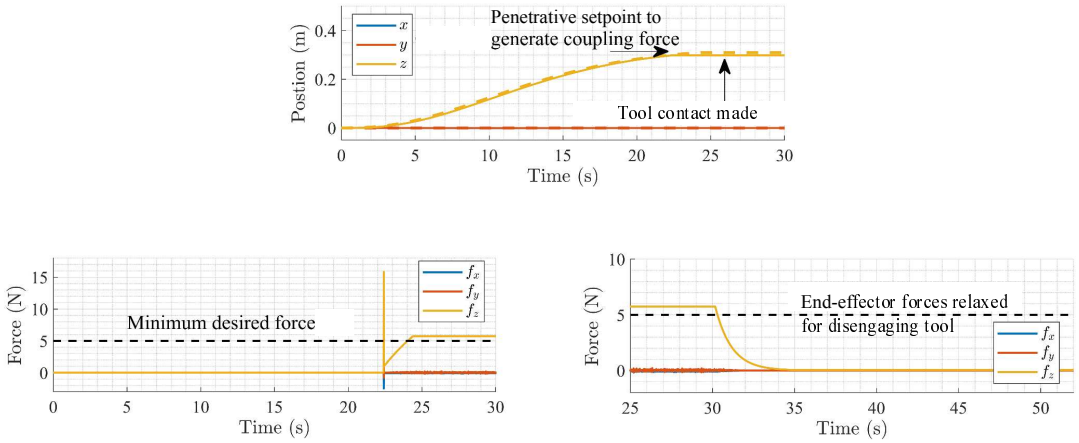

Figure 7.19: *Tool docking* – indirect force application using impedance control with a penetrating setpoint.

7.4 Summary

This chapter presented several applications of control strategies for mission analysis and on-ground testing relevant to three missions, EROSS, DIANE and RISE. In particular, this chapter helps to concretely contextualize the benefits of the novel strategies proposed and validated in previous chapters by contrasting them with the limitations of free-floating and decoupled control seen in several of the mission analysis conducted here. While a wide range of applications are discussed in this chapter, the underlying concepts utilized in the previous chapters were evidently seen to transfer, inspire and tackle real challenges encountered in the design and development of OOS robotic missions.

CHAPTER 8

CONCLUSION AND OUTLOOK

Since the birth of the space age nearly seven decades ago, space infrastructure has progressed from Sputnik, a radio wave transmitter, to the James Webb Space Telescope that can peer 13.5 billion years into the past. This infrastructure has evolved from single-satellite payloads to complex communication and navigation constellations, and to large-scale structures such as the ISS, constructed and expanded by astronauts in orbit. On-orbit servicing is one piece of the puzzle that seeks to sustain past, present, and future infrastructure in space.

The goal of this thesis was to design control strategies motivated by the operational challenges of space robots in orbital servicing and ground testing. Chapter 1 showed the impressive achievements of humans in space servicing critical missions, such as the Hubble Space Telescope. As the space industry expands, multiple sectors require sustainable development. Rocket launch providers have realized the advantages of transitioning from single-use rockets to reusable launch systems, while resupply cargo vehicles have proven effective in replenishing resources for astronauts aboard the ISS. Today, robotic OOS solutions offer scalable, autonomous systems to service the increasing number of satellites in orbit.

In particular, this thesis addressed the challenges of approaching, grasping, and stabilizing spinning satellites. Chapters 3 and 4 progressively developed unified control strategies. Tasks were prioritized according to mission-phase objectives, leveraging the servicer's whole-body nullspace for both post-grasp stabilization and subsequent client reconfiguration. During stabilization, the servicer performed simultaneous detumbling and joint reconfiguration, maintaining attitude after capture with reaction wheel redundancy to decouple manipulator and base motions, improving efficiency by reducing reliance on thrusters.

Quadratic programming was used to systematically incorporate mission constraints within the control hierarchy. For post-grasp stabilization, interaction forces at the grasp interface were limited

Table 8.1: Summary of different applications, hierarchies and methodologies used in the thesis. Boxes highlight primary subsystems decoupled from the motion of secondary subsystems.

Chapter	**Chapter 3**	**Chapter 4**	**Chapter 5**	**Chapter 6**
Considered application	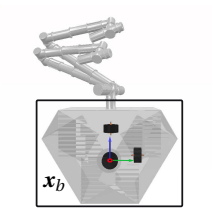 Base attitude undisturbed by manipulator reconfiguration	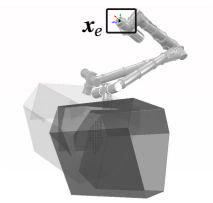 End-effector undisturbed by manipulator reconfiguration	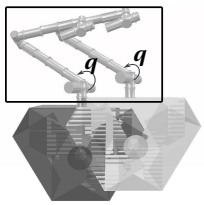 Manipulator undisturbed by spacecraft reconfiguration	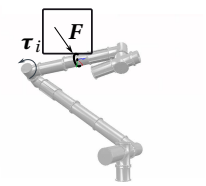 Carrier undisturbed by manipulator compensation
Hierarchy type	Two-level task hierarchy	Multi-level task hierarchy	Task hierarchy in control coordinates	Control input hierarchy
Methodology	Extension using nullspace coordinates	Partition using nullspace-projected task coordinates	Substitution of secondary task dynamics into primary task dynamics	QP formulation with equality constraint and unweighted primary control

through optimization, removing the need for force-torque sensing. Reaction wheel speed limits and saturation were managed by adapting damping torques. The unified control framework, using reaction wheels and thrusters, was applied from approach through stabilization, leveraging actuator redundancy for greater efficiency.

A hybrid control scheme was introduced in Chapter 5 to address the challenge of operating the spacecraft and manipulator at different control frequencies. Manipulator control was prioritized at high rate, with low-rate spacecraft control projected into the manipulator's nullspace. Sample-aware terms compensated for energy leaks, improving stability and overall system performance.

On-ground validation under gravity was tackled in Chapter 6 by optimizing support from external carriers, generalizable to any degrees of freedom or coupling points. This method minimized manipulator joint torques, compensated for gravity across a wide workspace, and balanced actuation limits with external supports, effectively mitigating gravity-induced torques during testing.

The benefits of the novel strategies were particularly evident during several mission studies of the RISE, EROSS, and DIANE missions in Chapter 7. Several applications tackled during mission development phases illustrated the transfer of concepts, and the limitations of existing control strategies, which can be overcome by the proposed control strategies validated in the previous chapters.

Although the strategies presented are tailored to specific problems, these applications, summarized in Table 8.1, may be adapted to other scenarios by selecting the hierarchy that best character-



Figure 8.1: Methods proposed in the thesis can be adapted to other mobile-base and vehicle-manipulator systems. Clockwise: aerial, underwater, legged, mobile platform, wheeled, and whole body robotic systems.

izes the manipulator system in a new context. They can find application in other vehicle manipulator systems, such as terrestrial mobile-base robots, underwater robots, and aerial robots, see Figure 8.1. For instance, Chapter 3 addresses problems that require prioritizing the base pose. Chapters 3 and 4 discuss scenarios involving the prioritization of a whole-body actuated end-effector. Chapter 5 focuses on floating-base manipulator problems where manipulator joints are prioritized over base control. Chapter 6 examines cases involving the prioritization of an external input, such as two robots coupled and operating in tandem. Table 8.1 also summarizes the different methodologies and hierarchy types explored in the thesis.

Chapters 3 to 6 explore hierarchical control of space manipulators using different nullspace-based strategies: nullspace coordinates with whole-body control, explicit nullspace partitioning for specific task control, decoupled control via secondary dynamics, and optimally weighted control allocation. A primary distinction between the methodologies employing nullspace coordinates in Chapters 3, 4, and 5 and the optimal formulation in Chapter 6 is that the former facilitates task prioritization, whereas the latter enables actuator prioritization.

Notably, the optimal distribution of control between reaction wheels and thrusters in Chapter 4 parallels the approach in Chapter 6, as both involve redistribution within the nullspace and prioritize control inputs through cost function weighting. Further, the distribution of torques to the reaction wheels differs between Chapter 3 and Chapter 4. Unlike the reduced Jacobian approach in Chapter 3, which activates the reaction wheels through the primary task, the primary and secondary tasks in Chapter 4 do not directly activate the reaction wheels (excluding Coriolis cross-couplings),

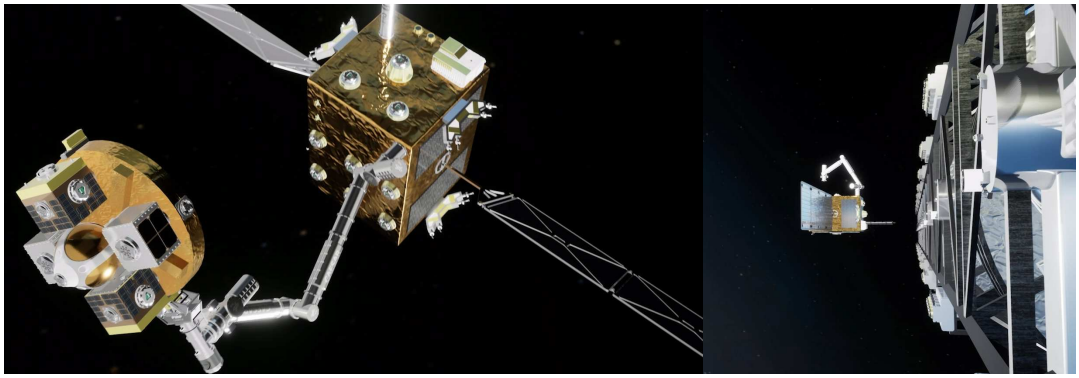

Figure 8.2: Image credit: © EROSS SC. The vision for OOS involves servicing multiple satellites and resupplying with ORUs (left) from a dedicated supply platform (right) in space.

as the reaction wheels are in a separate kinematic chain from the arm. Instead, the reaction wheels in Chapter 4 are activated through the optimal redistribution of base torques within the nullspace.

Furthermore, nullspace coordinates provide a systematic approach for the strict decoupling of tasks, including Coriolis cross-couplings, while the optimal formulation permits damped nullspace projections by weighting the control inputs. The damped projection guarantees existence in cases involving kinematic singularities, albeit at the expense of some coupling to the primary task. This was beneficial in Chapter 6 since the nullspace of the fixed-base robot depended on kinematic singularity.

Future research could investigate floating-base dynamics and control of long-link manipulators in scenarios where flexibility becomes significant. Further extensions of multi-rate control to accommodate quantized inputs and time delays also present valuable research opportunities. Additionally, examining the dynamic coupling of cable-driven parallel robots may be beneficial for fine manipulation tasks to be robust to cable flexion and noise, and delay in force tracking.

The combined control strategies presented in this thesis show significant potential for robotic servicing applications. Future OOS scenarios will require advanced autonomy to sustain large-scale supply platforms in space, enabling servicing robots to replenish supplies and maintain continuous operations (see Figure 8.2). Therefore, the scope for future research in space robotics remains extensive and is anticipated to expand further. In this vein, the results of this thesis have contributed to advancing control strategies for OOS applications, as well as to mission development and technology maturation, with the goal of enabling robotic servicing and life extension of space infrastructure.

APPENDIX A

OPERATORS, IDENTITIES AND EXPRESSIONS FOR REL FORMULATION

A.1 Useful operators and identities

Notation for partial derivatives

The partial derivative operator is considered in vector form using the notation as follows:

$$\bullet \quad \partial_{\boldsymbol{q}}^{T} \boldsymbol{v} = \begin{bmatrix} \frac{\partial}{\partial q_1} \boldsymbol{v} & \cdots & \frac{\partial}{\partial q_n} \boldsymbol{v} \end{bmatrix} \qquad \bullet \quad \partial_{\boldsymbol{q}} \boldsymbol{v}^{T} = \begin{bmatrix} \frac{\partial}{\partial q_1} \boldsymbol{v}^{T} \\ \vdots \\ \frac{\partial}{\partial q_n} \boldsymbol{v}^{T} \end{bmatrix}$$

where $\partial_{\boldsymbol{q}}^{T} \boldsymbol{v}$ is a matrix of the partial derivative of $\boldsymbol{v}$ with respect to the elements of $\boldsymbol{q}$. A useful property when multiplying a time-derivative of a matrix $\boldsymbol{A}$, which is a function of $\boldsymbol{x}$ with a vector $\boldsymbol{y}$, is:

$$\bullet \quad \dot{\boldsymbol{A}}(\boldsymbol{x})\boldsymbol{y} = \partial_{\boldsymbol{x}}^{T}(\boldsymbol{A}(\boldsymbol{x})\boldsymbol{y})\dot{\boldsymbol{x}}$$

Lie operators and some useful identities

The adjoint action, $\mathrm{Ad}_{\boldsymbol{g}}$, uses an element of the Lie group (the homogeneous transform, $\boldsymbol{g} \in \mathrm{SE}(3)$) and the Lie bracket, $\mathrm{ad}_{\boldsymbol{V}}$, uses an element of the Lie algebra (the body twist, $\boldsymbol{V}$). The operator $\mathrm{ad}^{\sim}$ is defined such that $\mathrm{ad}_{\boldsymbol{V}}^{T}\boldsymbol{h} = \mathrm{ad}_{\boldsymbol{h}}^{\sim}\boldsymbol{V}$ [M+23]. Written in matrix form, these are:

$$\mathrm{Ad}_{\boldsymbol{g}} = \begin{bmatrix} \boldsymbol{R} & \boldsymbol{p}^{\times}\boldsymbol{R} \\ \boldsymbol{0} & \boldsymbol{R} \end{bmatrix}, \qquad \mathrm{ad}_{\boldsymbol{V}} = \begin{bmatrix} \boldsymbol{\omega}^{\times} & \boldsymbol{v}^{\times} \\ \boldsymbol{0} & \boldsymbol{\omega}^{\times} \end{bmatrix}, \qquad \mathrm{ad}_{\boldsymbol{h}}^{\sim} = \begin{bmatrix} \boldsymbol{0} & \boldsymbol{h}_{v}^{\times} \\ \boldsymbol{h}_{v}^{\times} & \boldsymbol{h}_{\omega}^{\times} \end{bmatrix}$$

where $\bullet^{\times}$ is the notation for the skew-symmetric matrix formed by the vector $\bullet$. The rotation matrix $\boldsymbol{R} \in \mathbb{R}^{3\times3}$ and the position $\boldsymbol{p} \in \mathbb{R}^{3}$ is associated with the homogeneous transformation matrix $\boldsymbol{g}$. The

linear and angular velocities are $\boldsymbol{v} \in \mathbb{R}^3$ and $\boldsymbol{\omega} \in \mathbb{R}^3$ and the body twist $\boldsymbol{V} = (\boldsymbol{v}, \boldsymbol{\omega})$. The linear and angular parts of the generalized momentum $\boldsymbol{h} \in \mathbb{R}^6$ are $\boldsymbol{h}_v \in \mathbb{R}^3$ and $\boldsymbol{h}_\omega \in \mathbb{R}^3$.

The identities used for the derivation of the REL equations are,

- $\widetilde{\mathrm{ad}}_{\boldsymbol{h}}^T = -\widetilde{\mathrm{ad}}_{\boldsymbol{h}}$
- $\mathrm{ad}_{\boldsymbol{V}}^T \boldsymbol{h} = \widetilde{\mathrm{ad}}_{\boldsymbol{h}} \boldsymbol{V}$
- $\partial_{\boldsymbol{q}}^T (\mathrm{Ad}_{bk}^{-T} \boldsymbol{h}) = -\mathrm{Ad}_{bk}^{-T} \widetilde{\mathrm{ad}}_{\boldsymbol{h}} \boldsymbol{J}_k$
- $\partial_{\boldsymbol{q}}^T (\mathrm{Ad}_{bk}^{-1} \boldsymbol{V}) = \mathrm{ad}_{\mathrm{Ad}_{bk}^{-1} \boldsymbol{V}} \boldsymbol{J}_k$
- $\partial_{\boldsymbol{q}}^T (\boldsymbol{J}_k^T \boldsymbol{h}) - \partial_{\boldsymbol{q}} (\boldsymbol{J}_k^T \boldsymbol{h})^T = -\boldsymbol{J}_k^T \widetilde{\mathrm{ad}}_{\boldsymbol{h}} \boldsymbol{J}_k$
- $\partial_{q_j} (\boldsymbol{J}_k^i) = -\mathrm{ad}_{\boldsymbol{J}_k^j} \boldsymbol{J}_k^i$

A.2 Complete expressions for Reduced Euler-Lagrange formulation

The expressions in (2.18) of the Reduced Euler-Lagrange formulation can be further expanded using the identities in Appendix A.1 as follows.

$$
\begin{aligned}
S(\boldsymbol{\nu}_L) &= \partial_{\boldsymbol{q}}^T (\boldsymbol{M}_{bb} \boldsymbol{\nu}_L) \\
S_1(\boldsymbol{\nu}_L) &= \boldsymbol{A}_l^T S(\boldsymbol{\nu}_L) - S^T(\boldsymbol{\nu}_L) \boldsymbol{A}_l + \partial_{\boldsymbol{q}}^T (\boldsymbol{M}_{bm}^T \boldsymbol{\nu}_L) - \partial_{\boldsymbol{q}} (\boldsymbol{M}_{bm}^T \boldsymbol{\nu}_L)^T \\
S_2(\dot{\boldsymbol{q}}) &= S_1(\boldsymbol{A}_l \dot{\boldsymbol{q}}) + \partial_{\boldsymbol{q}}^T (\boldsymbol{M}_{mm} \dot{\boldsymbol{q}}) - \partial_{\boldsymbol{q}} (\boldsymbol{M}_{mm} \dot{\boldsymbol{q}})^T - \boldsymbol{A}_l^T \partial_{\boldsymbol{q}}^T (\boldsymbol{M}_{bm} \dot{\boldsymbol{q}}) + \partial_{\boldsymbol{q}} (\boldsymbol{M}_{bm} \dot{\boldsymbol{q}})^T \boldsymbol{A}_l
\end{aligned}
$$

These can be computed as follows.

$$
\begin{aligned}
\partial_{\boldsymbol{q}}^T (\boldsymbol{M}_{bb} \boldsymbol{\nu}_L) &= \sum_k \mathrm{Ad}_{bk}^{-T} (\boldsymbol{M}_k \mathrm{ad}_{\mathrm{Ad}_{bk}^{-1} \boldsymbol{\nu}_L} - \widetilde{\mathrm{ad}}_{\boldsymbol{M}_k \mathrm{Ad}_{bk}^{-1} \boldsymbol{\nu}_L}) \boldsymbol{J}_k \\
\partial_{\boldsymbol{q}}^T (\boldsymbol{M}_{bm}^T \boldsymbol{\nu}_L) - \partial_{\boldsymbol{q}} (\boldsymbol{M}_{bm}^T \boldsymbol{\nu}_L)^T &= \sum_k \boldsymbol{J}_k^T (\boldsymbol{M}_k \mathrm{ad}_{\mathrm{Ad}_{bk}^{-1} \boldsymbol{\nu}_L} - \mathrm{ad}_{\mathrm{Ad}_{bk}^{-1} \boldsymbol{\nu}_L}^T \boldsymbol{M}_k) \boldsymbol{J}_k - \boldsymbol{J}_k^T \widetilde{\mathrm{ad}}_{\boldsymbol{M}_k \mathrm{Ad}_{bk}^{-1} \boldsymbol{\nu}_L} \boldsymbol{J}_k \\
\partial_{\boldsymbol{q}}^T (\boldsymbol{M}_{mm} \dot{\boldsymbol{q}}) - \partial_{\boldsymbol{q}} (\boldsymbol{M}_{mm} \dot{\boldsymbol{q}})^T &= \sum_k \boldsymbol{J}_k^T \boldsymbol{M}_k \partial_{\boldsymbol{q}}^T (\boldsymbol{J}_k \dot{\boldsymbol{q}}) - \partial_{\boldsymbol{q}} (\boldsymbol{J}_k \dot{\boldsymbol{q}})^T \boldsymbol{M}_k \boldsymbol{J}_k - \boldsymbol{J}_k^T \widetilde{\mathrm{ad}}_{\boldsymbol{M}_k \boldsymbol{J}_k \dot{\boldsymbol{q}}} \boldsymbol{J}_k \\
\partial_{\boldsymbol{q}} (\boldsymbol{M}_{bm} \dot{\boldsymbol{q}})^T \boldsymbol{A}_l - \boldsymbol{A}_l^T \partial_{\boldsymbol{q}}^T (\boldsymbol{M}_{bm} \dot{\boldsymbol{q}}) &= \sum_k \boldsymbol{A}_l^T \mathrm{Ad}_{bk}^{-T} \widetilde{\mathrm{ad}}_{\boldsymbol{M}_k \boldsymbol{J}_k \dot{\boldsymbol{q}}} \boldsymbol{J}_k + \boldsymbol{J}_k^T \widetilde{\mathrm{ad}}_{\boldsymbol{M}_k \boldsymbol{J}_k \dot{\boldsymbol{q}}} \mathrm{Ad}_{bk}^{-1} \boldsymbol{A}_l \\
&\quad - \boldsymbol{A}_l^T \mathrm{Ad}_{bk}^{-T} \boldsymbol{M}_k \partial_{\boldsymbol{q}}^T (\boldsymbol{J}_k \dot{\boldsymbol{q}}) + \partial_{\boldsymbol{q}} (\boldsymbol{J}_k \dot{\boldsymbol{q}})^T \boldsymbol{M}_k \mathrm{Ad}_{bk}^{-1} \boldsymbol{A}_l \\
\partial_{q_j} (\boldsymbol{J}_k \dot{\boldsymbol{q}}) &= -\mathrm{ad}_{\boldsymbol{J}_k^j} \sum_{i<j} \boldsymbol{J}_k^i \dot{q}_i
\end{aligned}
$$

APPENDIX B

DEFINITIONS FOR CONDITIONAL STABILITY

The following definitions of stability are presented as in [Kha08] and [SL$^+$91], with those pertaining to conditional stability following [SJK12].

Consider a time-invariant system with state vector $x \in \mathbb{R}^n$ of the form

$$\dot{x} = f(x). \tag{B.1}$$

Let $\bar{x}$ denote an equilibrium of (B.1), that is, $f(\bar{x}) = 0$, and let $x_0 = x(0)$ represent the initial condition.

Definition 1. *The equilibrium $\bar{x} = 0$ of (B.1) is*

- stable *if, for each $\varepsilon > 0$, there is $\delta = \delta(\varepsilon) > 0$ such that*

$$\|x_0\| < \delta \implies \|x(t)\| < \varepsilon, \quad \forall\, t \geq 0$$

- unstable *if it is not stable.*
- asymptotically stable *if it is stable and δ can be chosen such that*

$$\|x_0\| < \delta \implies \lim_{t\to\infty} x(t) = 0$$

Definition 2. *If asymptotic stability holds for all initial states, the equilibrium point is termed globally asymptotically stable.*

Assume that a solution $x(t)$ to (B.1) exists for an initial state $x_0 = x(0)$ and for all times $t > 0$. For conditional stability, the requirements of the stability definitions are only required to hold for initial conditions within a specified set $A \subset \mathbb{R}^n$. Therefore, conditional stability is a weaker property than Lyapunov stability.

Definition 3. *A stationary point $\bar{x}$ of (B.1) is defined as stable conditionally to the set $A \subset \mathbb{R}^n$ if $\bar{x} \in A$ and, for each $\varepsilon > 0$, there exists $\delta(\varepsilon) > 0$ such that the following implication holds for any initial condition $x_0 \in A$:*

$$\|x_0 - \bar{x}\| < \delta(\varepsilon) \implies \|x(t) - \bar{x}\| < \varepsilon, \quad \forall\, t \geq 0. \tag{B.2}$$

Definition 4. *A stationary point $\bar{x}$ of (B.1) is defined as attractive conditionally to $A \subset \mathbb{R}^n$ if $\bar{x} \in A$ and there exists $\eta(\bar{x}) > 0$ such that the following implication holds for any initial condition $x_0 \in A$:*

$$\|x_0 - \bar{x}\| < \eta(\bar{x}) \implies \lim_{t \to \infty} x(t) = \bar{x}. \tag{B.3}$$

Definition 5. *A stationary point $\bar{x}$ of (B.1) is defined as asymptotically stable conditionally to $A \subset \mathbb{R}^n$ if it is both stable and attractive conditionally with respect to A.*

Definition 6. *A stationary point $\bar{x}$ of (B.1) is defined as globally asymptotically stable conditionally to $A \subset \mathbb{R}^n$ if it is asymptotically stable conditionally with respect to A and $\eta(\bar{x}) = +\infty$.*

APPENDIX C

COMPUTING NULLSPACE BASES USING EIGEN DECOMPOSITION

Consider that a rectangular matrix, $A \in \mathbb{R}^{m \times n}$ where $m > n$ is given, and it is desired to compute its nullspace basis. Let $B \in \mathbb{R}^{m \times (m-n)}$ denote its nullspace basis, such that $B^T A = 0_{n \times n}$. Consider a symmetric positive-definite weight $W \in \mathbb{R}^{m \times m}$, and the generalized left-inverse $A^{W+} \in \mathbb{R}^{n \times m}$ with weight W^{-1}, and generalized left-inverse $B^{W\dagger} \in \mathbb{R}^{(m-n) \times m}$ with weight W:

$$A^{W+} = (A^T W^{-1} A)^{-1} A^T W^{-1} \tag{C.1}$$

$$B^{W\dagger} = (B^T W B)^{-1} B^T W \tag{C.2}$$

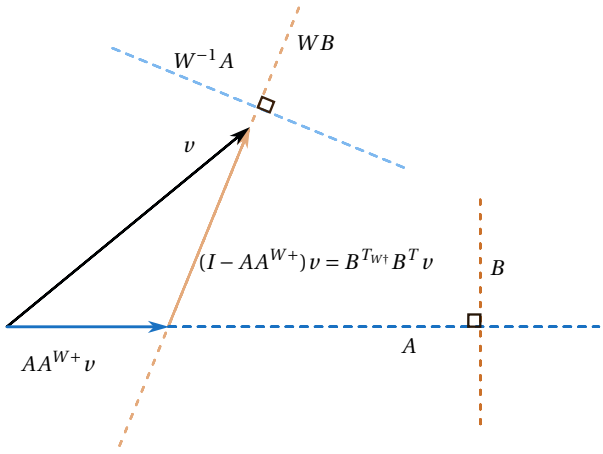

Figure C.1: The weighted projection of a vector v onto A along W^{-1} corresponds to its projection along the direction WB which is orthogonal to $W^{-1}A$. In the special case when $W = I$, the projection is perpendicular.

Then, the following relations hold.

$$B^{W\dagger}B = I \tag{C.3}$$
$$A^{W+}A = I$$
$$B^T A = A^T B = 0$$

In particular, as seen in Figure C.1, the weighted nullspace of A is analogous to the weighted range space of WB:

$$I - AA^{W+} = B^{T_{W\dagger}} B^T \tag{C.4}$$

In other words, the nullspace of A weighted along the metric W^{-1} is equivalent to the range space of WB weighted along the metric W^{-1}.

Observe that right-multiplying (C.4) with B^T and using the relations in (C.3) results in

$$B^T(I - AA^{W+}) = B^T B^{T_{W\dagger}} B^T = B^T \tag{C.5}$$

This implies that B^T is the left-eigenspace of the projection matrix $(I - AA^{W+})$. Similarly, right-multiplying (C.4) with $B^{T_{W\dagger}}$ and using the relations in (C.3) results in

$$(I - AA^{W+})B^{T_{W\dagger}} = B^{T_{W\dagger}} B^T B^{T_{W\dagger}} = B^{T_{W\dagger}} \tag{C.6}$$

This implies that $B^{T_{W\dagger}}$ is the right-eigenspace of the projection matrix $(I - AA^{W+})$. Therefore, the nullspace basis B or its generalized inverse $B^{W\dagger}$ can be computed using standard libraries that compute eigenvectors. For example, the MATLAB function `eig` can be used to compute both left and right eigenvectors of a matrix.

APPENDIX D

LINEAR ANALYSIS FOR PRE- AND POST-GRASP CONTROL GAIN SELECTION

In general, the controller gains from the approach to post-grasp phase are updated in order to be more compliant to impact, yet more dissipative for stabilization. The initial estimates of the gains can be guided by an analysis of the eigenvalues, step and impulse responses of the linearized closed-loop dynamics.

D.1 Linearized hierarchical dynamics

For this analysis, we can write the closed-loop system by equating the dynamics in (4.8), with the control law in (4.9).

$$\begin{matrix}\text{T1:}\\ \text{T2:}\\ \text{T3:}\end{matrix} \underbrace{\begin{bmatrix} \boldsymbol{\Lambda}_{ee} & \mathbf{0} & \mathbf{0} \\ \boldsymbol{\Lambda}_{me} & \boldsymbol{\Lambda}_{mm} & \mathbf{0} \\ \boldsymbol{\Lambda}_{re} & \boldsymbol{\Lambda}_{rm} & \boldsymbol{\Lambda}_{rr} \end{bmatrix}}_{\boldsymbol{\Lambda}'} \begin{bmatrix} \dot{\boldsymbol{v}}_e \\ \ddot{\boldsymbol{q}} \\ \ddot{\boldsymbol{r}} \end{bmatrix} + \underbrace{\begin{bmatrix} \boldsymbol{\mu}_{ee} & \mathbf{0} & \mathbf{0} \\ \boldsymbol{\mu}'_{me} & \boldsymbol{\mu}_{mm} & \mathbf{0} \\ \boldsymbol{\mu}'_{re} & \boldsymbol{\mu}'_{rm} & \boldsymbol{\mu}_{rr} \end{bmatrix}}_{\boldsymbol{\mu}'} \begin{bmatrix} \boldsymbol{v}_e \\ \dot{\boldsymbol{q}} \\ \dot{\boldsymbol{r}} \end{bmatrix} = \boldsymbol{\Lambda}' \begin{bmatrix} \dot{\boldsymbol{v}}_e^d \\ \ddot{\boldsymbol{q}}^d \\ \mathbf{0} \end{bmatrix} + \boldsymbol{\mu}' \begin{bmatrix} \boldsymbol{v}_e^d \\ \dot{\boldsymbol{q}}^d \\ \mathbf{0} \end{bmatrix} + \begin{bmatrix} \boldsymbol{E}\boldsymbol{K}_{Pe}\Delta\boldsymbol{x}_e + \boldsymbol{K}_{De}\Delta\boldsymbol{v}_e \\ \boldsymbol{K}_{Pm}\Delta\boldsymbol{q} + \boldsymbol{K}_{Dm}\Delta\dot{\boldsymbol{q}} \\ \mathbf{0} \end{bmatrix}$$

For designing the gains of the impedance tasks T1 and T2, we can eliminate task T3 on the reaction wheels and consider them in a locked state. This is because the wheels are redundant DoF with respect to tasks T1 and T2 in the nominal control law. As the linearization considers a neighborhood around the equilibrium point where the variation of states are small, we can approximate the pose error including quaternions as, $\Delta\boldsymbol{x}_e \approx \boldsymbol{x}_e^d - \boldsymbol{x}_e$, and the Cartesian velocity as, $\boldsymbol{v}_e \approx \dot{\boldsymbol{x}}_e$. Lastly, as we shall analyze the response to a step input (zero velocity and acceleration) feedforward terms are eliminated. About an equilibrium of the servicer, $\boldsymbol{x}_T : (\boldsymbol{x}_e, \boldsymbol{q}) = \boldsymbol{x}_{T0} : (\boldsymbol{x}_{e0}, \boldsymbol{q}_0)$ and $\dot{\boldsymbol{x}}_{T0} = \mathbf{0}$, the

simplified linear closed-loop dynamics is derived from the first-order Taylor's expansion:

$$\begin{matrix}\text{T1:}\\ \text{T2:}\end{matrix} \underbrace{\begin{bmatrix} \boldsymbol{\Lambda}_{ee} & \mathbf{0} \\ \boldsymbol{\Lambda}_{me} & \boldsymbol{\Lambda}_{mm} \end{bmatrix}}_{\bar{\boldsymbol{\Lambda}}(\boldsymbol{x}_{T0})} \begin{bmatrix} \ddot{\boldsymbol{x}}_e \\ \ddot{\boldsymbol{q}} \end{bmatrix} + \underbrace{\begin{bmatrix} \boldsymbol{K}_{De} & \mathbf{0} \\ \mathbf{0} & \boldsymbol{K}_{Dm} \end{bmatrix}}_{\boldsymbol{K}_D} \begin{bmatrix} \dot{\boldsymbol{x}}_e \\ \dot{\boldsymbol{q}} \end{bmatrix} + \underbrace{\begin{bmatrix} \boldsymbol{K}_{Pe} & \mathbf{0} \\ \mathbf{0} & \boldsymbol{K}_{Pm} \end{bmatrix}}_{\boldsymbol{K}_P} \underbrace{\begin{bmatrix} \boldsymbol{x}_e \\ \boldsymbol{q} \end{bmatrix}}_{\boldsymbol{x}_T} = \underbrace{\begin{bmatrix} \boldsymbol{K}_{Pe} & \mathbf{0} \\ \mathbf{0} & \boldsymbol{K}_{Pm} \end{bmatrix}}_{} \underbrace{\begin{bmatrix} \boldsymbol{x}_e^d \\ \boldsymbol{q}^d \end{bmatrix}}_{\boldsymbol{x}_T^d} + \underbrace{\begin{bmatrix} \boldsymbol{f}_d \\ \boldsymbol{\tau}_d \end{bmatrix}}_{\boldsymbol{d}_T}$$

$$\text{Linearized dynamics :} \qquad \bar{\boldsymbol{\Lambda}}(\boldsymbol{x}_{T0})\ddot{\boldsymbol{x}}_T + \boldsymbol{K}_D\dot{\boldsymbol{x}}_T + \boldsymbol{K}_P\boldsymbol{x}_T = \boldsymbol{K}_P\boldsymbol{x}_T^d + \boldsymbol{d}_T \tag{D.1}$$

The disturbance $\boldsymbol{d}_T : (\boldsymbol{f}_d, \boldsymbol{\tau}_d)$ is considered in (D.1) to analyze external disturbance (impulse) for the post-grasp stabilization, presented later.

D.2 Transfer functions

Using the Laplace transform $\mathscr{L}[\bullet]$, the transfer functions $\boldsymbol{G}_\bullet$ from $\boldsymbol{X}_T(s) = \mathscr{L}[\boldsymbol{x}_T]$, to a desired input $\boldsymbol{X}_T^d(s) = \mathscr{L}[\boldsymbol{x}_T^d]$, and to a disturbance input $\boldsymbol{D}_T(s) = \mathscr{L}[\boldsymbol{d}_T]$, are:

$$\boldsymbol{X}_T(s) = \underbrace{(\bar{\boldsymbol{\Lambda}}(\boldsymbol{x}_{T0})s^2 + \boldsymbol{K}_D s + \boldsymbol{K}_P)^{-1}\boldsymbol{K}_P}_{\boldsymbol{G}_{desired}(s)}\ \boldsymbol{X}_T^d(s) + \underbrace{(\bar{\boldsymbol{\Lambda}}(\boldsymbol{x}_{T0})s^2 + \boldsymbol{K}_D s + \boldsymbol{K}_P)^{-1}}_{\boldsymbol{G}_{disturbance}(s)}\ \boldsymbol{D}_T(s) \tag{D.2}$$

Using these closed-loop transfer functions, the gains can be tuned iteratively to the desired performance metrics. Such tuning can be easily done with standard control theory libraries such as in MATLAB[1].

The idea is to tune the tracking performance for the approach phase using step responses, and the compliance performance for the grasp and stabilization phase using impulse responses. The damping design (DD) method [AS+03] is also exploited for task T2 of the manipulator, (noted in Table 4.2 as DD) which adapts the damping gains to the stiffness and inertia (which changes with joint angles of the robot).

D.3 Step and impulse responses

The transfer functions in(D.2) are matrices of dimension 13 (6 DoF T1 + 7 DoF T2). The step and impulse responses in Figure D.1 show, as examples, one DoF for the end-effector (T1) and one DoF for the 7-joint manipulator (T2), in the approach and post-grasp phase. Figure D.1 considers the equilibria about the initial and final configurations of the servicer with the gains presented for the SIM setup in Table 4.2.

For the approach phase, Table D.1 shows the performance metrics corresponding to the exemplary step responses in Figure D.1 i. and iii. of T1 and T2 (settling time ≈7sec). It is worth noting that the step response is used as a benchmark to characterize the performance and get first estimates. In

[1]Alternatively, pole-placement may be used with the open-loop transfer functions to obtain gains with desired eigenvalues and performance metrics.

SIM	**Approach phase**	**Post-grasp phase**
Task#	Response $\boldsymbol{X}_T$ to step input $\boldsymbol{X}_T^d$	Response of $\boldsymbol{X}_T$ to impulse input $\boldsymbol{D}_T$
T1: e.g., end-effector position in 'z'	i. 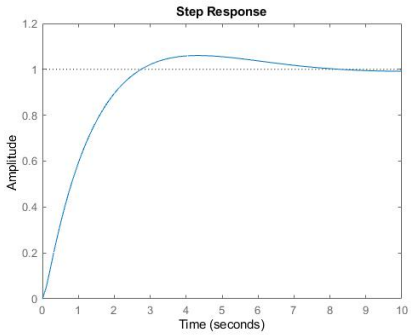	ii. 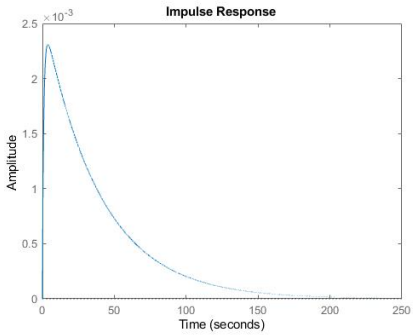
T2: e.g., joint 1 of manipulator	iii. 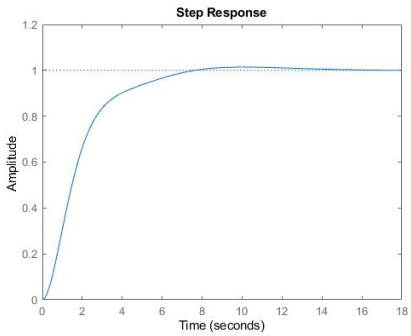	iv. 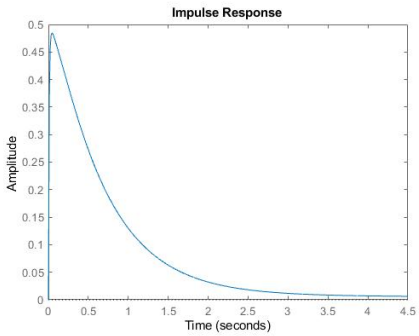

Figure D.1: Step response for approach phase, and Impulse response for post-grasp phase

Step response metrics	**T1 (end-effector 'z')**	**T2 (manipulator joint 1)**
RiseTime	1.8499	3.4606
SettlingTime	6.8688	6.5520
SettlingMin	0.9177	0.9003
SettlingMax	1.0603	1.0142
Overshoot	6.0328	1.4195
Undershoot	0	0
Peak	1.0603	1.0142
PeakTime	4.3521	10.0926

Table D.1: Step response metrics for T1 (end-effector 'z'), T2 (manipulator joint 1).

reality, the performance of a tracking controller with a smooth interpolated trajectory is expected to be better.

For the post-grasp phase, the impulse response in Figure D.1 ii. shows how a fast response (≈4sec) is enforced by the task T2. This is a design choice since the manipulator is responsible for

keeping the servicer's base at a safe distance from the client, which is desired to be faster. Whereas, task T1 on the end-effector in Figure D.1 iv. has a slow response (≈150sec) to enhance compliance for soft stabilization. For the stabilization, the gains on the end-effector (T1) are intentionally chosen this way since the absolute pose of the servicer-client system is not critical, rather the damping of the relative motion, which is ensured by the fast response of the manipulator (T2).

APPENDIX E

DERIVING THE DISCRETE LYAPUNOV DIFFERENCE EQUATION

The evaluation of the discrete Lyapunov difference equation starting from (5.10) and resulting in (5.14) is derived here. The notation ahead is generalized to a second-order system, and boldface dropped to make the exposition less cumbersome. Therefore, the states, dynamic matrices and control input specific to the low-rate spacecraft dynamics in Section 5.3.3 are renamed as follows.

(E.1)

- $\boldsymbol{v}_b \equiv x_2$ — $\dot{x}_1 = E^T x_2$
- $\Delta\boldsymbol{x}_b \equiv -x_1$ — $\ddot{x}_1 = E^T \dot{x}_2 + \dot{E}^T x_2$
- $\boldsymbol{E} \equiv E$ — $\dot{u} = 0$, for ZOH [KK99]
- $\boldsymbol{F}_b \equiv u$ — $M\dot{x}_2 + Cx_2 = u$
- $\boldsymbol{M}_{bb} \equiv M$ — $\dot{x}_2 = -M^{-1}Cx_2 + M^{-1}u$
- $\boldsymbol{C}_{bb} \equiv C$ — $\ddot{x}_2 = M^{-1}\dot{M}M^{-1}Cx_2 - M^{-1}\dot{C}x_2 - M^{-1}C\dot{x}_2 - M^{-1}\dot{M}M^{-1}u$

The discretized dynamics using Taylor's expansion gives:

$$x_2[k+1] = x_2[k] + h\dot{x}_2[k] + \frac{1}{2}h^2\ddot{x}_2[k] + \frac{1}{3!}h^3(\ldots) + \ldots \tag{E.2}$$

$$x_1[k+1] = x_1[k] + h\dot{x}_1[k] + \frac{1}{2}h^2\ddot{x}_1[k] + \frac{1}{3!}h^3(\ldots) + \ldots \tag{E.3}$$

$$M[k+1] = M[k] + h\dot{M}[k] + \frac{1}{2}h^2\ddot{M}[k] + \frac{1}{3!}h^3(\ldots) + \ldots \tag{E.4}$$

The (...) indicates the higher derivatives. Using the above expressions, the Lyapunov difference (5.10) is evaluated for parts associated with potential energy V_P, and with kinetic energy V_M. Notice that the factor $\frac{1}{h}$ in (5.10) captures the system power as $h \to 0$. Rewriting (5.10) in simplified notation,

$$V_b[k] = \underbrace{\frac{1}{2h}x_2^T[k]M[k]x_2[k]}_{V_M} + \underbrace{\frac{1}{2h}x_1^T[k]K_P x_1[k]}_{V_P} \tag{E.5}$$

E.1 Power associated with potential energy

The Lyapunov difference equation (E.5) is evaluated for the potential on the position error x_1 as follows. Note that K_P is symmetric and positive-definite.

(E.6) $V_P[k+1] - V_P[k]$

$$= \frac{1}{2h} x_1^T[k+1] K_P x_1[k+1] - \frac{1}{2h} x_1^T[k] K_P x_1[k]$$

substitute $x_1[k+1]$ from (E.3)

$$= \frac{1}{2h} (x_1[k] + h\dot{x}_1[k] + \frac{1}{2}h^2\ddot{x}_1[k])^T K_P(\ldots) - \frac{1}{2h} x_1^T[k] K_P x_1[k]$$

expand using $(a+b+c)^2 = a^2+b^2+c^2+2ab+2ac+2bc$ and omit k for brevity

$$= \frac{1}{2h}(x_1^T \cancel{K_P} x_1 + h^2 \dot{x}_1^T K_P \dot{x}_1 + \frac{1}{4}h^4 \ddot{x}_1^T \cancel{K_P} \ddot{x}_1 + 2h x_1^T K_P \dot{x}_1 + 2\frac{1}{2}h^2 x_1^T K_P \ddot{x}_1 + 2\frac{1}{2}h^3 x_2^T \cancel{K_P} \ddot{x}_1)$$

$$- \frac{1}{2h} x_1^T \cancel{K_P} x_1 + \mathcal{O}(h^2)$$

substitute $\dot{x}_1 = E^T x_2$ and $\ddot{x}_1 = E^T \dot{x}_2 + \dot{E}^T x_2$ and $\dot{x}_2$ from (E.1)

$$= \frac{h}{2} x_2^T E K_P E^T x_2 + x_1^T K_P E^T x_2 + \frac{h}{2} x_1^T K_P E^T(-M^{-1}Cx_2 + M^{-1}u) + \frac{h}{2} x_1^T K_P \dot{E}^T x_2 + \mathcal{O}(h^2)$$

re-arrange by factoring x_2^T on the left

$$= \left(x_2 - \frac{h}{2}M^{-1}Cx_2 + \frac{h}{2}M^{-1}u\right)^T E K_P x_1 + \frac{h}{2} x_2^T \dot{E} K_P x_1 + \frac{h}{2} x_2^T E K_P E^T x_2 + \mathcal{O}(h^2)$$

re-arrange equivalently

$$= \left(x_2 - \frac{h}{2}M^{-1}Cx_2 + \frac{h}{2}M^{-1}u\right)^T \left(E + \frac{h}{2}\dot{E}\right) K_P \left(x_1 + \frac{h}{2}E^T x_2\right) + \mathcal{O}(h^2)$$

E.2 Power associated with kinetic energy

The Lyapunov difference equation (E.5) is evaluated for the kinetic energy associated with the velocity x_2 as follows. Note that M is symmetric and positive-definite, and $\dot{M} = C + C^T$ for a suitable choice of C [WS26].

(E.7) $V_M[k+1] - V_M[k]$

$$= \frac{1}{2h} x_2^T[k+1] M[k+1] x_2[k+1] - \frac{1}{2h} x_2^T[k] M[k] x_2[k]$$

substitute $x_2[k+1]$ and $M[k+1]$ from (E.2) and (E.4)

$$= \frac{1}{2h}\left(x_2[k] + h\dot{x}_2[k] + \frac{1}{2}h^2\ddot{x}_2[k]\right)^T \left(M[k] + h\dot{M}[k] + \frac{1}{2}h^2\ddot{M}[k]\right)(\ldots) - \frac{1}{2h} x_2^T[k] M[k] x_2[k]$$

The (...) indicates the same expansion as $x_2[k+1]$ on the left of the inertia terms. The expansion of (E.7) continues ahead.

split the middle paranthesis

$$
\begin{aligned}
&= \frac{1}{2h}(x_2[k] + h\dot{x}_2[k] + \frac{1}{2}h^2\ddot{x}_2[k])^T M[k](\ldots) \\
&+ \frac{1}{2h}(x_2[k] + h\dot{x}_2[k] + \frac{1}{2}h^2\ddot{x}_2[k])^T h\dot{M}[k](\ldots) \\
&+ \frac{1}{2h}(x_2[k] + h\dot{x}_2[k] + \frac{1}{2}h^2\ddot{x}_2[k])^T \frac{1}{2}h^2\ddot{M}[k](\ldots) \\
&- \frac{1}{2h}x_2^T[k]M[k]x_2[k] + \mathcal{O}(h^2)
\end{aligned}
$$

expand using $(a+b+c)^2 = a^2+b^2+c^2+2ab+2ac+2bc$ and omit k for brevity

$$
\begin{aligned}
&= \frac{1}{2h}(x_2^T\cancel{M}x_2 + h^2\dot{x}_2^T M\dot{x}_2 + \frac{1}{4}\cancel{h^4}\ddot{x}_2^T M\ddot{x}_2 + 2hx_2^T M\dot{x}_2 + 2\frac{1}{2}h^2x_2^T M\ddot{x}_2 + 2\frac{1}{2}\cancel{h^3}\dot{x}_2^T M\ddot{x}_2) \\
&+ \frac{1}{2h}(hx_2^T\dot{M}x_2 + \cancel{h^3}\dot{x}_2^T\dot{M}\dot{x}_2 + \frac{1}{4}\cancel{h^5}\ddot{x}_2^T\dot{M}\ddot{x}_2 + 2h^2x_2^T\dot{M}\dot{x}_2 + 2\frac{1}{2}\cancel{h^3}x_2^T\dot{M}\ddot{x}_2 + 2\frac{1}{2}\cancel{h^4}\dot{x}_2^T\dot{M}\ddot{x}_2) \\
&+ \frac{1}{4h}(h^2x_2^T\ddot{M}x_2 + \cancel{h^4}\dot{x}_2^T\ddot{M}\dot{x}_2 + \frac{1}{4}\cancel{h^6}\ddot{x}_2^T\ddot{M}\ddot{x}_2 + 2\cancel{h^3}x_2^T\ddot{M}\dot{x}_2 + 2\frac{1}{2}\cancel{h^4}x_2^T\ddot{M}\ddot{x}_2 + 2\frac{1}{2}\cancel{h^5}\dot{x}_2^T\ddot{M}\ddot{x}_2) \\
&- \frac{1}{2h}x_2^T\cancel{M}x_2 + \mathcal{O}(h^2)
\end{aligned}
$$

cancel, collect and expand terms up to $\mathcal{O}(h)$ and factor out $\frac{1}{2}$

$$
\begin{aligned}
&= \frac{1}{2}(h\dot{x}_2^T M\dot{x}_2 + 2x_2^T M\dot{x}_2 + hx_2^T M\ddot{x}_2) \\
&+ \frac{1}{2}(x_2^T\dot{M}x_2 + 2hx_2^T\dot{M}\dot{x}_2) \\
&+ \frac{1}{2}(\frac{1}{2}hx_2^T\ddot{M}x_2) + \mathcal{O}(h^2)
\end{aligned}
$$

combine and substitute for $\dot{x}_2$ from (E.1)

$$
\begin{aligned}
&= \frac{1}{2}\left(h(-M^{-1}Cx_2 + M^{-1}u)^T M(-M^{-1}Cx_2 + M^{-1}u) + 2x_2^T(M + h\dot{M})(-M^{-1}Cx_2 + M^{-1}u)\right) \\
&+ \frac{1}{2}\left(x_2^T\dot{M}x_2 + hx_2^T M\ddot{x}_2 + \frac{1}{2}hx_2^T\ddot{M}x_2\right) + \mathcal{O}(h^2)
\end{aligned}
$$

expand using $(a-b)^2 = a^2+b^2-2ab$

$$
\begin{aligned}
&= \frac{1}{2}\left(hx_2^T C^T M^{-1}Cx_2 + hu^T M^{-1}u - 2hx_2^T C^T M^{-1}u\right) \\
&+ \frac{1}{2}(-2x_2^T\cancel{C}x_2 - 2hx_2^T\dot{M}M^{-1}Cx_2 + 2x_2^T u + 2hx_2^T\dot{M}M^{-1}u) \\
&+ \frac{1}{2}\left(x_2^T\cancel{\dot{M}}x_2 + hx_2^T M\ddot{x}_2 + \frac{1}{2}hx_2^T\ddot{M}x_2\right) + \mathcal{O}(h^2)
\end{aligned}
$$

using skew-symmetry of $\dot{M} - 2C$, or passivity, re-arrange and factor x_2^T on the left

$$
\begin{aligned}
&= \frac{1}{2}\left(-hx_2^T C^T M^{-1}Cx_2 - 2hx_2^T CM^{-1}Cx_2\right) \\
&+ \frac{1}{2}\left(2x_2^T u + 2hx_2^T CM^{-1}u + hu^T M^{-1}u\right) \quad \text{: terms in } u \\
&+ \frac{1}{2}\left(hx_2^T M\ddot{x}_2 + \frac{1}{2}hx_2^T\ddot{M}x_2\right) + \mathcal{O}(h^2) \qquad \text{: second derivatives}
\end{aligned}
$$

substitute for second derivatives with $\ddot{x}_2$ from (E.1)

$$
\begin{aligned}
&= \frac{1}{2}\left(-hx_2^T C^T M^{-1} C x_2 - 2hx_2^T C M^{-1} C x_2\right) \\
&+ \frac{1}{2}\left(2x_2^T u + 2hx_2^T C M^{-1} u + hu^T M^{-1} u\right) \\
&+ \frac{1}{2}\left(hx_2^T \dot{M} M^{-1} C x_2 - hx_2^T \cancel{C} x_2 - hx_2^T C\dot{x}_2 - hx_2^T \dot{M} M^{-1} u + \frac{1}{2} hx_2^T \cancel{\ddot{M}} x_2\right) + \mathcal{O}(h^2)
\end{aligned}
$$

using passivity, $\dot{M} = C + C^T$, skew-symmetry of $\frac{d}{dt}(\dot{M} - 2C)$ and $\dot{x}_2$ from (E.1)

$$
\begin{aligned}
&= \frac{1}{2}\left(-hx_2^T \cancel{C^T} M^{-1} C x_2 - 2hx_2^T C M^{-1} \cancel{C} x_2\right) \\
&+ \frac{1}{2}\left(2x_2^T u + 2hx_2^T \cancel{C} M^{-1} u + hu^T M^{-1} u\right) \\
&+ \frac{1}{2}\left(hx_2^T (\cancel{C} + \cancel{C^T}) M^{-1} C x_2 - hx_2^T C(-M^{-1}\cancel{C} x_2 + \cancel{M^{-1}} u) - hx_2^T (\cancel{C} + C^T) M^{-1} u\right) + \mathcal{O}(h^2)
\end{aligned}
$$

cancel and collect terms

$$
= \left(x_2 - \frac{h}{2} M^{-1} C x_2 + \frac{h}{2} M^{-1} u\right)^T u + \mathcal{O}(h^2)
$$

E.3 Total power

Combining the final expressions for (E.6) and (E.7), results in the Lyapunov difference equation equivalent to (5.14), which corresponds to the power of the system in the limit $h \to 0$.

(E.8)
$$
\begin{aligned}
V_b[k+1] - V_b[k] &= V_P[k+1] - V_P[k] + V_M[k+1] - V_M[k] \\
&= \left(x_2 - \frac{h}{2} M^{-1} C x_2 + \frac{h}{2} M^{-1} u\right)^T \left(u + \left(E + \frac{h}{2}\dot{E}\right) K_P \left(x_1 + \frac{h}{2} E^T x_2\right)\right) \\
&= \underbrace{\left(x_2 + \frac{h}{2}\dot{x}_2\right)^T}_{\approx x_2[k+\frac{1}{2}]^T} (u + \underbrace{(E + \frac{h}{2}\dot{E})}_{\approx E[k+\frac{1}{2}]} K_P \underbrace{\left(x_1 + \frac{h}{2} E^T x_2\right)}_{\approx x_1[k+\frac{1}{2}]}) + \mathcal{O}(h^2)
\end{aligned}
$$

APPENDIX F

ONE-DOF SAMPLED-DATA SYSTEM

Consider a one-DoF double integrator plant, with state x, mass M and control u. Its continuous-time dynamics can be used to obtain the transfer function G in the frequency domain using the Laplace transform and zero initial conditions as follows.

$$\ddot{x}(t) = M^{-1}u(t) \tag{F.1}$$

$$\mathscr{L}[\ddot{x}] = \mathscr{L}[M^{-1}u]$$

$$s^2X(s) = M^{-1}U(s)$$

$$G(s) = \frac{X(s)}{U(s)} = \frac{1}{Ms^2} \tag{F.2}$$

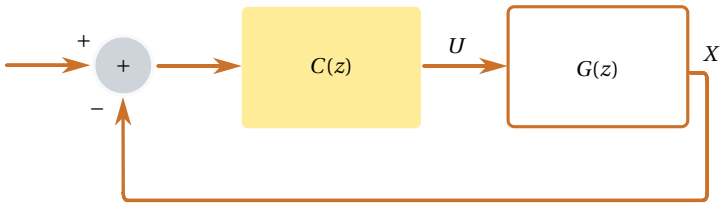

Figure F.1: One-DoF sampled-data system

The transfer functions of the zero-order (C_0) and first-order sample-aware (C_1) PD control laws can be expressed as follows.

$$C_0(s) = K_P + K_D s \tag{F.3}$$

$$C_1(s) = \bar{K}_P + \bar{K}_D s$$

where the sample-aware gains from (5.9) for the one-DoF system reduce to,

$$\bar{K}_P = K_P - \frac{h}{2} K_D M^{-1} K_P$$
$$\bar{K}_D = K_D + \frac{h}{2} K_P - \frac{h}{2} K_D M^{-1} K_D$$

In the discrete domain the equivalent Z-transforms of the transfer functions in (F.2) and (F.3) can be obtained by substituting for the integral and derivative in the frequency domain with the following.

$$\frac{1}{s} \approx \frac{h}{z-1} \tag{F.4}$$

$$s \approx \frac{z-1}{hz} \tag{F.5}$$

The open loop transfer function G_{ol} of the plant is in series with the controller $C_\bullet$, see Figure F.1, where $\bullet$ replaces 0 or 1 based on zero- or first-order PD control in (F.3).

$$G_{ol}(z) = C_\bullet(z) G(z) \tag{F.6}$$

Finally, the closed-loop transfer function G_{cl} for negative feedback is given by

$$G_{cl} = \frac{G_{ol}}{1 + G_{ol}} \tag{F.7}$$

The transfer function G_{cl} enables evaluation of the step response for specified values of M, K_P, K_D, and h. Conversely, for a given mass and natural frequency $\omega_n = \sqrt{K_P/M}$, the system response can be analyzed, as described in Section 5.4, across a range of sampling ratios $\omega_r = 2\pi h/\omega_n$ and damping ratios $\zeta = K_D/(2\sqrt{K_P M})$ by determining the corresponding gains K_P, K_D, and sampling interval h.

APPENDIX G

MULTIMEDIA AND CREDITS

G.1 Multimedia

Table G.1 summarizes a list of supplementary videos of the simulations and experiments with the HIL facilities, OOS-Sim and MSS, at DLR validating the results across different chapters.

Table G.1: Multimedia

Experimental Videos
Post-grasp stabilization of a tumbling satellite [VDSO22] IEEE Xplore supplemental items (Chapter 3, Figure 3.12) (Accessed: 5 July 2026) https://ieeexplore.ieee.org/abstract/document/9812067/media#media
Unified approach, grasp and stabilization of a free-floating satellite [VDSDO25] DLR Robotics & Mechatronics YouTube (Chapter 4, Figure 4.6, Figure 4.14, Figure 4.16) (Accessed: 5 July 2026) https://www.youtube.com/watch?v=Zx7bE3vWLbA
Multi-rate orbital manipulator control [VDSO22] IEEE Xplore supplemental items (Chapter 5, Figure 5.8) (Accessed: 5 July 2026) https://ieeexplore.ieee.org/document/11359689/media#media
Gravity-compensation experiment of CAESAR with MSS [DSVS+23] IEEE Xplore supplemental items (Chapter 6, Figure 6.8) (Accessed: 5 July 2026) https://ieeexplore.ieee.org/document/10161480/media#media
DLR's Advancements in Space Robotic Manipulation DLR Robotics & Mechatronics YouTube (Chapter 6, Figure 6.13) (Accessed: 5 July 2026) https://www.youtube.com/watch?v=8OtwR-S6QUs

G.2 Credits and disclosure

This LaTeX template was adapted from the University of Bristol Thesis Template by Víctor F. Breña-Medina available under the license Creative Commons CC BY 4.0. AI language tools were used for checking grammar and typos, and improving phrasing and consistency.

BIBLIOGRAPHY

[A+15] J. Artigas et al. The OOS-SIM: An on-ground simulation facility for on-orbit servicing robotic operations. In *Robotics and Automation (ICRA), IEEE International Conference on*, pages 2854–2860, May 2015.

[AATA24] Keyvan Arezoo, Jamal Arezoo, Bahram Tarvirdizadeh, and Khalil Alipour. Modeling and control of robotic manipulators equipped with the flexible cable-pulley based gravity compensation mechanism. *Journal of Vibration and Control*, 30(7-8):1524–1547, 2024.

[ABB+11] Aydemir Arisoy, M Kemal Bayrakceken, Suleyman Basturk, Metin Gokasan, and O Seta Bogosyan. High order sliding mode control of a space robot manipulator. In *Proceedings of 5th international conference on recent advances in space technologies-RAST2011*, pages 833–838. IEEE, 2011.

[ABDS+16] J. Artigas, R. Balachandran, M. De Stefano, M. Panzirsch, R. Lampariello, A. Albu-Schaeffer, J. Harder, and J. Letschnik. Teleoperation for on-orbit servicing missions through the astra geostationary satellite. In *2016 IEEE Aerospace Conference*, pages 1–12, March 2016.

[Agh08] Farhad Aghili. Optimal control for robotic capturing and passivation of a tumbling satellite with unknown dynamics. In *AIAA guidance, navigation and control conference and exhibit*, page 7274, 2008.

[Agh09] Farhad Aghili. Optimal control of a space manipulator for detumbling of a target satellite. In *2009 IEEE International Conference on Robotics and Automation*, pages 3019–3024, 2009.

[Agh20] Farhad Aghili. Optimal trajectories and robot control for detumbling a non-cooperative satellite. *Journal of Guidance, Control, and Dynamics*, 43(5):981–988, 2020.

[Agh23] Farhad Aghili. Autonomous sequential submanoeuvres in pre-and post-capturing space objects using obstructed 3-d vision data. *IEEE Transactions on Aerospace and Electronic Systems*, 59(6):7626–7639, 2023.

[Ale22] Stella Alexandrova. Future trends of commercial in-orbit satellite servicing, active debris removal and end-of life services. In *Journal of Physics: Conference Series*, volume 2255, page 012014. IOP Publishing, 2022.

[ALH06] S. Abiko, R. Lampariello, and G. Hirzinger. Impedance control for a free-floating robot in the grasping of a tumbling target with parameter uncertainty. In *Intelligent Robots and Systems, 2006 IEEE/RSJ International Conference on*, pages 1020–1025, Oct 2006.

[Ara16] Vigen Arakelian. Gravity compensation in robotics. *Advanced robotics*, 30(2):79–96, 2016.

[ARB25] Yeshurun Alemayehu Adde, Yury N Razoumny, and Araya Abera Betelie. Contact force minimization for space robot manipulators using optimized sliding mode controller. *IEEE Access*, 2025.

[AS+03] A. Albu-Schaffer et al. Cartesian impedance control of redundant robots: recent results with the dlr-light-weight-arms. In *IEEE International Conference on Robotics and Automation*, volume 3, page 3704, 2003.

[ASOH07] Alin Albu-Schäffer, Christian Ott, and Gerd Hirzinger. A unified passivity-based control framework for position, torque and impedance control of flexible joint robots. *The international journal of robotics research*, 26(1):23–39, 2007.

[AZ24] Mohammad Alizadeh and Zheng H Zhu. A comprehensive survey of space robotic manipulators for on-orbit servicing. *Frontiers in Robotics and AI*, 11:1470950, 2024.

[BCH+11] Brent W Barbee, J Russell Carpenter, Scott Heatwole, F Landis Markley, Michael Moreau, Bo J Naasz, and John Van Eepoel. A guidance and navigation strategy for rendezvous and proximity operations with a noncooperative spacecraft in geosynchronous orbit. *The Journal of the Astronautical Sciences*, 58(3):389–408, 2011.

[BD94] H. Benjamin Brown and John M. Dolan. A Novel Gravity Compensation System for Space Robots. In *Robotics Institute. Paper 217*, 1 1994.

[Bel77] Leland F Belew. *Skylab, our first space station*, volume 400. Scientific and Technical Information Office, National Aeronautics and Space ..., 1977.

[BGH+18] Alexander Beyer, Gerhard Grunwald, Martin Heumos, Manfred Schedl, Ralph Bayer, Wieland Bertleff, Bernhard Brunner, Robert Burger, Jörg Butterfaß, Robin Gruber, et al. Caesar: Space robotics technology for assembly, maintenance, and repair. In *Proceedings of the International Astronautical Congress, IAC*, 2018.

[BLHB20] Roland Boumann, Patrik Lemmen, Robin Heidel, and Tobias Bruckmann. Optimization of trajectories for cable robots on automated construction sites. In *Proceedings of the 37th International Symposium on Automation and Robotics in Construction (ISARC)*, pages 465–472, October 2020.

[BPB+24] Federico Basana, Zeno Pavanello, Francesco Branz, Alessandro Francesconi, Giacomo Borelli, Davide Invernizzi, Mauro Massari, Marco Lovera, Alessia Nocerino, Roberto Opromolla, et al. Satellite and robotic arm combined control for spacecraft close-proximity operations. *CEAS Space Journal*, 2024.

[BSBG16] Jose Nuno AD Bueno, Wenderson G Serrantola, Rayza Araujo Bezerra, and Valdir Grassi. Lqr and h-infinity controls of a free-floating space manipulator with two arms. In *2016 XIII Latin American Robotics Symposium and IV Brazilian Robotics Symposium (LARS/SBR)*, pages 85–90. IEEE, 2016.

[BST+17] Riccardo Benvenuto, M Schlotterer, S Theil, M Lavagna, et al. Experimental setup and tests' results for uncooperative objects capture and manoeuvring with robotic arm. In *7th European conference on space debris, ESA/ESOC*, pages 1–13. ESA, 2017.

[C+16] Lei Chen et al. Characteristic model-based discrete-time sliding mode control for spacecraft with variable tilt of flexible structures. *IEEE/CAA Journal of Automatica Sinica*, 3(1):42–50, 2016.

[C+18] P. Colmenarejo et al. Methods and outcomes of the comrade project - design of robust combined control for robotic spacecraft and manipulator in servicing missions. In *69th International Astronautical Congress*, Sept 2018.

[CA00] C. R. Carignan and D. L. Akin. The reaction stabilization of on-orbit robots. *IEEE Control Systems Magazine*, 20(6):19–33, Dec 2000.

[CHD22] Alec J Cavaciuti, Joseph H Heying, and Joshua Davis. In-space servicing, assembly, and manufacturing for the new space economy. *Aerospace Center for Space Policy and Strategy*, pages 2022–07, 2022.

[CJGM17] Yogeshkumar R. Chheta, Rajesh M. Joshi, Krishan Kumar Gotewal, and M. Manoah-Stephen. A review on passive gravity compensation. In *2017 International conference of Electronics, Communication and Aerospace Technology (ICECA)*, volume 1, pages 184–189, 2017.

[CKK+26] Gwangyeol Cha, Junsik Kim, Sunhong Kim, Daehee Won, and Youngjin Choi. Gravity compensation strategy of space robotic arm for on-ground testing using gyroscope-type coupling interface and cable-driven parallel robot. *IEEE Robotics and Automation Letters*, 2026.

[CNSV99] F. Caccavale, C. Natale, B. Siciliano, and L. Villani. Six-dof impedance control based on angle/axis representations. *IEEE Transactions on Robotics and Automation*, 15(2):289–300, 1999.

[CSS+20] Pablo Colmenarejo, Nuno Santos, Pedro Serra, Juergen Telaar, Hans Strauch, Marco De Stefano, Alessandro Massimo Giordano, Hrishik Mishra, Roberto Lampariello, Christian Ott, et al. Results of the comrade project: combined control for robotic spacecraft and manipulator in servicing missions: active debris removal and refuelling. In *11th International ESA Conference on Guidance, Navigation & Control Systems*, 2020.

[CW93] Y. C. Chen and I.D. Walker. A consistent null-space based approach to inverse kinematics of redundant robots. In *[1993] Proceedings IEEE International Conference on Robotics and Automation*, pages 374–381 vol.3, 1993.

[CWG23] Kecai Cao, Changyun Wen, and Juping Gu. Sampled-data stabilization of nonholonomic chained form systems with multi-rate samplings. In *IECON 49th Annual Conference of the IEEE Industrial Electronics Society*, pages 1–6, 2023.

[D+22] Mathieu Deremetz et al. Demonstrator design of a modular multi-arm robot for on-orbit large telescope assembly. In *Advanced Space Technologies for Robotics and Automation (ASTRA)*, 2022.

[DLGD10] Zongquan Deng, Zhen Liu, Haibo Gao, and Liang Ding. An approach for gravity compensation of planetary rovers. In *2010 3rd International Symposium on Systems and Control in Aeronautics and Astronautics*, pages 1053–1058. IEEE, 2010.

[DNBS06] N. Diolaiti, G. Niemeyer, F. Barbagli, and J.K. Salisbury. Stability of haptic rendering: Discretization, quantization, time delay, and coulomb effects. *Robotics, IEEE Transactions on*, 22(2):256–268, April 2006.

[DO20] Alexander Dietrich and Christian Ott. Hierarchical impedance-based tracking control of kinematically redundant robots. *IEEE Transactions on Robotics*, 36(1):204–221, 2020.

[DOAS15] Alexander Dietrich, Christian Ott, and Alin Albu-Schäffer. An overview of null space projections for redundant, torque-controlled robots. *The International Journal of Robotics Research*, 34(11):1385–1400, 2015.

[DP93] S. Dubowsky and E. Papadopoulos. The kinematics, dynamics, and control of free-flying and free-floating space robotic systems. *Robotics and Automation, IEEE Transactions on*, 9(5):531–543, oct 1993.

[DP12] Emilio De Pasquale. Atv jules verne: a step by step approach for in-orbit demonstration of new rendezvous technologies. In *SpaceOps 2012*, page 1314619. 2012.

[DS+19] M. De Stefano et al. Multi-rate tracking control for a space robot on a controlled satellite: A passivity-based strategy. *IEEE Robotics and Automation Letters*, 4(2):1319–1326, April 2019.

[DSBAS17] M. De Stefano, R. Balachandran, J. Artigas, and C. Secchi. Reproducing physical dynamics with hardware-in-the-loop simulators: A passive and explicit discrete integrator. In *Robotics and Automation (ICRA), 2017 IEEE International Conference on*, pages 5899–5906, May 2017.

[DSBS20] Marco De Stefano, Ribin Balachandran, and Cristian Secchi. A passivity-based approach for simulating satellite dynamics with robots: Discrete-time integration and time-delay compensation. *IEEE Transactions on Robotics*, 36(1):189–203, 2020.

[DSMG+21] Marco De Stefano, Hrishik Mishra, Alessandro M. Giordano, Roberto Lampariello, and Christian Ott. A relative dynamics formulation for hardware- in-the-loop simulation of on-orbit robotic missions. *IEEE Robotics and Automation Letters*, 6(2):3569–3576, 2021.

[DSOV+23] Marco De Stefano, Christian Ott, Ria Vijayan, Hrishik Mishra, and Ferdinand Elhardt. Method for controlling a robot device. *Deutsches Zentrum fuer Luft und Raumfahrt eV*, (US20240391102A1), granted 2023.

[DSPO23] Hemjyoti Das, Bjørn Krare Sæbø, Kristin Y. Pettersen, and Christian Ott. Hardware-in-the-loop simulation of vehicle-manipulator systems for physical interaction tasks. In *2023 IEEE/RSJ International Conference on Intelligent Robots and Systems (IROS)*, pages 4390–4396, 2023.

[DSRB+24] Marco De Stefano, Máximo A. Roa, Ribin Balachandran, Alessandro M.Giordano, Hrishk Mishra, Nassir Oumer, Bernhard Brunner, Martin Lingenauber, Martin Stelzer, and Roberto Lampariello. *Design and Validation of Orbital Robotic Missions*, pages 281–304. Springer Nature Switzerland, Cham, 2024.

[DSVS+23] Marco De Stefano, Ria Vijayan, Andreas Stemmer, Ferdinand Elhardt, and Christian Ott. A gravity compensation strategy for on-ground validation of orbital manipulators. In *2023 IEEE International Conference on Robotics and Automation (ICRA)*, pages 11859–11865, 2023.

[DY04] D.N. Dimitrov and K. Yoshida. Momentum distribution in a space manipulator for facilitating the post-impact control. In *2004 IEEE/RSJ International Conference on*

Intelligent Robots and Systems (IROS) (IEEE Cat. No.04CH37566), volume 4, pages 3345–3350 vol.4, 2004.

[EBDS+23] Ferdinand Elhardt, Roland Boumann, Marco De Stefano, Robin Heidel, Patrik Lemmen, Martin Heumos, Christoph Jeziorek, Maximo A. Roa, Manfred Schedl, and Tobias Bruckmann. The motion suspension system – MSS: A cable-driven system for on-ground tests of space robots. In Masafumi Okada, editor, *Advances in Mechanism and Machine Science*, pages 379–388, Cham, 2023. Springer Nature Switzerland.

[EDSS+24] Ferdinand Elhardt, Marco De Stefano, Manfred Schedl, Martin Stelzer, Andreas Stemmer, Ismael Rodriguez, Ria Vijayan, Máximo A Roa, and Tobias Bruckmann. The motion suspension system for on-ground tests of space robots: Demonstration and results. In *2024 IEEE Aerospace Conference*, pages 1–9. IEEE, 2024.

[FAMPU14] Angel Flores-Abad, Ou Ma, Khanh Pham, and Steve Ulrich. A review of space robotics technologies for on-orbit servicing. *Progress in Aerospace Sciences*, 68:1–26, 2014.

[FANGT18] Angel Flores-Abad, Manuel Nandayapa, and Miguel A. Garcia-Teran. Force sensorless impedance control for a space robot to capture a satellite for on-orbit servicing. In *2018 IEEE Aerospace Conference*, pages 1–7, 2018.

[FAWMP13] Angel Flores-Abad, Zheng Wei, Ou Ma, and Khanh D Pham. Optimal control of a space robot to approach a tumbling object for capture with uncertainties in the boundary conditions. In *AIAA Guidance, Navigation, and Control (GNC) Conference*, page 4522, 2013.

[FAWMP14] Angel Flores-Abad, Zheng Wei, Ou Ma, and Khanh Pham. Optimal control of space robots for capturing a tumbling object with uncertainties. *Journal of Guidance, Control, and Dynamics*, 37(6):2014–2017, 2014.

[FAZWM17] Angel Flores-Abad, Lin Zhang, Zheng Wei, and Ou Ma. Optimal capture of a tumbling object in orbit using a space manipulator. *Journal of Intelligent & Robotic Systems*, 86(2):199–211, 2017.

[FDP+10] Pral J From, Vincent Duindam, Kristin Y Pettersen, Jan T Gravdahl, and Shankar Sastry. Singularity-free dynamic equations of vehicle–manipulator systems. *Simulation Modelling Practice and Theory*, 18(6):712–731, 2010.

[FK97] Roy Featherstone and Oussama Khatib. Load independence of the dynamically consistent inverse of the jacobian matrix. *The International Journal of Robotics Research*, 16(2):168–170, 1997.

[FKP+14a] Hans Joachim Ferreau, Christian Kirches, Andreas Potschka, Hans Georg Bock, and Moritz Diehl. qpoases: A parametric active-set algorithm for quadratic programming. *Mathematical Programming Computation*, 6(4):327–363, 2014.

[FKP+14b] Joachim Ferreau, Christian Kirches, Andreas Potschka, Hans Bock, and Moritz Diehl. qpOASES: A parametric active-set algorithm for quadratic programming. *Mathematical Programming Computation*, 6, 12 2014.

[Fri08] Robert B Friend. Orbital express program summary and mission overview. In *Sensors and Systems for space applications II*, volume 6958, pages 11–21. SPIE, 2008.

[GBB+25] Gerhard Grunwald, Bernhard Brunner, Alexander Beyer, Roberto Lampariello, Maximilian Maier, Manfred Schedl, Marco De Stefano, Martin Stelzer, Andreas Stemmer, and Máximo Alejandro Roa Garzon. Development and applications of space robotic manipulation technology at dlr. In *Symposium on Advanced Space Technologies in Robotics and Automation-ASTRA*. ESA, 2025.

[GGAS17] A. M. Giordano, G. Garofalo, and A. Albu-Schaffer. Momentum dumping for space robots. In *IEEE 56th Conference on Decision and Control (CDC)*, pages 5243–5248, Dec 2017.

[GHEO15] Gianluca Garofalo, Bernd Henze, Johannes Englsberger, and Christian Ott. On the inertially decoupled structure of the floating base robot dynamics. *IFAC-PapersOnLine*, 48(1):322–327, 2015.

[GK01] J.W. Grizzle and Jun-Mo Kang. Discrete-time control design with positive semidefinite lyapunov functions. *Systems & Control Letters*, 43(4):287–292, 2001.

[GLdR19] Rabindra A. Gangapersaud, Guangjun Liu, and Anton H. J. de Ruiter. Detumbling a non-cooperative space target with model uncertainties using a space manipulator. *Journal of Guidance, Control, and Dynamics*, 42(4):910–918, 2019.

[GOAS13] Gianluca Garofalo, Christian Ott, and Alin Albu-Schäffer. On the closed form computation of the dynamic matrices and their differentiations. In *2013 IEEE/RSJ International Conference on Intelligent Robots and Systems*, pages 2364–2359. IEEE, 2013.

[GP15] Paolo Gasbarri and Andrea Pisculli. Dynamic/control interactions between flexible orbiting space-robot during grasping, docking and post-docking manoeuvres. *Acta Astronautica*, 110:225–238, 2015.

[H+16] Panfeng Huang et al. Attitude coordinated control for docked spacecraft based on estimated coupling torque. *Journal of Aerospace Engineering*, 29(6), 2016.

[HASH14] Thomas Hulin, Alin Albu-Schäffer, and Gerd Hirzinger. Passivity and stability boundaries for haptic systems with time delay. *IEEE Transactions on Control Systems Technology*, 22(4):1297–1309, 2014.

[HBDH94] Gerd Hirzinger, Bernhard Brunner, Johannes Dietrich, and Johann Heindl. Rotex-the first remotely controlled robot in space. In *Proceedings of the 1994 IEEE international conference on robotics and automation*, pages 2604–2611. IEEE, 1994.

[HCT+19] D. Henry, J. Cieslak, J. Zenteno Torres, P. Colmenarejo, J. Branco, N. Santos, P. Serra, J. Telaard, H. Strauch, A.M. Giordano, M. De Stefano, C. Ott, M. Reiner, J. Jaworsk, E. Papadopoulos, G. Visentin, F. Ankersen, and J.G. Fernandez. Model-based fault diagnosis and tolerant control: the esa's e.deorbit mission. In *2019 18th European Control Conference (ECC)*, pages 4356–4361, 2019.

[Hol07] John M Hollerbach. A recursive lagrangian formulation of maniputator dynamics and a comparative study of dynamics formulation complexity. *IEEE Transactions on Systems, Man, and Cybernetics*, 10(11):730–736, 2007.

[Hol11] Darryl D Holm. *Geometric mechanics-part II: rotating, translating and rolling*. World Scientific, 2011.

[Hom22] Mohamadreza Homayounzade. Adaptive robust nonlinear control of spacecraft formation flying: a novel disturbance observer-based control approach. *International Journal of Dynamics and Control*, 10(5):1471–1484, 2022.

[HRO16] Bernd Henze, Maximo A Roa, and Christian Ott. Passivity-based whole-body balancing for torque-controlled humanoid robots in multi-contact scenarios. *Int. J. Robotics Res.*, 35(12):1522–1543, 2016.

[HS87] J. Hollerbach and Ki Suh. Redundancy resolution of manipulators through torque optimization. *IEEE Journal on Robotics and Automation*, 3(4):308–316, 1987.

[HWM+16] Panfeng Huang, Dongke Wang, Zhongjie Meng, Fan Zhang, and Jian Guo. Adaptive postcapture backstepping control for tumbling tethered space robot–target combination. *Journal of Guidance, Control, and Dynamics*, 39(1):150–156, 2016.

[HYL07] Panfeng Huang, Jianping Yuan, and Bin Liang. Adaptive sliding-mode control of space robot during manipulating unknown objects. In *2007 IEEE International Conference on Control and Automation*, pages 2907–2912. IEEE, 2007.

[Ike17] Yuichi Ikeda. Discrete-time nonlinear attitude tracking control of spacecraft. In *11th IEEE Asian Control Conference (ASCC)*, pages 617–622, 2017.

[IKO96] Abderrhaman Iggidr, Boris Kalitine, and Rachid Outbib. Semidefinite lyapunov functions stability and stabilization. *Mathematics of Control, Signals and Systems*, 9(2):95–106, 1996.

[J+16] Hiranya S. Jayakody et al. Robust adaptive coordination controller for a spacecraft equipped with a robotic manipulator. *Journal of Guidance, Control, and Dynamics*, 39(12):2699–2711, 2016.

[J+18] S. Jaekel et al. Design and operational elements of the robotic subsystem for the e.deorbit debris removal mission. *Frontiers in Robotics and AI*, 5:100, 2018.

[JCD17] Jinping Jia, Weisheng Chen, and Hao Dai. Multi-rate sampled-data control for a class of nonlinear systems via input-lyapunov matching. In *36th Chinese Control Conference (CCC)*, pages 868–871, 2017.

[JDLY19] Jinping Jia, Hao Dai, Jing Li, and Xiaoli Yang. Global stabilization by means of a new sampled-data control scheme for a class of nonlinear time-delay systems. In *9th International Conference on Information Science and Technology (ICIST)*, pages 24–28, 2019.

[JSKK16] Hiranya S Jayakody, Lingling Shi, Jay Katupitiya, and Nathan Kinkaid. Robust adaptive coordination controller for a spacecraft equipped with a robotic manipulator. *Journal of Guidance, Control, and Dynamics*, 39(12):2699–2711, 2016.

[KAA20] Atal Anil Kumar, Jean-Franccois Antoine, and Gabriel Abba. Control of an underactuated 4 cable-driven parallel robot using modified input-output feedback linearization. *IFAC-PapersOnLine*, 53(2):8777–8782, 2020.

[KdR23a] Serdar Kalaycioglu and Anton de Ruiter. Dual arm coordination of redundant space manipulators mounted on a spacecraft. *Robotica*, 41(8):2489–2518, 2023.

[KDR23b] Serdar Kalaycioglu and Anton De Ruiter. Passivity based nonlinear model predictive control (pnmpc) of multi-robot systems for space applications. *Frontiers in Robotics and AI*, 10:1181128, 2023.

[Kha95] Oussama Khatib. Inertial properties in robotic manipulation: An object-level framework. *The international journal of robotics research*, 14(1):19–36, 1995.

[Kha08] Hassan K. Khalil. *Nonlinear Systems Third Edition*. 2008.

[KK99] Nikolaos Kazantzis and Costas Kravaris. Time-discretization of nonlinear control systems via taylor methods. *Computers & Chemical Engineering*, 23(6):763–784, 1999.

[KRH10] Hamid Khaloozadeh and M Reza Homaeinejad. Real-time regulated sliding mode controller design of multiple manipulator space free-flying robot. *Journal of Mechanical Science and Technology*, 24(6):1337–1351, 2010.

[KSKP17] Sharmila Kayastha, Lingling Shi, Jay Katupitiya, and Garth Pearce. Nonlinear model predictive control of a planar three-link space manipulator. In *2017 11th Asian Control Conference (ASCC)*, pages 635–640. IEEE, 2017.

[KT11] Takuro KOBAYASHI and Shinichi TSUDA. Sliding mode control of space robot for unknown target capturing. *Engineering Letters*, 19(2):105, 2011.

[L+18] R. Lampariello et al. Tracking control for the grasping of a tumbling satellite with a free-floating robot. *IEEE Robotics and Automation Letters*, 3(4):3638–3645, Oct 2018.

[LS76] J. P. La Salle. *The Stability of Dynamical Systems*. Society for Industrial and Applied Mathematics, 1976.

[LXB97] Bin Liang, Yangsheng Xu, and Marcel Bergerman. Dynamically equivalent manipulator for space manipulator system. 1. In *Proceedings of International Conference on Robotics and Automation*, volume 4, pages 2765–2770. IEEE, 1997.

[M+15] Gan Ma et al. Hand-eye servo and impedance control for manipulator arm to capture target satellite safely. *Robotica*, 33(4), 2015.

[M+21] Mattia Mattioni et al. On feedback passivation under sampling. In *American Control Conference (ACC)*, pages 3578–3583, 2021.

[M+23] Hrishik Mishra et al. Reduced euler-lagrange equations of floating-base robots: Computations, properties and applications. *IEEE Transactions on Robotics*, 39(2):1439–1457, 2023.

[MAB01] M Marchesi, F Angrilli, and C Bettanini. On ground experiments of free-flyer space robot simulator in intervention missions. In *proceedings of 6th International Symposium on Artificial Intelligence, Robotics and Automation in Space 'i-SAIRAS*, 2001.

[MB17] Gaurav Misra and Xiaoli Bai. Task-constrained trajectory planning of free-floating space-robotic systems using convex optimization. *Journal of Guidance, Control, and Dynamics*, 40(11), 2017.

[MBC+07] Carlo Menon, S. Busolo, S. Cocuzza, A. Aboudan, A. Bulgarelli, C. Bettanini, M. Marchesi, and F. Angrilli. Issues and solutions for testing free-flying robots. *Acta Astronautica*, 60(12):957–965, 2007.

[MBDSO21] Hrishik Mishra, Ribin Balachandran, Marco De Stefano, and Christian Ott. A compliant partitioned shared control strategy for an orbital robot. *IEEE Robotics and Automation Letters*, 6(4):7317–7324, 2021.

[MDF+20] Jaret Matthews, Caitlin Driscoll, Edward Fouad, Andrew Welter, Marc Jarmulowicz, and Jessica Ipnar. Design, development, testing, and flight of the crew dragon docking system. In *45th Aerospace mechanisms symposium*, pages 483–494, 2020.

[MDSGO20] Hrishik Mishra, Marco De Stefano, Alessandro M. Giordano, and Christian Ott. Output feedback stabilization of an orbital robot. In *2020 59th IEEE Conference on Decision and Control (CDC)*, pages 1503–1501, 2020.

[MGDS+20] Hrishik Mishra, Alessandro M. Giordano, Marco De Stefano, Roberto Lampariello, and Christian Ott. Inertia-decoupled equations for hardware-in-the-loop simulation of an orbital robot with external forces. In *2020 IEEE/RSJ International Conference on Intelligent Robots and Systems (IROS)*, pages 1879–1886, 2020.

[MIG16] Narendran Muraleedharan, Douglas R. Isenberg, and Iacopo Gentilini. Recreating planar free-floating environment via model-free force-feedback control. In *2016 IEEE Aerospace Conference*, pages 1–12, 2016.

[MLS94] Richard M Murray, Zexiang Li, and S Shankar Sastry. *A mathematical introduction to robotic manipulation*. CRC press, 1994.

[MM89] Yasuhiro Masutani and Fumio Miyazaki. Sensory feedback control for space manipulators. *Journal of the Robotics Society of Japan*, 7(6):647–655, 1989.

[MMMANC22] Mattia Mattioni, Alessio Moreschini, Salvatore Monaco, and Doroth A©e Normand-Cyrot. Discrete-time energy-balance passivity-based control. *Automatica*, 146:110662, 2022.

[MP07] S. Ali A. Moosavian and Evangelos Papadopoulos. Free-flying robots in space: an overview of dynamics modeling, planning and control. *Robotica*, 25(5):537–547, 2007.

[Nat01] National Aeronautics and Space Administration. The human touch: The history of the skylab program, 2001. Accessed: 01-May-2026.

[Nat23] National Aeronautics and Space Administration. Hubble space telescope – servicing missions, 2023. Accessed: 01-May-2026.

[NP22] I Napoli and M Pontani. Discrete-variable-thrust guidance for orbital rendezvous based on feedback linearization. *Aerotecnica Missili & Spazio*, 101(4):351–360, 2022.

[NY99] D.N. Nenchev and K. Yoshida. Impact analysis and post-impact motion control issues of a free-floating space robot subject to a force impulse. *IEEE Transactions on Robotics and Automation*, 15(3):548–557, 1999.

[NYVU02] Dragomir N Nenchev, Kazuya Yoshida, Prasart Vichitkulsawat, and Masaru Uchiyama. Reaction null-space control of flexible structure mounted manipulator systems. *IEEE Transactions on Robotics and Automation*, 15(6):1011–1023, 2002.

[OANY11] Tomohisa Oki, Satoko Abiko, Hiroki Nakanishi, and Kazuya Yoshida. Time-optimal detumbling maneuver along an arbitrary arm motion during the capture of a target satellite. In *2011 IEEE/RSJ International Conference on Intelligent Robots and Systems*, pages 625–630, 2011.

[OKN08] Christian Ott, Andreas Kugi, and Yoshihiko Nakamura. Resolving the problem of non-integrability of nullspace velocities for compliance control of redundant manipulators by using semi-definite lyapunov functions. In *IEEE International Conference on Robotics and Automation*, pages 1999–2004, 2008.

[ONY08] Tomohisa Oki, Hiroki Nakanishi, and Kazuya Yoshida. Time-optimal manipulator control of a free-floating space robot with constraint on reaction torque. In *2008 IEEE/RSJ International Conference on Intelligent Robots and Systems*, pages 2828–2833, 2008.

[Ott08] Christian Ott. *Cartesian impedance control of redundant and flexible-joint robots*. Springer, 2008.

[PAML21a] Evangelos Papadopoulos, Farhad Aghili, Ou Ma, and Roberto Lampariello. Robotic manipulation and capture in space: A survey. *Frontiers in Robotics and AI*, 8:686723, July 2021.

[PAML21b] Evangelos Papadopoulos, Farhad Aghili, Ou Ma, and Roberto Lampariello. Robotic manipulation and capture in space: A survey. *Frontiers in Robotics and AI*, 8, 2021.

[PD93] E. Papadopoulos and S. Dubowsky. Dynamic singularities in free-floating space manipulators. *Journal of Dynamic Systems, Measurement, and Control*, 115(1):44–52, 03 1993.

[PLK17] Christopher D Petersen, Frederick Leve, and Ilya Kolmanovsky. Model predictive control of an underactuated spacecraft with two reaction wheels. *Journal of Guidance, Control, and Dynamics*, 40(2):320–332, 2017.

[PM94] E. Papadopoulos and S. Ali A. Moosavian. Dynamics and control of multi-arm space robots during chase and capture operations. In *Proceedings of IEEE/RSJ Interna-*

tional Conference on Intelligent Robots and Systems (IROS'94), volume 3, pages 1554–1561 vol.3, 1994.

[PMK+13] Andreas Pott, Hendrik Mütherich, Werner Kraus, Valentin Schmidt, Philipp Miermeister, Thomas Dietz, and Alexander Verl. Cable-driven parallel robots for industrial applications: The ipanema system family. In *IEEE ISR 2013*, pages 1–6, 2013.

[Por95] David SF Portree. *Mir hardware heritage*, volume 1357. Lyndon B. Johnson Space Center, 1995.

[PP88] Brad Paden and Ravi Panja. Globally asymptotically stable 'pd+' controller for robot manipulators. *International Journal of Control*, 47(6):1697–1712, 1988.

[PP13a] Iosif S Paraskevas and Evangelos G Papadopoulos. On the use of the center of percussion for space manipulators during impacts. In *2013 IEEE International Conference on Robotics and Automation*, pages 3469–3474. IEEE, 2013.

[PP13b] Iosif S. Paraskevas and Evangelos G. Papadopoulos. On the use of the center of percussion for space manipulators during impacts. In *2013 IEEE International Conference on Robotics and Automation*, pages 3469–3474, 2013.

[PP23] Mauro Pontani and Marco Pustorino. Low-thrust lunar capture leveraging nonlinear orbit control. *The Journal of the Astronautical Sciences*, 70(5):28, 2023.

[R+] Máximo A. Roa et al. Eross: In-orbit demonstration of european robotic orbital support services. In *2024 IEEE Aerospace Conference*, pages 1–9.

[RM25] DLR Robotics and Mechatronics. DLR's advancements in space robotic manipulation. (YouTube video. Accessed: 2026-08-02), `https://www.youtube.com/watch?v=8OtwR-S6QUs` 2025.

[RMNL11] P Rank, Q Mühlbauer, W Naumann, and K Landzettel. The deos automation and robotics payload. In *Symp. on Advanced Space Technologies in Robotics and Automation, ASTRA, the Netherlands*, 2011.

[RPA+24] Gerasimos Rigatos, Jorge Pomares, Masoud Abbaszadeh, Krishna Busawon, Zhiwei Gao, and Farouk Zouari. Nonlinear optimal control for free-floating space robotic manipulators. *Spacecraft and Satellites*, 1:2450001, 2024.

[RSS17] Tomasz Rybus, Karol Seweryn, and Jurek Z Sasiadek. Control system for free-floating space manipulator based on nonlinear model predictive control (nmpc). *Journal of Intelligent & Robotic Systems*, 85(3):491–509, 2017.

[Ryb24] Tomasz Rybus. Robotic manipulators for in-orbit servicing and active debris removal: Review and comparison. *Progress in Aerospace Sciences*, 151:101055, 2024.

[S+05] Russell Smith et al. Open dynamics engine. 2005.

[S+18] Karol Seweryn et al. Validation of the robot rendezvous and grasping manoeuvre using microgravity simulators. In *IEEE International Conference on Robotics and Automation (ICRA)*, pages 873–880, 2018.

[SB08] Karol Seweryn and Marek Banaszkiewicz. Optimization of the trajectory of a general free-flying manipulator during the rendezvous maneuver. In *AIAA Guidance, Navigation and Control Conference and Exhibit*, 2008.

[SBR22] Karol Seweryn, Fatina L. Basmadji, and Tomasz Rybus. Space robot performance during tangent capture of an uncontrolled target satellite. *The Journal of the Astronautical Sciences*, 69(4):1017–1047, 2022.

[SDSMV26] Francesco Sena, Marco De Stefano, Hrishik Mishra, and Ria Vijayan. Verfahren zur Steuerung eines Robotermanipulators im Weltraum. *Deutsches Zentrum fuer Luft und Raumfahrt eV*, (DE102025118932.3), submitted, May 2026.

[Sil82] William M Silver. On the equivalence of lagrangian and newton-euler dynamics for manipulators. *The International Journal of Robotics Research*, 1(2):60–70, 1982.

[SJK12] Rodolphe Sepulchre, Mrdjan Jankovic, and Petar V Kokotovic. *Constructive nonlinear control*. Springer Science & Business Media, 2012.

[SL+91] Jean-Jacques E Slotine, Weiping Li, et al. *Applied nonlinear control*, volume 199. Prentice hall Englewood Cliffs, NJ, 1991.

[SMVDS25] Francesco Sena, Hrishik Mishra, Ria Vijayan, and Marco De Stefano. A control strategy for an orbital manipulator equipped with an external actuator at the end-effector. In *2025 IEEE International Conference on Robotics and Automation (ICRA)*, pages 14617–14623, 2025.

[SPH03] Jana L. Schwartz, Mason A. Peck, and Christopher D. Hall. Historical review of air-bearing spacecraft simulators. In *Journal of Guidance, Control and Dynamics*, pages AAS 03–125, 2003.

[SRdF22] Rogerio R Santos, Domingos A Rade, and Ijar M da Fonseca. A machine learning strategy for optimal path planning of space robotic manipulator in on-orbit servicing. *Acta Astronautica*, 191:41–54, 2022.

[SS19] Asma Seddaoui and Chakravarthini M Saaj. Combined nonlinear h-infinity controller for a controlled-floating space robot. *Journal of Guidance, Control, and Dynamics*, 42(8):1878–1885, 2019.

[SSN21] Asma Seddaoui, Chakravarthini Mini Saaj, and Manu Harikrishnan Nair. Modeling a controlled-floating space robot for in-space services: A beginner's tutorial. *Frontiers in Robotics and AI*, 8:725333, 2021.

[SSVdSF05] S. Stramigioli, C. Secchi, A.J. Van der Schaft, and C. Fantuzzi. Sampled data systems passivity and discrete port-Hamiltonian systems. *Robotics, IEEE Transactions on*, 21(4):574–587, Aug 2005.

[SSVO08] Bruno Siciliano, Lorenzo Sciavicco, Luigi Villani, and Giuseppe Oriolo. *Robotics: Modelling, Planning and Control - Chapter 8: Motion Control*. Springer Publishing Company, Incorporated, 1st edition, 2008.

[ST22] Esubalew W Shibabw and Gerbaw Y Tamiru. Fuzzy sliding mode controller based trajectory tracking control of free flying space robot manipulator system. In *International Conference on Advances of Science and Technology*, pages 137–158. Springer, 2022.

[SUM+04] Hirokata Sawada, Kyoichi Ui, Makoto Mori, Hiroshi Yamamoto, Ryoichi Hayashi, Saburo Matunaga, and Yoshiaki Ohkami. Micro-gravity experiment of a space robotic arm using parabolic flight. *Advanced Robotics*, 18(3):247–267, 2004.

[SVMDS26] Francesco Sena, Ria Vijayan, Hrishik Mishra, and Marco De Stefano. Center-of-mass and attitude control of an orbital manipulator: A novel control strategy. *IEEE Robotics and Automation Letters (RA-L)*, 2026.

[SXSW22] Lingling Shi, Xiaolong Xiao, Minghe Shan, and Xiaoyi Wang. Force control of a space robot in on-orbit servicing operations. *Acta Astronautica*, 193:469–482, 2022.

[TD92] Miguel A Torres and Steven Dubowsky. Minimizing spacecraft attitude disturbances in space manipulator systems. *Journal of guidance, control, and dynamics*, 15(4):1010–1017, 1992.

[TMNC16] Valentin Tanasa, Salvatore Monaco, and Dorothée Normand-Cyrot. Backstepping control under multi-rate sampling. *IEEE Transactions on Automatic Control*, 61(5):1208–1222, 2016.

[TMSL24] Pedro Taborda, Hugo Matias, Daniel Silvestre, and Pedro Lourencco. Convex mpc and thrust allocation with deadband for spacecraft rendezvous. *IEEE Control Systems Letters*, 8:1132–1137, 2024.

[TWF10] Zhixiang Tian, Hongtao Wu, and Chun Feng. Hierarchical adaptive backstepping sliding mode control for underactuated space robot. In *2010 2nd International Asia Conference on Informatics in Control, Automation and Robotics (CAR 2010)*, volume 1, pages 500–503. IEEE, 2010.

[ULA+10] Naohiro Uyama, Hravard Lund, Koki Asakimori, Yuki Ikeda, Daichi Hirano, Hiroki Nakanishi, and Kazuya Yoshida. Integrated experimental environment for orbital robotic systems, using ground-based and free-floating manipulators. In *2010 IEEE/SICE International Symposium on System Integration*, pages 108–113, 2010.

[UY87] Yoji Umetani and Kazuya Yoshida. Continuous path control of space manipulators mounted on omv. *Acta Astronautica*, 15(12):981–986, 1987.

[UY89] Yoji Umetani and Kazuya Yoshida. Experimental study on two-dimensional free-flying robot satellite model. In *JPL, California Inst. of Tech., Proceedings of the NASA Conference on Space Telerobotics, Volume 5*, 1989.

[VD87] Z Vafa and Steven Dubowsky. On the dynamics of manipulators in space using the virtual manipulator approach. In *Proceedings. 1987 IEEE International Conference on Robotics and Automation*, volume 4, pages 579–585. IEEE, 1987.

[VDO22] Ria Vijayan, Marco De Stefano, and Christian Ott. Control of an orbital manipulator with reaction wheels for on-orbit servicing. *IFAC-PapersOnLine*, 55(38), 2022. 13th IFAC Symposium on Robot Control.

[VdS00] A.J. Van der Schaft. *L_2-Gain and Passivity Techniques in Nonlinear Control*. Communication and Control Engineering. Springer Verlag, 2000.

[VDSDO25] Ria Vijayan, Marco De Stefano, Alexander Dietrich, and Christian Ott. Unified control of an orbital manipulator for the approach and grasping of a free-floating satellite. *IEEE/ASME Transactions on Mechatronics*, 30(6):5710–5721, 2025.

[VDSO22] Ria Vijayan, Marco De Stefano, and Christian Ott. A detumbling strategy for an orbital manipulator in the post-grasp phase. In *IEEE International Conference on Robotics and Automation*, 2022.

[VDSO25] Ria Vijayan, Marco De Stefano, and Christian Ott. Method for controlling a space manipulator. *Deutsches Zentrum fuer Luft und Raumfahrt eV*, (DE102025111079.4), submitted, March 2025.

[VDSO26a] Ria Vijayan, Marco De Stefano, and Christian Ott. Method and system for operating an orbital manipulator arranged on a spacecraft. *Deutsches Zentrum fuer Luft und Raumfahrt eV*, (DE102026101406.2), submitted, March 2026.

[VDSO26b] Ria Vijayan, Marco De Stefano, and Christian Ott. Sampling-aware multi-rate combined control of an orbital manipulator. *IEEE Robotics and Automation Letters (RA-L)*, 2026.

[W+08] Z.M. Wang et al. On stability properties of nonlinear time-varying systems by semi-definite time-varying lyapunov candidates. *IFAC Proceedings Volumes*, 41(2):1123–1128, 2008.

[W+23] Yuedong Wu et al. Adaptive fault-tolerant control for spacecraft formation under external disturbances with guaranteed performance. *Advances in Space Research*, 72(5):1583–1592, 2023.

[WLW16] Mingming Wang, Jianjun Luo, and Ulrich Walter. A non-linear model predictive controller with obstacle avoidance for a space robot. *Advances in Space Research*, 57(8):1737–1746, 2016.

[WOD22] Xuwei Wu, Christian Ott, and Alexander Dietrich. A comparative experimental study of multi-tasking tracking and interaction control on a torque-controlled humanoid robot. In *2022 American Control Conference (ACC)*, pages 1933–1940, 2022. accepted.

[WRS24] Mateusz Wojtunik, Tomasz Rybus, and Karol Seweryn. An adaptive backstepping control for a free-floating space manipulator using a linearly parametrized dynamic model. *Journal of Aerospace Engineering*, 37(2):04023117, 2024.

[WS26] Patrick M. Wensing and Jean-Jacques E. Slotine. Coriolis factorizations and their connections to riemannian geometry. *IEEE Transactions on Automatic Control*, 71(6):3788–3803, 2026.

[WW93] Liang-Boon Wee and M.W. Walker. On the dynamics of contact between space robots and configuration control for impact minimization. *IEEE Transactions on Robotics and Automation*, 9(5):581–591, 1993.

[WX94] Gregory C White and Yangsheng Xu. An active vertical-direction gravity compensation system. *IEEE transactions on instrumentation and measurement*, 43(6):786–792, 1994.

[X+20] Yaen Xie et al. Obstacle avoidance and path planning for multi-joint manipulator in a space robot. *IEEE Access*, 8, 2020.

[XHW+13] Yongchun Xie, Jun Hu, Min Wang, Haixia Hu, and Hao Zhang. Accurate and stable control of shenzhou spacecraft in rendezvous and docking. *IFAC Proceedings Volumes*, 46(19):524–528, 2013.

[XSK+20] Zhicheng Xie, Tao Sun, Trevor Hocksun Kwan, Zhongcheng Mu, and Xiaofeng Wu. A new reinforcement learning based adaptive sliding mode control scheme for free-floating space robotic manipulator. *IEEE Access*, 8:127048–127064, 2020.

[YHKMP15] Wei Yang Ho, Werner Kraus, Alexander Mangold, and Andreas Pott. Haptic interaction with a cable-driven parallel robot using admittance control. In Andreas Pott and Tobias Bruckmann, editors, *Cable-Driven Parallel Robots*, pages 201–212, Cham, 2015. Springer International Publishing.

[YN95] Kazuya Yoshida and Dragomir N. Nenchev. Space robot impact analysis and satellite-base impulse minimization using reaction null-space. *Proceedings - IEEE International Conference on Robotics and Automation*, 2:1271–1277, 1995.

[YN03] K. Yoshida and H. Nakanishi. Impedance matching in capturing a satellite by a space robot. In *Proceedings 2003 IEEE/RSJ International Conference on Intelligent Robots and Systems (IROS 2003) (Cat. No.03CH37453)*, volume 4, pages 3059–3064 vol.3, 2003.

[YNU+04] Kazuya Yoshida, Hiroki Nakanishi, Hiroshi Ueno, Noriyasu Inaba, Takeshi Nishimaki, and Mitsushige Oda. Dynamics, control and impedance matching for robotic capture of a non-cooperative satellite. *advanced robotics*, 18(2):175–198, 2004.

[Yos94] Kazuya Yoshida. Experimental study on the dynamics and control of a space robot with experimental free-floating robot satellite. *Advanced Robotics*, 9(6):583–602, 1994.

[Yos00] Kazuya Yoshida. Space robot dynamics and control: to orbit, from orbit, and future. In *Robotics Research: The Ninth International Symposium*, pages 449–456. Springer, 2000.

[Yos03] Kazuya Yoshida. Engineering test satellite vii flight experiments for space robot dynamics and control: Theories on laboratory test beds ten years ago, now in orbit. *The International Journal of Robotics Research*, 22(5):321–335, 2003.

[YXHL19] Lei Yan, Wenfu Xu, Zhonghua Hu, and Bin Liang. Virtual-base modeling and coordinated control of a dual-arm space robot for target capturing and manipulation. *Multibody system dynamics*, 45(4):431–455, 2019.

[ZD25] Qin Zhao and Guangren Duan. Adaptive backstepping tracking control of space manipulator based on neural network. In *2025 4th Conference on Fully Actuated System Theory and Applications (FASTA)*, pages 2198–2202. IEEE, 2025.

[ZE20] Lijun Zong and M Reza Emami. Concurrent base-arm control of space manipulators with optimal rendezvous trajectory. *Aerospace Science and Technology*, 100:105822, 2020.